An Adaptive
Shallow Water Model
on the Sphere

von Thomas Heinze

Dissertation

zur Erlangung des Grades eines Doktors der Naturwissenschaften
- Dr. rer. nat. -

Datum des Promotionskolloquiums: 30. Januar 2009

Gutachter: PrivDoz. Dr. Jörn Behrens (Universität Bremen)
Prof. Dr. Klaus Dethloff (Universität Potsdam)

Zusammenfassung:

Diese Arbeit beschreibt das adaptive Flachwassermodell **PLASMA-FEM*m*E**. Es löst auf einer Kugel die Flachwassergleichungen, den Prototyp partieller Differentialgleichungen in der Atmosphärenmodellierung, mit Hilfe eines semi-impliziten semi-Lagrangeschen Zeitschrittes und linearer finiter Elemente. Der Gittergenerator *amatos* erzeugt das Rechengitter - untersucht werden sowohl statische als auch dynamische Gittergenerierung. Die Ergebnisse werden mit denen des Vorläufermodells **FEM*m*E** verglichen, das ein statisches, uniformes Gitter benutzt.

Die Resultate demonstrieren sowohl die Leistungsfähigkeit und auch die Grenzen des verwendeten Ansatzes. Die Gitteranpassung lässt sich mit *amatos* leicht bewerkstelligen und es treten keine Reflexionen an den Gittergrenzen auf. Allerdings werden an den Gittergrenzen in einem Testfall Instabilitäten ausgelöst. In einem anderen Testfall, bei dem die analytische Lösung bekannt ist, werden mit dem gewählten Verfahren die numerischen Fehler sowohl mit statischer als auch mit dynamischer Gitteranpassung deutlich reduziert ohne den Rechenaufwand stark zu erhöhen. Bei den Erhaltungsgrößen ergibt sich ein differenziertes Bild. Die Massenerhaltung lässt sich mit einem geeigneten statischen Gitter in einem der untersuchten Testfälle erreichen. Bei komplexen Strömungen verlieren sich die Erhaltungseigenschaften im Laufe der Simulation mit dynamischer Gitteranpassung jedoch mehr und mehr.

Dennoch lassen die Ergebnisse insgesamt den Schluss zu, dass es sich um einen geeigneten Ansatz handelt. Allerdings gibt es zusätzlichen Forschungsbedarf, um ein noch tieferes Verständnis der Wechselwirkung zwischen den beteiligten physikalischen Vorgängen und der numerischen Verfahren zu entwickeln. Es besteht begründete Hoffnung, dass mit diesem Verständnis und unter Verwendung sowohl konservativer Advektionsschemata als auch modifizierter Adaptionskriterien die angesprochenen Probleme behoben werden können.

Summary:

This thesis describes the adaptive shallow water model **PLASMA-FEMmE**. It solves on the sphere the shallow water equations, the prototype for partial differential equations in atmospheric modeling, using a semi-implicit semi-Lagrangian time step and linear finite elements. Both statically and dynamically adapted grids created by the grid generator *amatos* are investigated. The results are compared with those of the predecessor model **FEMmE** that uses a static uniform grid.

The outcome demonstrates the capability of the chosen approach as well as its limits. Grid adaptation can easily be achieved with *amatos*. No reflexions at the grid interfaces are observed. Though in one test case instabilities are released at the grid interfaces. The numerical errors are reduced without a considerable enhancement of the computational effort in another test case with a well-known analytical solution. In respect to the conservation properties the results are more complicated. Mass conservation can be achieved in one test case with an appropriate static grid. In case of complex flow regimes all conservation properties are weakened during the simulation using dynamic grid adaptation.

Nevertheless it can be concluded that the investigated scheme works out fine within the expectations. There is additional research effort to get a deeper understanding of the interactions between the involved physical processes and the numerical schemes. Together with that understanding and conservative advection schemes as well as more sophisticated adaption criteria there is hope that the aforementioned problems can be overcome.

Author's address:

Thomas Heinze
Niersteiner Str. 7
D-60598 Frankfurt am Main

für Sia und Vitus

La filosofia è scritta in questo grandissimo libro che continuamente ci sta aperto innanzi a gli occhi (io dico l'universo), ma non si può intendere se prima non s'impara a intender la lingua, e conoscer i caratteri, ne' quali è scritto. Egli è scritto in lingua matematica, e i caratteri sono triangoli, cerchi, ed altre figure geometriche, senza i quali mezi è impossibile a intenderne umanamente parola; senza questi è un aggirarsi vanamente per un'oscuro laberinto.

Philosophy is written in that great book which continually lies open before us (I mean the Universe). But one cannot understand this book until one has learned to understand the language and to know the letters in which it is written. It is written in the language of mathematics, and the letters are triangles, circles and other geometric figures. Without these means it is impossible for mankind to understand a single word; without these means there is only vain stumbling in a dark labyrinth.

Die Philosophie steht in jenem großen Buch geschrieben, das uns ständig offen vor Augen liegt (ich spreche vom Universum). Aber dieses Buch ist nicht zu verstehen, ehe man nicht gelernt hat, die Sprache zu verstehen, und die Buchstaben kennt, in denen es geschrieben ist. Es ist in der Sprache der Mathematik geschrieben, und die Buchstaben sind Dreiecke, Kreise und andere geometrische Figuren. Ohne diese Mittel ist es dem Menschen unmöglich, ein einziges Wort davon zu verstehen; ohne sie ist es ein vergebliches Umherirren in einem dunklen Labyrinth.

Galileo Galilei, Il saggiatore, 1623

Contents

List of Figures

List of Tables

Introduction

During the last decade simulations with state-of-the-art global circulation models (GCMs) led to a much better understanding of the earth's climate system. One of the prominent results is that our climate has been changing perpetually. This concludes an ongoing process.

The third assessment report of the Intergovernmental Panel of Climate Change (Houghton et al. (2001)) stated that the mean global temperature of the earth will increase by $0.5°$ to $1.5°C$ within the next 25 years. Depending on political actions implemented now there will be (or will not be) a further increase up to $5.6°C$ above the 1990 temperature level until the end of this century.

There is an anthropogenic impact to this increase. But its amount is disputed, because the internal variability of the climate system is still unsettled. Also no assured insight in the regional impacts of these changes can be given with these GCMs. The reason is that those models are stuck to a more or less uniform horizontal resolution of the globe. So even on modern supercomputers a high resolution model simulation for a century would take months. Even worse - because of the uncertainty of the models one simulation is not enough. Many simulations with different initial conditions and a statistical analysis of all runs would be necessary to make a statement. Thus today only global statements are available, achieved with coarse resolution GCMs.

Hence one task for the modellers is to overcome these restrictions. One approach is to use so called adaptive grids with a regionally varying resolution. The total number of grid points should stay at the level of coarse GCMs, but in "areas of interest" a higher resolution is used. The price to pay is the reduced number of grid points elsewhere.

Two types of adaptive grids are used, static and dynamic ones. The first approach uses fixed grids that are determined at the beginning of the simulation. In the second approach the grids are adapted during the simulation after a certain number of time steps. In this thesis the adaptive grid approach with both types is investigated. The techniques and difficulties of using a spherical grid generator are described and adaption criteria are given.

One attempt using the full set of equations describing the atmospheric processes would fail because of the complexity of the system. It is wise to start with a well-investigated small coupled system of partial differential equations (PDEs) as a prototype. Most atmospheric models first investigate a shallow water model (SWM). It is based on the shallow water equations (SWE), a set of equations derived from the principles of conservation of mass and momentum. They describe the interaction of velocity and pressure of a hydrostatic and incompressible fluid. Williamson et al. (1992) proposed a collection of test cases for SWM. They also classified the different forms of the SWE and provided reference solutions for those test cases where no analytical solution is known. These solutions are based on the NCAR* spectral model with T213 resolution. Just recently a revised version of these

---

*National Center for Atmospheric Research, Boulder, Colorado, USA

reference solutions were presented within the ICON[**] project of Deutscher Wetterdienst (DWD) and Max Planck Institute for Meteorology (MPI-M) (Rípodas et al. (2005)). They are now available with double precision in T426 respectively T511 resolution. Besides that, some known errors in the code were corrected and the associated Legendre polynomials were calculated with a higher order. In this thesis, results for test case 2 and test case 5 of the Williamson test suite are discussed.

The model **PLASMA-FEM*m*E** presented here is one outcome of the joint research project "Dynamic of large scale atmospheric circulation patterns" in the framework of the German climate research program (DEKLIM) and one basis of the parallel large scale model of the atmosphere (**PLASMA**). **PLASMA-FEM*m*E** itself is based on the finite element model for meteorological equations **FEM*m*E**. This grid point model was developed by the author over the last years and solves the SWE taken in advective form by a semi-implicit semi-Lagrangian approach leading to a PDE of Helmholtz type. With the aid of linear finite elements (FE) this PDE is solved. The uniform grids used are derived from the bucky ball also known as soccer ball. It is one of the generalised icosahedral grids introduced by Giraldo (2000). A full description of the model can be found in Heinze (1998). Heinze and Hense (2002) concentrate on the main features and results.

In this thesis the focus lies on the adaptive grid refinement. The used grid generator called *amatos* has been developed by Behrens (2004). Some details about it are given in the first chapter of this thesis.

The other basis of **PLASMA** is the model **PLASMA-P** developed at the Alfred Wegener Institute (AWI) for Marine and Polar Research in Potsdam by Läuter (2004). It also uses *amatos*, but the basis polyhedron is the icosahedron itself and the SWE are taken in vorticity divergence form. The numerical solutions are also obtained by the Lagrange-Galerkin method. In his thesis Läuter also introduced new test cases. One of them, the unsteady solid body rotation, is also investigated here.

Other models also use the icosahedron as basis grid. Giraldo (2000) takes a similar Lagrange-Galerkin approach as **FEM*m*E** , but using the three-dimensional (3d) constrained form of the SWE. Stuhne and Peltier (1999) start with that form but transform it into a 3d flux form introducing Rossby and Froude number. For solving the equations they take finite difference (FD) operators and a leapfrog time step scheme. **GME**, the present-day operational GCM of DWD (Majewski et al. (2002)), uses similar FD operators, a semi-implicit Eulerian time step, but its shallow water version is given in the two-dimensional (2d) flux form. ICON, the successor of **GME**, is currently under development. Its grids are also derived from the icosahedron. Additionally it will support a local zooming option for using static adaptive grids. The SWE are given in flux form, but include vorticity and kinetic energy as diagnostic quantities. Another feature of ICON is the finite volume (FV) approach using a staggered C grid for solving the SWE with the aid of semi-implicit Eulerian time step schemes. Preliminary results are presented in Bonaventura (2004). Pesch (2002) presented in his diploma thesis a FV approach in combination with Eulerian time step schemes based on the icosahedral grid, but taking the vorticity divergence form of the SWE. Tomita et al. (2001) optimised the icosahedral grid by spring dynamics. The SWE are used in the flux form of the ICON model and solved by FV with an explicit Adams-Bashforth time discretisation.

The dual grid of the icosahedron is the dodecahedron. Instead of triangles this grid consists of pentagons and hexagons. There are some models that operate on that. Among them are a twisted icosahedral model by Heikes and Randall (1995), a potential vorticity approach

---

[**]Icosahedral non-hydrostatic GCM

by Thuburn (1997) and the comparison of an unstaggered Z grid with a staggered ZM grid by Ringler and Randall (2002).

In the last year also adaptive approaches based on quadrilateral grids have been developed. Blikberg and Sørevik (2003) used for that purpose the package CLAWPACK developed by Leveque et al. (2000). Jablonowski et al. (2006) took a spherical adaptive block-structured mesh refinement library developed at the University of Michigan by Oehmke and Stout (2001) and Oehmke (2003). Both models use FV techniques and introduced well elaborated techniques to handle the pole problem that naturally occurs in the quadrilateral approach.

This thesis is grouped into five chapters. The first one deals with the sphere and the computational grid. The adaptive grid generator *amatos* is introduced as well as the used refinement and coarsening criteria. In-depth two refinement techniques and one coarsening strategy are presented.

In chapter 2 the spherical shallow water equations are outlined and a dimensionless version is deduced. They are discretised in time with the semi-Lagrangian approach along trajectories in the following chapter. The obtained equations are combined to one PDE of Helmholtz type. This one is solved with the aid of FE. Therefore, the appropriate Sobolev space is determined and the weak formulation of the Helmholtz problem is given. For linear FE stiffness and mass matrix are specified at the end of that chapter.

Detailed information about the model **PLASMA-FEMmE** itself and the algorithm are given in chapter four. Description of a second order interpolation scheme on the triangles with the help of barycentric coordinates, about the way of calculating derivatives at the grid points and evaluating values at the departure and mid point of the trajectories can be found there. At the end of that chapter particulars of the grid adaption process are given among them modifications of the standard procedure used in *amatos*.

The last chapter with the discussion of the numerical results is the largest one. After identifying the test quantities three test cases are presented. The first one features a steady state situation with a balanced geostrophic flow. In the second one a 2000 meter high mountain is placed into that flow as an obstacle. Thereby different kind of waves are initiated. Both test cases are studied with several configurations of the adaptive grid and compared among each other as well as with results of the non adaptive model **FEMmE**. . The third test case is an unsteady solid body rotation. Here static grids are compared in respect to conservation properties and numerical errors. A deep insight into one adaptive experiment is given where instabilities were released.

This last chapter enfolds more than 80 pages and 90 figures. Some reader might object that the layout of this thesis at hand looks like a "picture book". But it is the intention of the author as there are good reasons for this. It is his conviction that figures contains more information than can be described by words and they are a better description of the discussed points. Additionally the reader should have the possibility to get his own view. In other publications one has to focus only on certain aspects due to several limitations. In contrast to that in a thesis there is the freedom to discuss many details. The last point explains the large number of figures here.

Chapter 1

The sphere and its discretisation

Two different type of GCMs are nowadays operational in climate mode and for numerical weather prediction (NWP), spectral and grid point models. The sphere is the appropriate simplification of the globe and the basis for both types of models. Spectral NWP models, like the Integrated Forecast System (IFS) of ECMWF[1] (Barros et al. 1995), are based on spherical harmonics. They are the eigenfunctions of the Laplacian on the sphere. This property makes operations on the sphere easy and numerically cheap. But one drawback is the so called pole problem. The equations are not defined at the pole and in its vicinity the suitable Gaussian grid has many grid points. On the other side near the equator the resolution is coarse. An additional disadvantage is the impossibility of locally refined grids.

In the last decade grid point oriented approaches have become more and more popular. Grid point models use a discretisation of the sphere. The five platonic bodies seem to be an adequate choice. Substantial progress has been achieved by models based on the icosahedron, such as e.g. **GME** of DWD (Majewski et al. 2002).

A classification of generalised icosahedral grids (GIG) of order p was introduced by Giraldo (2000). Due to reasons given later, here this classification is extended to a more general class, the so called extended generalised icosahedral grids of order p and refinement index q (EGIG(p,q)). They have the following properties:

$$\text{Number of points:} \quad N_{p,q} = 10\,p^2\,q + 2 \tag{1.1}$$

$$\text{Number of triangles:} \quad N_t = 2\,(N_{p,q} - 2) \tag{1.2}$$

$$\text{Number of edges:} \quad N_e = 3\,(N_{p,q} - 2) \tag{1.3}$$

q is the number of similar triangles that are obtained during the refinement process within
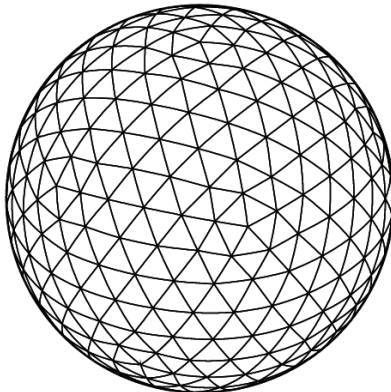
Figure 1.1: **FEM*m*E**'s EGIG(6,1)
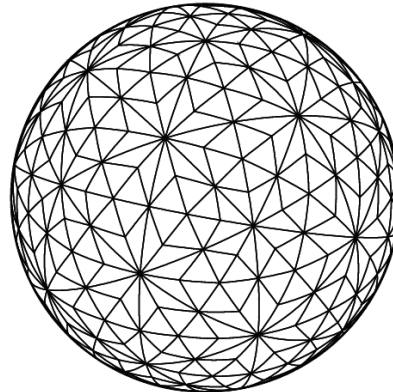
Figure 1.2: **PLASMA-FEM*m*E**'s EGIG(3,4)

---

[1]European Centre for Medium Range Weather Forecast, Reading, UK
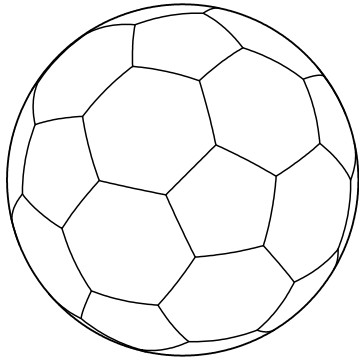
Figure 1.3: Bucky or soccer ball   Figure 1.4: Macro triangulation EGIG(3,1)
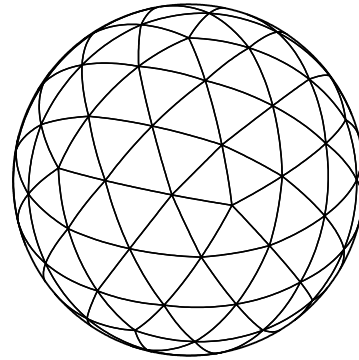
a triangle of the coarsest resolution, the macro triangulation. EGIG(1,1) is the before mentioned icosahedron.

Giraldo only considered refinement strategies where all arising triangles are similar to each other. Thus, taking $q = 1$ one gets Giraldo's GIG classification. With the refinement strategies introduced later in section 1.2 a different types of grids occur. Figures 1.1 and 1.2 show two grids with the same number of grid points, triangles and edges. Apparently they are not equal. The grid points are connected in a different way. But both grids are of level 6 according to Giraldo's classification. One main feature of the discussion in chapter 5 is the comparison of both types of grids in respect to their numerical properties. So, the first reason for introducing EGIG is easy distinction of both types of grids.

The developer of **FEMmE** did not take one of the platonic bodies. Inspired by the soccer game he started with the bucky ball (Figure 1.3). This polyhedron consists of 12 pentagons and 20 hexagons. Adding the mid points of each polygon and connecting this point with the original points of the polygon a body with 180 triangles is obtained with grid level $p = 3$ in Giraldo's system (Figure 1.4). Applicable EGIGs have an almost uniform distribution of the grid points over the sphere. The 12 grid points of the icosahedron, that are the mid points of the pentagons in EGIG(3,1), are special, because they have only 5 neighbouring points, in contrast to all others that have 6 neighbours. One problem with this kind of grid point models is the treatment of those 12 points. But the numerical results of **FEMmE** showed that EGIG(3,1) is a good choice, one reason why it also became the basic grid of **PLASMA-FEMmE**.

1.1 Adaptive mesh generation

The bucky ball or the icosahedron are a coarse approximation of the sphere. For reasonable results many more grid points are needed. The idea behind **PLASMA-FEMmE** is to add as many points as needed but as few as necessary. Additional the points should be added in those areas where the quality of the simulation is poor and reduced in regions with high quality results.

For those purposes **PLASMA-FEMmE** uses the *a*daptive *m*esh generator for *at*mosphere and *o*cean *s*imulations *amatos*. It was developed by Jörn Behrens (2003) originally for 2d planar problems and has now been extended to spherical applications within the DEKLIM project PLASMA.

Instead of grid points the objects of *amatos* are the related triangles τ of the triangulation T with $\|T\|$ triangles. Whether a triangle has to be adapted or not depends on an indicator function ϑ and two thresholds θ_{crs} and θ_{ref} satisfying $0 < \theta_{crs} < \theta_{ref}$. $\vartheta : T \to \mathbb{R}^+$ indicates

the "local quality" of the simulation. Details about the choice of this indicator in **PLASMA-FEMmE** are given in section 4.5. Here the general concept is outlined.

Benchmark $\widetilde{\vartheta}$ for the adaption are either the maximum ϑ_{max} of ϑ or the average $\overline{\vartheta}$ of ϑ:

$$\vartheta_{max} = \max_{\tau \in T} \vartheta(\tau) \tag{1.4}$$

$$\overline{\vartheta} = \frac{1}{\|T\|} \sum_{\tau \in T} \vartheta(\tau) \tag{1.5}$$

A triangle τ is flagged for refinement, if $\qquad \vartheta(\tau) > \theta_{ref} \cdot \widetilde{\vartheta}$

and for coarsening, if $\qquad \vartheta(\tau) < \theta_{crs} \cdot \widetilde{\vartheta} \qquad$ with $\widetilde{\vartheta} \in \{\overline{\vartheta}, \vartheta_{max}\}$.

In chapter 5 simulation of test cases with both criteria, $\overline{\vartheta}$ and ϑ_{max}, are presented. In the case of the maximum criteria the range of θ_{crs} and θ_{ref} are:

$$0.05 \leq \theta_{crs} \leq 0.5 \qquad\qquad 0.5 \leq \theta_{ref} \leq 0.9$$

With the average benchmark they are chosen as:

$$0.3 \leq \theta_{crs} \leq 0.6 \qquad\qquad 1.2 \leq \theta_{ref} \leq 1.6$$

Adapting a grid is numerically expensive. Because of that *amatos* uses the watermark $w \in (0, 1)$ as additional parameter. Grid adaption is only done if the ratio of flagged triangles in comparison to the total number of triangles is greater than the watermark. Otherwise the grid remains unchanged. Detailed information about the setting of the watermark are given in 4.11 on page 28.

1.1 Admissible and κ-regular triangulation:

Using FE it is favourable that the triangulations are admissible and κ-regular. After Braess (2001) this denotes:

1. $T = \{\tau_1, \tau_2, \ldots, \tau_m\}$ is admissible:

   (a) $\overline{S_h} = \bigcup_{i=1}^{m} \tau_i$

   (b) If $\tau_i \cap \tau_j (i \neq j)$ consists of exactly one point, then it is a common vertex of τ_i and τ_j.

   (c) If $\tau_i \cap \tau_j (i \neq j)$ consists of more than one point, then it is a common edge of τ_i and τ_j.

2. T is κ-regular:
   A triangulation T is called κ-regular provided there exists a number $\kappa < 0$ such that every $\tau_i \in T$ contains a circle of radius ρ_i with

   $$\rho_i \leq \frac{h}{\kappa}$$
   $$h = \max_i \{h_i\}$$

   whereas h_i is half the diameter of τ_i.

Bänsch (1991b) showed that the triangulations T generated by *amatos* have these properties.

refinement	EGIG		#points	#triangles	#edges	resolution
level	p	q	$N_{p,q}$	N_t	N_e	(longest edge)
0	3	1	92	180	270	2627.564 km
1	6	1	362	720	1080	1341.991 km
2	12	1	1442	2880	4320	674.611 km
3	24	1	5762	11520	17280	337.760 km
4	48	1	23042	46080	69120	168.937 km

Table 1.1: Characteristics of the grids used in **FEM**m**E**

1.2 Refinement and coarsening techniques

Two different techniques are widely used for triangular refinement, regular refinement and bisection. The first is used in **FEM**m**E**, the latter in *amatos* and **PLASMA-FEM**m**E**.

1.2.1 Regular refinement

Partition of a triangle into four similar smaller triangles by connecting the three mid points of the edges is the so called regular refinement (Figure 1.5). Applied to each triangle this leads to a uniform refinement of the domain. This strategy is used in **FEM**m**E**. Table 1.1 gives an overview of the different grids starting from the macro triangulation of the sphere (Figure 1.4). The first column shows the refinement level, the next two the EGIG(p,g) classification. The following three columns give the number of grid points, triangles and edges and the last one contains the length of the longest edge on the globe.
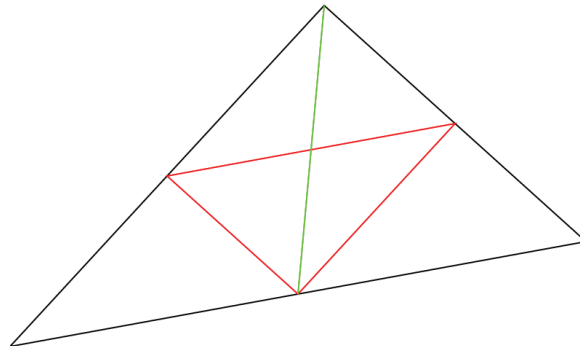
Figure 1.5: Regular refinement (red) and bisection (green) of a triangle

Using the before mentioned adaption criterion and thus applying regular refinement only to a subset of all triangles, the new grid is not any more admissible. In an unchanged triangle neighboured to an adapted one a so called hanging node appears. This offends condition 1.(c). The remedy to cure this problem is bisection of the unchanged triangle.

1.2.2 Bisection

Bisection is another way of dividing a triangle (Figure 1.5). Here the mid point of only one edge of the triangle is connected with the opposite vertex. The original triangle is divided into two equal area smaller triangles. Applying this technique in one triangle also a hanging node occurs in the neighbouring triangle adjacent to the bisected edge. Avoiding this the neighbouring triangle also has to be bisected. Because there are three ways a triangle can be bisected a strategy must be set up which one to choose. *amatos* uses bisection of marked edges according to Rivara (1984) and Bänsch (1991b). During the refinement procedure the situation of Figure 1.6 can occur. The lower triangle is bisected. The result is a hanging node in the upper triangle. In this triangle the blue edge is marked. With one
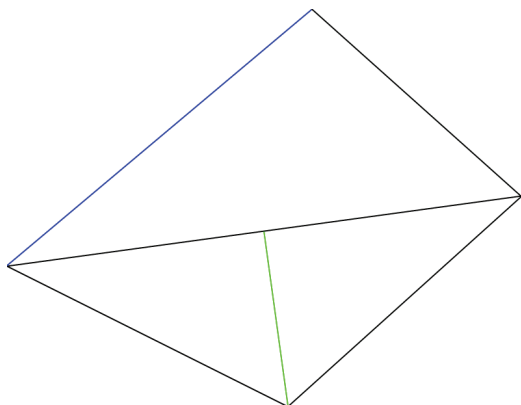
Figure 1.6: Bisection: hanging node
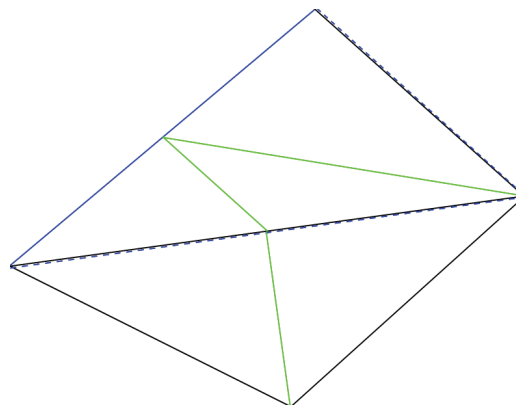
Figure 1.7: Bisection: no hanging node

bisection step there is still the hanging node. The situation is solved as shown in Figure 1.7. Bisection is applied twice. First in the upper triangle. Then in both new triangles the edges of the parent triangle is marked (blue dashed line). Now the bisection is done in the triangle with the hanging node and as a result the hanging node is gone. Rivara (1984) and Bänsch (1991b) showed that this procedure always generates admissible and κ-regular triangulations. Bänsch (1991b) extended this also to the third dimension.

In each triangle of the macro triangulation one edge must be marked. This is done with the constraint that in two neighbouring triangles either the common edge is marked or in each triangle one of the two other edges is marked. One way to fulfil this condition for the macro triangulation (Figure 1.4) used for **PLASMA-FEM***m***E** is to mark all the edges already existing in the bucky ball (Figure 1.3). After bisection in each new triangle the remaining edge of the parent triangle is marked. Starting with a macro triangulation and applying bisection to each triangle as described the grids of Table 1.2 are obtained. Figure 1.2 shows the level 3 grid.

A close look into Table 1.2 reveals the second reason for extending Giraldo's system. Using his classification for the even levels one gets non integer indices, e.g $p = 3\sqrt{2}$ fulfils equation (1.1) for level 2 with 182 grid points. But it is good practice that indices are integers.

1.2.3 Coarsening
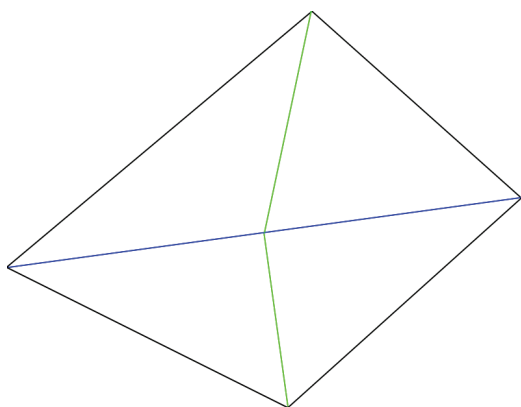
Figure 1.8: Bisection with a common edge

If two triangles with a common marked edge are refined the result with bisection are four daughter triangles. Bänsch (1991a) calls this a resolvable patch. The situation is demonstrated in Figure 1.8. *amatos* embark the following coarsening strategy. If at least three of the four triangles are marked for coarsening then all four triangles are coarsened and the two parent triangles remain.

But there are side effects possible. The refinement used in *amatos* might imply refinement of other neighbour triangles than the one with the marked edge as discussed in previous section 1.2.2. In that case coarsening also has consequences

| refinement level | EGIG | | #points | #triangles | #edges | resolution |
	p	q	$N_{p,q}$	N_t	N_e	(longest edge)
1	3	1	92	180	270	2627.564 km
2	3	2	182	360	540	2627.564 km
3	3	4	362	720	1080	2311.755 km
4	3	8	722	1440	2160	1341.991 km
5	3	16	1442	2880	4320	1166.767 km
6	3	32	2882	5760	8640	674.611 km
7	3	64	5762	11520	17280	584.752 km
8	3	128	11522	23040	34560	337.760 km
9	3	256	23042	46080	69120	292.548 km
10	3	512	46082	92160	138240	168.937 km
11	3	1024	92162	184320	276480	146.295 km

Table 1.2: Characteristics of non-adaptive grids used in **PLASMA-FEMmE**

to those triangles. Bänsch (1991a) demonstrated that for resolvable patches coarsening is always possible.

1.3 *amatos*

At the end of this chapter two special features of *amatos* are described that makes this grid generator efficient. The problem with numerical calculations on adaptive grids arises in the fact that grid handling and numerical calculation needs different data structures to be efficient. The numerics can be done very efficiently on vectorised data structures, while for mesh modification object oriented data structures like linked lists, hash tables or tree structures for the refinement are desired. So *amatos* strictly distinguishes between grid adaptation and numerical calculation. The exchange between the two phases is done in a gather and scatter step. Figure 1.9 gives a schematic overview. Once the grid is modified all the needed objects for the numerical calculation are gathered. After the numerics everything is scattered back to the grid objects.

Secondly the space filling curve (SFC) algorithm for ordering the unstructured grid improves the efficiency. The details are described in Behrens (2005). Here the results are summarised. SFC map the 2d domain to a curve as demonstrated in Figure 1.10. This figure also presents a very efficient way of creating the SFC during grid generation by setting just one bitmap tag per triangle.

There are more advantages of using SFC. It fits perfectly to the gather scatter paradigm. The grid is vectorised with preserving the data locality. With this 1d vector the computational domain easily can be associated with processors for code parallelisation. Moreover the data locality minimises the communication between the processors. Though the model presented here has not been parallelised so far, there is the potential to do so.

But there are other properties of the SFC that also improves the computation time of a serial code. The performance of the search algorithm finding the starting point of the trajectories as described in section 4 benefits from the data locality as well as the calculation of the stiffness matrix. The cache hits here are improved by 60%. Another point is the structure of the matrix used for solving the Helmholtz problem if a reverse SFC ordering is used. Table 2 in Behrens et al. (2005) compares CPU times for solving a similar system with 4 different orderings of the data structure, two of them known to be very efficient. Reverse

SFC ordering turns out to be the most efficient, 16% faster than the second best.
Recent application of *amatos* by Bader et al. (2008) improved those results. They used a
special SFC, the Sierpinski curve and also demonstrated the memory efficient grid genera-
tion. Furthermore the locality properties of the Sierpinski curve can be used building very
cache-efficient algorithms for solving PDEs. In the mentioned publication level 2 cache hit
rates over 99% are reported.
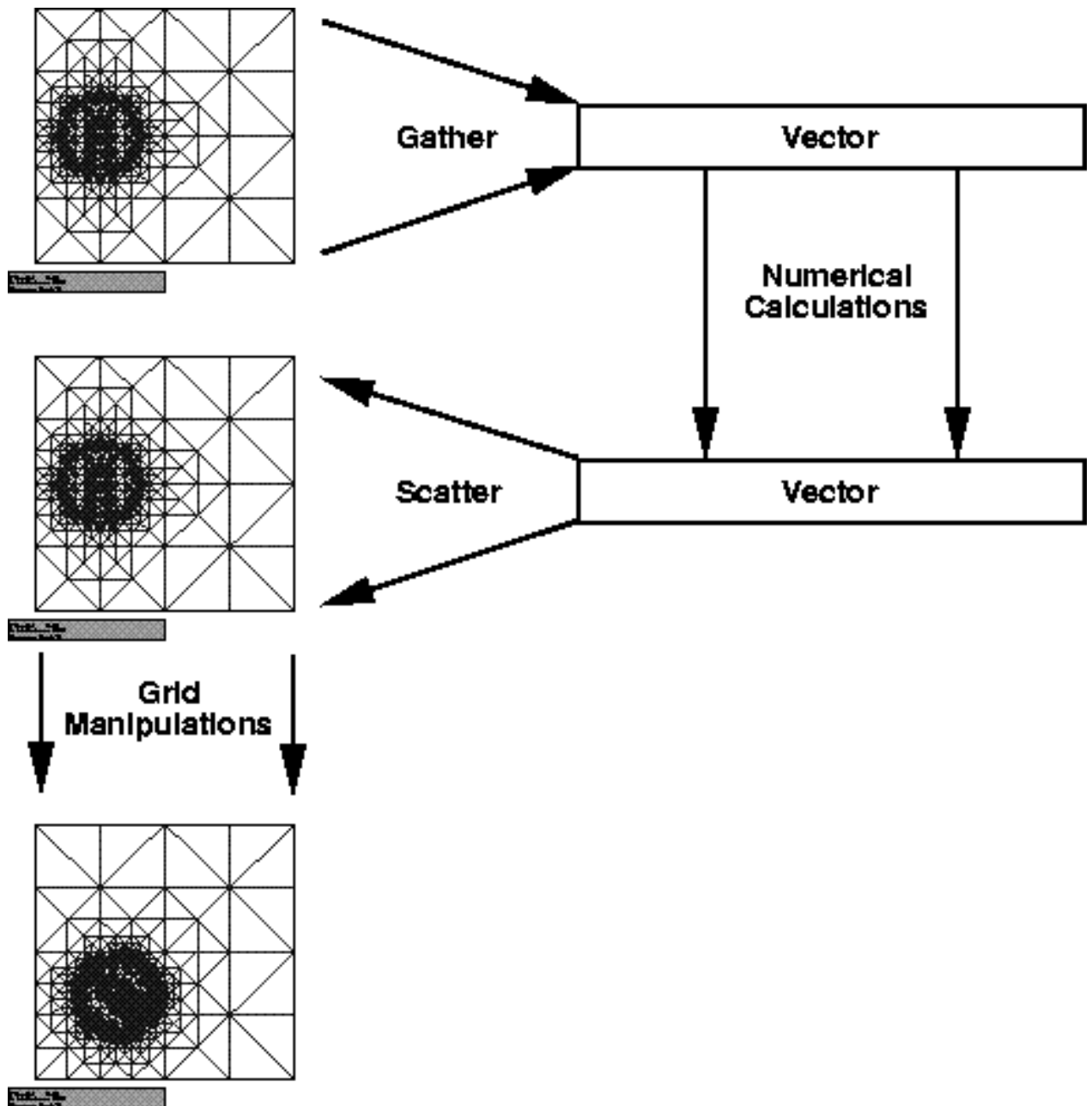
Figure 1.9: Gather and scatter step*
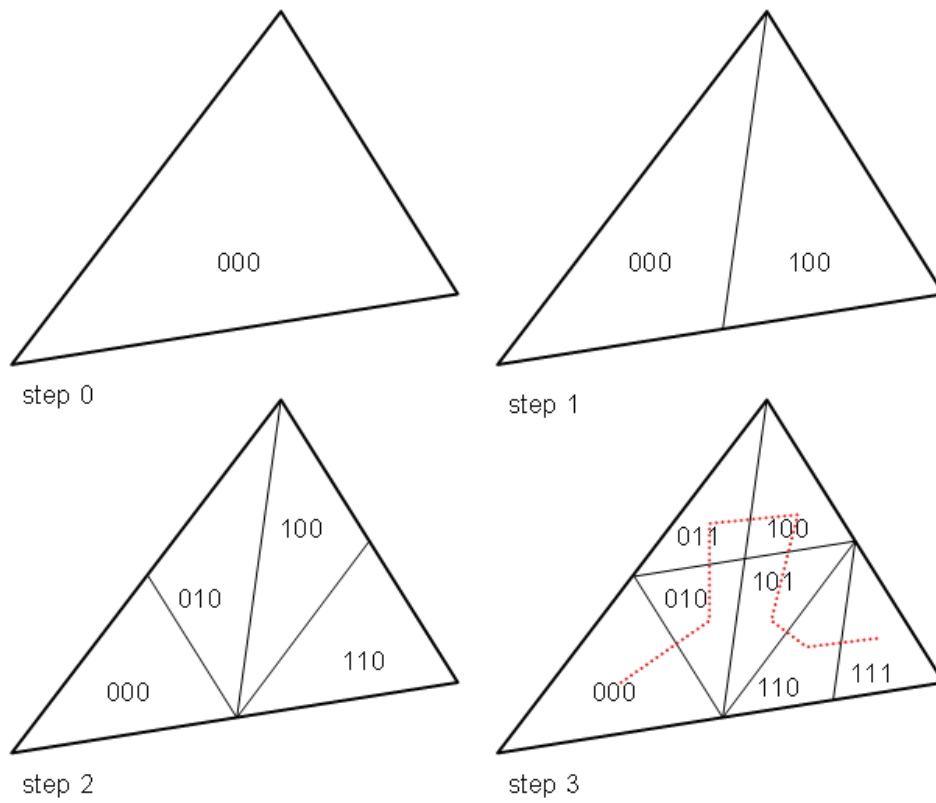
Figure 1.10: Space filling curve bitmap algorithm*

Chapter 2

Dimensionless SWE

2.1 SWE on the sphere

This section introduces the notation used in this thesis and a coupled system of PDEs - the SWE. Starting from the initial problem of the SWE given in Heinze and Hense (2002) a dimensionless version is derived using the angular velocity and the radius of the earth as characteristic values for this system.

In each point $\vec{x} \in S$ of the sphere $S = \{\vec{x} \in \mathbb{R}^3 \mid |\vec{x}| = r_e\}$ with the mean radius of the earth r_e exists a tangential plane $T_S = \{\vec{y} \in \mathbb{R}^3 \mid \vec{y} \cdot \vec{x} = r_e^2\}$ and the outward unit vector $\vec{e}_r = r_e^{-1}\vec{x}$ normal to the sphere. The initial problem of the SWE is investigated and numerical solutions for the time $t \in I = [0, T] \subset \mathbb{R}_0^+$ are calculated.

The SWE describe the interaction of the geopotential $\phi : S \times I \to \mathbb{R}$ with the tangential velocity $\vec{v}_S : S \times I \to T_S$ in consideration of the orography $\phi_H : S \to \mathbb{R}$. The difference in geopotential of the free surface elevation ϕ and the orography (which is constant in time), $\phi - \phi_H$, is split into a basic state geopotential $\breve{\phi} = const > 0$ and a disturbance $\widehat{\phi} : S \times I \to \mathbb{R}$

$$\widehat{\phi}(\vec{x}, t) := \phi(\vec{x}, t) - \phi_H(\vec{x}) - \breve{\phi}. \tag{2.1}$$

$\vec{v}_S$ is the tangential component of the velocity $\vec{v}$ on the sphere which is obtained by

$$\vec{v}_S = \vec{v} - \vec{e}_r (\vec{e}_r \cdot \vec{v}). \tag{2.2}$$

Starting from the principles of conservation of mass and momentum a derivation of the spherical SWE is given in appendix A.

Let $\phi_o, \phi_{Ho} : S \to \mathbb{R}$ and $\vec{v}_o : S \to T_S$ be the initial fields of geopotential, orography and tangential velocity. Thus, the initial problem for the SWE on the sphere is given by:

2.1 Initial problem of spherical SWE

$$\frac{d\widehat{\phi}}{dt} = -\left(\widehat{\phi} + \breve{\phi}\right) \nabla_S \cdot \vec{v}_S \qquad \text{in } S \times I \tag{2.3}$$

$$\frac{d\vec{v}_S}{dt} = -\nabla_S \left(\widehat{\phi} + \phi_H\right) - f(\vec{e}_r \times \vec{v}_S) \quad \text{in } S \times I \tag{2.4}$$

$$\widehat{\phi}(\vec{x}, 0) = \phi_o(\vec{x}) - \phi_{Ho}(\vec{x}) - \breve{\phi} \qquad \text{in } S$$

$$\phi_H(\vec{x}) = \phi_{Ho}(\vec{x}) \qquad \text{in } S$$

$$\vec{v}_S(\vec{x}, 0) = \vec{v}_o(\vec{x}) \qquad \text{in } S$$

$\dfrac{d}{dt}$ is the Lagrangian representation which is correlated to the Eulerian form by

$$\frac{d\widehat{\phi}}{dt} = \frac{\partial \widehat{\phi}}{\partial t} + (\vec{v} \cdot \nabla)\widehat{\phi} \tag{2.5}$$

$$\frac{d\vec{v}_S}{dt} = \frac{\partial \vec{v}_S}{\partial t} + (\vec{v} \cdot \nabla)\vec{v}_S. \tag{2.6}$$

∇ is the usual 3d differential operator. The tangential gradient is calculated similar to $\vec{v}_S$ by

$$\nabla_S \, q = \nabla q - \vec{e}_r \, (\vec{e}_r \cdot \nabla) \, q \tag{2.7}$$

where q is any scalar variable. If $\vec{q}$ is of vectorial type we define analogously the tangential divergence

$$\nabla_S \cdot \vec{q} = \nabla \cdot \vec{q} - \vec{e}_r \cdot (\vec{e}_r \cdot \nabla) \, \vec{q}. \tag{2.8}$$

Later on two more operators are needed. The tangential rotation $\nabla_S \times$ of a vector $\vec{q}$ is defined by

$$\nabla_S \times \vec{q} = e_r \cdot (\nabla \times \vec{q}) \tag{2.9}$$

and for a scalar q the Laplace-Beltrami operator ∇_S^2 by

$$\nabla_S^2 \, q = \nabla_S \cdot \nabla_S \, q. \tag{2.10}$$

It should be alluded that the tangential rotation of the tangential flow is defined as one-dimensional quantity in contrast to $\nabla \times \vec{q}$ that is a full 3d vector. This is done by analogy to the usual procedure of 2d flows in fluid dynamics.
Finally f is the Coriolis parameter

$$f = 2|\vec{\Omega}| \sin \varphi \tag{2.11}$$

with latitude $\varphi \in [-\frac{\pi}{2}, \frac{\pi}{2}]$ and angular velocity $|\vec{\Omega}|$.

2.2   Dimensionless version

Using an earlier version of the grid generator *amatos* transformation to the unit sphere $S_1 = \{\vec{x} \in \mathbb{R} \mid |\vec{x}| = 1\}$ has been necessary. Therefore a dimensionless version of the SWE has been derived.
Characteristic values of this system for length and angular velocity are the radius of the earth and the mean rotation rate

$$L = r_e \;\; \approx 6.371 \cdot 10^6 \text{ m} \tag{2.12}$$

$$F = |\vec{\Omega}| \approx 7.2921 \cdot 10^{-5} \text{ s}^{-1}. \tag{2.13}$$

From this characteristic values for time, velocity and the geopotential are derived

$$T = \mu F^{-1} \tag{2.14}$$

$$U = \frac{L}{T} \tag{2.15}$$

$$G = \nu^2 U^2. \tag{2.16}$$

Stuhne and Peltier (1999) define the external scaling parameters Rossby Ro and Froude number Fr by

$$Ro = \frac{U}{2\,F\,L} \tag{2.17}$$

$$Fr = \frac{U}{\sqrt{G}} \tag{2.18}$$

With these definitions ν and μ are

$$\nu = \frac{\sqrt{G}}{U} \; = \; \frac{1}{Fr} \tag{2.19}$$

$$\mu = F \cdot T \; = \; \frac{F \cdot L}{U} \; = \; \frac{1}{2Ro} \tag{2.20}$$

the reciprocal of Froude and twice the Rossby number.
Pichler (1997) defines the Froude number by the square of the definition given here. In this case ν^2 is the reciprocal of the Froude number.

For achieving a dimensionless version of the SWE new, dimensionless variables are introduced:

$$\widetilde{\widehat{\phi}} = G^{-1} \cdot \widehat{\phi} \qquad\qquad \widetilde{\vec{v}}_S = U^{-1} \cdot \vec{v}_S$$

$$\overline{\phi} = G^{-1} \cdot \breve{\phi} \qquad\qquad \widetilde{\vec{v}}_o = U^{-1} \cdot \vec{v}_o$$

$$\widetilde{\phi}_H = G^{-1} \cdot \phi_H \qquad\qquad \widetilde{f} = F^{-1} \cdot f$$

$$\widetilde{\phi}_o = G^{-1} \cdot \phi_o \qquad\qquad \widetilde{\Omega} = F^{-1} \cdot |\vec{\Omega}| \; = \; 1$$

$$\widetilde{\phi}_{Ho} = G^{-1} \cdot \phi_{Ho} \qquad\qquad \widetilde{r} = L^{-1} \cdot r_e \; = \; 1$$

$$\widetilde{t} = T^{-1} \cdot t.$$

Replacing the old variables by the new ones the continuity equation (2.3) transforms to

$$\frac{G}{T}\frac{d\widetilde{\widehat{\phi}}}{d\widetilde{t}} = -G\left(\widetilde{\widehat{\phi}} + \overline{\phi}\right)\frac{U}{L}\nabla_S \cdot \widetilde{\vec{v}}_S. \tag{2.21}$$

A multiplication by TG^{-1} yields to

$$\frac{d\widetilde{\widehat{\phi}}}{d\widetilde{t}} = -\underbrace{G\frac{U}{L}\frac{T}{G}}_{1}\left(\widetilde{\widehat{\phi}} + \overline{\phi}\right)\nabla_S \cdot \widetilde{\vec{v}}_S. \tag{2.22}$$

The equation of motion (2.4) changes to

$$\frac{U}{T}\frac{d\widetilde{\vec{v}}_S}{d\widetilde{t}} = -\frac{G}{L}\nabla_S\left(\widetilde{\widehat{\phi}} + \widetilde{\phi}_H\right) - UF\widetilde{f}(\vec{e}_r \times \widetilde{\vec{v}}_S). \tag{2.23}$$

The dimensionless equation of motion is obtained by multiplication with TU^{-1}

$$\frac{d\widetilde{\vec{v}}_S}{d\widetilde{t}} = -\frac{T}{U}\frac{G}{L}\nabla_S\left(\widetilde{\widehat{\phi}} + \widetilde{\phi}_H\right) - \frac{T}{U}UF\widetilde{f}(\vec{e}_r \times \widetilde{\vec{v}}_S) \tag{2.24}$$

$$\frac{d\widetilde{\vec{v}}_S}{d\widetilde{t}} = -\underbrace{\frac{G}{U^2}}_{\nu^2}\nabla_S\left(\widetilde{\widehat{\phi}} + \widetilde{\phi}_H\right) - \underbrace{TF}_{\mu}\widetilde{f}(\vec{e}_r \times \widetilde{\vec{v}}_S). \tag{2.25}$$

Hence the dimensionless version of the SWE are:

2.2 Initial problem of dimensionless spherical SWE

$$\frac{d\widetilde{\widehat{\phi}}}{d\widetilde{t}} = -\left(\widetilde{\widehat{\phi}} + \overline{\phi}\right) \nabla_S \cdot \widetilde{v}_S \qquad\qquad \text{in } S_1 \times I \qquad\qquad (2.26)$$

$$\frac{d\widetilde{v}_S}{d\widetilde{t}} = -\nu^2 \, \nabla_S \left(\widetilde{\widehat{\phi}} + \widetilde{\phi}_H\right) - \mu \widetilde{f}(\vec{e}_r \times \widetilde{v}_S) \quad \text{in } S_1 \times I \qquad\qquad (2.27)$$

$$\widetilde{\widehat{\phi}}(\vec{x}, 0) = \widetilde{\phi}_o(\vec{x}) - \widetilde{\phi}_{Ho}(\vec{x}) - \overline{\phi} \qquad\qquad \text{in } S_1$$

$$\widetilde{\phi}_H(\vec{x}) = \widetilde{\phi}_{Ho}(\vec{x}) \qquad\qquad\qquad\quad \text{in } S_1$$

$$\widetilde{v}_S(\vec{x}, 0) = \widetilde{v}_o(\vec{x}) \qquad\qquad\qquad\quad \text{in } S_1$$

Both versions of the SWE, the dimensional on the sphere S and the dimensionless on the unit sphere S_1, were numerically solved by **FEMmE** with Rossby and Froude number set to 1. It turns out that there was no noticeable difference in the results besides the transformation itself.

Chapter 3

Discretisation of the SWE

In this chapter the discretisation of problem 2.2 in time and space is given. The time discretisation is done by a two time level semi-Lagrangian scheme. The usual scheme for the plane is adapted to the sphere. After that a PDE of Helmholtz type is derived. This equation is solved with the aid of linear FE. Here we give the main aspects of this approach as the theoretical background and the full derivation is already outlined in Heinze (1998) and Heinze and Hense (2002) in the case of the SWE on the sphere S. In the following this concept is applied to the dimensionless SWE on the unit sphere S_1.

3.1 Semi-Lagrangian discretisation in time

The Lagrangian formulation of the SWE describes the flow along trajectories. Hence, first for each grid point $\vec{x}_g$ the trajectory must be determined. With the aid of

$$\frac{d\vec{x}}{dt} = \widetilde{\vec{v}}_S \tag{3.1}$$

the displacement $\vec{\xi}$ in the midpoint of a trajectory is calculated. The departure point $\vec{x}_d$ of the trajectory is then just

$$\vec{x}_d = \vec{x}_g - 2 \cdot \vec{\xi}. \tag{3.2}$$

An overview of the method and its applications in atmospheric models is given in Staniforth and Côté (1991).

The basic concept of a two time level semi-Lagrangian scheme is to extrapolate a velocity $\vec{V}^*$ at the mid point $\vec{x}_g - \vec{\xi}$ of the trajectory on the intermediate time level $t_{n+1/2}$ (in the following t_n^*) using the velocities of the last two known time levels t_n and t_{n-1}.

On the sphere the conventional planar semi-Lagrangian technique has to be modified due to the fact that a particle with tangential velocity $\widetilde{\vec{v}}_S$ will travel off the sphere. This tangential condition is naturally fulfiled on a plane. But on a sphere a scaling factor $c_* \geq 1$ must be added to guarantee that any moving particle stays on the surface of the sphere. The following iterative scheme satisfies this condition for the unit sphere S_1.

3.1 Semi-Lagrangian scheme for unit sphere S_1

$(\forall k \in \mathbb{N}_0)$:
$$\vec{V}^*(\vec{x}, t_n^*) = \frac{3}{2}\, \widetilde{\vec{v}}_S(\vec{x}, t_n) - \frac{1}{2}\, \widetilde{\vec{v}}_S(\vec{x}, t_n - \Delta t) \tag{3.3}$$

$$\vec{\xi}^{(0)}(\vec{x}) = (\, 0, 0, 0\,)^T \tag{3.4}$$

$$\vec{\xi}_*^{(k+1)}(\vec{x}) = \frac{\Delta t}{2} \cdot \vec{V}^*(\vec{x} - \vec{\xi}^{(k)}(\vec{x}), t_n^*) \tag{3.5}$$

$$e = |\,\vec{\xi}_*^{(k+1)}\,| \tag{3.6}$$

$$c_* = \frac{\tan e}{|\,\vec{\xi}_*^{(k+1)}\,|} \tag{3.7}$$

$$\vec{\xi}^{(k+1)} = c_* \cdot \vec{\xi}_*^{(k+1)} \tag{3.8}$$

The iteration converges very fast. The experience made with **FEM*m*E** shows that two iteration steps are sufficient:

$$\vec{\xi} = \vec{\xi}^{(2)}. \tag{3.9}$$

Next, some short forms are introduced to simplify the notation. The subscript $n{+}1$ indicates values at the arrival point of the trajectory, that is the grid point itself at time level $n + 1$. Values at the departure point at time level n are indicated by this subscript and values at the mid point at the intermediate time level by $\,_n^*$.

$$\phi_{n+1}, \phi_n^*, \, \phi_n, \, \phi_{Hn+1}, \, \phi_{Hn} : S_1 \times I \to \mathbb{R} \qquad\qquad \vec{v}_{n+1}, \vec{v}_n^*, \, \vec{v}_n, \, \vec{c}_n^* : S_1 \times I \to T_S$$

$$\phi_{n+1} := \widetilde{\widetilde{\phi}}(\vec{x}, t_{n+1}) \qquad\qquad\qquad \vec{v}_{n+1} := \widetilde{\vec{v}}_S(\vec{x}, t_{n+1})$$

$$\phi_n^* := \frac{3}{2}\, \widetilde{\widetilde{\phi}}(\vec{x} - \vec{\xi}, t_n) - \frac{1}{2}\, \widetilde{\widetilde{\phi}}(\vec{x} - \vec{\xi}, t_{n-1}) \qquad \vec{v}_n^* := \vec{V}^*(\vec{x} - \vec{\xi}, t_n^*)$$

$$\phi_n := \widetilde{\widetilde{\phi}}(\vec{x} - 2\,\vec{\xi}, t_n) \qquad\qquad\qquad \vec{v}_n := \widetilde{\vec{v}}_S(\vec{x} - 2\,\vec{\xi}, t_n)$$

$$\phi_{Hn+1} := \widetilde{\phi}_H(\vec{x}) \qquad\qquad\qquad\qquad \vec{c}_n^* := \left[f(\vec{e}_r \times \vec{V}^*) \right](\vec{x} - \vec{\xi}, t_n^*)$$

$$\phi_{Hn} := \widetilde{\phi}_H(\vec{x} - 2\,\vec{\xi})$$

The dimensionless SWE are discretised with a two time level semi implicit semi-Lagrangian scheme introduced by Temperton and Staniforth (1987) as one of their alternative schemes.

$$\frac{\phi_{n+1} - \phi_n}{\Delta t} = -\,\phi_n^* \cdot \nabla_S \cdot \vec{v}_n^* - \overline{\phi}\cdot\left[\omega\, \nabla_S \cdot \vec{v}_{n+1} + (1 - \omega)\, \nabla_S \cdot \vec{v}_n\right] \tag{3.10}$$

$$\frac{\vec{v}_{n+1} - \vec{v}_n}{\Delta t} = -\,\mu\, \vec{c}_n^* - \nu^2\left[\omega\, \nabla_S \left(\phi_{n+1} + \phi_{Hn+1}\right) + (1 - \omega)\, \nabla_S \left(\phi_n + \phi_{Hn}\right)\right]. \tag{3.11}$$

$\omega \in [0, 1)$ is a fixed weight, in the above citation set to $1/2$.

Multiplying equation (3.11) by Δt and applying the ∇_S - operator leads to

$$\nabla_S \cdot \vec{v}_{n+1} = \nabla_S \cdot \vec{v}_n - \Delta t \left\{\mu \nabla_S \cdot \vec{c}_n^* + \nu^2 \omega\, \nabla_S^2 \left(\phi_{n+1} + \phi_{Hn+1}\right) + \nu^2 (1 - \omega) \nabla_S^2 \left(\phi_n + \phi_{Hn}\right)\right\}. \tag{3.12}$$

Inserting the result into equation (3.10) one receives

$$
\begin{aligned}
\frac{\phi_{n+1} - \phi_n}{\Delta t} = &-\phi_n^* \cdot \nabla_S \cdot \vec{v}_n^* - \omega\,\overline{\phi} \cdot \nabla_S \cdot \vec{v}_n - (1-\omega)\,\overline{\phi} \cdot \nabla_S \cdot \vec{v}_n \\
&+ \omega\,\overline{\phi}\Delta t \Big\{ \mu \nabla_S \cdot \vec{c}_n^* + \nu^2 \omega\,\nabla_S^2 \left(\phi_{n+1} + \phi_{Hn+1} \right) + \nu^2(1-\omega)\,\nabla_S^2 \left(\phi_n + \phi_{Hn} \right) \Big\}.
\end{aligned}
\tag{3.13}
$$

After the multiplication with Δt, reordering

$$
\begin{aligned}
\phi_{n+1} - \phi_n = &\;\nu^2 \omega^2\,\overline{\phi}\,(\Delta t)^2\,\nabla_S^2\,\phi_{n+1} + \nu^2 \omega^2\,\overline{\phi}\,(\Delta t)^2\,\nabla_S^2\,\phi_{Hn+1} \\
&+ \nu^2 \omega\,(1-\omega)\,\overline{\phi}\,(\Delta t)^2 \nabla_S^2\,\phi_n + \nu^2 \omega\,(1-\omega)\,\overline{\phi}\,(\Delta t)^2 \nabla_S^2\,\phi_{Hn} \\
&- \overline{\phi}\,\Delta t\,\nabla_S \cdot \vec{v}_n - \Delta t\,\phi_n^* \cdot \nabla_S \cdot \vec{v}_n^* + \mu\,\omega\,\overline{\phi}\,(\Delta t)^2\,\nabla_S \cdot \vec{c}_n^*
\end{aligned}
\tag{3.14}
$$

and another multiplication with the positive constant $c = \left(\nu^2 \omega^2\,\overline{\phi}(\Delta t)^2 \right)^{-1}$ a Helmholtz equation for ϕ_{n+1} is obtained

$$
\begin{aligned}
-\nabla_S^2\,\phi_{n+1} + c \cdot \phi_{n+1} = &\;\frac{1-\omega}{\omega}\,\nabla_S^2\,\phi_n + c \cdot \phi_n + \nabla_S^2\,\phi_{Hn+1} + \frac{1-\omega}{\omega}\,\nabla_S^2\,\phi_{Hn} \\
&- c\,\overline{\phi}\,\Delta t\,\nabla_S \cdot \vec{v}_n - c\,\Delta t\,\phi_n^* \cdot \nabla_S \cdot \vec{v}_n^* + \frac{\mu}{\nu^2 \omega}\,\nabla_S \cdot \vec{c}_n^*.
\end{aligned}
\tag{3.15}
$$

Having solved this system for ϕ_{n+1} the result is used in equation (3.11) to calculate the new velocity $\vec{v}_{n+1}$:

$$
\vec{v}_{n+1} = \vec{v}_n - \mu\Delta t\,\vec{c}_n^* - \nu^2\Delta t \Big[\omega\,\nabla_S \left(\phi_{n+1} + \phi_{Hn+1} \right) + (1-\omega)\,\nabla_S \left(\phi_n + \phi_{Hn} \right) \Big]
\tag{3.16}
$$

Thus the main task is to solve the Helmholtz equation (3.15). This is done with the aid of FE. The details are described in the next section.

3.2 Weak formulation of the Helmholtz problem

The FE discretisation of the Helmholtz equation (3.15) is straightforward and done in the same way as on a plane. Some slight modifications arise from the fact that the computational domain is the discretised unit sphere S_h composed of a certain number of planar triangles. On each triangle τ the outward unit vector $\vec{n}_\tau$ is well defined. It should be mentioned that the following arguments hold for any discretised sphere $S_{h,r}$ with radius r, not only for $r = 1$.

Let $q : S_h \to \mathbb{R}$ be piecewise differentiable on each triangle τ and

$$
\nabla_h = \nabla\big|_\tau
\tag{3.17}
$$

the discrete gradient operator on each triangle. Then the discrete tangential gradient is defined by

$$
\nabla_{S_h} q = \nabla_h\,q - \vec{n}_\tau \left(\vec{n}_\tau \cdot \nabla_h \right) q.
\tag{3.18}
$$

If $\vec{q} : S_h \to \mathbb{R}^3$ is piecewise differentiable on each triangle τ and $\nabla_h \cdot$ is the discrete divergence operator, then the discrete tangential divergence is defined analogously

$$
\nabla_{S_h} \cdot \vec{q} = \nabla_h \cdot \vec{q} - \vec{n}_\tau \left(\vec{n}_\tau \cdot \nabla_h \right) \cdot \vec{q}
\tag{3.19}
$$

and the discrete Laplace-Beltrami operator for $q : S_h \rightarrow \mathbb{R}$ piecewise differentiable on each triangle τ by

$$\nabla^2_{S_h} q = \nabla_{S_h} \cdot \nabla_{S_h} q. \tag{3.20}$$

Putting the unknowns and the extrapolated geopotential of the right hand side onto S_h

$$\phi^h_{n+1} = \phi_{n+1}\big|_{S_h} \tag{3.21}$$

$$\phi^\star_n = \phi^*_n\big|_{S_h} \tag{3.22}$$

and handle all other terms in the same way, the discrete right hand side has the form

$$rhs^h_n = \frac{1-\omega}{\omega} \nabla^2_{S_h} \phi^h_n \,+\, c \cdot \phi^h_n \,+\, \nabla^2_{S_h} \phi^h_{Hn+1} \,+\, \frac{1-\omega}{\omega} \nabla^2_{S_h} \phi^h_{Hn}$$
$$- c\,\overline{\phi}\,\Delta t\,\nabla_{S_h} \cdot \vec{v}^h_n \,-\, c\,\Delta t\,\phi^\star_n \cdot \nabla_{S_h} \cdot \vec{v}^\star_n \,+\, \frac{\mu}{\nu^2\omega}\,\nabla_{S_h} \cdot \vec{c}^\star_n. \tag{3.23}$$

With the discrete operator

$$L^h = -\nabla^2_{S_h} + c \tag{3.24}$$

the Helmholtz problem of equation (3.15) on the discrete sphere is formulated by

$$L^h \phi^h_{n+1} = rhs^h_n \qquad \text{in } S_h. \tag{3.25}$$

Next steps are defining the appropriate Sobolev space $H^1_S(S_h)$ and posing the weak formulation of problem (3.25). With $(x, y, z)^T \in \mathbb{R}^3$, the multi index $v = (v_1, v_2, v_3) \in \mathbb{N}^3_0$ and its modulus $|v| = v_1 + v_2 + v_3$ the differential operators D^v and D^v_S and Sobolev space $H^1_S(S_h)$ are defined by

$$D^v = \frac{\partial^{|v|}}{\partial x^{v_1} \partial y^{v_2} \partial z^{v_3}} \tag{3.26}$$

$$D^v_S = D^v - \vec{e}_r\,(\vec{e}_r \cdot D^v) \tag{3.27}$$

$$H^1_S(S_h) = \left\{ u \in L^2(S_h) \ \big| \ D^v_S u \in L^2(S_h) \quad \forall\,|v| \le 1 \right\}. \tag{3.28}$$

L^2 is the ordinary Lebesgue space and for S_h $\vec{e}_r$ are the outward unit vectors $\vec{n}_\tau$ on each triangle τ. Remembering $\overline{S_h} = \bigcup^m_{i=1} \tau_i$ the scalar product of $\{u, v\} \in L^2(S_h)$ is given by

$$\langle u, v \rangle = \int\limits_{S_h} u \cdot v \, dA = \sum^m_{i=1} \int\limits_{\tau_i} u \cdot v \, dA. \tag{3.29}$$

Let $u, v \in H^1_S(S_h)$ and $rhs^h_n \in L^2(S_h)$. With the definitions of the bilinear form a^h

$$a^h(u, v) = \langle L^h u, v \rangle \tag{3.30}$$

and the functional f^h

$$f^h(v) = \langle rhs^h_n, v \rangle \tag{3.31}$$

the weak formulation of problem (3.25) is as follows:
At every point of time $t_{n+1}(n \in \mathbb{N}_0)$ find the unknown geopotential $\phi^h_{n+1} \in H^1_S(S_h)$ with

$$a^h(\phi^h_{n+1}, \psi^h) = f^h(\psi^h) \quad \forall \psi^h \in H^1_S(S_h) \tag{3.32}$$

$$\langle \phi^h_{n+1}, 1 \rangle = c_0. \tag{3.33}$$

The last condition guarantees the uniqueness of the solution. After Dziuk (1988) the weak solution of equation (3.32) is unique except for an additive constant. In his paper Dziuk also showed the following helpful analogon to Green's formula on the discrete sphere. Let $u, v \in H^1_S(S_h)$. Then

$$\langle -\nabla^2_{S_h} u, v \rangle = \langle \nabla_{S_h} u, \nabla_{S_h} v \rangle. \tag{3.34}$$

3.3 FE discretisation

Problem (3.32) is solved with the aid of linear FE. So the infinite dimensional Sobolev space $H^1_S(S_h)$ is replaced by the finite dimensional FE space $V^1_M(S_h)$.

$$V^1_M(S_h) = \{\psi \in C^0(S_h) \mid \psi|_\tau \in \mathcal{P}^1 \quad \forall \tau \in T\} \tag{3.35}$$

$$dim \, V^1_M(S_h) = M \tag{3.36}$$

$C^0(S_h)$ is the space of continuous functions on S_h and $\mathcal{P}^1$ is the space of first order polynomials. M is the number of grid points of S_h. In the context of FE the grid points are denoted as nodes. Hackbusch (1986) specifies some properties of V^1_M:

1. $V^1_M \subset H^1_S(S_h)$

2. Every function $\psi \in V^1_M$ is uniquely determined by the values of $\psi(\vec{x}_k)$ in the nodes $\vec{x}_k \, (1 \leq k \leq M)$.

3. For any $\widetilde{\psi}_k \, (1 \leq k \leq M)$ exist exactly one $\psi \in V^1_M$ with $\psi(\vec{x}_k) = \widetilde{\psi}_k$. It can be expanded by

$$\psi = \sum_{k=1}^{M} \widetilde{\psi}_k b_k \tag{3.37}$$

   with basis functions b_k and coefficients $\widetilde{\psi}_k$

$$b_k(\vec{x}_j) = \delta_{kj}, \tag{3.38}$$

with the Kronecker symbol δ_{kj}. These M linear independent basis functions b_k are the so called FE.

Replacing the Sobolev space by the FE space in the weak formulation of the Helmholtz problem (3.32) we get to the Ritz-Galerkin formulation of the problem. Instead of solving it for all test functions $\psi^h \in V^1_M(S_h)$ it is enough to do it for all basis functions b_i. As a result one get M integral equations of the type

$$a^h(\phi^h_{n+1}, b_i) = f^h(b_i) \quad \forall i \in \{1, 2, \ldots, M\}. \tag{3.39}$$

Expanding ϕ_{n+1}^h with the coefficients $\widetilde{\phi}_j$

$$\phi_{n+1}^h = \sum_{j=1}^{M} \widetilde{\phi}_j b_j \tag{3.40}$$

equation (3.39) can be rewritten as

$$\sum_{j=1}^{M} \widetilde{\phi}_j \cdot a^h(b_j, b_i) = f^h(b_i) \quad \forall i \in \{1, 2, \ldots, M\}. \tag{3.41}$$

This corresponds to the linear system of equations

$$\mathbf{A} \cdot \vec{\phi} = \vec{f} \tag{3.42}$$

with the vector of unknown coefficients

$$\vec{\phi} := (\widetilde{\phi}_1, \ldots, \widetilde{\phi}_M)^T \tag{3.43}$$

the vector of the right hand side

$$\vec{f} := (f^h(b_1), \ldots, f^h(b_M)^T \tag{3.44}$$

and the symmetric $M \times M$ matrix $\mathbf{A}$ with the elements

$$\mathbf{A}(i, j) = a^h(b_j, b_i). \tag{3.45}$$

Let $u, v \in V_M^1$. With the definition of the two new bilinear forms s^h and m^h

$$s^h(u, v) = \langle \nabla_{S_h} u, \nabla_{S_h} v \rangle \tag{3.46}$$

$$m^h(u, v) = \langle u, v \rangle \tag{3.47}$$

a^h can be split into

$$a^h(u, v) = s^h(u, v) + c \cdot m^h(u, v) \tag{3.48}$$

with the aid of equation (3.34). The corresponding symmetric $M \times M$ matrices $\mathbf{S}$ and $\mathbf{M}$

$$\mathbf{S}(i, j) = s^h(b_j, b_i) \tag{3.49}$$

$$\mathbf{M}(i, j) = m^h(b_j, b_i) \tag{3.50}$$

are called stiffness and mass matrix. In the same way as the bilinear form a^h the matrix $\mathbf{A}$ can be split into

$$\mathbf{A} = \mathbf{S} + c \cdot \mathbf{M}. \tag{3.51}$$

For the details of calculating the stiffness and mass matrix the reader is referred to section 3.4 of Heinze (1998).

Chapter 4

The dynamical core of PLASMA-FEM*m*E

In this chapter the numerical schemes used in the model **PLASMA-FEM*m*E** are described. In NWP models this part is called the dynamical core of the model. The dynamical core of **PLASMA-FEM*m*E** contains well-known schemes that are adapted to the situation on the sphere. In addition the combination of these schemes is novel.

In particular this chapter deals with the interpolation on a triangle. The search algorithm finding points within a triangle that are no grid points is described. The calculation of derivatives and evaluating quantities of the right hand side at departure and mid point of trajectories are given. For the adaptive mesh generation the grid adaption parameters are specified. In this context a new diminishing watermark approach is introduced.

Solving the dimensionless spherical SWE 2.2 the considerations in the last chapter lead to following algorithm. For a static grid it was proposed by Staniforth and Côté (1991). Here this strategy is extended to an adaptive scheme adding the last step according to Behrens (1998) with a slight modification.

4.1 Algorithm

In each time step

1. Calculate the displacement for all grid points with the semi-Lagrangian scheme 3.1.

2. Calculate the right hand side of equation (3.23).

3. Solve the Helmholtz problem (3.25) with the aid of linear FE and update the geopotential at each grid point.

4. Calculate new velocities with discretisation of equation (3.16):

$$\vec{v}_{n+1}^h = \vec{v}_n^h - \mu \Delta t \, \vec{c}_n^\star - \nu^2 \Delta t \Big[\omega \, \nabla_{S_h} \big(\phi_{n+1}^h + \phi_{Hn+1}^h\big) + (1 - \omega) \, \nabla_{S_h} \big(\phi_n^h + \phi_{Hn}^h\big) \Big] \tag{4.1}$$

5. Do we have to adjust the grid?
   If yes, than adapt the grid and calculate everything needed on the new grid for the next time step; if not, than continue the algorithm with the next time step.

Behrens (1998) proposed to recalculate the same time step after grid adaptation until the adaption algorithm does not change the grid any more. But there are always triangles that are marked for adaption. Thus, the stop criterion is the watermark, that means the number

of marked triangles is low in comparison to all triangles. There are more reasons to abandon the recalculation in **PLASMA-FEM***m***E**. First the described scheme is faster. Second flows in the shallow water regime are smooth, so changes of the grid should only lead to small modifications of the flow field. Third for unsteady flows the true numerical solutions are unknown and in general no analytical solution is known. So the grid adaptation process cannot use a mathematical a posteriori error estimator. Instead an error indicator must be used that turns out to be an appropriate choice. But there is no guarantee that always those triangles are adapted that are responsible for an error growth. Altogether a recalculation after grid adaptation seems to be an overhead that can be avoided.

4.1 Interpolation on a triangle

A closer look into the semi-Lagrangian scheme 3.1 reveals in equation (3.5) the extrapolated velocity V^* at $\vec{x} - \vec{\xi}^{(k)}$ has to be calculated. In general this is no grid point. So an interpolation scheme on the triangles is necessary.
For interpolating any value at the point $\vec{x}$ on a triangle with the vertices $\vec{x}_1$, $\vec{x}_2$ and $\vec{x}_3$ a second order interpolating scheme proposed by Baumgardner (1995) is used. It is based on the barycentric coordinates α, β and γ:

$$\vec{x} = \alpha\,\vec{x}_1 + \beta\,\vec{x}_2 + \gamma\,\vec{x}_3 \tag{4.2}$$

$$\alpha + \beta + \gamma = 1 \tag{4.3}$$

Given the values Θ_1, Θ_2 and Θ_3 at the vertices, as well as Θ_4, Θ_5 and Θ_6 at the mid point of the edges one gets the interpolated value by

$$\begin{aligned}
\Theta(\alpha, \beta, \gamma) = {}& \alpha(2\,\alpha - 1)\,\Theta_1 \;+\; \beta(2\,\beta - 1)\,\Theta_2 \;+\; \gamma(2\,\gamma - 1)\,\Theta_3 \\
& + 4\,(\alpha\beta\,\Theta_4 \;+\; \beta\gamma\,\Theta_5 \;+\; \gamma\alpha\,\Theta_6)
\end{aligned} \tag{4.4}$$

But the values at the mid points are unknown. For their calculation the method of least squares is used. For all grid points $\vec{x}_m$ a local 2d Eulerian coordinate system (ζ, η) is introduced. The origin of the new system is the grid point itself and the neighbours are transformed isogonally onto the tangent plane $\mathcal{T}_m$ of $\vec{x}_m$. The distance to the origin in the new system is its great circle distance on the unit sphere:

4.2 Transformation F_K

$$F_K : S_1 \to \mathcal{T}_m$$

$$\vec{x} \mapsto \begin{pmatrix} \zeta \\ \eta \end{pmatrix} = \begin{cases} \sigma_K \begin{pmatrix} \vec{x} \cdot \vec{e}_\zeta \\ \vec{x} \cdot \vec{e}_\eta \end{pmatrix} & \text{if } \vec{x} \neq \vec{x}_m \\[2ex] \begin{pmatrix} 0 \\ 0 \end{pmatrix} & \text{if } \vec{x} = \vec{x}_m \end{cases} \tag{4.5}$$

At the origin $\vec{x}_m = (x_m, y_m, z_m)^T$ the unit vectors $\vec{e}_\zeta$ and $\vec{e}_\eta$ are

$$\vec{e}_\zeta = \frac{1}{\sqrt{x_m^2 + y_m^2}} \begin{pmatrix} -y_m \\ x_m \\ 0 \end{pmatrix} \qquad\qquad \vec{e}_\eta = \frac{1}{\sqrt{x_m^2 + y_m^2}} \begin{pmatrix} -z_m x_m \\ -z_m y_m \\ x_m^2 + y_m^2 \end{pmatrix} \tag{4.6}$$

and the scaling factor σ_K is

$$\sigma_K = \frac{\arccos(\vec{x}_m \cdot \vec{x})}{\sqrt{1 - (\vec{x}_m \cdot \vec{x})^2}} \tag{4.7}$$

In Heinze (1998) it is shown that F_K is continuous and continuously differentiable.

4.3 Methods of least squares

The methods of least squares is then applied to the quadratic polynomial

$$\Psi_m(\zeta, \eta) = \Theta(\vec{x}_m) + a_1\zeta + a_2\eta + a_3\zeta^2 + a_4\eta^2 + a_5\zeta\eta \tag{4.8}$$

in the local coordinate system with the unknowns $a_1, \dots, a_5$. The problem is uniquely solvable if the grid point has at least 5 neighbours. During the refinement process with bisection it can happen that there are less neighbours. In this case the remaining vertices of all neighbouring triangles are added. Now there are at least 6 grid points. The method itself can be found in any textbook about numerical analysis, like e.g. Deuflhard and Hohmann (2003) or Schwarz and Klöckler (2004).

4.4 Conclusions:

$$\Psi_m(0,0) = \Theta(\vec{x}_m) \tag{4.9}$$

$$\begin{pmatrix} \frac{\partial}{\partial\zeta} \\ \frac{\partial}{\partial\eta} \end{pmatrix} \Psi_m(0,0) = \begin{pmatrix} a_1 \\ a_2 \end{pmatrix} \tag{4.10}$$

Then, in the grid point $\vec{x}_m$ a derivative Ψ'_{mj} in direction to the neighbour point $\vec{x}_j = (\zeta_j, \eta_j)^T$ is defined by

$$\Psi'_{mj} = \begin{pmatrix} a_1 \\ a_2 \end{pmatrix} \begin{pmatrix} \zeta_j \\ \eta_j \end{pmatrix} \tag{4.11}$$

Finally the value Θ_{mid} at the mid point between the vertices $\vec{x}_i$ and $\vec{x}_j$ is interpolated by

$$\Theta_{mid} = \frac{\Theta_i + \Theta_j}{2} + \frac{\Psi'_{ij} + \Psi'_{ji}}{8} \tag{4.12}$$

4.2 Search algorithm

Before the interpolation routine of the previous section can be applied another problem has to be solved. To which triangle does the mid point of the trajectory belong? The barycentric coordinates gives the answer.

4.5 Does a point $\vec{x}$ belong to a triangle τ?

$\vec{x}, \alpha, \beta$ and γ fulfil equation (4.2) and equation (4.3):

Then $\vec{x} \in \tau$ if and only if $0 \leq \alpha \leq 1$ and $0 \leq \beta \leq 1$ and $0 \leq \gamma \leq 1$.

If the point $\vec{x}$ do not belong to triangle τ than at least one of the barycentric coordinates is negative. From equation (4.3) we know that at least one of them is positive. With this information a search algorithm is build:

4.6   Search algorithm

1. Check if $\vec{x}$ belongs to triangle τ with condition 4.5.

   - If yes, than the triangle is found.
   - If not, than check the barycentric coordinates.

2. Two cases have to be distinguished:

   (a) If one coordinate is negative and two are positive than choose the neighbouring triangle opposite of the vertex the negative value corresponds to.

   (b) If one coordinate is positive and two are negative than choose a triangle that has no common edge but a common vertex. This vertex is the one the positive value corresponds to.

3. Redo algorithm with the chosen triangle.

4.7   Remarks to 4.6

- The triangle to choose in 2.(b) is not unique. Hence a sequence have to be determined for example by ordering the triangles clockwise.

- If a point lies on a triangle edge it can happen, for example by numerical inaccuracy, that the algorithm flips between both neighbouring triangles. To prevent this a special treatments of those points is necessary.

- If the two before mentioned points are considered the experience in **FEM***m***E** showed that the proposed algorithm is a suitable and efficient search tool.

4.3   Calculating derivatives

Updating the velocities with equation (4.1) $\nabla_{S_h}\left(\phi_{n+1}^h + \phi_{Hn+1}^h\right)$ has to be calculated. In the local coordinate system the derivatives in the origins can be calculated easily with the aid of equation (4.10). The chain rule applied to any scalar Θ yields to

$$\nabla\Theta(\vec{x}_m) = \left(\frac{\partial\Psi_m}{\partial\zeta}(F_K(\vec{x}_m)) \quad \frac{\partial\Psi_m}{\partial\eta}(F_K(\vec{x}_m))\right) \cdot \begin{pmatrix} \frac{\partial\zeta}{\partial x}(\vec{x}_m) & \frac{\partial\zeta}{\partial y}(\vec{x}_m) & \frac{\partial\zeta}{\partial z}(\vec{x}_m) \\ \frac{\partial\eta}{\partial x}(\vec{x}_m) & \frac{\partial\eta}{\partial y}(\vec{x}_m) & \frac{\partial\eta}{\partial z}(\vec{x}_m) \end{pmatrix} \tag{4.13}$$

In Heinze (1998) the following statements are proved:

$$\nabla\zeta(\vec{x}_m) = \vec{e}_\zeta \tag{4.14}$$
$$\nabla\eta(\vec{x}_m) = \vec{e}_\eta \tag{4.15}$$
$$\nabla_S\,\Theta(\vec{x}_m) = \nabla\Theta(\vec{x}_m) \tag{4.16}$$

Thus,

$$\nabla_{S_h}\Theta(\vec{x}_m) = a_1 \cdot \vec{e}_\zeta \, + \, a_2 \cdot \vec{e}_\eta \tag{4.17}$$

For any tangential vector $\vec{v}_S = (u, v, w)^T$ similar considerations leads to

$$\nabla_{S_h} \cdot \vec{v}_S(\vec{x}_m) = \begin{pmatrix} u_1 & v_1 & w_1 \end{pmatrix} \cdot \vec{e}_\zeta + \begin{pmatrix} u_2 & v_2 & w_2 \end{pmatrix} \cdot \vec{e}_\eta \tag{4.18}$$

whereby u_1 and u_2 are the first two coefficients of the quadratic polynomial from equation (4.8) if the method of least squares is applied to the first component of $\vec{v}_S$. v_1 and v_2 are the analogue for the second and w_1 and w_2 for the third component.

4.4 Evaluation at departure and mid point of the trajectory

In equations (3.23) and (4.1) most of the terms of the right hand side must be evaluated at departure or mid point of the trajectory. Both points are no grid points. Thus the interpolation routine described in subsection 4.1 is used. But before using them the calculation of all terms at the grid points with the methods specified in the previous sections is necessary. Staniforth and Côté (1991) are explicitly pointing out that the evaluation and the interpolation step cannot be exchanged.

At time level t_n geopotential, orography and velocity are known at the grid points. Thus all the terms can be calculated and afterwards interpolated to the departure points.

The terms indicated with $\star$ in those two equations must be evaluated at the mid points. Here an additional difficulty occurs. Geopotential, orography and velocity are unknown at the intermediate time level between t_n and t_{n+1}. The strategy is to apply the concept of equation (3.3) to all unknowns Θ. Knowing the values at the grid points $\vec{x}_m$ of the last two time levels they are extrapolated to the intermediate one by

$$\Theta_n^\star(\vec{x}_m) := \frac{3}{2}\,\Theta_n(\vec{x}_m) - \frac{1}{2}\,\Theta_{n-1}(\vec{x}_m) \tag{4.19}$$
$$\text{with} \quad \Theta_{-1}(\vec{x}_m) := \Theta_0(\vec{x}_m)$$

The value at the midpoint can now be interpolated in the same way as described in section 4.1.

4.5 Refinement and coarsening criteria

At the end of this chapter the details of the grid adaptation are given. **PLASMA-FEM*m*E** adopts the mixed divergence vorticity criterion proposed by Läuter (2004) for the model **PLASMA-P**. For simplifications from now on the index n does not indicate a value at the departure point of a trajectory any more, but the value at a grid point. That has been indicated by $n + 1$ so far.

4.8 Discrete relative vorticity

The discrete relative vorticity ψ_n^h at time t_n is defined as the tangential rotation of the velocity $\vec{v}_n^h$

$$\psi_n^h = \nabla_{S_h} \times \vec{v}_n^h. \tag{4.20}$$

The calculation of the relative vorticity ψ_n^h itself is done with the aid of a useful identity proved by Läuter (2004)

$$\nabla_{S_h} \times \vec{v}_n^h = -\nabla_{S_h}(\vec{e}_r \times \vec{v}_n^h). \tag{4.21}$$

This right hand side can be evaluated with the divergence rule given in equation (4.18).

In the first chapter an indicator function for the grid adaptation was introduced. Here the function is specified as proposed by Läuter (2004).

4.9 Indicator function for a triangle τ

$$\vartheta(\tau) = \sqrt{\int\limits_{\tau} (\psi_n^h)^2 + (\nabla_{S_h} \cdot \vec{v}_n^h)^2 \, dA} \tag{4.22}$$

4.10 Numerical quadrature

The integral in equation (4.22) is calculated on a triangle τ by the simple first order quadrature

$$\int\limits_{\tau} \Theta \, dA = \frac{|\tau|}{6} \sum_{k=1}^{3} \Theta_k \tag{4.23}$$

where $|\tau|$ is the area of the triangle and Θ_k $(k = 1, 2, 3)$ are the values of the function Θ at the three vertices.

4.11 Grid adaptation parameters

The grid adaptation is controlled by the thresholds θ_{crs} and θ_{ref} and the watermark w. First preliminary tests reveal that finding a good choice of all three parameters is a difficult task. The watermark turns out to be most sensitive. Too small values forces the algorithm to change the grid each time step without reducing the error. Too big values suppress the adaption process at all and especially in the first test case presented in the next chapter the spread of the value between those two behaviours is small.

Another observation is the following. Due to the choice of the parameters the initial grid adaption process produces a high resolution. Within the first time steps the flow has changed largely only in an small region. So *amatos* increases the number of grid points in that area but coarsens it in the rest of the domain. If the total number of grid points decrease by a factor of 2 it turns out that in these experiments the conservation properties are destroyed. On the other side, starting with an coarser grid that will be refined only in the small region where the flow changes, does not harm the conservation properties. But if the refinement threshold is chosen too high the error grows fast due to the fact that too few grid points were used.

Altogether suggests a diminishing watermark approach. Start with a relative high watermark and reduce this value by a diminishing factor d each time step the grid remained unchanged. The diminished watermark w_k used after k time steps with unchanged grid is therefore

$$w_k = d^k \cdot w, \quad k = 0, 1, 2, \ldots \tag{4.24}$$

After grid adaptation the value is set back to the original value $(k = 0)$. This approach leads to reasonable numerical results, improves the conservation properties and is a good balance between avoiding over-adaptation and preventing adaptation at all.

In the numerical experiments presented in the next chapter the watermark w in most of the experiments is set to $w = 0.1$ and the diminishing factor d to $d = 0.9$.

Chapter 5

Test cases

In this chapter the numerical results are presented and the properties of the different grid adaption approaches are discussed. Three test cases are investigated. The first two belong to the Williamson et al. (1992) test suite, the third was proposed by Läuter (2004).

Test case 2 and 5 of the Williamson test suite are closely connected. Test case 2 is a steady state solution of a geostrophically balanced flow. On the first sight this test case seems not to be an adequate choice. Because of the steadiness of the flow the question arises, whether dynamical grid adaptation does make sense. But there are two good reasons for it. First, the analytical solution is known and the numerical error can easily be calculated. For test case 5 only high resolution numerical solutions are available, but no analytical one. Second, the static grid adaptation can be compared to the calculations without any grid adaptation and to the results of **FEM**_m_**E** with its slightly different grid. Hence the properties of the different grids in respect to the used operators can be checked and statements about the "grid quality" can be made.

Among all cases of the test suite, test case 5 is the one that is most appropriate for grid adaptation. A conical mountain is placed in the steady flow of test case 2. This obstacle disturbs the flow and releases fast moving gravity waves as well as slower Rossby waves. The flow pattern becomes more and more complex during the simulation, and the grid can be adapted dynamically.

The unsteady solid body rotation introduced by Läuter (2004) is the most challenging test case discussed here. It is an analytical solution of the spherical SWE, but small numerical inaccuracies can easily turn the flow to a numerical unstable situation that blows up. Due to the known analytical solution the errors can be calculated and the consequences to the flow can be studied.

Before discussing the test cases, detailed information about the test quantities and about the coordinate transformation between 3d Cartesian system and the usual geographic system are given in the first two sections.

5.1 Test quantities

5.1.1 Conservation properties

Good indicators for the quality of an algorithm are the change in time of physical quantities that are conserved in the system in theory. Arakawa and Lamb (1981) analysed the SW system and showed that mass, total energy, relative and absolute vorticity and potential enstrophy are conserved. The first is examined by the ratio of first moments RFM, the second by the ratio of total energy RTE, the next two by the ratio of relative RRV and

absolute vorticity RAV and the last by the ratio of potential enstrophy RPE.

5.1   Ratio of first moments RFM

$$RFM(t_n) = \frac{\displaystyle\int_{S_h} \phi_n^h \, dA}{\displaystyle\int_{S_h} \phi_o^h \, dA} \qquad n \in \mathbb{N}_0 \tag{5.1}$$

$\phi_o^h = \left.\widetilde{\phi}_o\right|_{S_h}$ is the geopotential at all grid points at the initial state.

5.2   Discrete total energy
The discrete total energy $E_{tot,n}^h$ at time t_n is defined as

$$E_{tot,n}^h = \frac{1}{2g} \int_{S_h} \left(\phi_n^h + \overline{\phi} \right) \cdot \left((\vec{v}_n^h)^2 + \phi_n^h + \overline{\phi} + 2\phi_{Hn}^h \right) \, dA \qquad n \in \mathbb{N}_0 \tag{5.2}$$

5.3   Ratio of total energy RTE

$$RTE(t_n) = \frac{E_{tot,n}^h}{E_{tot,o}^h} \qquad n \in \mathbb{N}_0 \tag{5.3}$$

The initial state of orography ϕ_{Ho}^h and velocity $\vec{v}_o^h$ at all grid points used in the denominator of equation (5.3) are defined by $\phi_{Ho}^h = \left.\widetilde{\phi}_{Ho}\right|_{S_h}$ and $\vec{v}_o^h = \left.\widetilde{\vec{v}}_o\right|_{S_h}$.

5.4   Discrete absolute vorticity
The discrete absolute vorticity $\psi_{abs,n}^h$ at time t_n is defined as

$$\psi_{abs,n}^h = (\psi_n^h + f^h) \qquad n \in \mathbb{N}_0 \tag{5.4}$$

with $f^h = \left.f\right|_{S_h}$.

5.5 Remark:
In both Williamson test cases studied relative and absolute vorticity are anti symmetric on the northern and the southern hemisphere at initial time. Thus their global integral is zero. Hence no ratio of these quantities are defined here and instead time series of the global integral itself are presented.

5.6   Discrete potential enstrophy
The discrete potential enstrophy $\Sigma_{Pot,n}^h$ at time t_n is defined as

$$\Sigma_{Pot,n}^h = \frac{g \cdot (\psi_{abs,n}^h)^2}{\phi_n^h + \overline{\phi}} \qquad n \in \mathbb{N}_0 \tag{5.5}$$

5.7   Ratio of potential enstrophy RPE

$$RPE(t_n) = \frac{\displaystyle\int_{S_h} \Sigma_{Pot,n}^h \, dA}{\displaystyle\int_{S_h} \Sigma_{Pot,o}^h \, dA} \qquad n \in \mathbb{N}_0 \tag{5.6}$$

In test case 2 also the ratio of second moments RSM is a conservation property.

5.8 Ratio of Second Moments RSM

$$RSM(t_n) = \sqrt{\frac{\displaystyle\int_{S_h} (\phi_n^h)^2 \, dA}{\displaystyle\int_{S_h} (\phi_o^h)^2 \, dA}} \qquad n \in \mathbb{N}_0 \tag{5.7}$$

With equation (4.23) the numerical integration on a triangle is set. Thus, the extension to the whole discrete sphere is just:

5.9 Numerical quadrature over the discrete unit sphere

The numerical integration over the discrete unit sphere S_h of a function Θ is the sum of the integrals over all triangles τ_i.

$$\int_{S_h} \Theta \, dA = \sum_{\tau_i \in S_h} \int_{\tau_i} \Theta \, dA \tag{5.8}$$

In a recent publication John Thuburn (2008) raised the question which quantities that are conserved in the continuous system can also be conserved in the discrete one. He points out that in atmospheric motions for most of the quantities transitions between different states occur, e.g. well known is the transition of potential energy to kinetic energy. Some of these transitions happen in scales that cannot be represented by the discrete system. In real NWP models these subscale processes are parametrised. In the SWM discussed here no such subscale parameterisation is done. After Thuburn for none of the discussed quantities, besides mass, that is not transferred into a different state, conservation in the discrete system can be expected.

In the steady state simulation of test case 2 no transition takes place. There the amount of gain or loss of a conserved quantity gives an idea of the conservation properties of the proposed dynamical core. In the two other test cases the arguments of Thuburn should always kept in mind.

5.1.2 Numerical errors

In test cases with analytical solution (ϕ_a, ψ_a, $\vec{v}_a$) at any point of time t_n the numerical error can be calculated. Three different kinds of errors are used, l_1, l_2 and l_∞ error. The errors of geopotential and relative vorticity are investigated.

5.10 l_p errors for $\Theta \in \{\phi, \psi, \vec{v}\}, n \in \mathbb{N}_0, p \in \mathbb{N} \cup \{\infty\}$

$$l_p(\Theta, t_n) = \frac{1}{|S_h|} \left(\int_{S_h} \left| \Theta_n^h - \Theta_a(t_n) \right|^p \, dA \right)^{\frac{1}{p}} \tag{5.9}$$

$$l_\infty(\Theta, t_n) = \max \left| \Theta_n^h - \Theta_a(t_n) \right| \tag{5.10}$$

5.11 Normalised nl_p errors for $\Theta \in \{\phi, \psi, \vec{v}\}, n \in \mathbb{N}_0, p \in \mathbb{N} \cup \{\infty\}$

$$nl_p(\Theta, t_n) = \frac{l_p(\Theta, t_n)}{\left\|\Theta_a(t_n)\right\|_p} \tag{5.11}$$

with

$$\left\|\Theta\right\|_p = \frac{1}{|S_h|}\left(\int\limits_{S_h} |\Theta|^p \; dA\right)^{\frac{1}{p}} \tag{5.12}$$

$$\left\|\Theta\right\|_\infty = \max |\Theta| \tag{5.13}$$

$|S_h|$ is the surface of the polyhedron S_h.

5.2   Coordinate systems

The customary coordinate system in the meteorological community is the geographical one. Hence, the initial conditions of the test cases are given in this system with longitude $\lambda \in [-\pi, \pi]$ and latitude $\varphi \in [-\frac{\pi}{2}, \frac{\pi}{2}]$. The corresponding 3d Cartesian coordinates $(x, y, z)^T \in \mathbb{R}^3$ used in **PLASMA-FEM*m*E** are obtained by polar coordinates transformation.

5.12 Transformation from geographical into Cartesian coordinates

$$\begin{aligned} x &= r \cdot \cos\varphi \cdot \cos\lambda \\ y &= r \cdot \cos\varphi \cdot \sin\lambda \\ z &= r \cdot \sin\varphi \end{aligned} \tag{5.14}$$

$r = 1$ transforms to the unit sphere S_1, $r = r_e$ to the sphere S.

In each point $\vec{x}_m = (x_m, y_m, z_m)^T$ of the sphere a zonal unit vector $\vec{e}_\zeta$ and a meridional one $\vec{e}_\eta$ are defined by (4.6).

5.13 Zonal and meridional velocity
The calculation of zonal v_ζ and meridional velocity v_η then is simply

$$v_\zeta = \vec{v}_S \cdot \vec{e}_\zeta, \qquad\qquad v_\eta = \vec{v}_S \cdot \vec{e}_\eta. \tag{5.15}$$

5.14 3d Cartesian velocity vector
Vice versa according to Cassirer et al. (1996) the Cartesian components $(u, v, w)^T$ of $\vec{v}_S$ are calculated by

$$\begin{pmatrix} u \\ v \\ w \end{pmatrix} = \begin{pmatrix} -\sin\lambda & -\sin\varphi \cdot \cos\lambda \\ \cos\lambda & -\sin\varphi \cdot \sin\lambda \\ 0 & \cos\varphi \end{pmatrix} \cdot \begin{pmatrix} v_\zeta \\ v_\eta \end{pmatrix}. \tag{5.16}$$

5.3 Test case 2

5.3.1 Test case 2 on the globe

The initial conditions for test case 2 of Williamson et al. (1992) are a divergence free zonal velocity field $\vec{v}_o = (v_{\zeta o}, v_{\eta o})^T$ with

$$v_{\zeta o} = U_o \cos \varphi \tag{5.17}$$

$$v_{\eta o} = 0 \tag{5.18}$$

$$U_o = \frac{2\pi r_e}{12\,\mathrm{d}} \approx 38.58\ \mathrm{m\ s^{-1}}$$

and a suitable geostrophically balanced geopotential field

$$\phi_o = \breve{\phi} + \cos^2\varphi \left(r_e \Omega U_o + \frac{1}{2} U_o^2 \right) \tag{5.19}$$

$$\breve{\phi} = gh_o - \left(r_e \Omega U_o + \frac{1}{2} U_o^2 \right) \tag{5.20}$$

$$gh_o = 29400\ \mathrm{m^2 s^{-2}}$$

$$\Omega = |\vec{\Omega}| = 7.2921 \cdot 10^{-5}\ \mathrm{s^{-1}}$$

The corresponding absolute vorticity is then

$$\psi_{abs,0} = 2 \left(\frac{U_o}{r_e} + \Omega \right) \sin \varphi \tag{5.21}$$

Test case 2 is a steady state solution.

5.3.2 Test case 2 on the unit sphere

For transferring the initial conditions to a dimensionless version on the unit sphere using the characteristic values defined in equations (2.12) to (2.16), the following changes have to be done.
The velocity is normalised by U to

$$\widetilde{U}_o = U^{-1} \cdot U_o \tag{5.22}$$

$$\widetilde{v}_{\zeta o} = \widetilde{U}_o \cos \varphi \tag{5.23}$$

$$\widetilde{v}_{\eta o} = 0 \tag{5.24}$$

The basic state of the geopotential (5.20) transforms to

$$\widetilde{gh}_o = G^{-1} \cdot gh_o \tag{5.25}$$

$$G \cdot \overline{\phi} = G \cdot \widetilde{gh}_o - U^2 \left(\underbrace{\frac{LF}{U}}_{\mu} \cdot \underbrace{\widetilde{r}}_{1} \underbrace{\widetilde{\Omega}}_{1} \widetilde{U}_o + \frac{1}{2} \widetilde{U}_o^2 \right) \tag{5.26}$$

$$\overline{\phi} = \widetilde{gh}_o - \underbrace{\frac{U^2}{G}}_{\nu^{-2}} \cdot \left(\mu \cdot \widetilde{U}_o + \frac{1}{2} \widetilde{U}_o^2 \right) \tag{5.27}$$

$$\overline{\phi} = \widetilde{gh}_o - \frac{\widetilde{U}_o}{\nu^2} \left(\mu + \frac{1}{2} \widetilde{U}_o \right) \tag{5.28}$$

error of gradient of geopotential
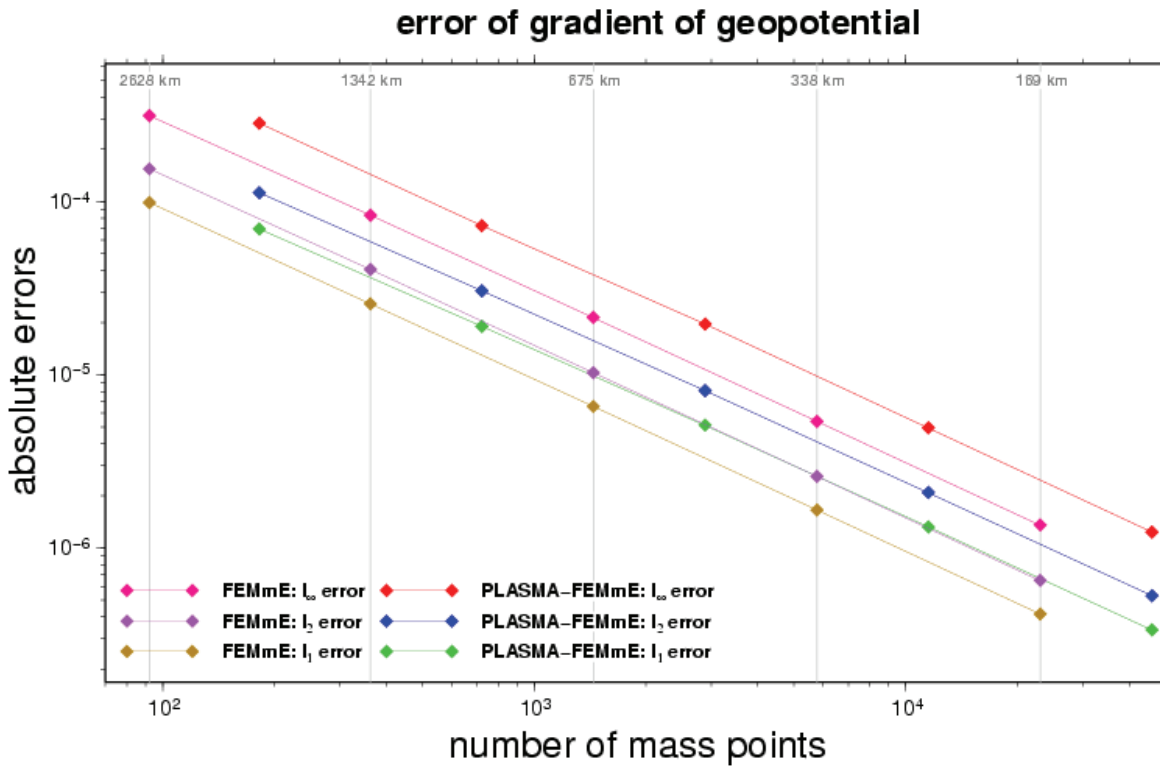
Figure 5.1: Test case 2 initial state: convergence of gradient of geopotential

error of relative vorticity
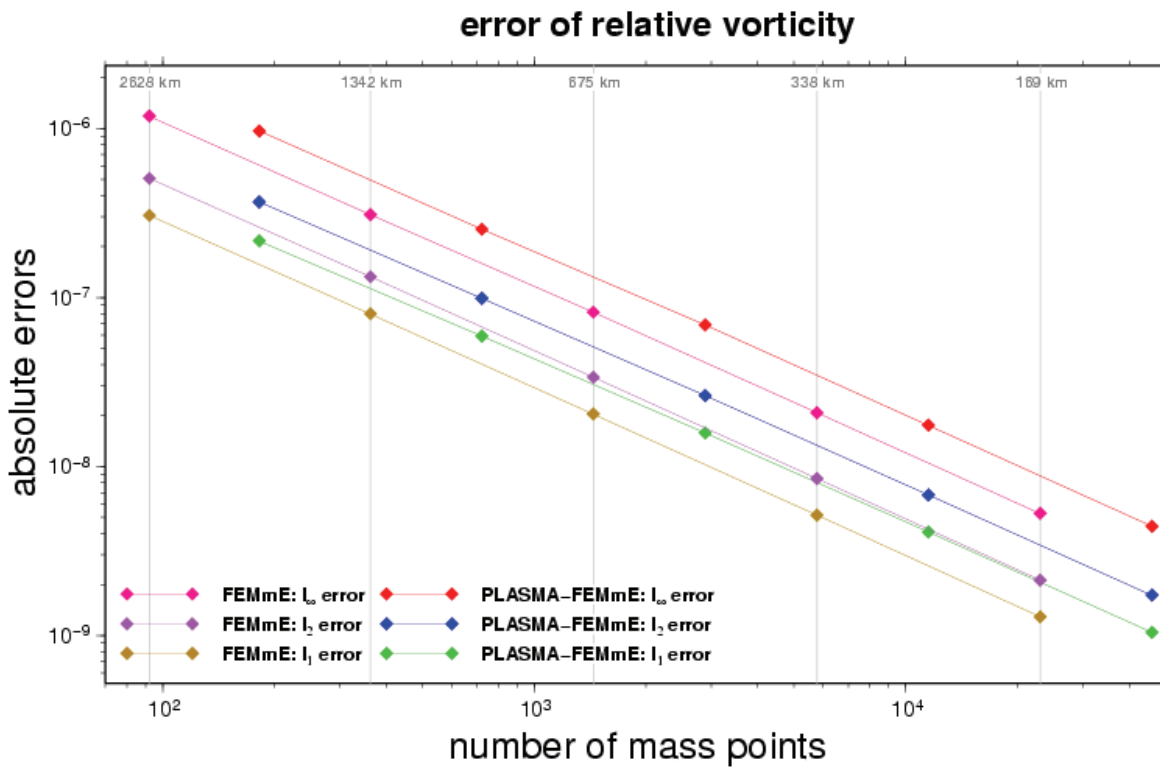
Figure 5.2: Test case 2 initial state: convergence of relative vorticity

The perturbation of the geopotential (5.19) changes to

$$G \cdot \widetilde{\phi}_o = G \cdot \overline{\phi} + U^2 \cdot \cos^2\varphi \left(\frac{LF}{U} \cdot \widetilde{r}\widetilde{\Omega}\,\widetilde{U}_o + \frac{1}{2}\widetilde{U_o}^2 \right) \tag{5.29}$$

$$\widetilde{\phi}_o = \overline{\phi} + \frac{\widetilde{U}_o}{\nu^2}\cos^2\varphi \left(\mu + \frac{1}{2}\widetilde{U}_o \right) \tag{5.30}$$

and the absolute vorticity to

$$F \cdot \widetilde{\psi}_{abs,0} = 2\left(\frac{U}{L} \cdot \frac{\widetilde{U}_o}{\widetilde{r}_e} + F \cdot \widetilde{\Omega} \right)\sin\varphi \tag{5.31}$$

$$\widetilde{\psi}_{abs,0} = 2\left(\frac{U}{LF} \cdot \widetilde{U}_o + 1 \right)\sin\varphi \tag{5.32}$$

$$\widetilde{\psi}_{abs,0} = 2\left(\frac{\widetilde{U}_o}{\mu} + 1 \right)\sin\varphi \tag{5.33}$$

5.3.3 Grid and operator properties

Before several setups of the grid are investigated with this test case, the numerical be-haviour of basic operators on the different grids are examined. For this purpose the ini-tial conditions of this test case are taken. The operators for calculating the gradient of the geopotential (4.17), the divergence (4.18) and the rotation (4.21) of velocity are tested. The latter is the relative vorticity and is calculated by applying the divergence operator to the 90° clockwise rotated velocity.
The gradient of geopotential is

$$\nabla_S \widetilde{\phi}_o = \widetilde{U}_o\,\nu^{-2}\,(2\,\mu + \widetilde{U}_o)\begin{pmatrix} xz^2 \\ yz^2 \\ -z(x^2+y^2) \end{pmatrix}. \tag{5.34}$$

The initial flow in test case 2 is divergence free and the relative vorticity is that part of the absolute vorticity that does not correspond to the Coriolis force. Hence

$$\widetilde{\psi}_{rel,0} = 2\,\widetilde{U}_o\,\mu^{-1}\sin\varphi \tag{5.35}$$

$$\nabla_S \vec{v}_o = 0 \tag{5.36}$$

Figures 5.1 to 5.3 show the absolute errors of the above quantities as function of the number of mass points. The grids used for this convergence study are the ones applying the re-finement strategy to all triangles. On the top of each figure in gray the corresponding grid resolution is given. These resolutions only relate to the **FEM*m*E** grid as given in Table 1.1. For the **PLASMA-FEM*m*E** grids only the even levels are displayed. From Table 1.2 one learns that only those levels increase the resolution notedly. The reason is that by bisection only one edge of a triangle is halved, the other two remains as they are. At first in the next refinement step those two edges are also halved. Identifying grid resolution with the length of the longest edge and comparing Table 1.1 and 1.2 it is obvious that the same grid resolution in **PLASMA-FEM*m*E** is obtained by nearly twice as much grid points. Thus, the corresponding grid resolution for the **PLASMA-FEM*m*E** grids in the Figures 5.1 to 5.3 are the ones left of each point.
Figures 5.1 and 5.2 show similar convergence for the gradient and the vorticity operators.
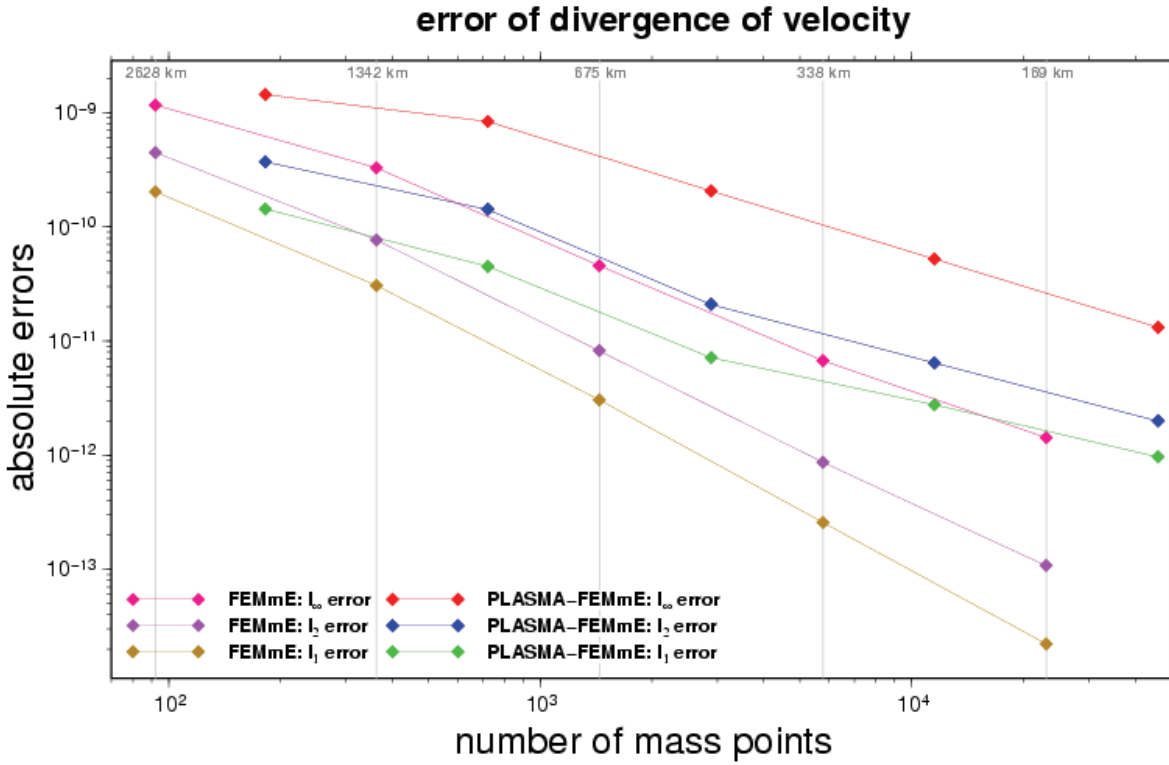
Figure 5.3: Test case 2 initial state: convergence of divergence of velocity

Doubling the grid resolution the error is reduced by a factor of 4. So those operators are second order convergent. It is also recognisable that similar grid resolution leads to similar errors for **FEMmE** and **PLASMA-FEMmE** grids. That implies receiving same accuracy in **PLASMA-FEMmE** grids twice as much grid points are necessary than in **FEMmE** grids.

The situation in Figure 5.3 is slightly different. The l_1 and l_2 error is third order convergent for **FEMmE** grids finer than level 2. The l_∞ errors shows a somewhat worse convergent but still better than second order. Here the **PLASMA-FEMmE** grids perform worse. From level 2 to level 4 there is only a small gain in accuracy. The l_∞ error converges for higher grids with second order, whereas the other two errors drop by a factor greater than 2 only between level 2 and 4. For higher levels the convergence is smaller, only between 1.3 to 1.7. From the construction of the operators as described in section 4.3 using a quadratic polynomial determined by the methods of least squares second order convergence can be expected. If the investigated field is nearly zero one observe superconvergence with the more symmetric stencils of the **FEMmE** grid and for the **PLASMA-FEMmE** stencils a convergence less than second order.

5.3.4 Experimental settings

Eight different settings are investigated, three with dynamic grid adaption (exp1 to exp3) and two with static ones before the first time step (exp4 and exp5). The coarsest grid level used is level 7, the finest level 11. These experiments are compared to three more settings without any grid adaption, two of **PLASMA-FEMmE** on level 7 and level 9 and one of **FEMmE**. This last experiment uses **FEMmE**'s grid level 4 that correspond to level 9. The details about the used error indicator, the watermark w and the thresholds Θ_{crs} and Θ_{ref} are given in Table 5.1. All experiments are run with a time step $\Delta t = 900 s$ and an off-centring weight $\omega = 0.7$. The reciprocals of Froude F_0 and Rossby R_0 number are set to $\nu = \mu = 1$. Table 5.2 shows the CPU time used for a 15 day simulation of each experiment. All simulations are run on a up-to-date LINUX workstation using one XEON processor with 3.07 GHz.

experiment	adaption type	error indicator	Θ_{crs}	Θ_{ref}	w	coarse grid level	fine grid level
7_11_exp1	dynamic	ave	0.5	1.5	0.1	7	11
7_11_exp2	dynamic	ave	0.6	1.6	0.1	7	11
7_11_exp3	dynamic	max	0.49	0.9	0.1	7	11
7_11_exp4	static	ave	0.6	1.6	0.1	7	11
7_11_exp5	static	max	0.2	0.83	0.05	7	11
7_7	none	-	-	-	-	7	7
9_9	none	-	-	-	-	9	9
FEM*m*E	none	-	-	-	-	9	9

Table 5.1: Experiments investigated in test case 2

Depending on the chosen configuration, a single run has required between 19 minutes and 10 hours of CPU time. The CPU time required for the **FEM*m*E** run cannot compared directly to the others because this program is written in C++ and uses a different compiler. **PLASMA-FEM*m*E** is written in FORTRAN 90. Compilation is done with Intel's ifort compiler 8.1.
The number of grids created during the dynamic grid adaption is also given in Table 5.2.

5.3.5   Grids and diagrams

Figures 5.4 - 5.9 present - for different model runs and integration times - the refinement levels of adaptive grids produced by *amatos*. The grids themselves are not included. Mind that the grid generation in experiment 3 is different from the others in so far as the algorithm forces the grid to adapt very often. In Figure 5.10, that gives an overview over the evolution of used grid points with time in the different experiments, the adaptive grid generation of experiment 3 shows periods where the grid flips between two stages. In Figures 5.6 and 5.7 two consecutive grids within this "bifurcation" period after 13.5 days are picked. The first one uses 13512 grid points, the second 980 grid points more. Though continuously adapting the grid is very time consuming and should therefore be avoided, the results presented in the following diagrams show that this does not worsen neither the errors nor the conservation properties.
On page 40 two diagrams with time series of the relative vorticity are presented. Mind, that the lower figure has a bigger scale as the experiments grouped there have a bigger amplitude. On pages 41 and 42 time series of the other conservation quantities are given followed by time series of l_1, l_2 and l_∞ errors of geopotential and vorticity. On the diagrams from page 46 onward some snapshots of those error patterns for each simulation are given.

experiment	CPU time [h]	number of grids	experiment	CPU time [h]
7_11_exp1	2.5011	41	7_11_exp5	1.6142
7_11_exp2	0.9092	27	7_7	0.2936
7_11_exp3	9.9933	808	9_9	1.1994
7_11_exp4	0.5272	1	**FEM*m*E**	1.5014

Table 5.2: CPU time of test case 2 experiments

Refinement levels of adapted grid
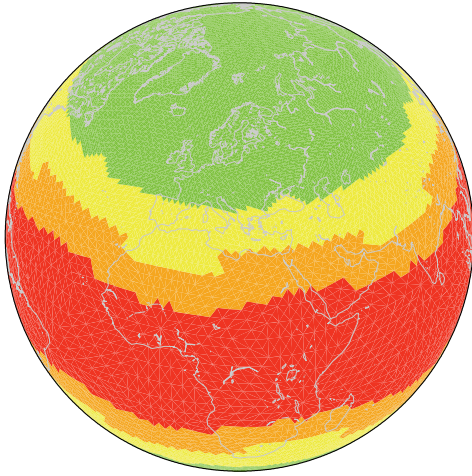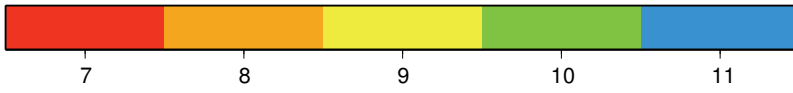
Figure 5.4: 7_11_exp1 after 10 days
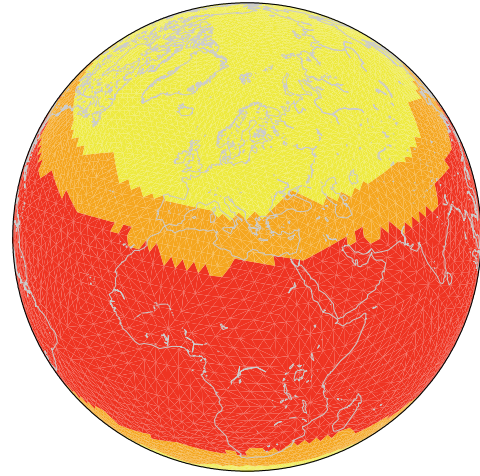
Figure 5.5: 7_11_exp2 after 10 days
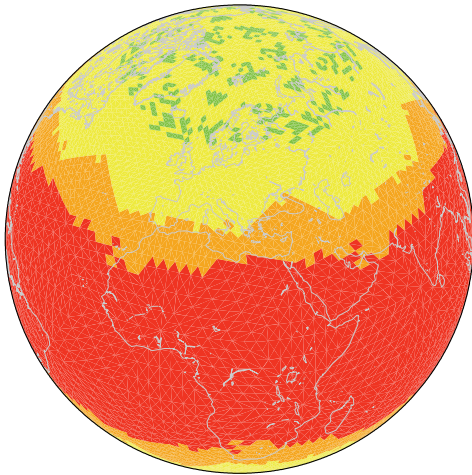
Figure 5.6: 7_11_exp3 after 1300 steps
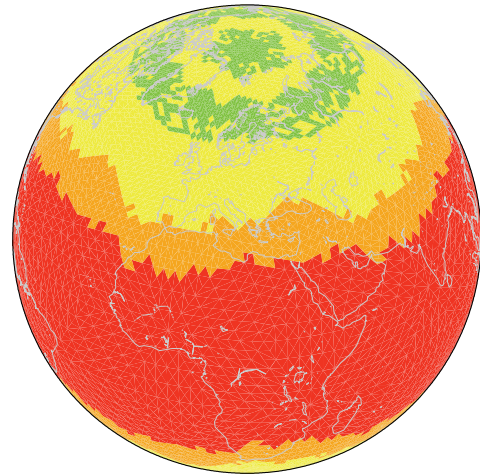
Figure 5.7: 7_11_exp3 after 1301 steps
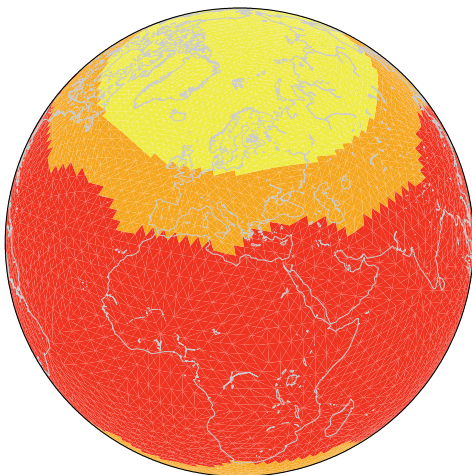
Figure 5.8: 7_11_exp4
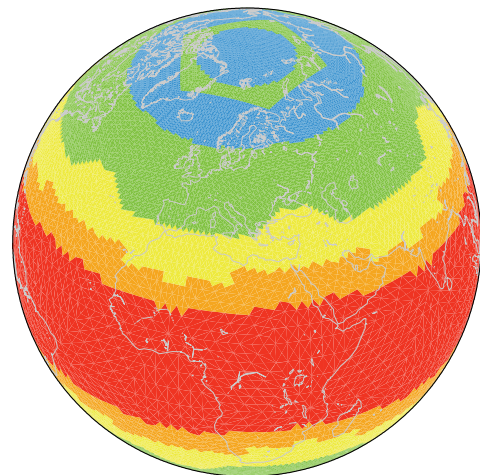
Figure 5.9: 7_11_exp5

5.3.6 Numerical results

Two things can be remarked at first sight. First, the scheme does not conserve potential enstrophy. As shown in Figure 5.16, there is a loss of more than 3% within the first 15 days, independent of the grid used. Second, the normalised errors of relative vorticity are about a factor of 3 larger than those of the geopotential. This can also be observed in other SWM like e.g. ICON (Bonaventura et al. (2005)). Analysing the error patterns of the vorticity outside the polar regions the experiments can be grouped into three types: mostly zonal error patterns, mostly wavenumber 5 (WN5) patterns and a mixed one where both can be observed. Experiment 1 and 5 belong to the first group, **FEM*m*E** and experiment 9_9 to the last and all others to WN5.

Characteristic of the first group are grids with many grid points. Most of the time the number is bigger than 20,000. Both, experiment 1 and 5, have a positive trend in the relative vorticity, they have the smallest increase of mass of all experiments besides **FEM*m*E** and they conserve RSM and total energy fairly well. The error performance gives a different picture. Together with **FEM*m*E** they have the largest error in geopotential. As shown in time series of the maximum error of vorticity (Figure 5.22), from day 5 onward experiment 5 is among the runs with highest error, experiment 1 among those showing the smallest error. But in the first days this error for experiment 1 is more than twice as high than in all other experiments. The error patterns of the geopotential are also zonal. In the high latitudes the solutions is smaller than the analytic one, in the tropics and subtropics vice versa. The two experiments of the mixed type give a direct comparison between the predecessor model **FEM*m*E** and the corresponding experiment of **PLASMA-FEM*m*E**. They use the same grid points and the same numerical schemes. The only difference is the refinement technique, on one side regular refinement, on the other bisection.
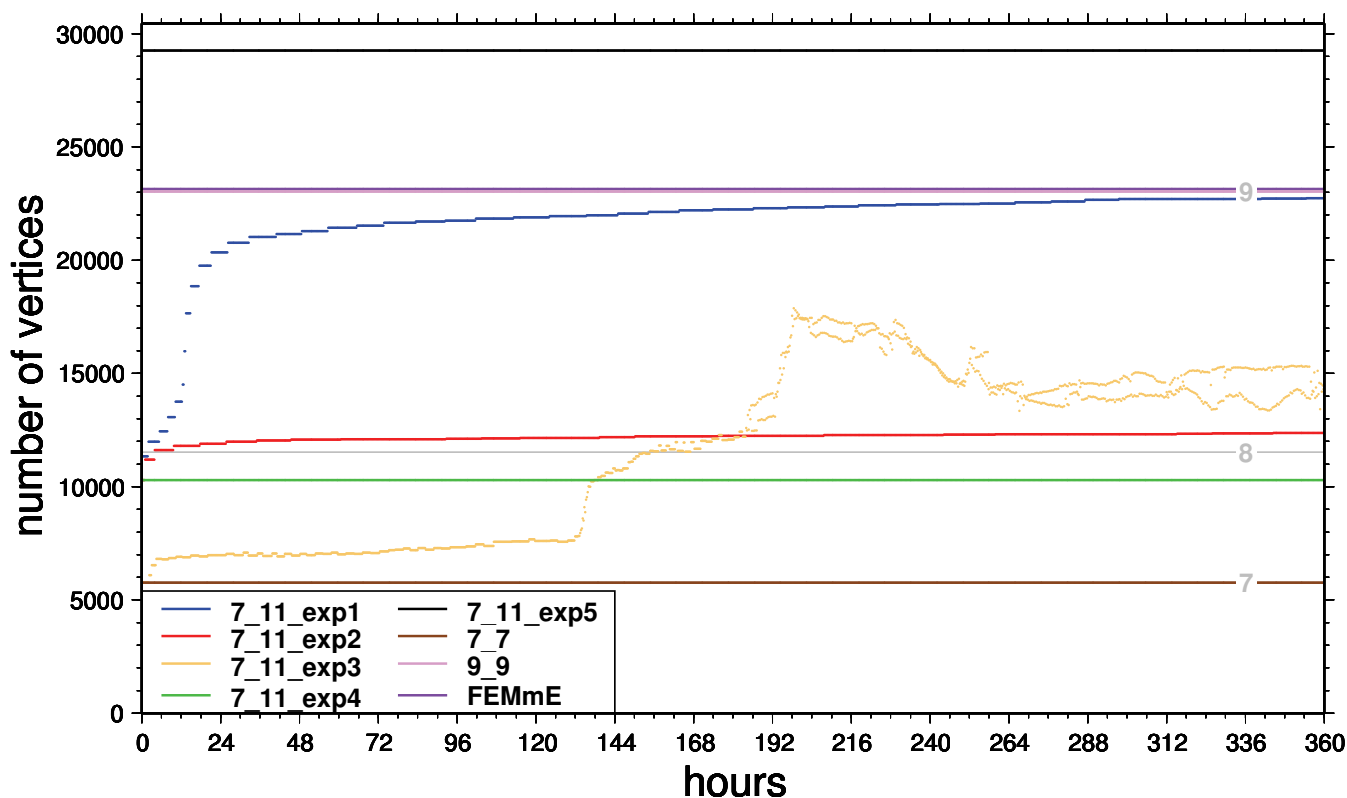
Figure 5.10: Test case 2: horizontal resolution of Experiments
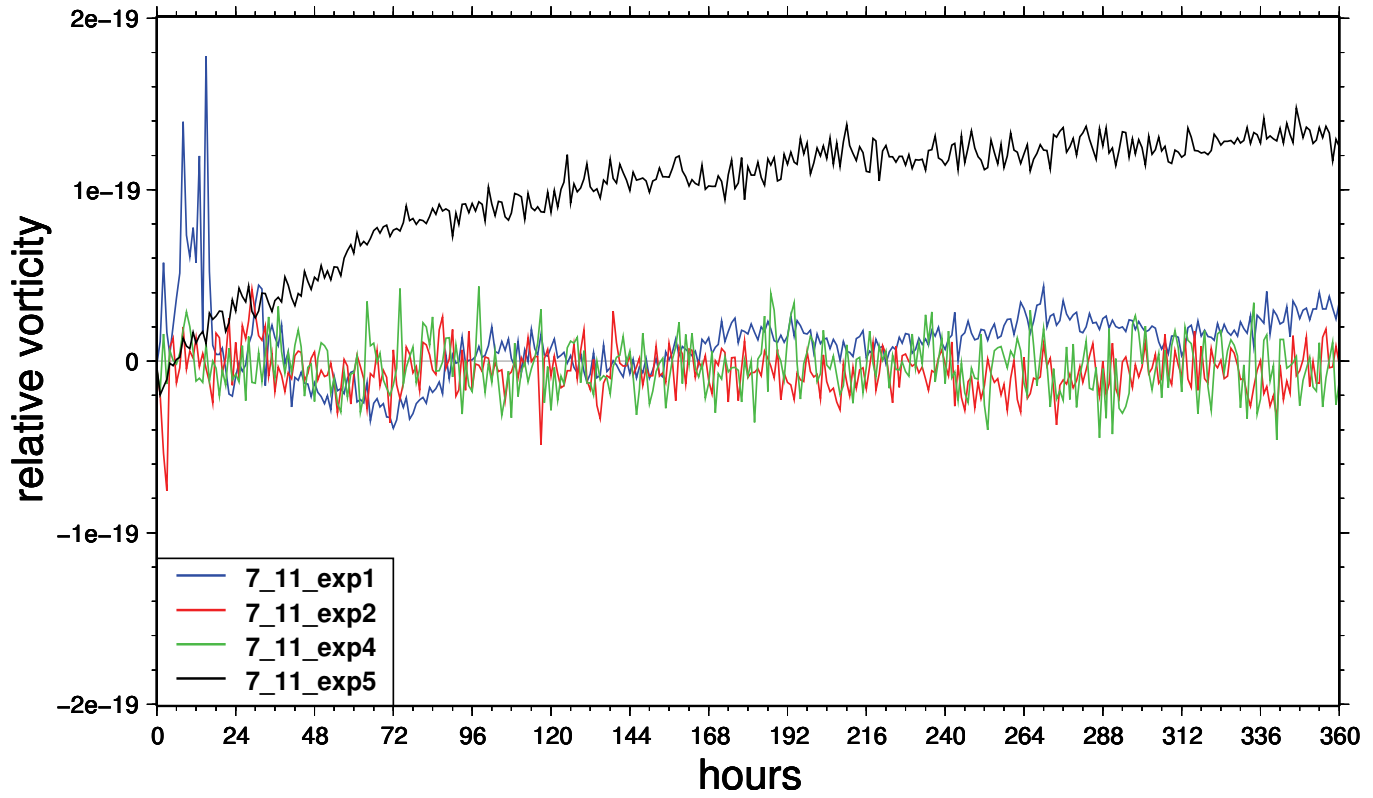
Figure 5.11: Test case 2: relative vorticity
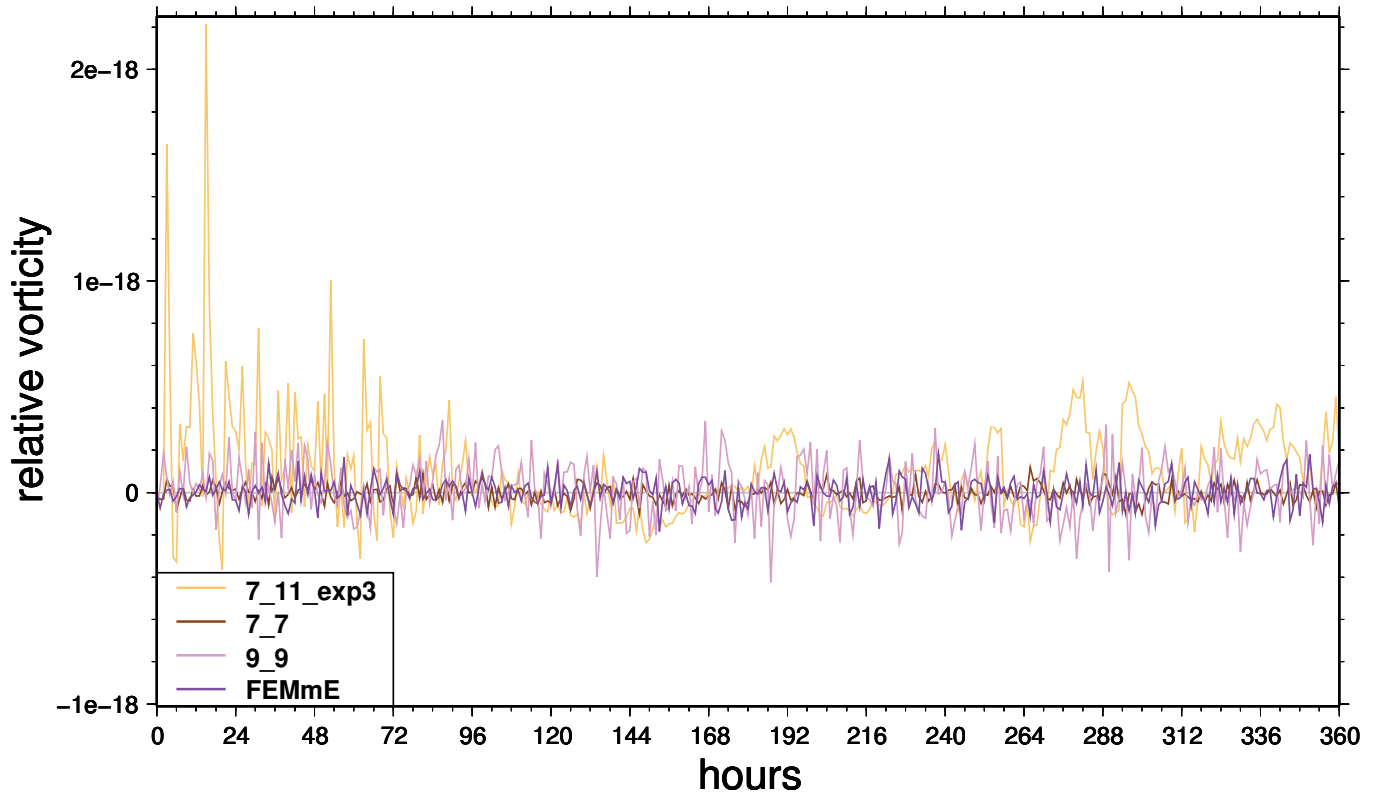
Figure 5.12: Test case 2: relative vorticity as Figure 5.11, but different scale
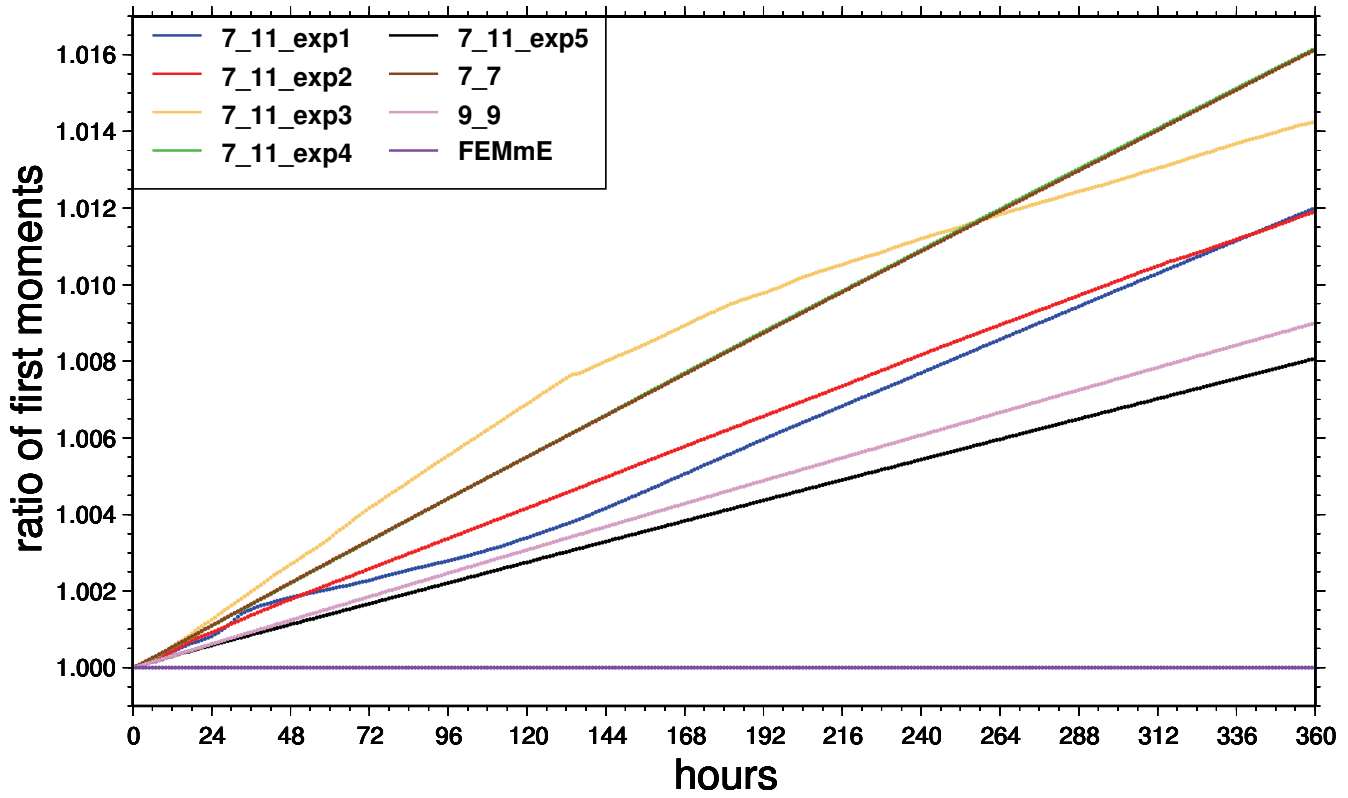
Figure 5.13: Test case 2: ratio of first moments
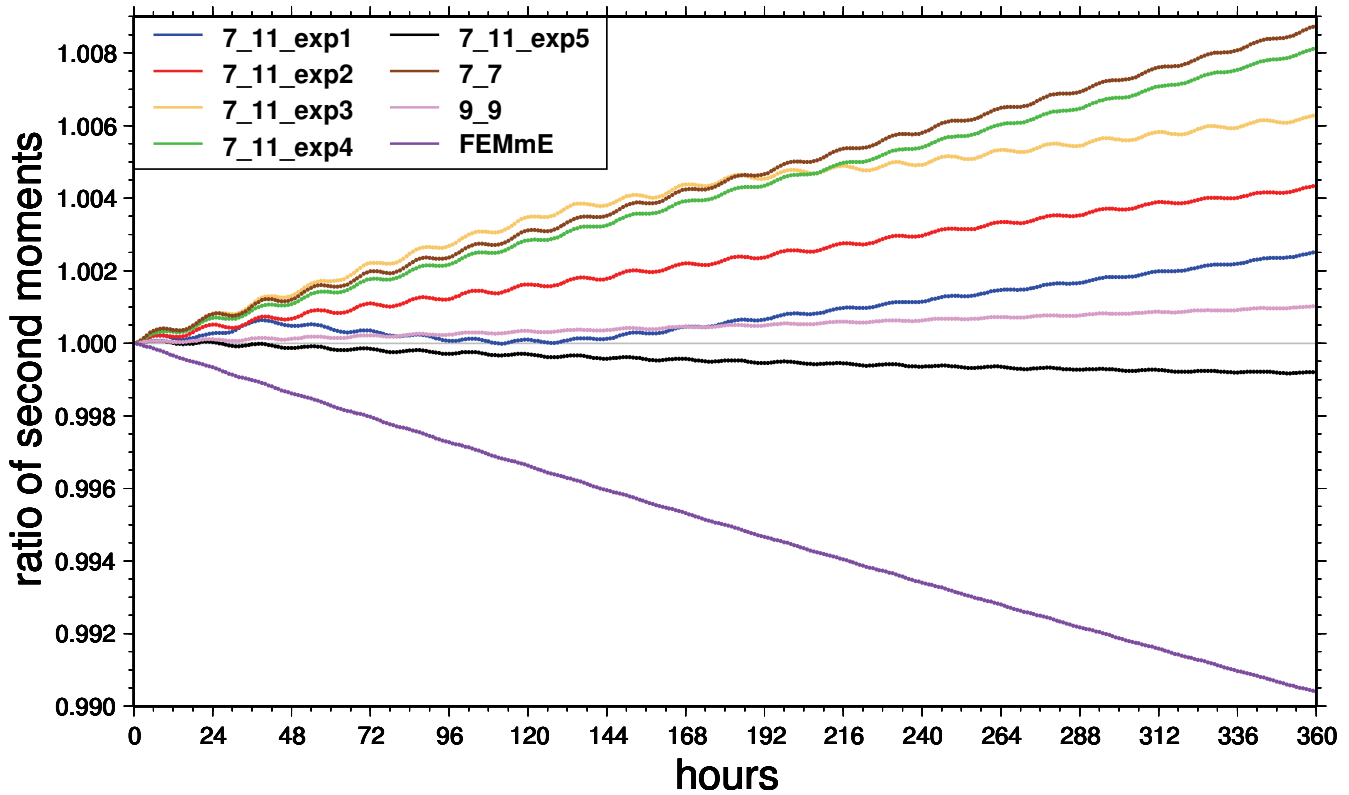
Figure 5.14: Test case 2: ratio of second moments
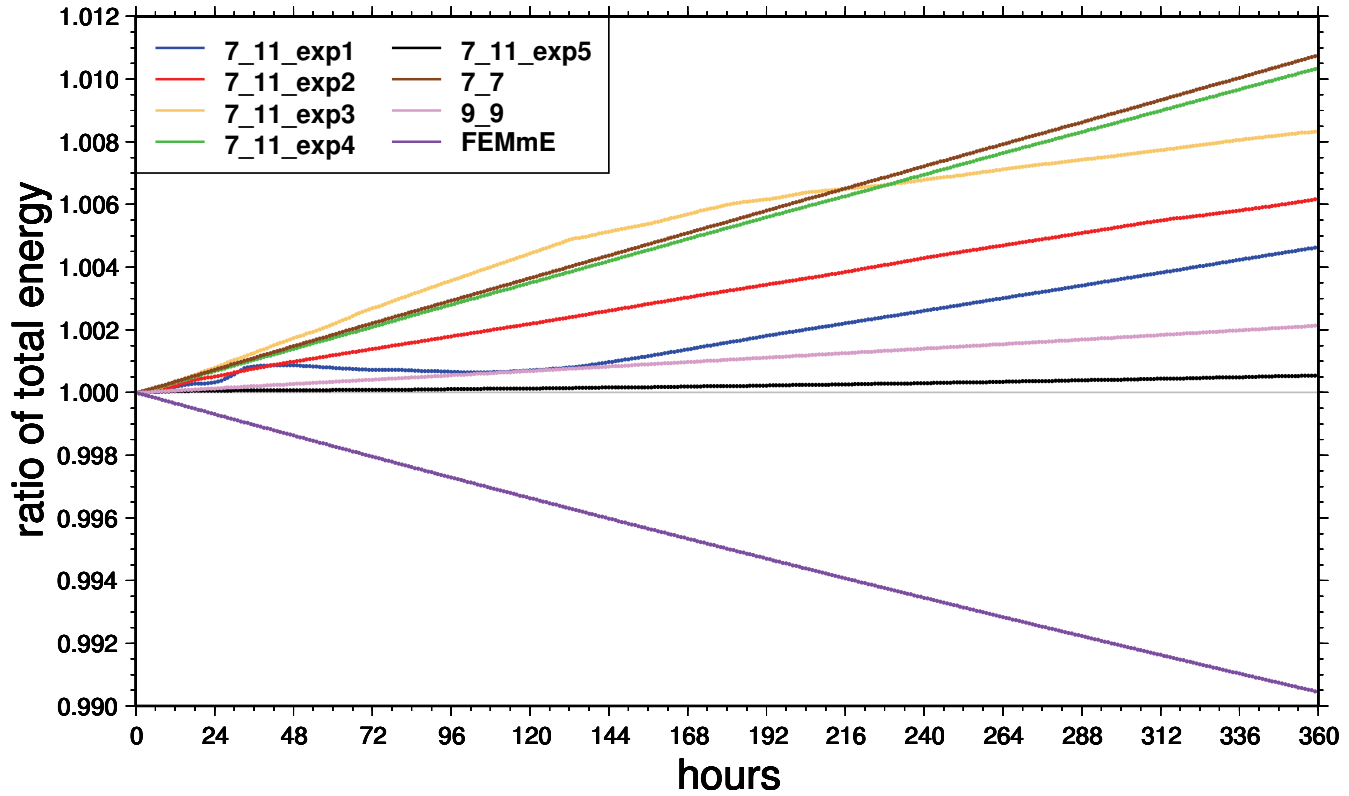
Figure 5.15: Test case 2: ratio of total energy
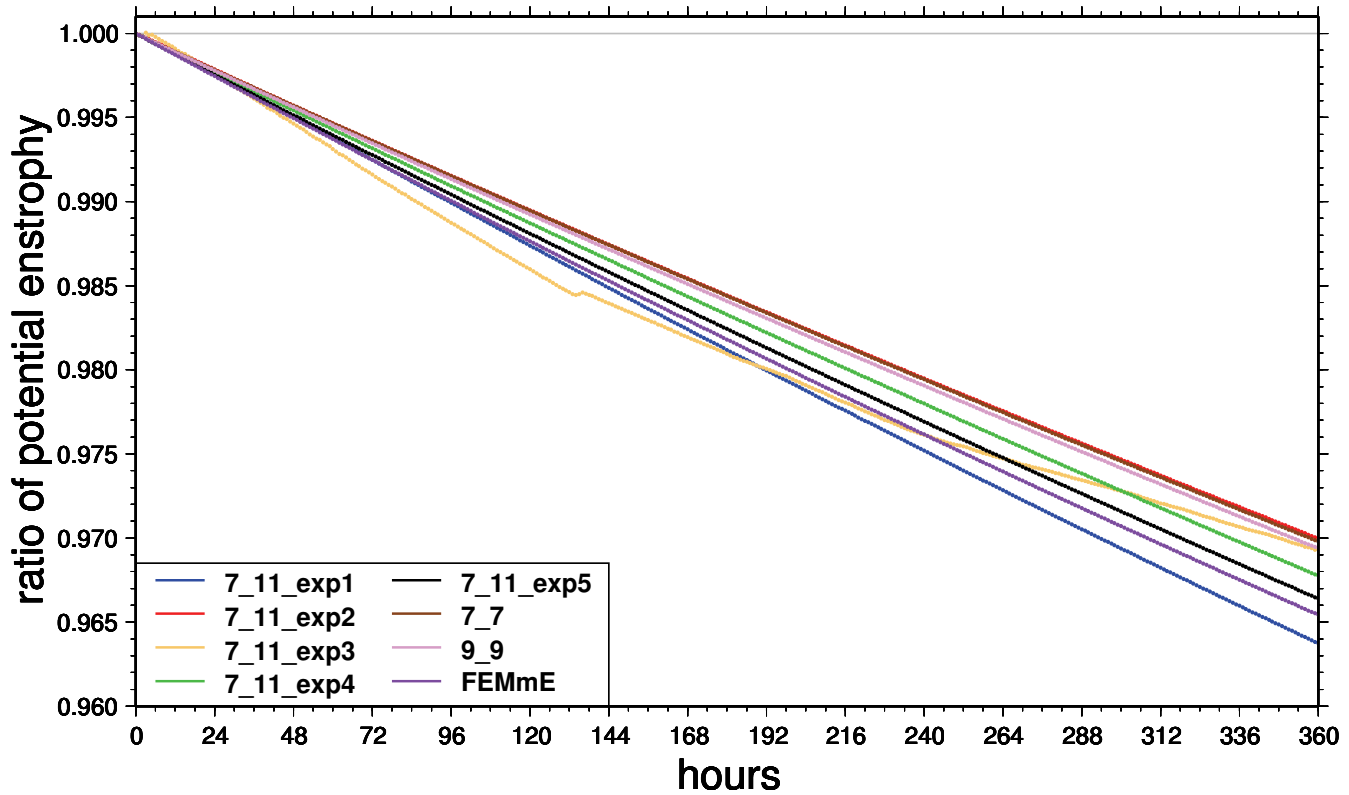
Figure 5.16: Test case 2: ratio of potential enstrophy
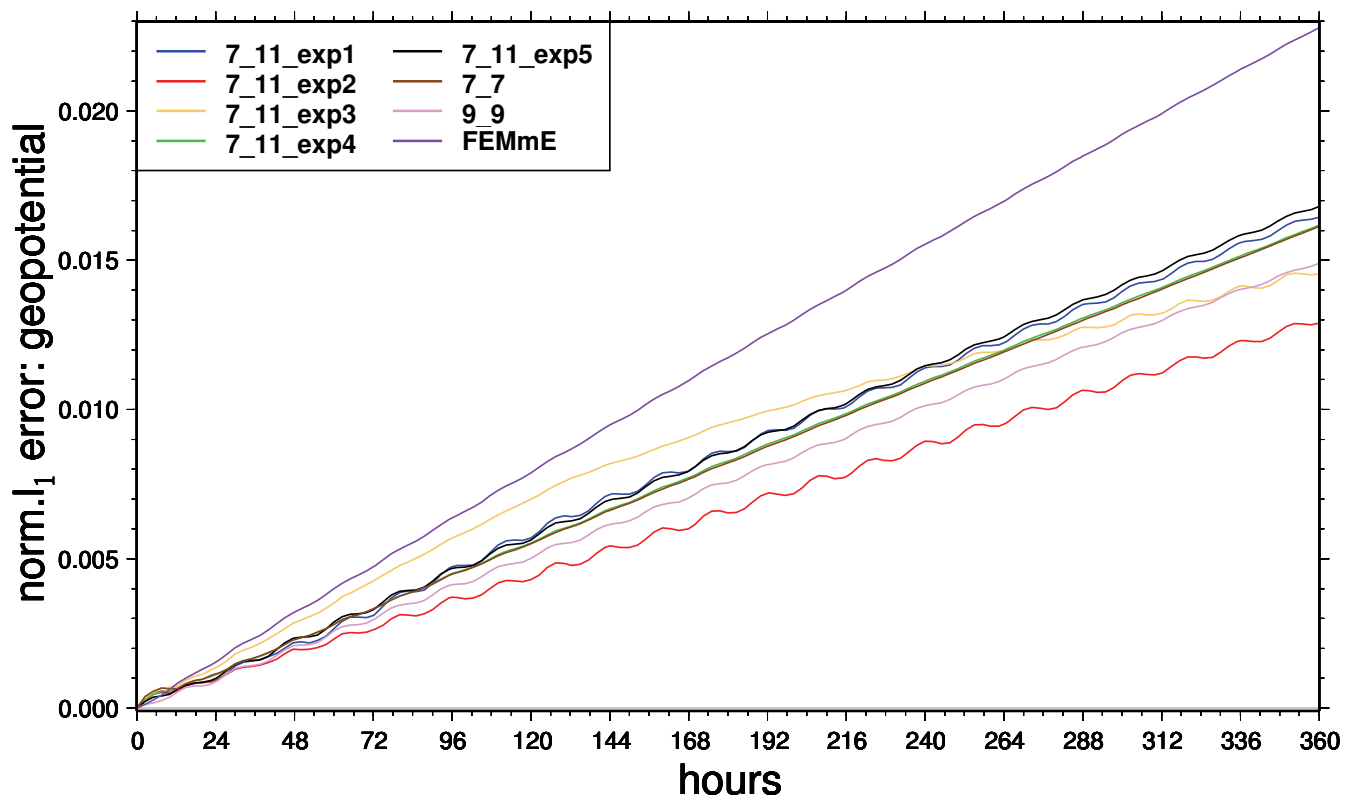
Figure 5.17: Test case 2: normalised l_1 error of geopotential
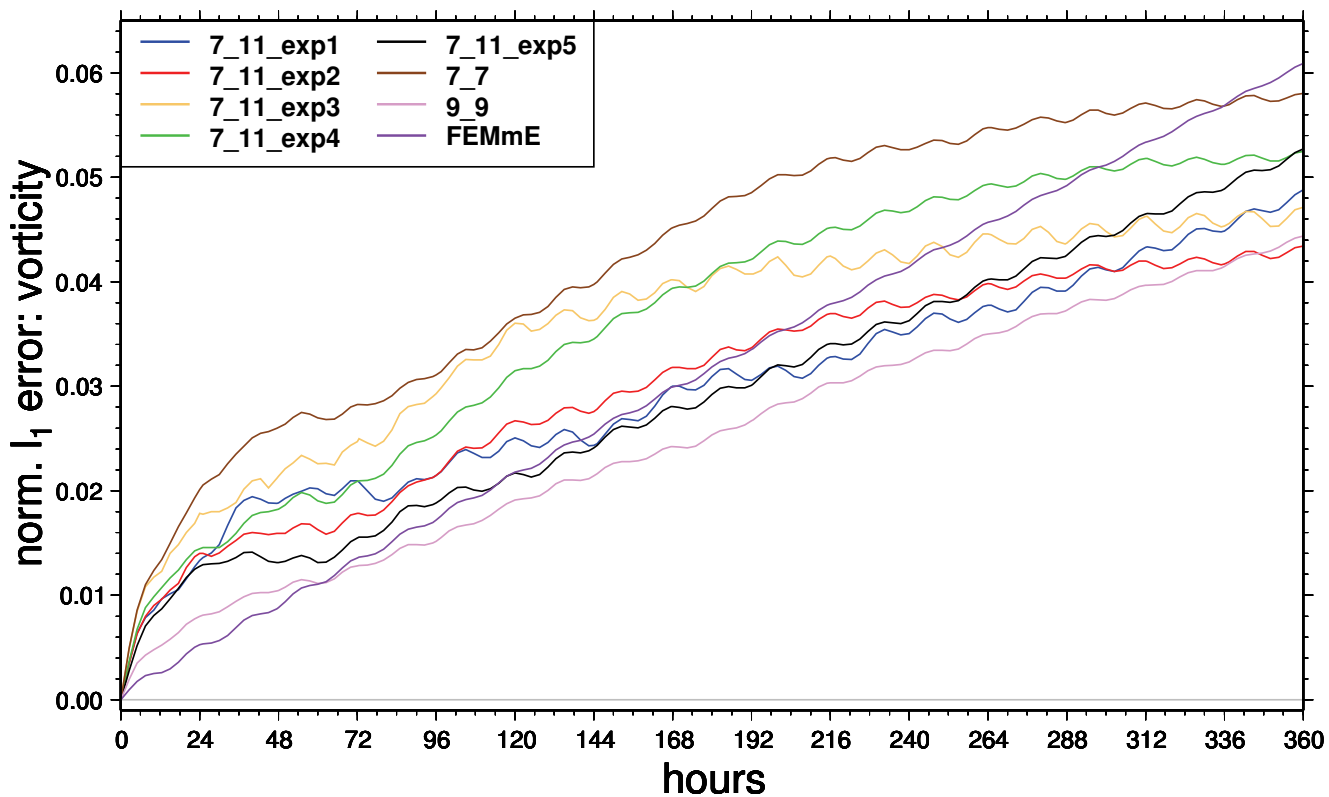
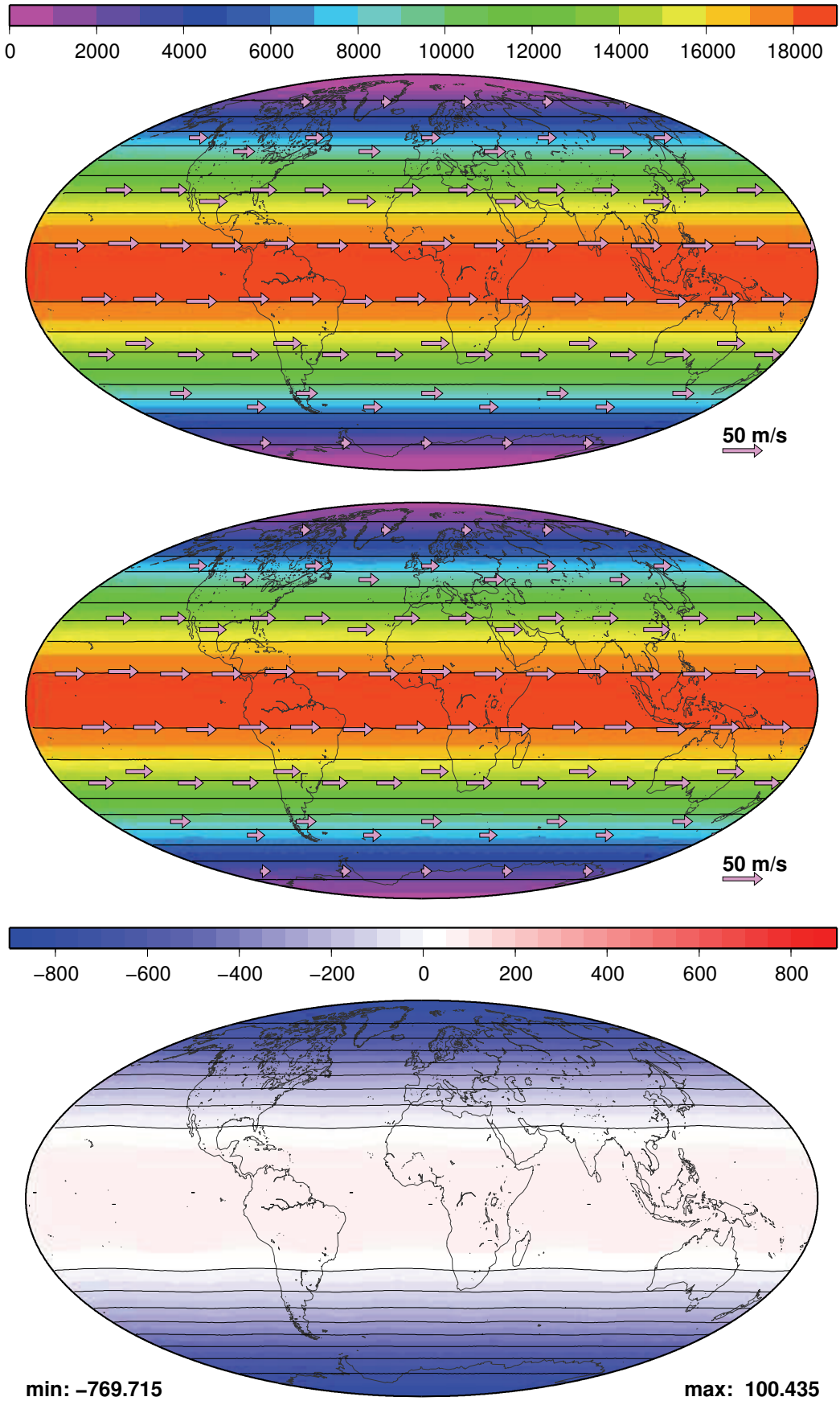Figure 5.18: Test case 2: normalised l_1 error of vorticity
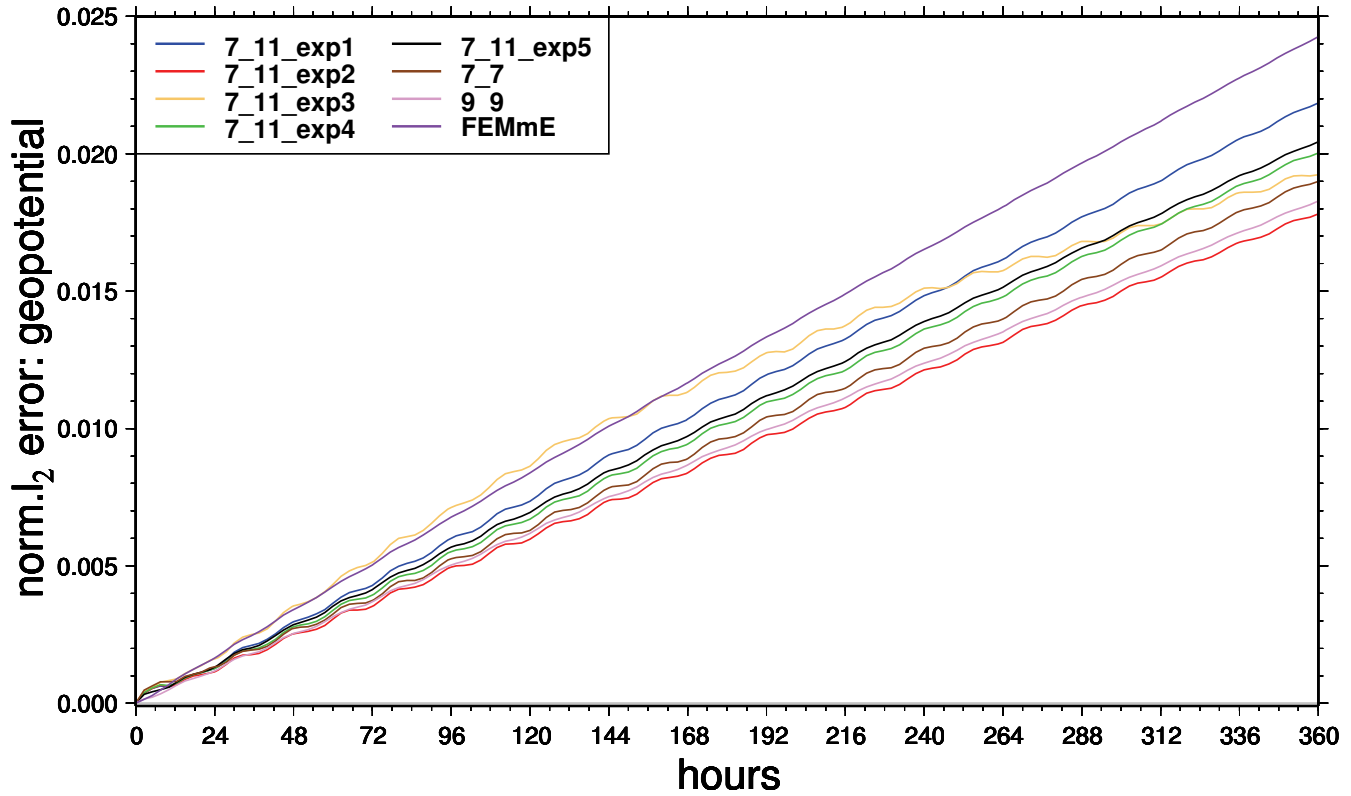
Figure 5.19: Test case 2: normalised l_2 error of geopotential
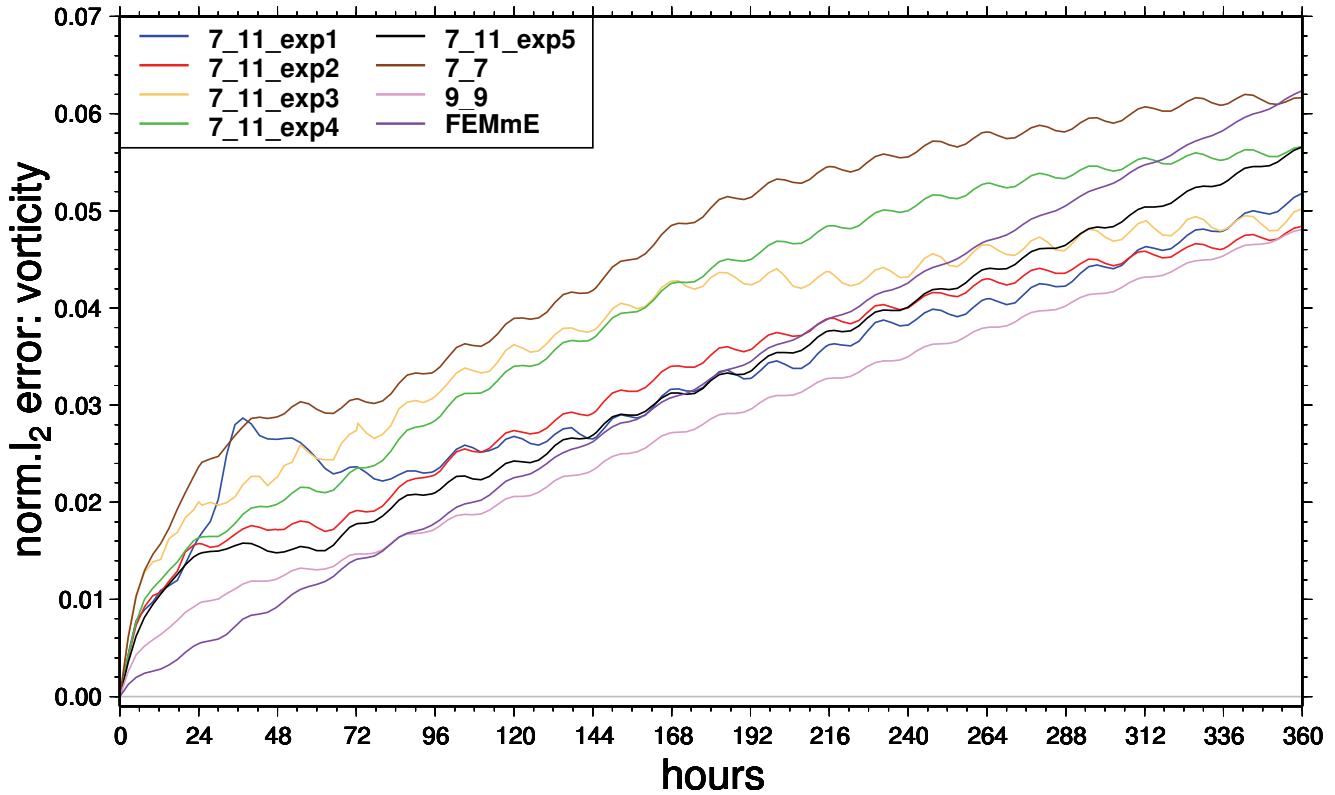
Figure 5.20: Test case 2: normalised l_2 error of vorticity
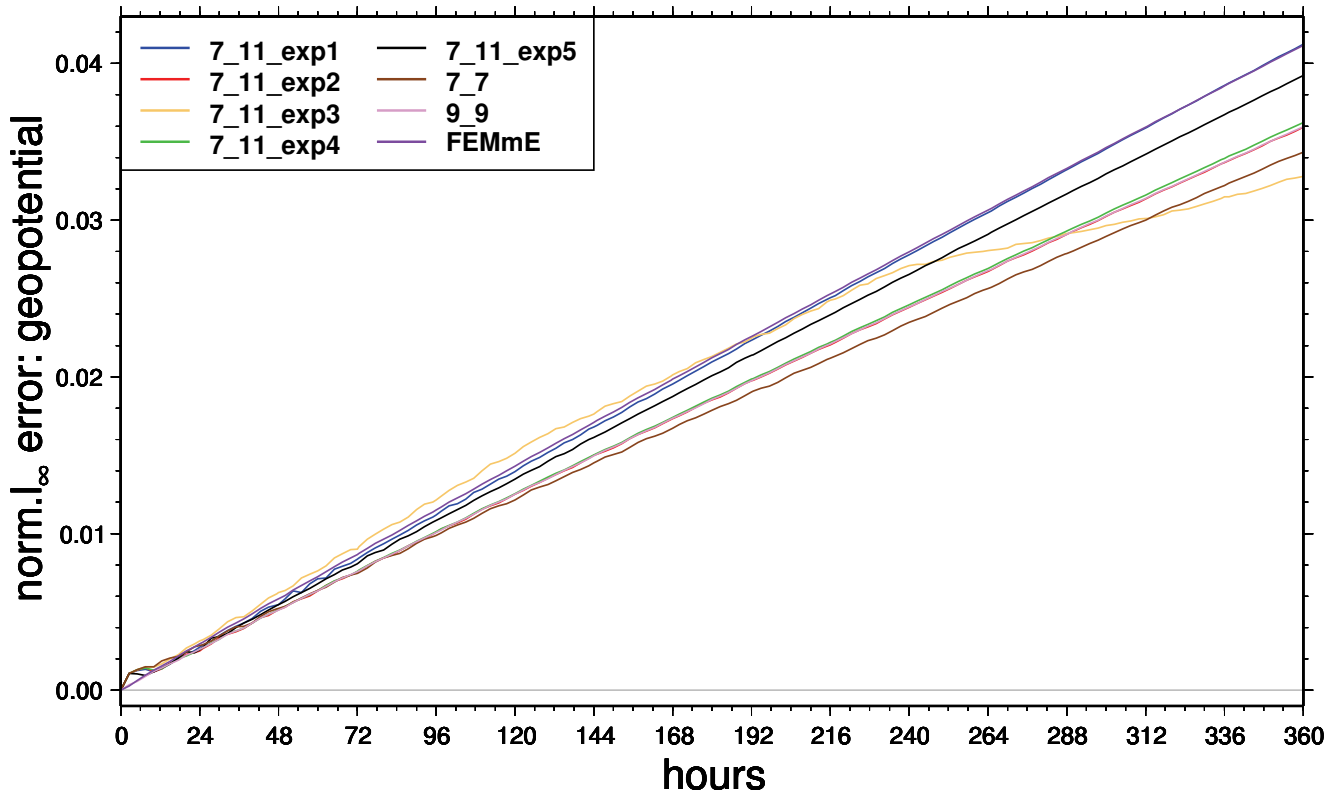
Figure 5.21: Test case 2: normalised l_∞ error of geopotential
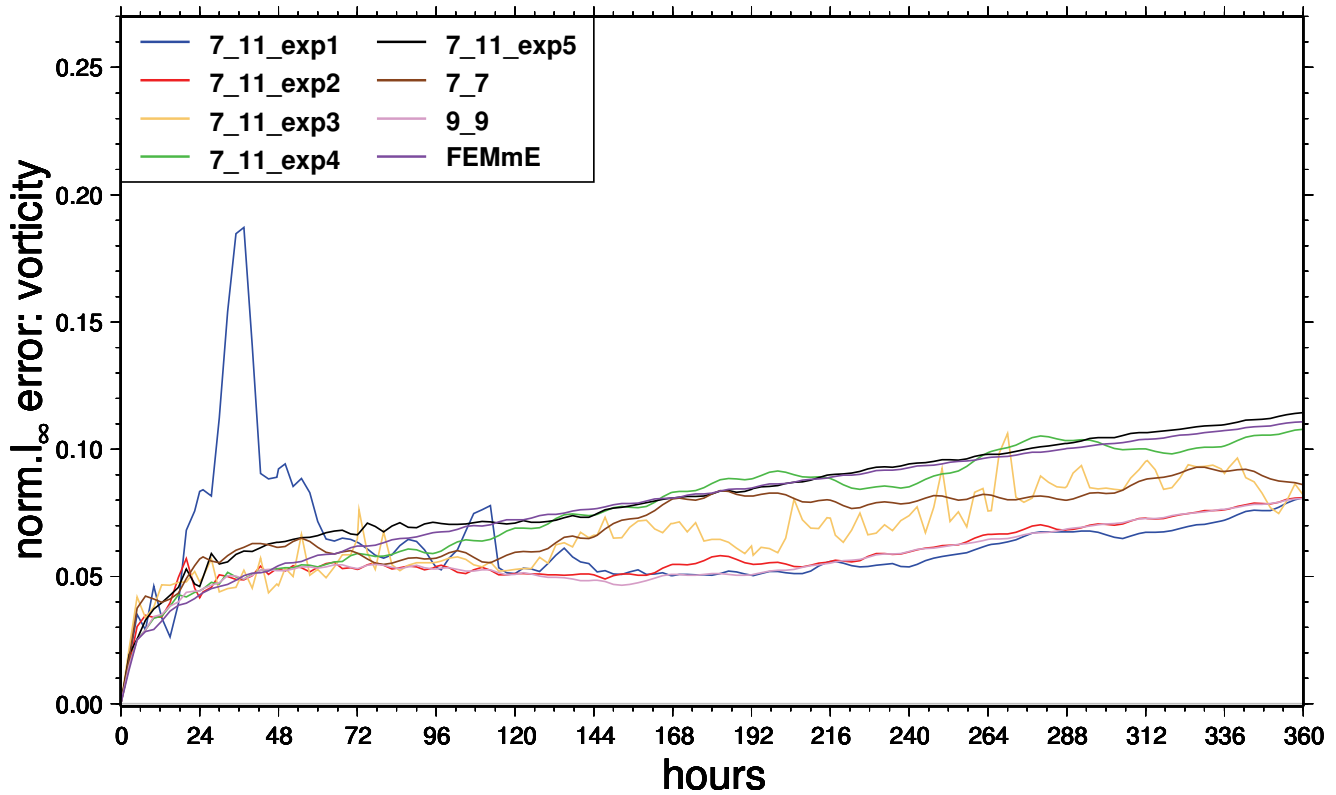
Figure 5.22: Test case 2: normalised l_∞ error of vorticity

Figure 5.23: Experiment 1, initial state of geopotential and after 15 days, error after 15 days
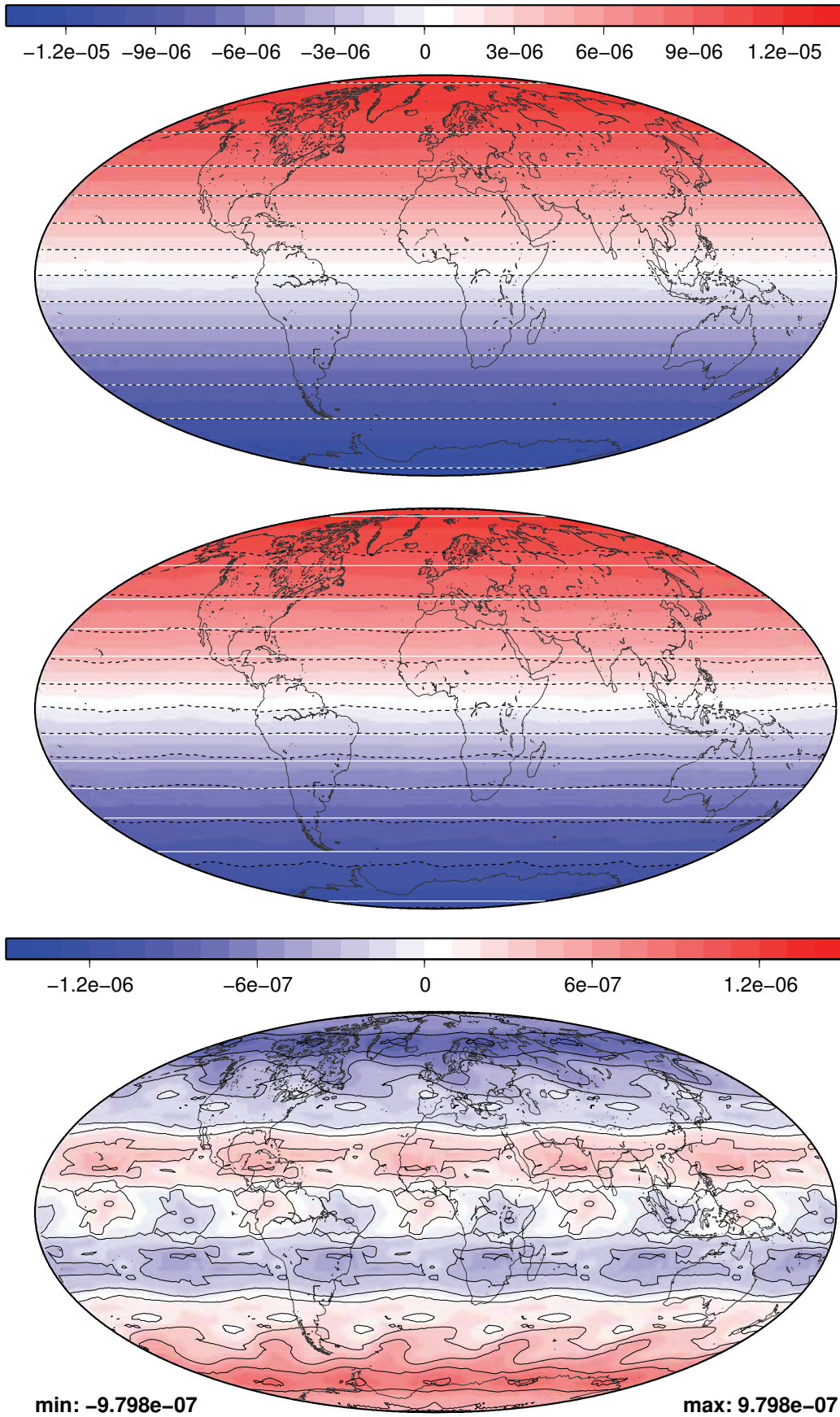
Figure 5.24: Experiment 1, initial state of vorticity and after 15 days, error after 15 days

min: –670.804   **max: 48.083**

min: –612.380   **max: 26.052**

min: –676.129   **max: 6.642**
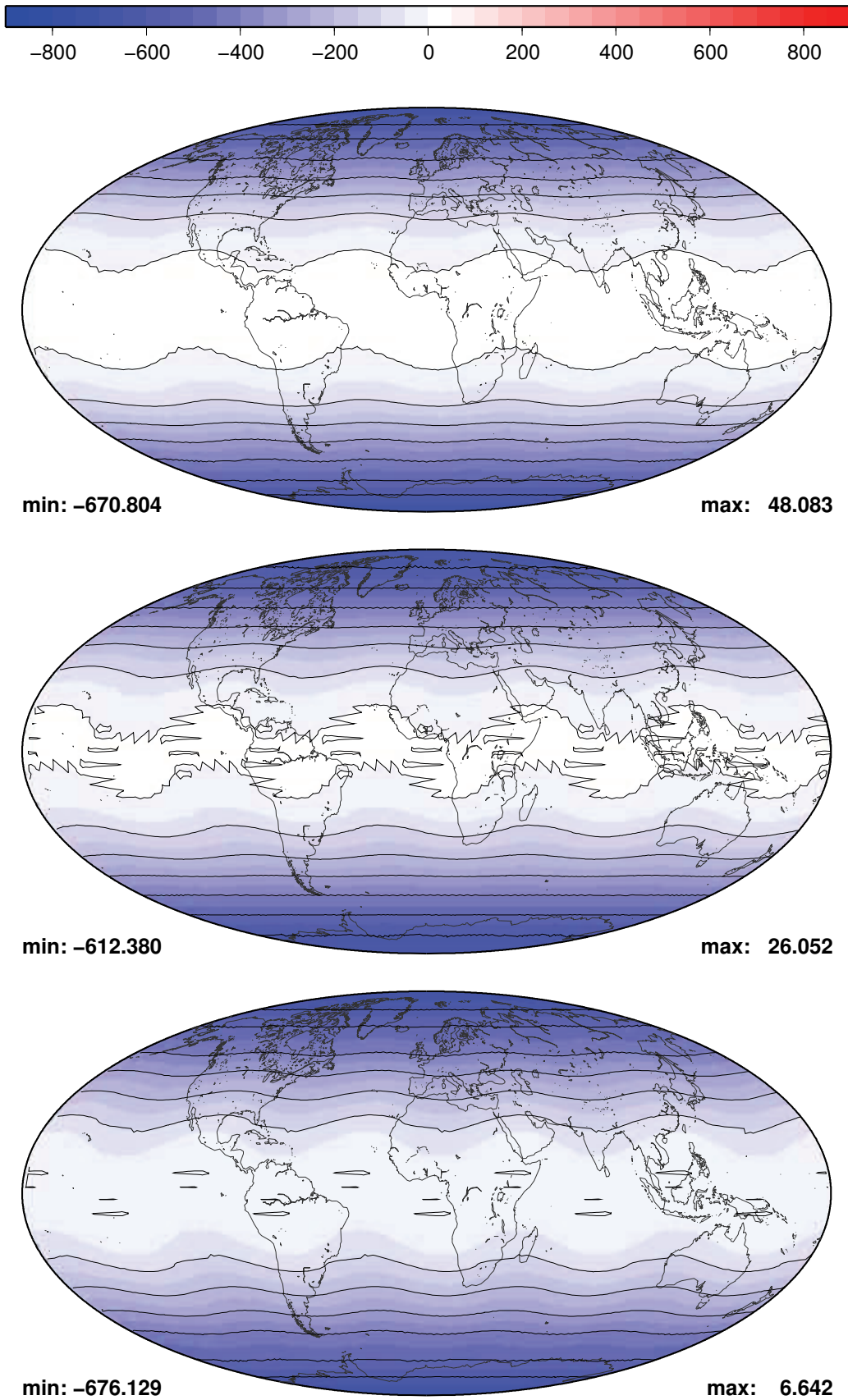
Figure 5.25: Experiment 2, 3 and 4, error of geopotential after 15 days

min: −9.790e−07   **max: 9.790e−07**

min: −9.898e−07   **max: 9.898e−07**

min: −1.305e−06   **max: 1.305e−06**
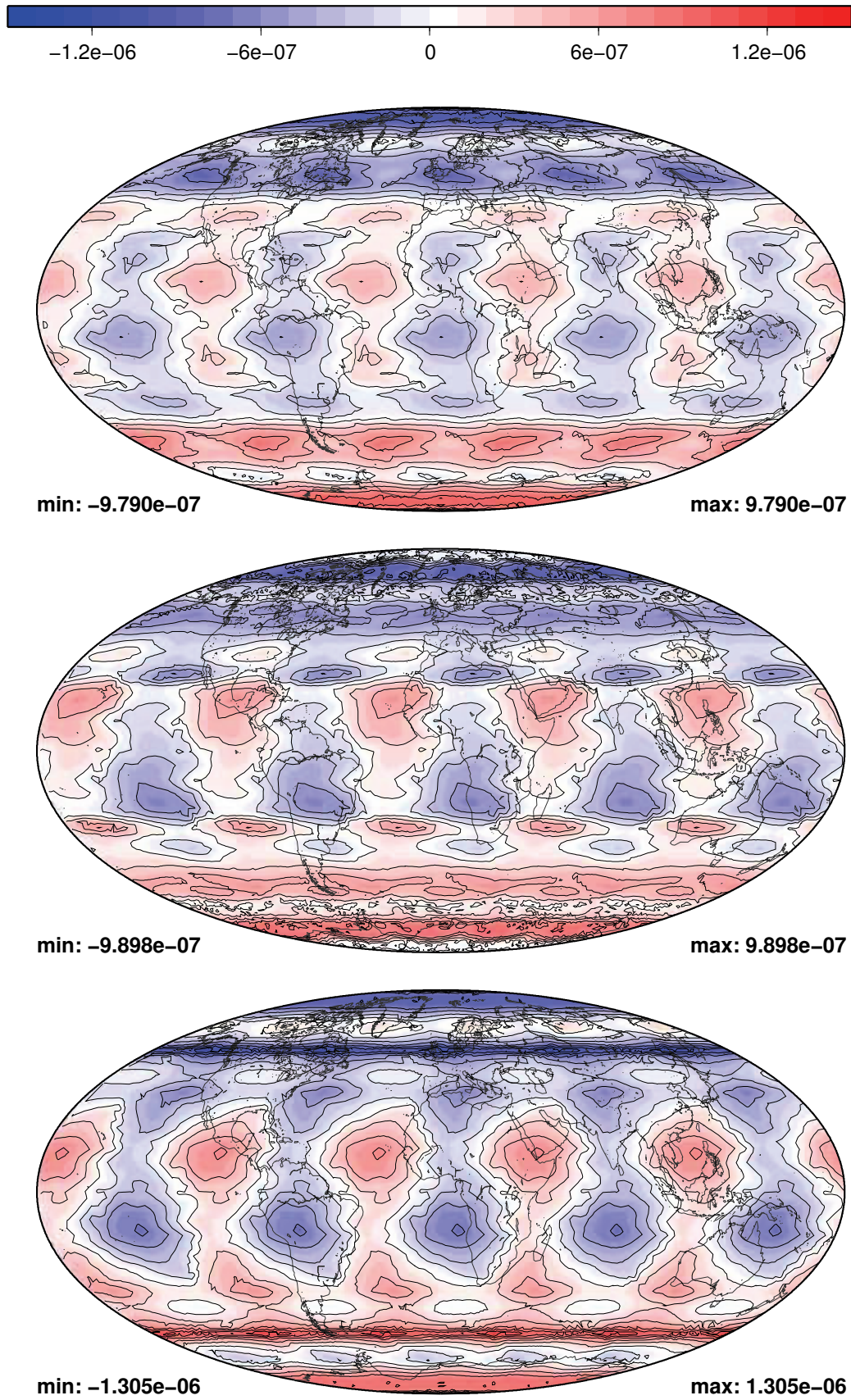
Figure 5.26: Experiment 2, 3 and 4, error of vorticity after 15 days

min: –732.294   max: 160.113

min: –641.139   max: –5.728

min: –671.384   max: 119.372
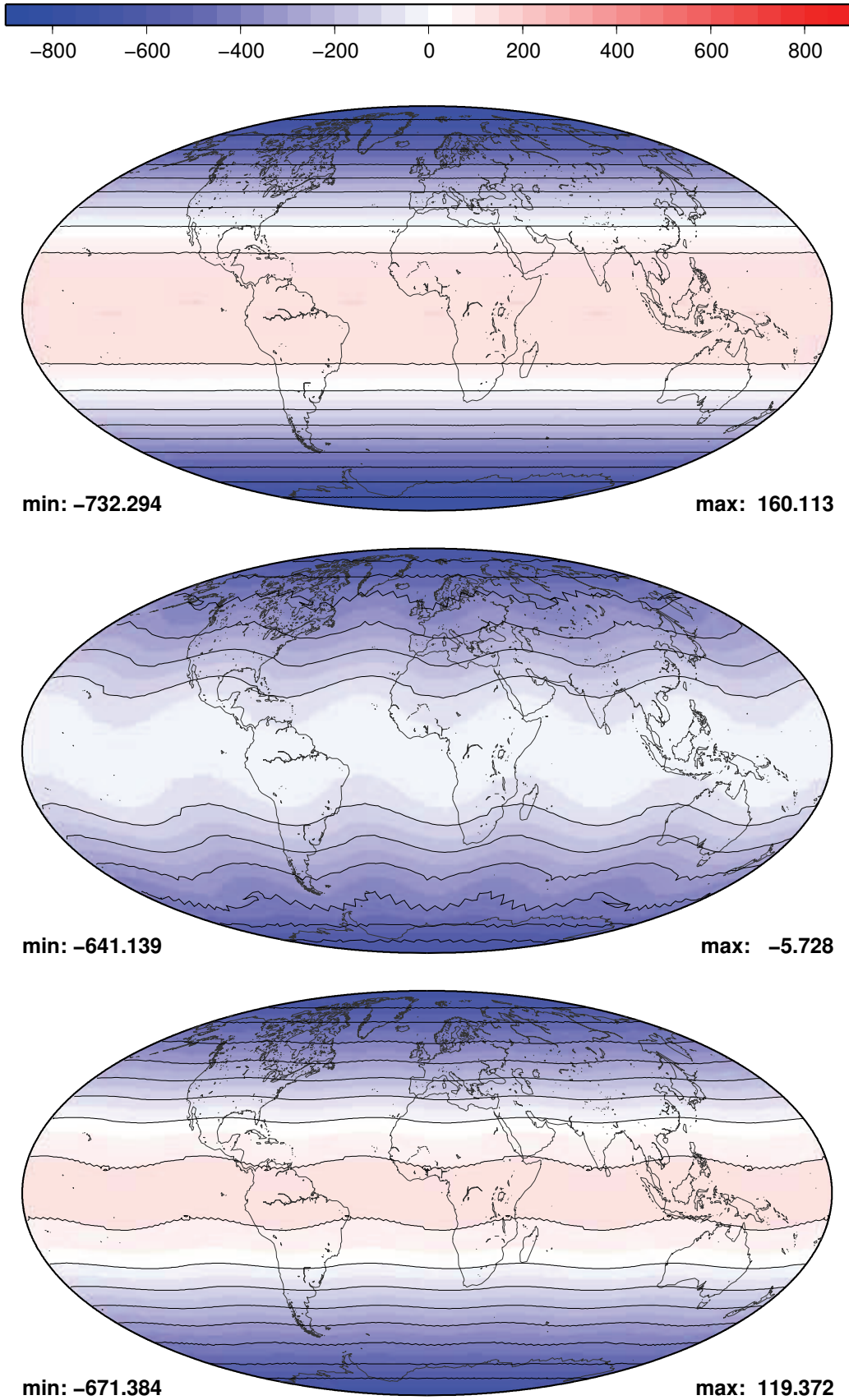
Figure 5.27: Experiment 5, 7_7 and 9_9, error of geopotential after 15 days

min: −1.386e−06   **max: 1.386e−06**

min: −1.039e−06   **max: 1.039e−06**

min: −9.749e−07   **max: 9.749e−07**
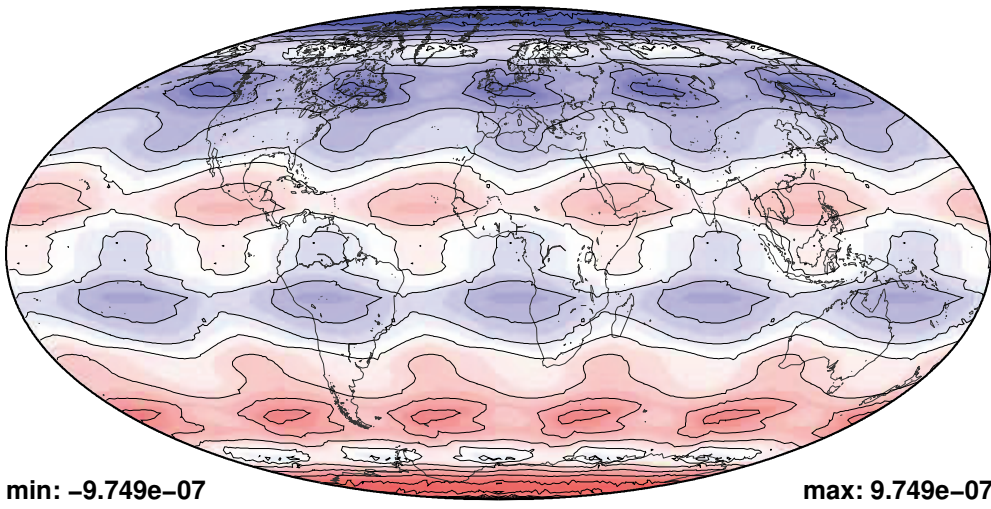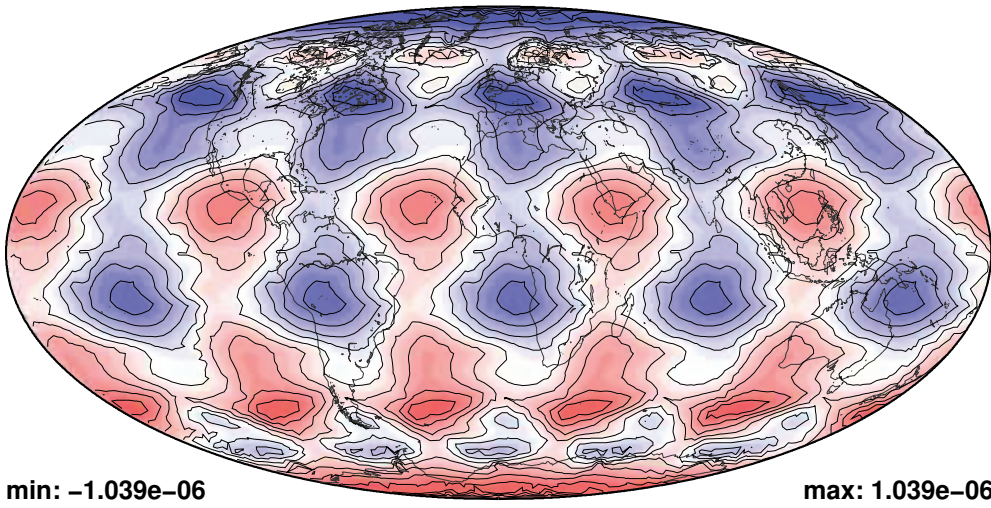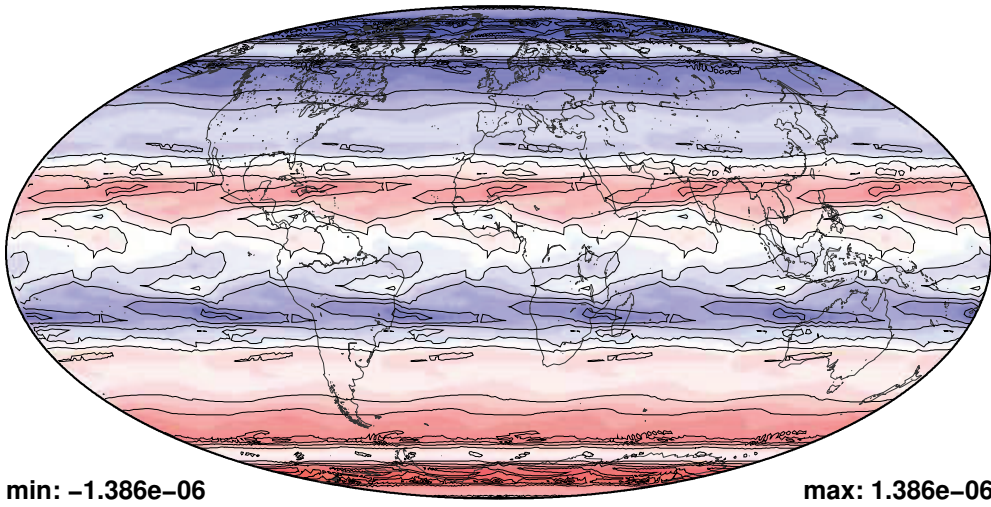
Figure 5.28: Experiment 5, 7_7 and 9_9, error of vorticity after 15 days
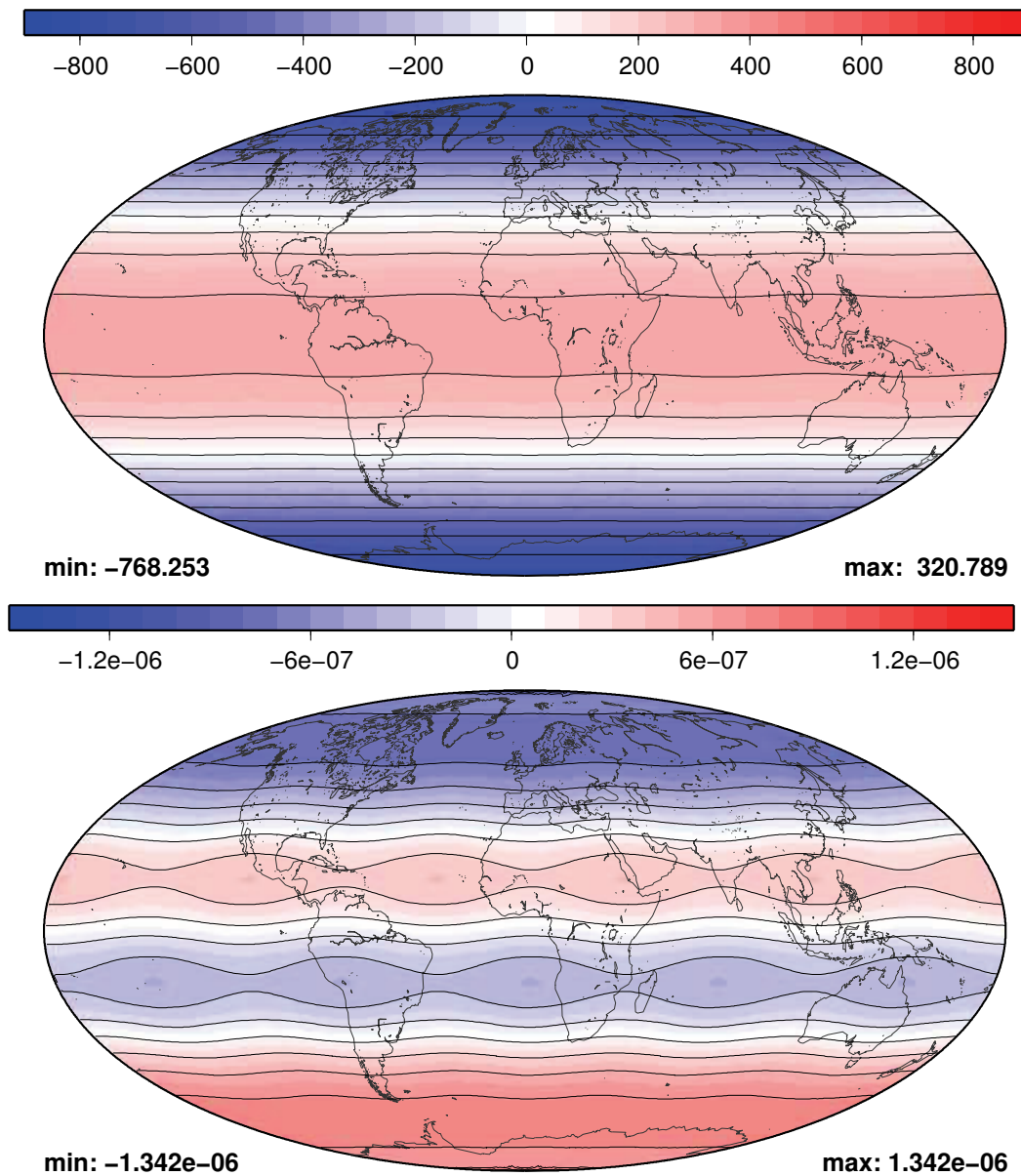
Figure 5.29: **FEMmE**, error of geopotential and vorticity after 15 days

Both have a big spread in the relative vorticity though no trend can be observed. **FEMmE** is the only experiment that conserves the mass nearly perfectly. One reason why it became the prototype of this model. Experiment 9_9 gains mass of around 9% within the 15 days, but is still one of the best among the experiments. The second moments and the total energy show the opposite picture. 9_9 grows only very little by 1% resp. 2% and **FEMmE** loses nearly 10%. In fact it is the only one that clearly loses conservation properties in contrast to all others that are gaining. **FEMmE** generates the biggest errors of all experiments, whereas 9_9 is among the smallest. Like in the error patterns of the vorticity (Figure 5.28), also in the geopotential WN5 features can be observed with experiment 9_9 (Figure 5.27). This is different for the **FEMmE** experiment where the error is only latitudinally dependent (Figure 5.29).

The other experiments are those with total number of grid points less than 18,000. Specific for these experiments are WN5 features in the error patterns of vorticity and geopotential. WN5 features in the error pattern are a well known phenomenom of models based on the

icosahedron. The 12 original grid points of the icosahedron are the reason. Apart from the poles they are located on two parallels $26.57°$ north and south of the equator, on each parallel 5 of them equiangular. These 12 points are in so far special as in all grids those points have 5 neighbours (or a multiple of 5). All other grid points of the macro triangulation for example have 6 neighbours. The results of test case 2 suggest that it is necessary to use grids with higher resolution to overcome this problem. But those "low resolution" experiments are not bad in all aspects. For example experiments 2 and 4 conserve the relative vorticity with a very small spread around 0 (Figure 5.11). Experiment 3 and 7_7 have a much wider spread, but also no trend is visible (Figure 5.12). The ratio of first and second moments as well as total energy proves that dynamic grid adaptation improves the results. Less surprising, experiments 3, 4 and 7_7 perform poor in these quantities. But in experiment 2, which is the dynamic version of experiment 4, the gain of those quantities is only half as big as in the other 3 experiments. Additionally, the time series of the errors show that this experiment can compete with the experiments 1 and 9_9. Experiment 2 reduces the error in comparison to experiment 4: the normalised l_∞ error of geopotential only slightly, all others noticeably by 10% to 25%.

5.3.7 Summary of test case 2 results

The five main points of the test case 2 experiments are:

1. The basic operators are second order convergent.

2. The dynamical core does not conserve potential enstrophy.

3. **FEMmE** grid conserves mass.

4. Normalised errors of relative vorticity are 3 orders of magnitude larger than those of the geopotential.

5. Coarse grids show WN5 error pattern.

5.4 Test case 5

5.4.1 Test case 5 on the globe

Test case 5 of the Williamson et al. (1992) test suite describes a flow over an isolated mountain. The initial condition of the velocity and the vorticity are basically the same as in test case 2, besides the reduced maximum wind speed of $U_o = 20$ ms^{-1}. The centre of the conical mountain is situated at $Z\left(-\frac{\pi}{2}, \frac{\pi}{6}\right)$ with the maximum height of $B_{max} = 2000$ m. Its shape is fixed by

$$\phi_{Ho}(\vec{x}) = gB_{max}\left(1 - \frac{r(\vec{x})}{R}\right) \tag{5.37}$$

$$R = \frac{\pi}{9} \tag{5.38}$$

$$r(\vec{x}(\lambda, \varphi)) = \sqrt{\min\left\{R^2, (\lambda + \frac{\pi}{2})^2 + (\varphi - \frac{\pi}{6})^2\right\}}. \tag{5.39}$$

The initial geopotential is symmetric to the equator

$$\phi_o = \breve{\phi} + \cos^2\varphi \left(r_e\,\Omega\,U_o + \frac{1}{2}\,U_o^2 \right) + gB_{max} \tag{5.40}$$

$$\breve{\phi} = gh_o - \left(r_e\,\Omega\,U_o + \frac{1}{2}\,U_o^2 \right) - gB_{max} \tag{5.41}$$

with

$$g = 9,80616\ \mathrm{ms}^{-2} \tag{5.42}$$

$$h_o = 5960\ \mathrm{m}. \tag{5.43}$$

5.4.2   Test case 5 on the unit sphere

Transforming this system to the unit sphere using the characteristic values of equations (2.12) to (2.16), gB_{max} and gh_o are transformed to

$$\widetilde{gB}_{max} = G^{-1} \cdot gB_{max} \tag{5.44}$$

$$\widetilde{gh}_o = G^{-1} \cdot gh_o. \tag{5.45}$$

Thus, equation (5.37) changes to

$$G \cdot \widetilde{\phi}_{Ho}(\vec{x}) = G \cdot \widetilde{gB}_{max} \left(1 - \frac{r(\vec{x})}{R} \right) \tag{5.46}$$

$$\widetilde{\phi}_{Ho}(\vec{x}) = \widetilde{gB}_{max} \left(1 - \frac{r(\vec{x})}{R} \right). \tag{5.47}$$

The basic state of the geopotential (5.41) then reads

$$G \cdot \overline{\phi} = G \cdot \widetilde{gh}_o - U^2 \left(\frac{LF}{U} \cdot \widetilde{r}\widetilde{\Omega}\,\widetilde{U}_o + \frac{1}{2}\,\widetilde{U}_o^2 \right) - G \cdot \widetilde{gB}_{max} \tag{5.48}$$

$$\overline{\phi} = \widetilde{gh}_o - \frac{\widetilde{U}_o}{\nu^2} \left(\mu + \frac{1}{2}\,\widetilde{U}_o \right) - \widetilde{gB}_{max} \tag{5.49}$$

and the perturbation (5.40) has the form

$$G \cdot \widetilde{\phi}_o = G \cdot \overline{\phi} + U^2 \cdot \cos^2\varphi \left(\frac{LF}{U} \cdot \widetilde{r}\widetilde{\Omega}\,\widetilde{U}_o + \frac{1}{2}\,\widetilde{U}_o^2 \right) + G \cdot \widetilde{gB}_{max} \tag{5.50}$$

$$\widetilde{\phi}_o = \overline{\phi} + \frac{\widetilde{U}_o}{\nu^2} \cos^2\varphi \left(\mu + \frac{1}{2}\,\widetilde{U}_o \right) + \widetilde{gB}_{max}. \tag{5.51}$$

5.4.3   Experimental settings and results

As a results of the previous test case, one conclusion for test case 5 is to enhance the numbers of grid points. Thus, the following changes are implemented:

5.15   Modified grid adaption strategy:

1. Set the minimum number of grid points to 15,000.

2. If the grid created by *amatos* has less then 15,000 grid points, set the threshold for coarsening to $\Theta_{crs} = 0$ and the watermark to $w = 0$. Readapt the grid and afterwards set Θ_{crs} and w back to the previous values.

experiment	adaption type	error indicator	Θ_{crs}	Θ_{ref}	w	coarse grid level	fine grid level
7_11_exp1	dynamic	ave	0.5	1.5	0.1	7	11
7_11_exp2	dynamic	ave	0.6	1.6	0.1	7	11
7_11_exp3	dynamic	max	0.05	0.8	0.25	7	11
7_11_exp4	dynamic	max	0.05	0.52	0.33	7	11
7_11_exp5	static	ave	0.3	1.2	0.1	7	11
7_11_exp6	static	max	0.2	0.72	0.3	7	11
9_9	none	-	-	-	-	9	9
FEM*m*E	none	-	-	-	-	9	9

Table 5.3: Experiments investigated in test case 5

3. If none of the triangles are marked for adaption, but the number of grid points is less than 15,000, than mark all the triangles of the then coarsest level for refinement and readapt the grid.

4. Redo step 2 and 3 until a grid with at least 15,000 grid points has been created.

5.16 Remark:
15,000 is an arbitrary choice set by inspection of Figure 5.10. This number is adapted to the situation of test case 2 that is similar to that of test case 5. It would be an asset to have an objective criterion for the setting of this number. But as long as such criterion is not available 15,000 is sufficient for the requirements of this test case.

All other settings are taken over from test case 2. Table 5.3 gives the details of the experimental settings. Here 4 experiments with a fixed grid and 4 with dynamic grid adaption are investigated. The control experiments, **FEM*m*E** and experiment 9_9, use the same grid points but different refinement strategies. 3 of the other experiments uses the maximum criterion for the thresholds, the other 3 the average criterion. It turns out that the average criterion fits much better to this test case. Finding settings for the maximum criterion that lead to reasonable results is a difficult job. Small changes of the parameters leads to completely different grids with a big spread in the numbers of grid points at the initial stage. This number is reduced in the first time steps and remains in the range between 15,000 and 20,000 in the following. The reason for this sensitive behaviour is that there are always a few triangles that get a high adaption index. So with the maximum criterion, *amatos* tends to coarsen the grid nearly everywhere. This obviously gets in conflict with the conclusion of the previous test case that at least a minimum number of grid points should be used. With an inappropriate choice of the settings at each time step several grid adaption cycles are performed before the conditions of 5.15 are fulfiled.

experiment	CPU time [h]	number of grids	experiment	CPU time [h]
7_11_exp1	7.6450	233	7_11_exp5	1.8450
7_11_exp2	7.4647	371	7_11_exp6	0.9961
7_11_exp3	5.7208	335	9_9	1.2917
7_11_exp4	5.2511	281	**FEM*m*E**	1.3761

Table 5.4: CPU time of test case 5 experiments

The time series in Figure 5.30 shows that the average criterion does a better job. During the model run with the flow patterns getting more and more complex, more grid points are used in those areas, without reducing the number of grid points elsewhere too much.

Nevertheless, from Table 5.4 one can learn that grid adaptation is time consuming. The CPU time of those experiments with static grid is between 1 and 2 hours. Dynamic grid experiments run between 5 and 8 hours - roughly 4 times longer. Whether this pays off is the question that has to be answered in the end.

Before discussing the conservation properties of Figures 5.30 to 5.35 it should be emphasised that here the scales are different from the previous test case. Particularly conspicuous is the potential enstrophy. Like in test case 2 with a steady flow potential enstrophy is not conserved in this test case and Figure 5.35 looks similar to Figure 5.16. But note the different ordinate labels: in test case 5, the loss of potential enstrophy is less than 1% in all simulations over the first 15 days, whereas it is more than 3% in test case 2.

The global integral of relative vorticity clearly distinguishes the experiments between dynamic grid adaptation and the others. From time step to time step there are only smooth changes for the latter experiments, whereas in the experiments with dynamic grid adaptation bigger jumps are observed. This is a clear indication that grid adaption itself has numerical consequences for the relative vorticity. The non adaptive simulations gain between day 5 and 13 relative vorticity up to $5 \cdot 10^{-8} m^2 s^{-1}$ and fall back to neutral at the end of the 15 day period. An exception is **FEMmE**. This is the only experiment that nearly conserves relative vorticity during the whole integration. The adaptive cases also gain $5 \cdot 10^{-8} m^2 s^{-1}$ of relative vorticity until day 8. Afterwards there is a loss of about $1 \cdot 10^{-7} m^2 s^{-1}$ in the second half.

FEMmE also conserves mass for the first 15 days as it is demonstrated in Figure 5.32. Experiment 5, the highest resolution simulation among the static ones, has a similar evolution. The deviation from perfect mass conservation are less than 0.2‰. On the other hand, the lowest resolution static grid simulation, experiment 6, loses nearly 0.5%. The second control run gains uniformly 0.1% of mass. The behaviour of the dynamic model runs are all similar. Until day 8 they stay close to conservation but losing 2.5‰ over the next 7 days.

The second moments are an indicator for conservation of potential energy. In this test case due to the wave development potential energy is continually transformed into kinetic energy. So only RTE is conserved in the continuous case, not RSM. But, comparing Figures 5.33 and 5.34, one can easily conclude that the reason for losing total energy is losing potential energy. However, not all simulations lose total energy. The control run experiment 9_9 nearly conserves this quantity over the 15 day period and the two simulations that conserve the mass, **FEMmE** and experiment 5, lose less than 1‰. The dynamic simulations performs worse by losing between 2 and 4‰, whereas most of this loss again takes place after day 8. In respect to energy conservation experiment 6 also obtains a poor result by losing more than 5‰.

5.4.4   Development in time

In this section the temporal development of geopotential and vorticity together with the grid adaptation is presented exemplary at experiment 1. The initial state is the geostrophically balanced flow well known from test case 2. At initial time a conical mountain is plugged into the flow field. Due to this obstacle immediately fast moving gravity waves are triggered which disperse in all directions. Later on behind the obstacle a large scale Rossby wave evolves. On the bottom of page 60 and the following pages some of the used grids are presented demonstrating the adaption process. The left figure is centred at the nadir of the mountain, the right one at its opposite of the globe. The index of the colour
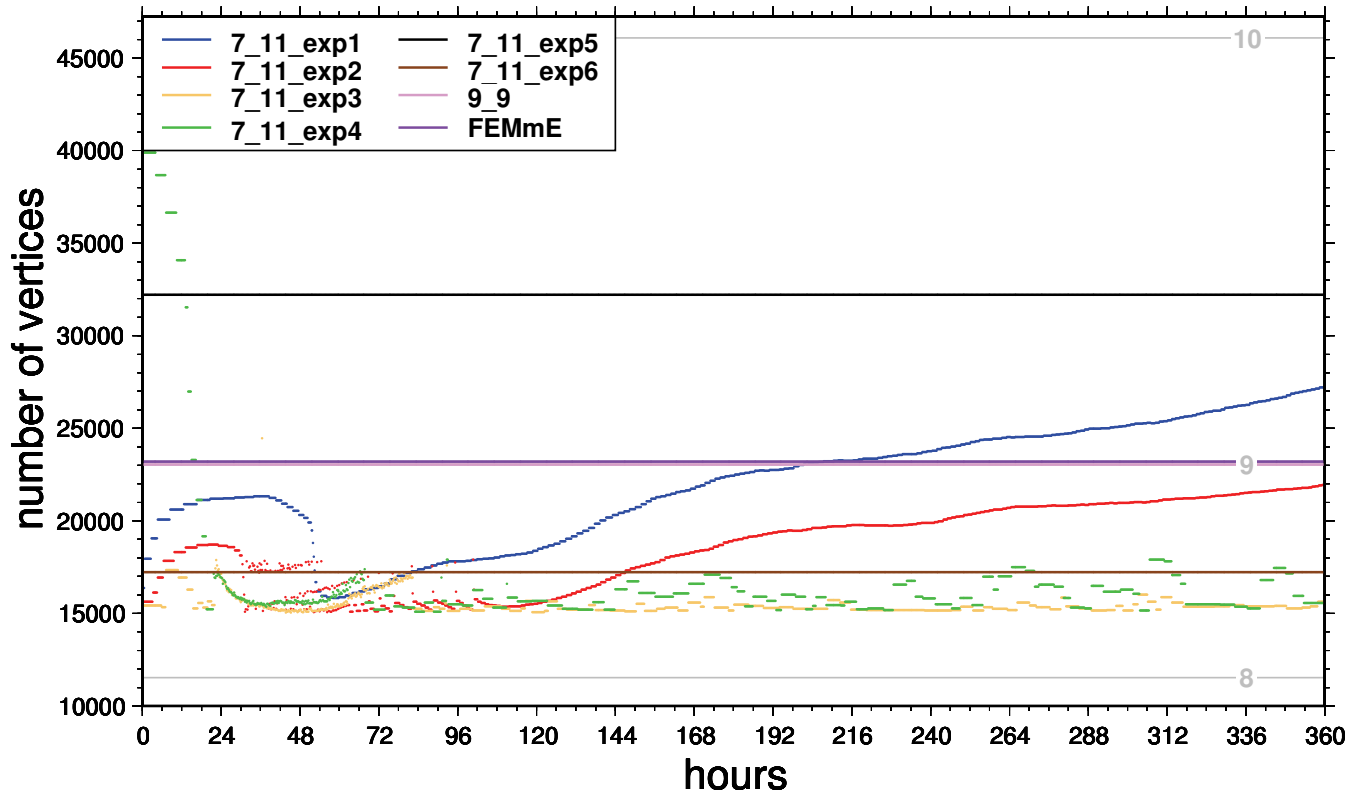
Figure 5.30: Test case 5: horizontal resolution of experiments
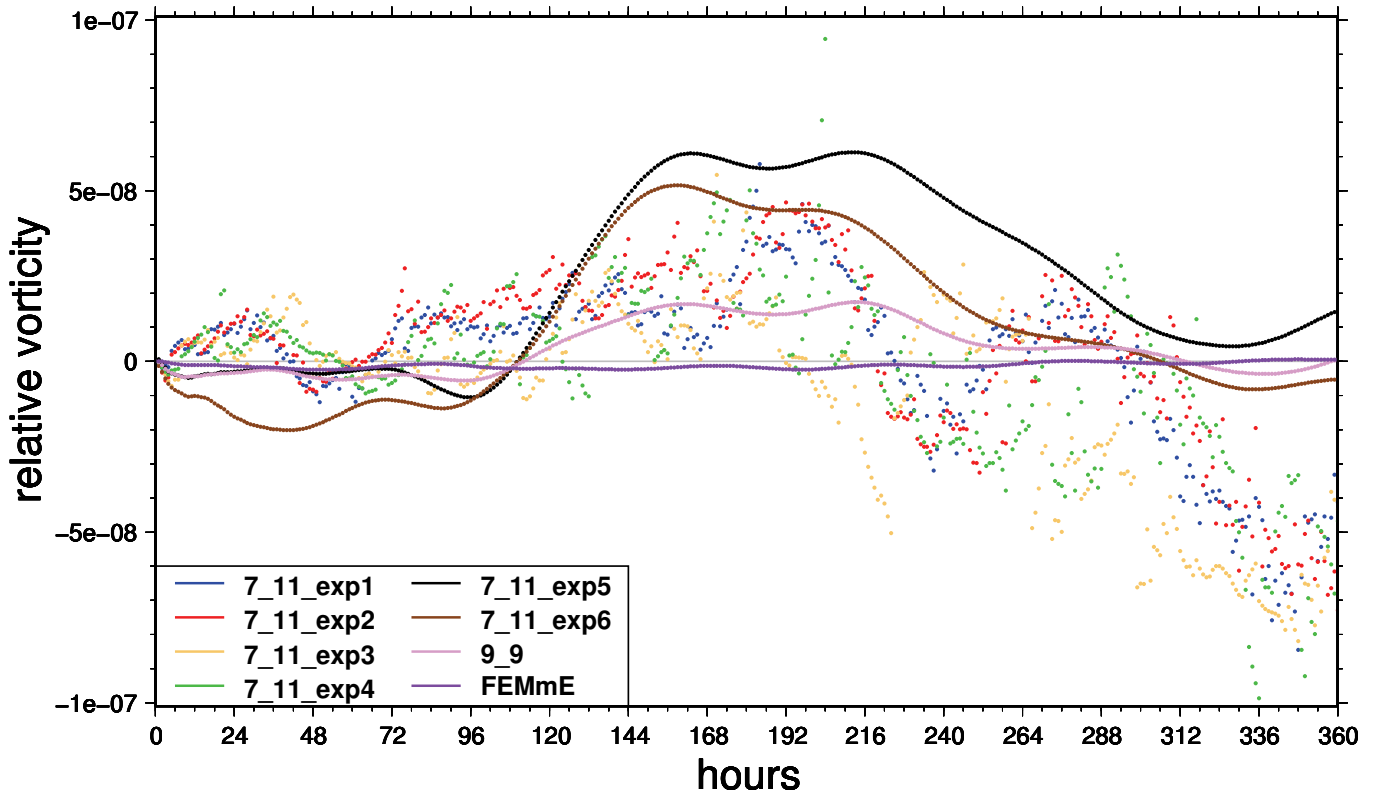
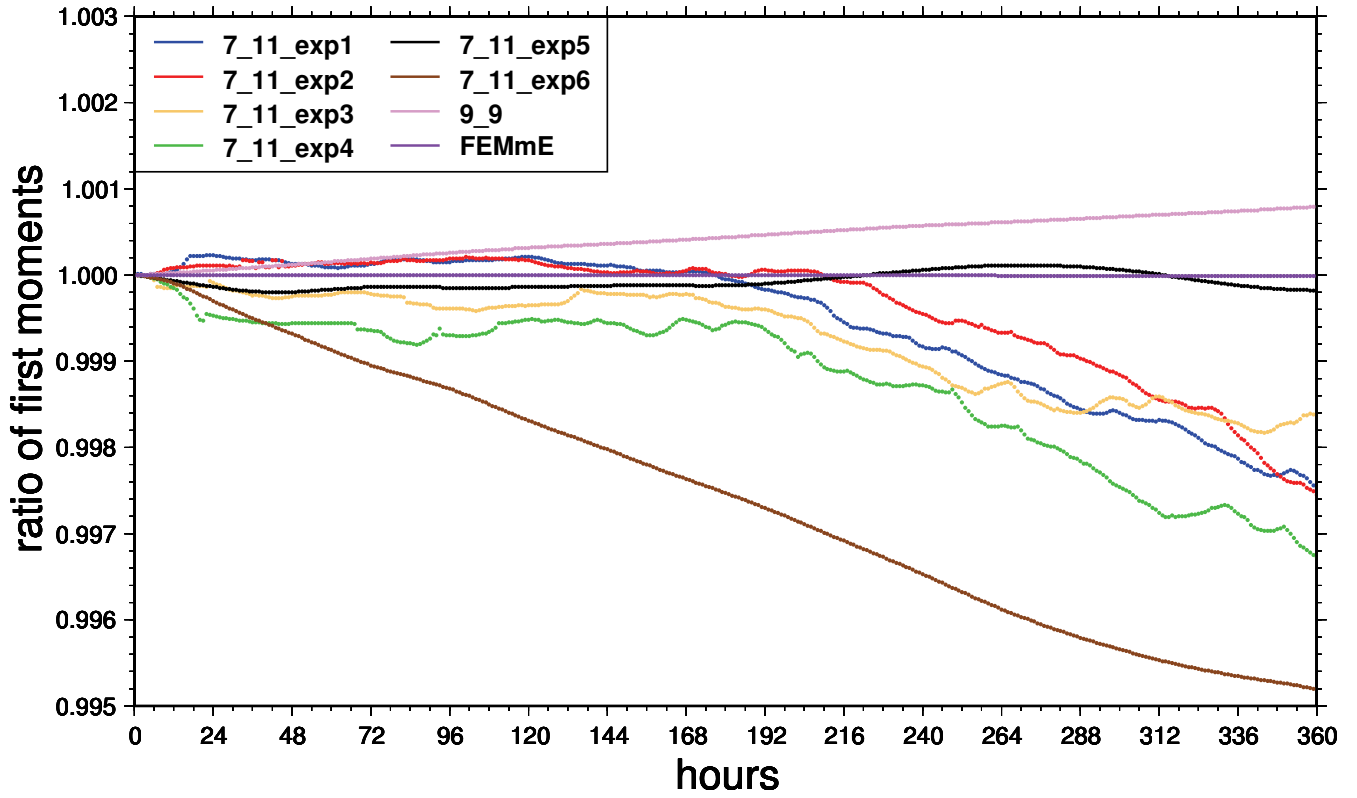Figure 5.31: Test case 5: relative vorticity

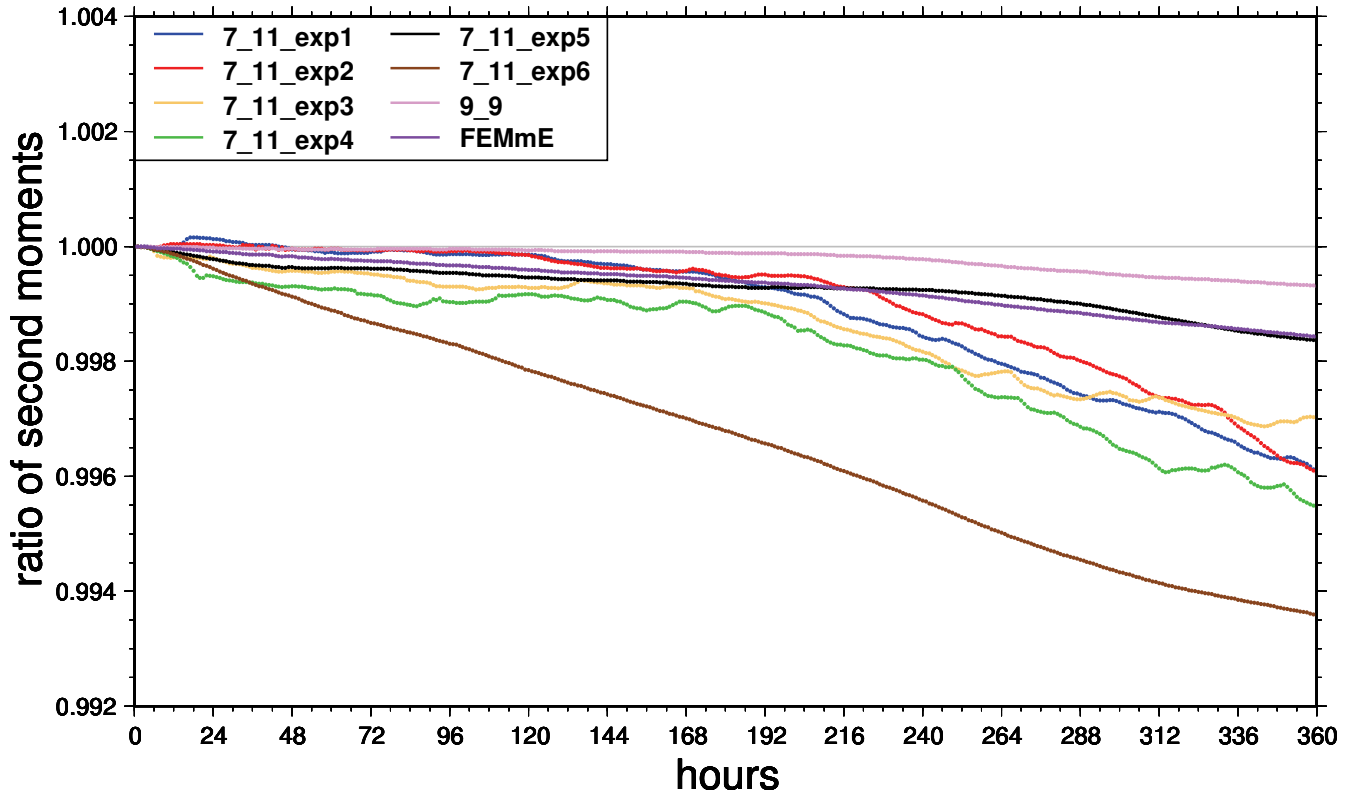Figure 5.32: Test case 5: ratio of first moments

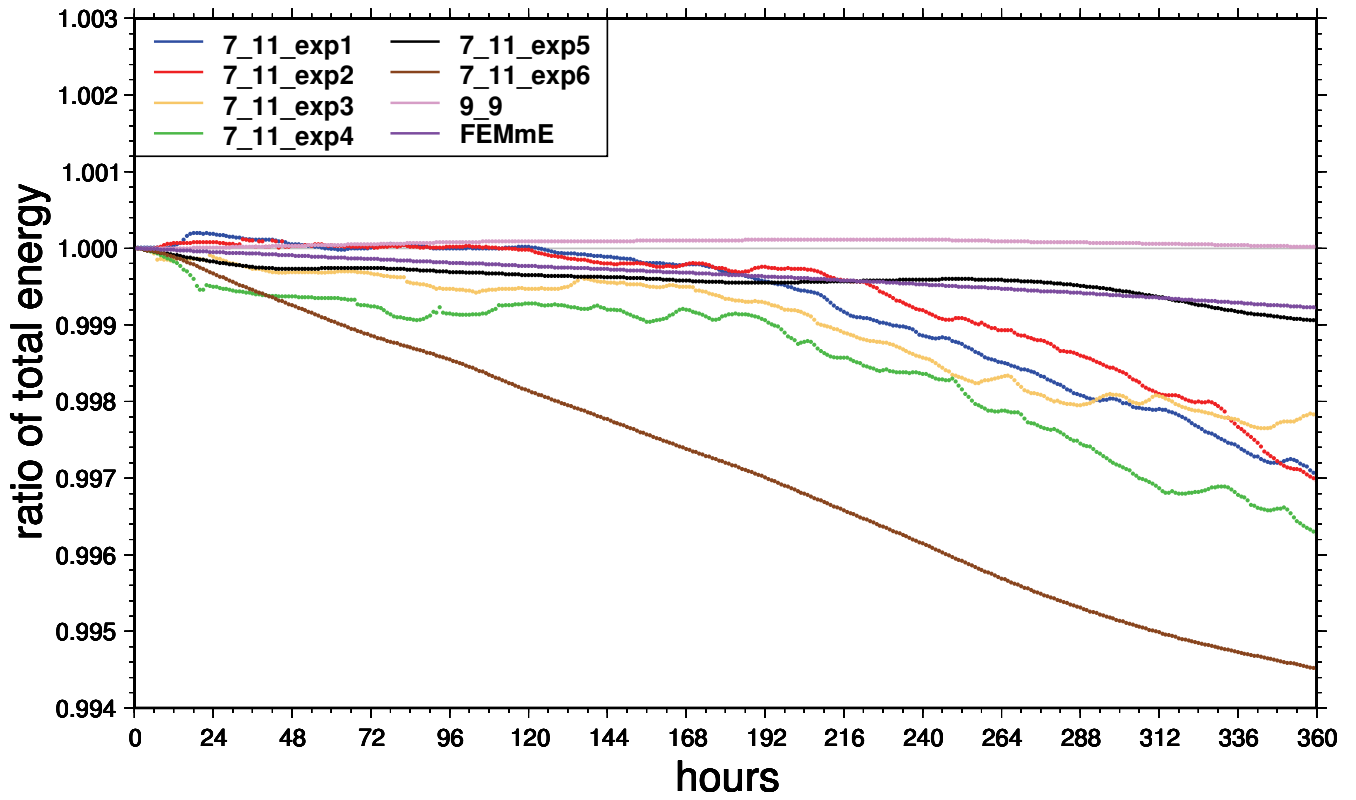Figure 5.33: Test case 5: ratio of second moments

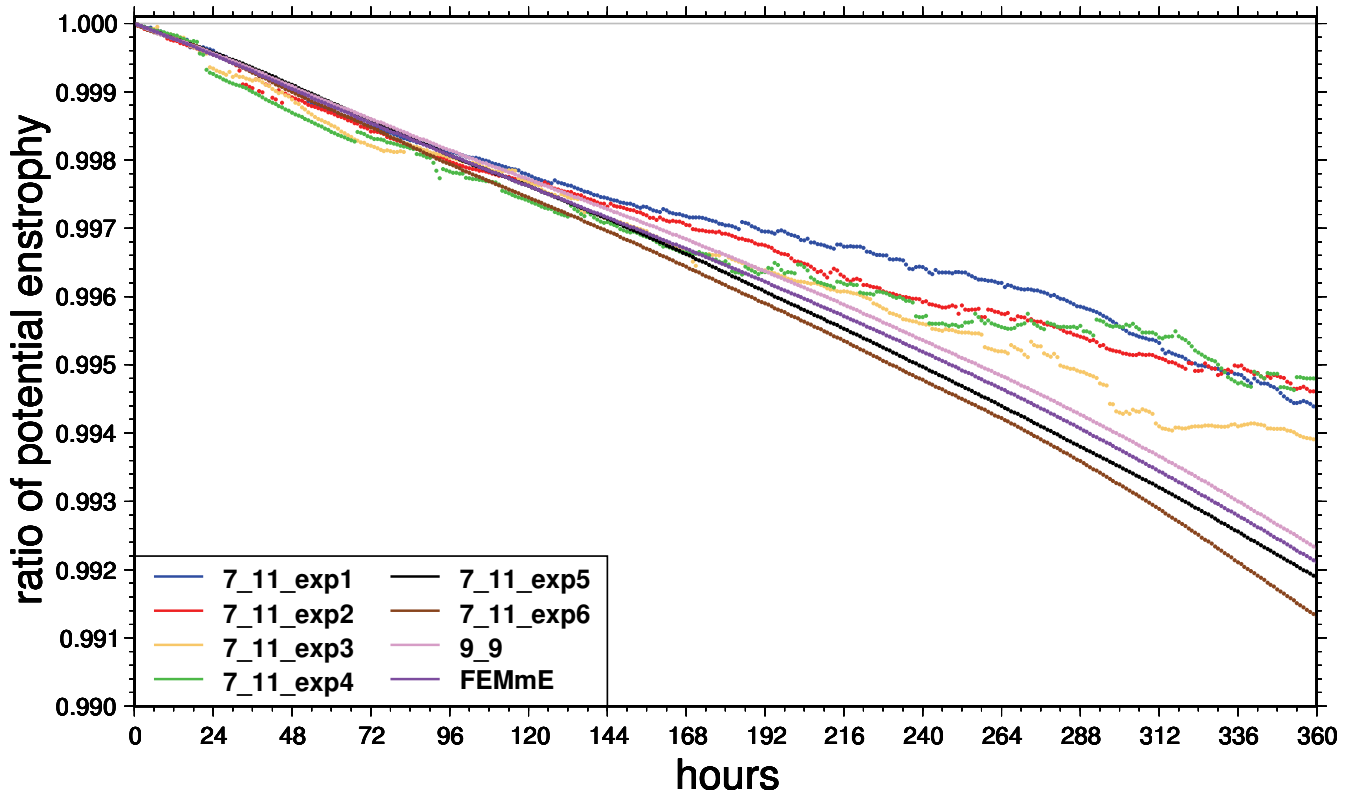Figure 5.34: Test case 5: ratio of total energy

Figure 5.35: Test case 5: ratio of potential enstrophy

scale is given on page 38. In the left figure also the contour lines of the mountain are included in white. The interval of the contour lines is 300 m and the first line indicates the 0 m level. Additionally, it should be noted that including the coast lines of the "real" earth in the figures does not imply that the earth's topography is used for the test cases. The reason for the coast lines is just giving easier orientation on the sphere.

On the top of the next pages the temporal evolution of the geopotential and the vorticity is given. Comparing these figures with the grids it is obvious that the vorticity fields determine the grid. This is no surprise at all having the indicator function (4.22) for the grid adaptation in mind.

Figures 5.45 and 5.46 present the static grids used for the experiments 5 and 6.

Detailed results of all experiments are discussed in the next section.

5.4.5 Difference to reference solution

In all experiments large scale patterns evolve in similar ways, but regional patterns differ. For detecting and discussing these differences, a comparison to a reference is useful. As there is no analytical solution known to this test case, a model result is needed for this purpose. In the SWM community the high resolution NCAR spectral models used for receiving the results of the original paper by Williamson et al. (1992) are widely accepted. The model details are given in Hack and Jakob (1992).

But especially with test case 5 this reference solution holds some problems. First its high resolution, T106, is state-of-the-art of the nineties of last century. Modern supercomputers nowadays can easily deal with much higher resolution. A thorough investigation at Max Planck Institute for Meteorology revealed that there are also some deficiencies in the coding. Hence within the ICON project those numerical problems were solved and a new T426 high resolution reference state was calculated. This solution can be downloaded from the ICON web page (Rípodas et al. 2005) and is used here as reference.

Second, the conical mountain cannot be represented exactly by spherical harmonics. In previous studies, e.g. Lanser et al. (2001), it has been shown, that the way the mountain is represented has a non neglecting impact on the numerical results.
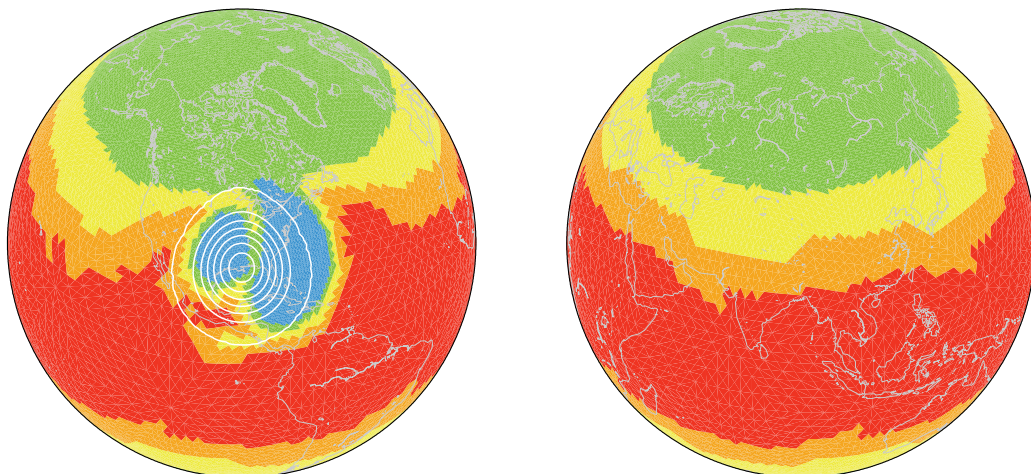
Figure 5.36: Experiment 1: grid after 82 steps (0 days 20.5 hours); left figure centred at 90°W 30°N, right figure centred at 90°E 30°N
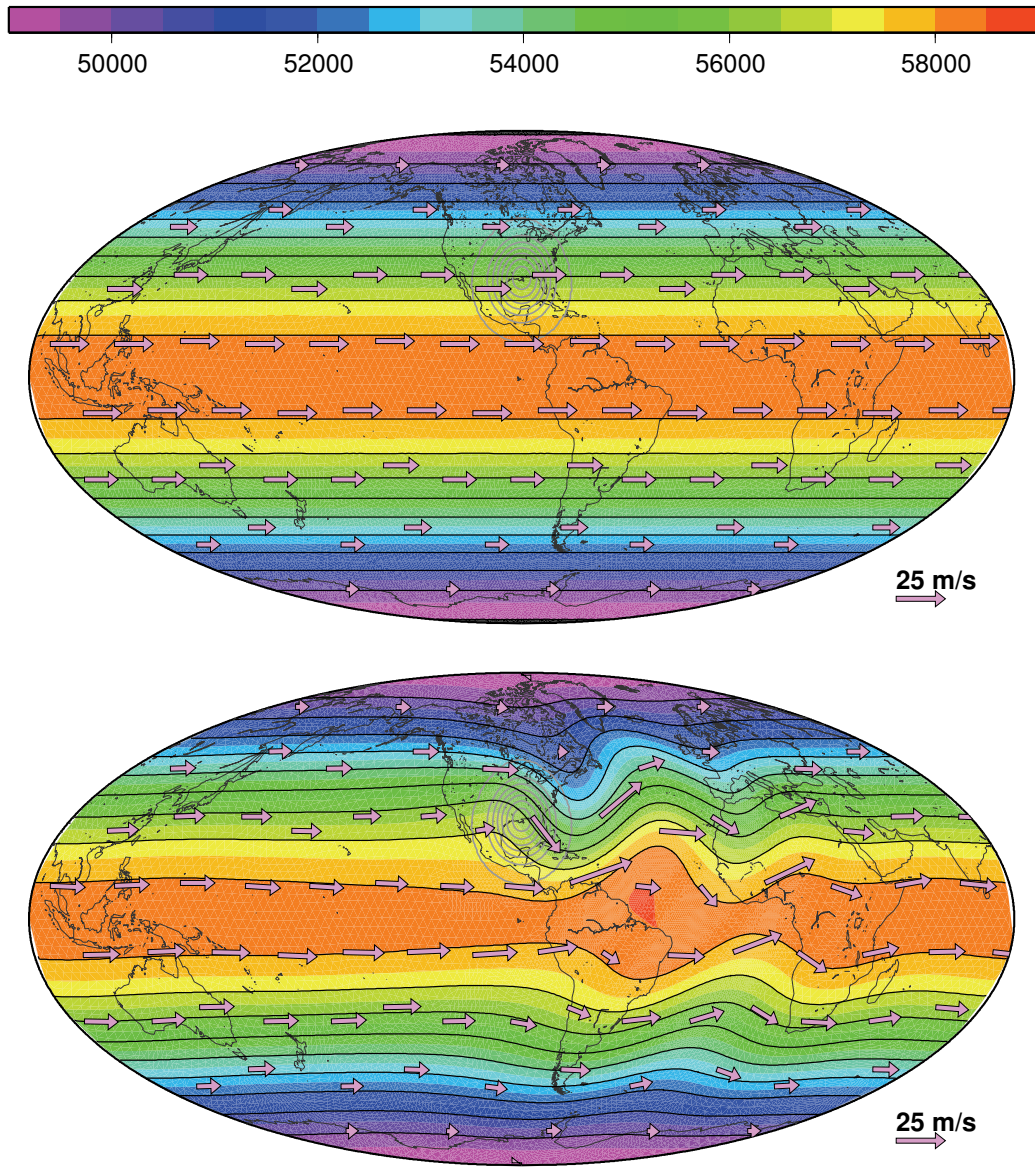
Figure 5.37: Experiment 1: geopotential and flow field at initial state and after 5 days
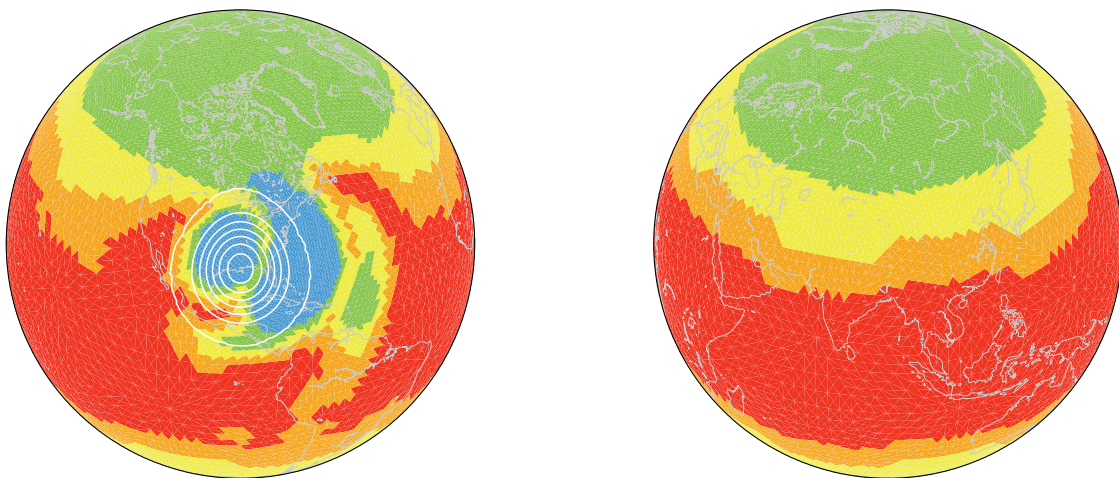
Figure 5.38: Experiment 1: grid after 135 steps (1 day 9.75 hours)
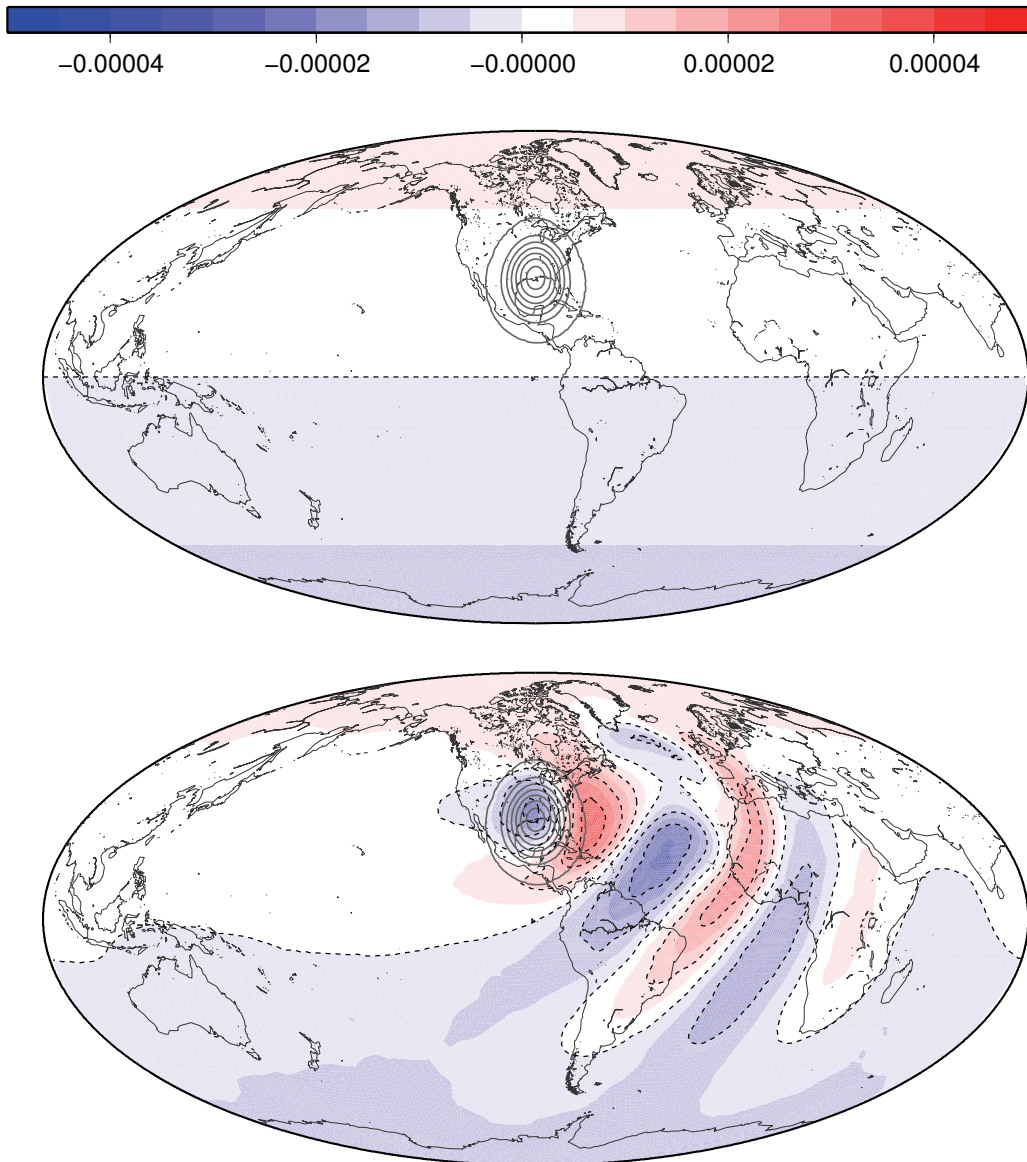
Figure 5.39: Experiment 1: vorticity at initial state and after 5 days
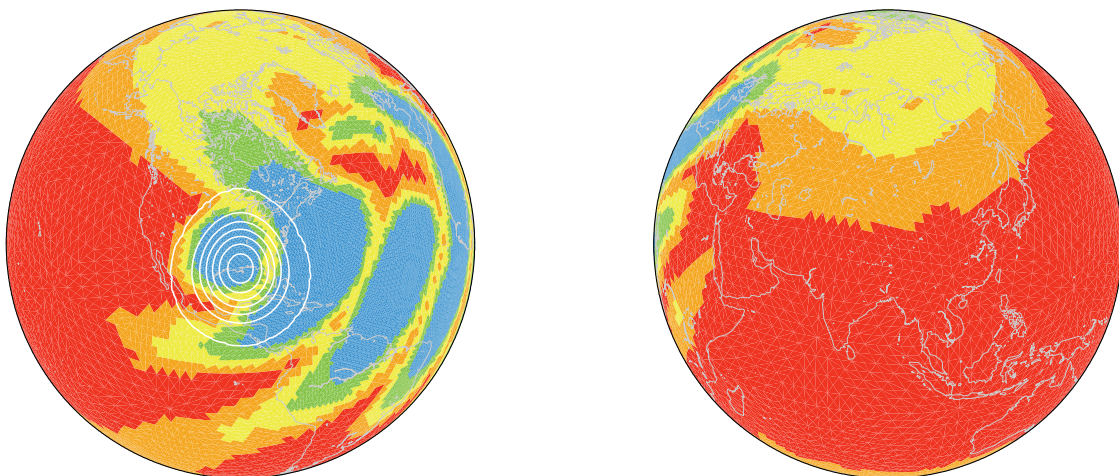
Figure 5.40: Experiment 1: grid after 475 steps (4 day 22.75 hours)
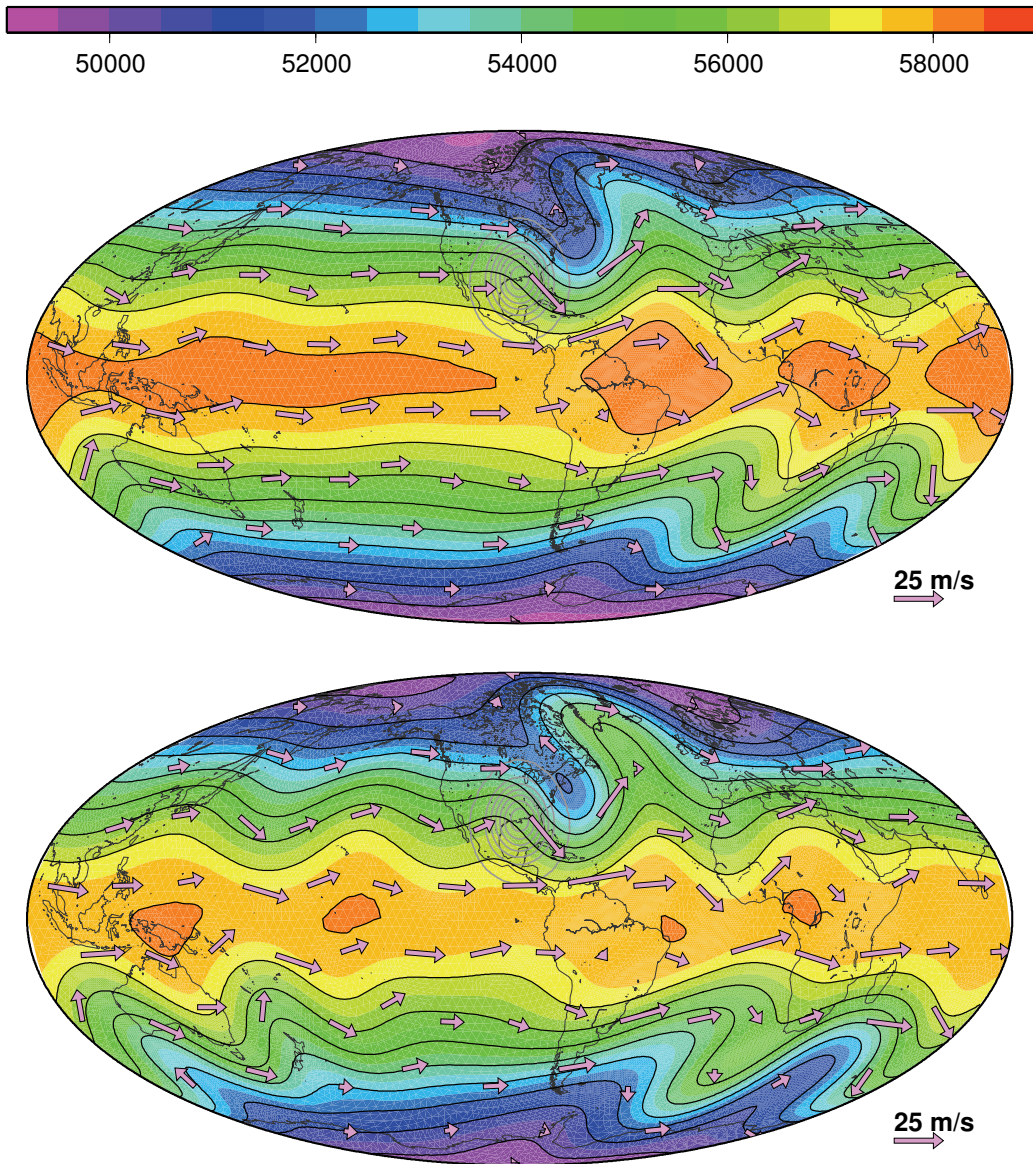
Figure 5.41: Experiment 1: geopotential and flow field after 10 and 15 days
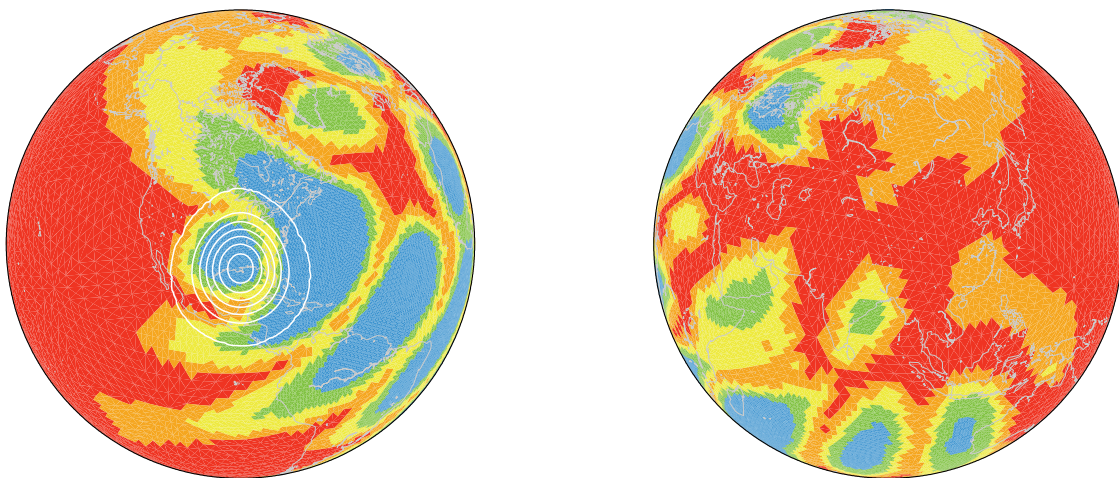
Figure 5.42: Experiment 1: grid after 955 steps (9 day 22.75 hours)
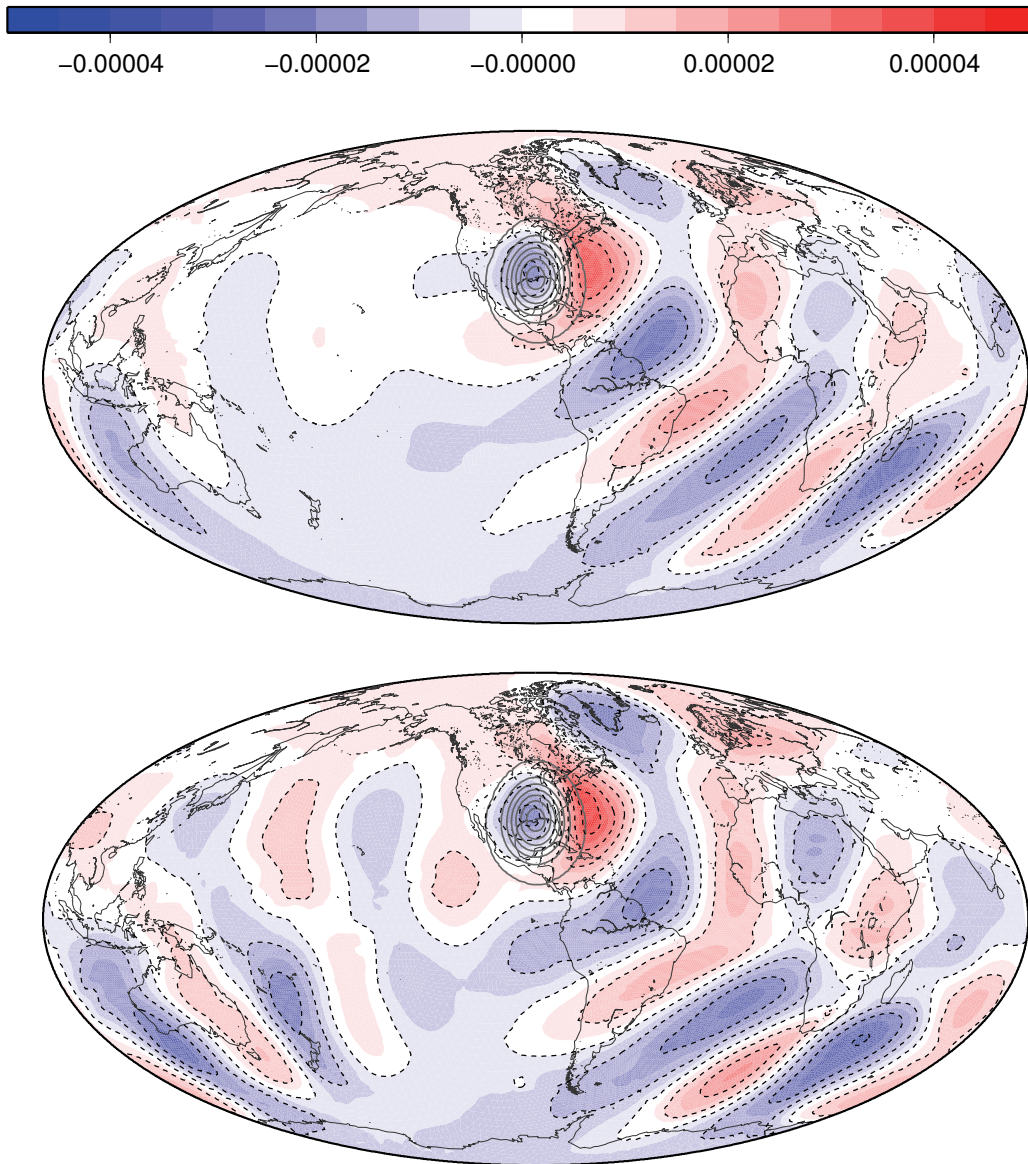
Figure 5.43: Experiment 1: vorticity after 10 and 15 days
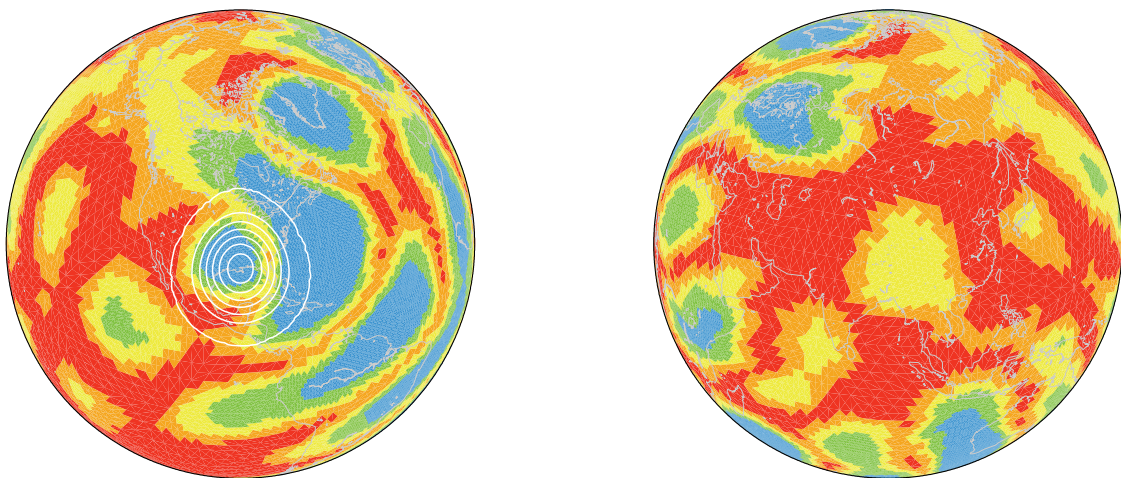
Figure 5.44: Experiment 1: grid after 1438 steps (14 day 23.5 hours)
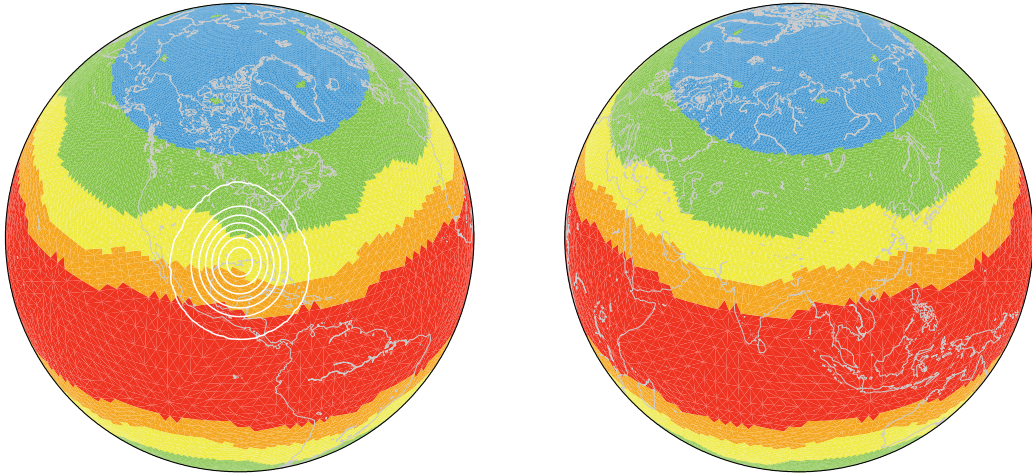
Figure 5.45: Experiment 5: static grid
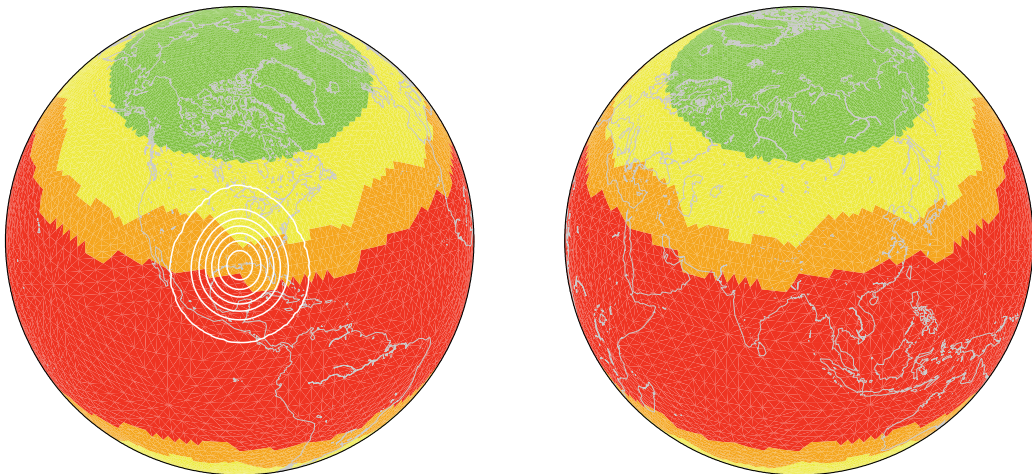
Figure 5.46: Experiment 6: static grid

Other problems occur from the fact the the reference solution uses totally different numerical concepts. It is a spectral model, the discretisation in time is done by a 3 time level semi-implicit Eulerian scheme and as a consequence this two types of filters are used. An Asselin filter prevents the solutions of the odd and the even time steps from falling apart and a second order artificial diffusion stabilises the model. Both is necessary for a good performance of that kind of model. But both filters also effect the numerical solution. In **PLASMA-FEM*m*E**, besides the off-centring, no numerical damping is used and necessary. On the next pages the differences between each experiment and the reference solution are presented. Because of the differences just mentioned, there is the danger of "comparing apples and oranges". On the other side, as these results are widely used in the literature there are good reasons to stay on that path. But one has to keep in mind that most of the dominant features are caused by the different numerical concepts used.

Especially remarkable in this context is the situation north east of the mountain. The development of the Rossby wave seems dramatically different, but what is observed is just a small phase shift of the wave caused by a slightly different group velocity. On the other hand the amplitude of this difference is an important attribute for the comparison of the

min: –330.000   **max: 203.299**

min: –396.193   **max: 491.416**

min: –665.962   **max: 1156.450**
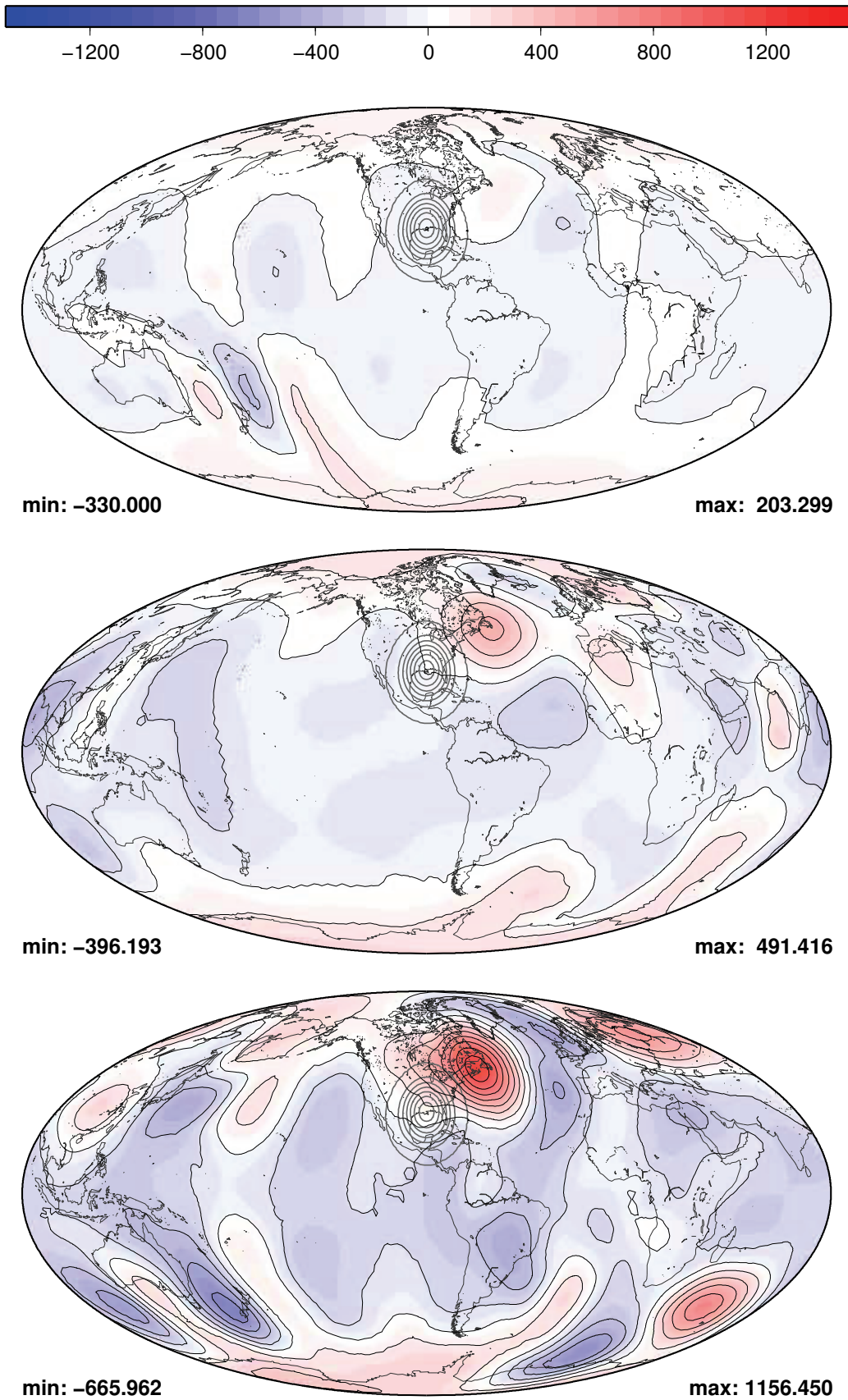
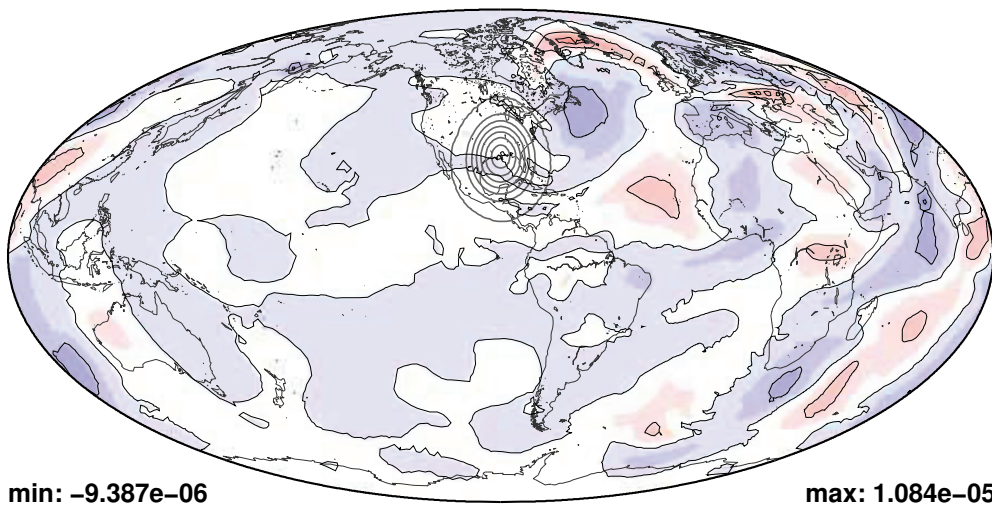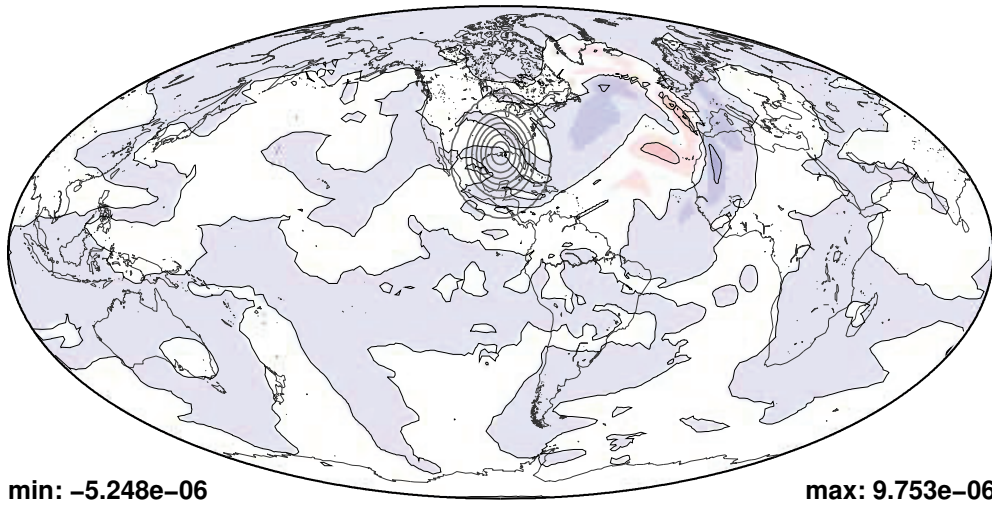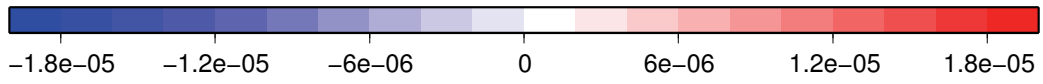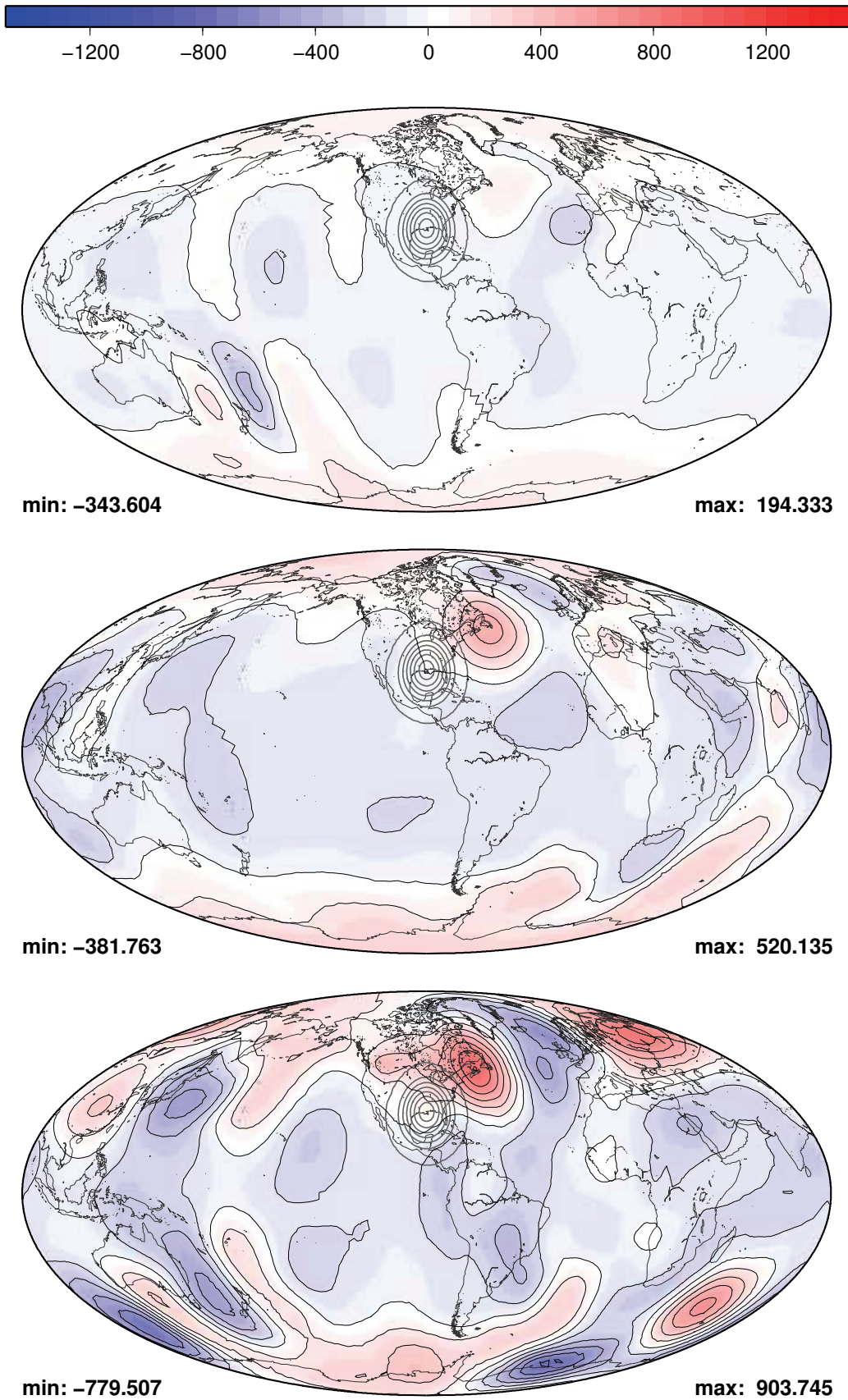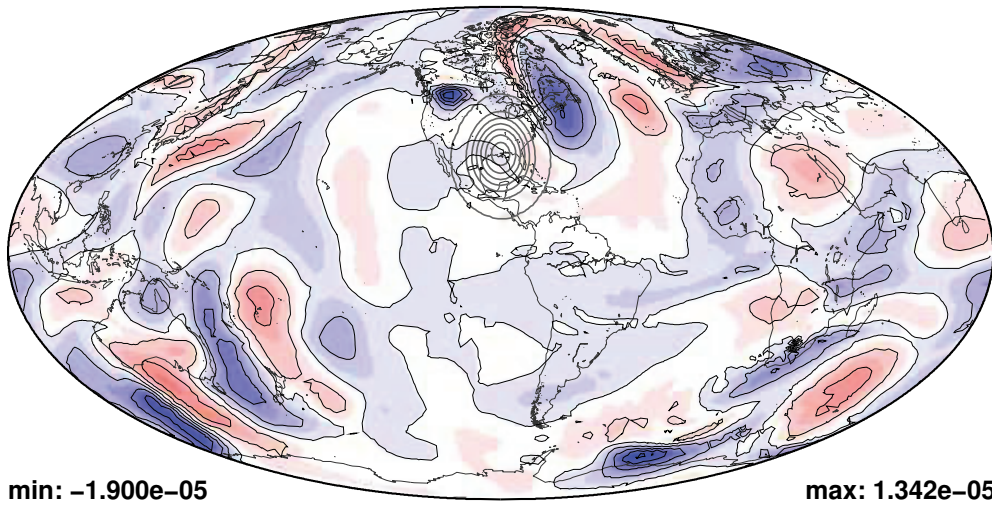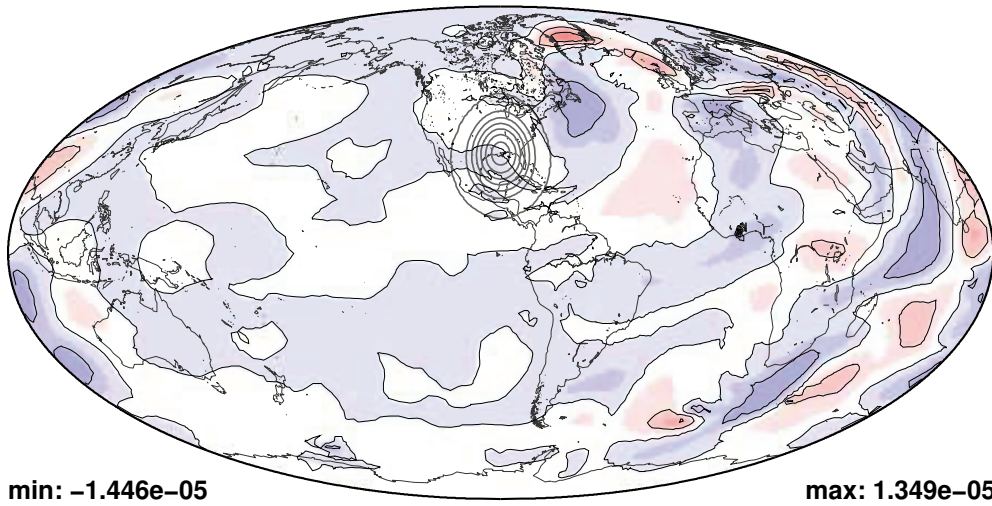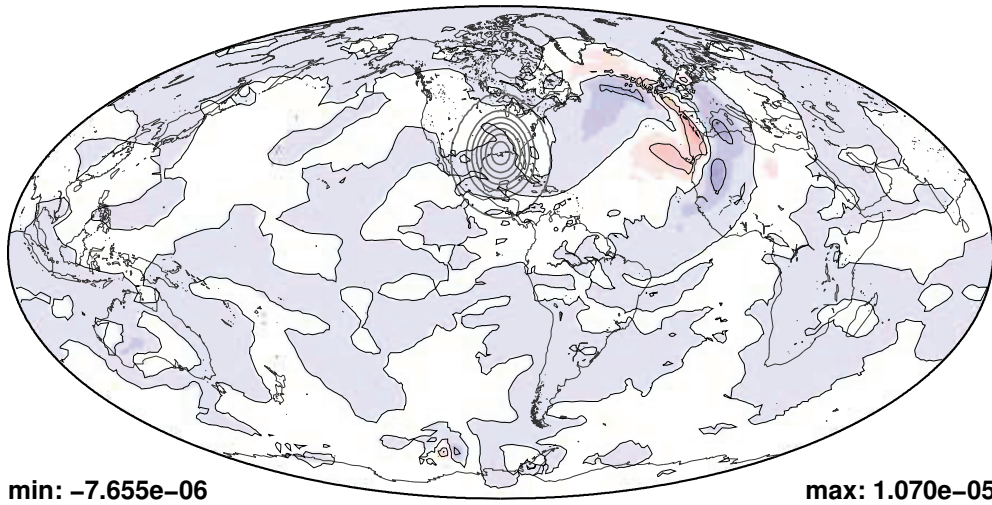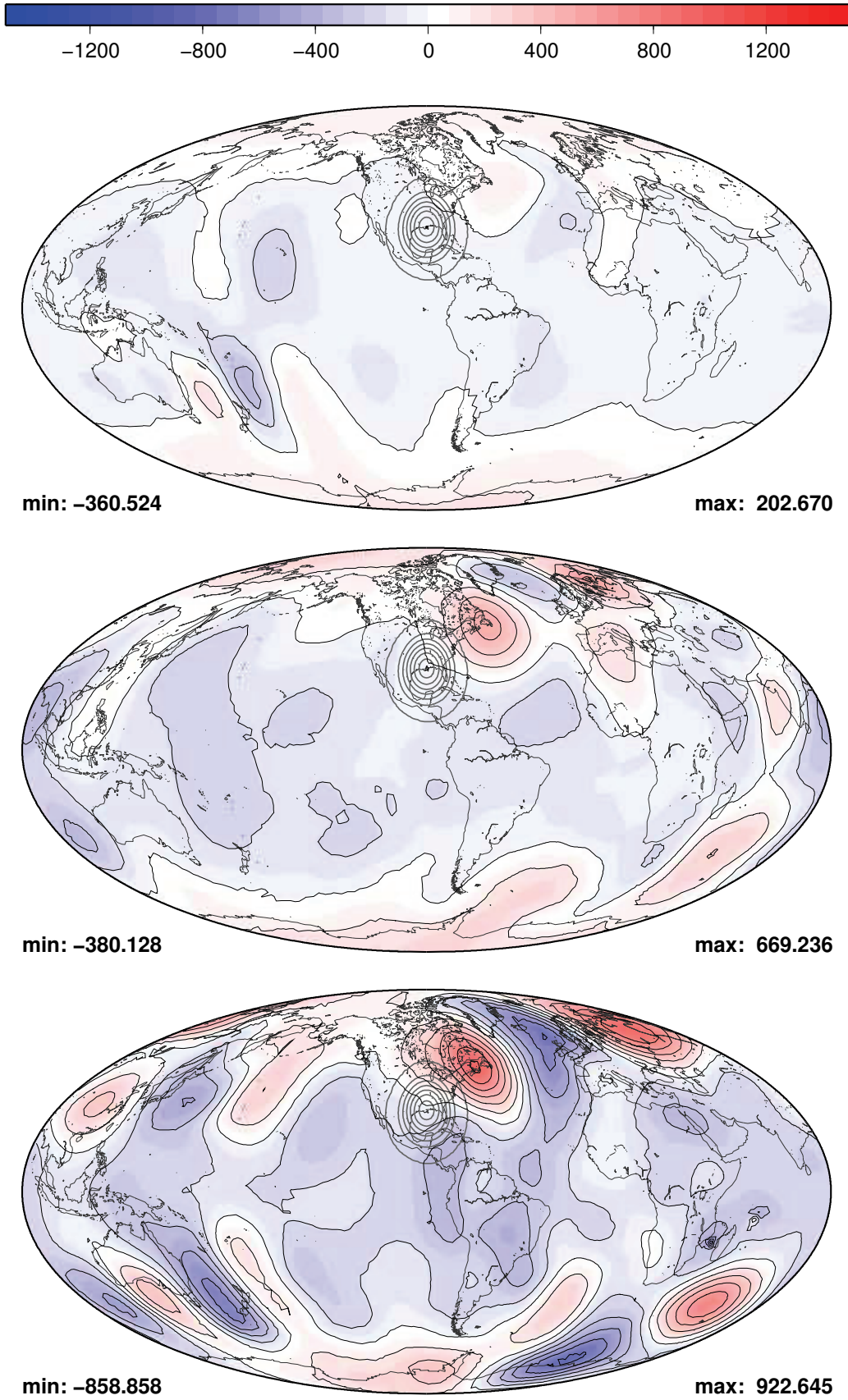Figure 5.47: Experiment 1: difference of geopotential after 5, 10 and 15 days
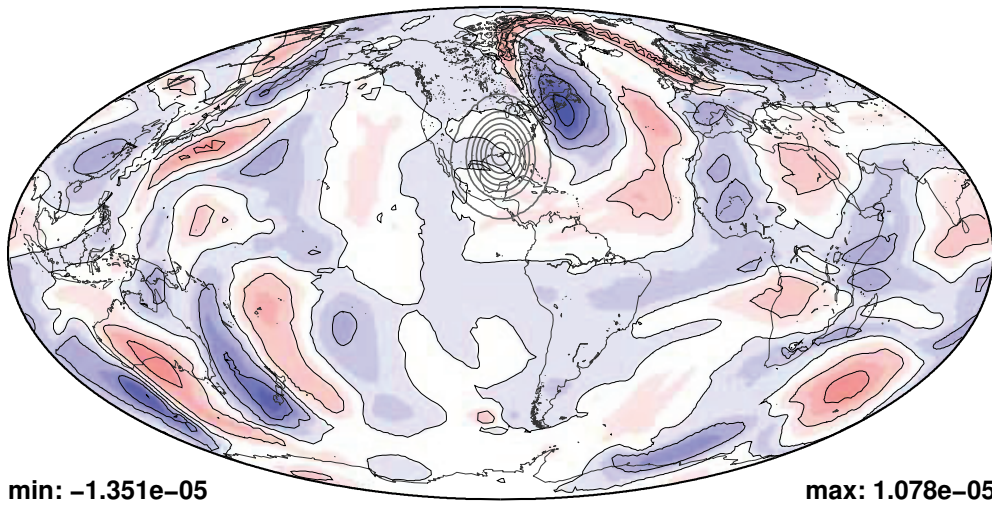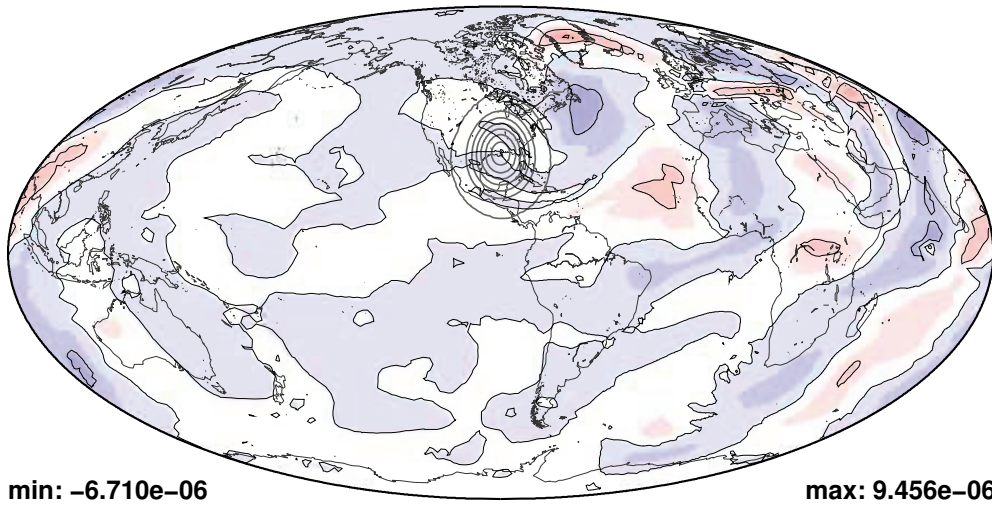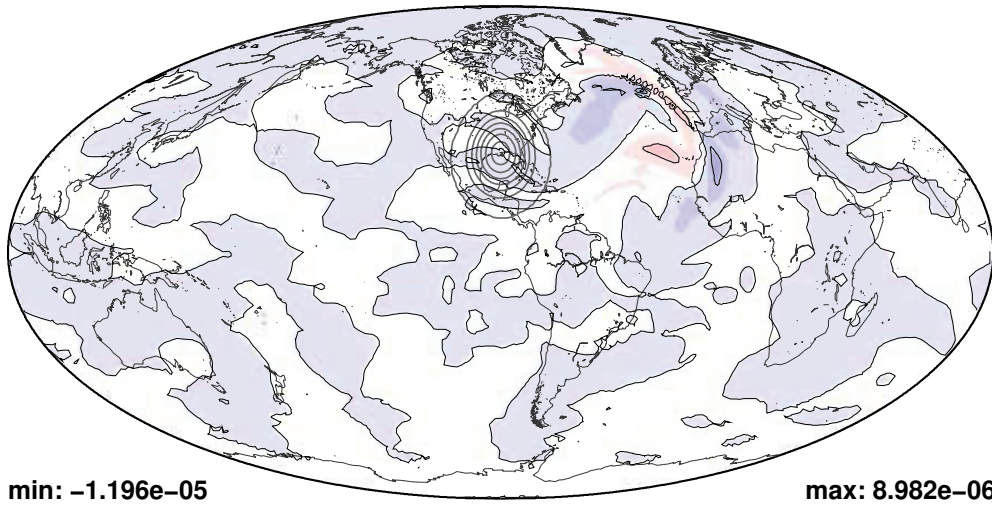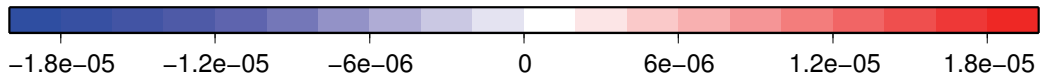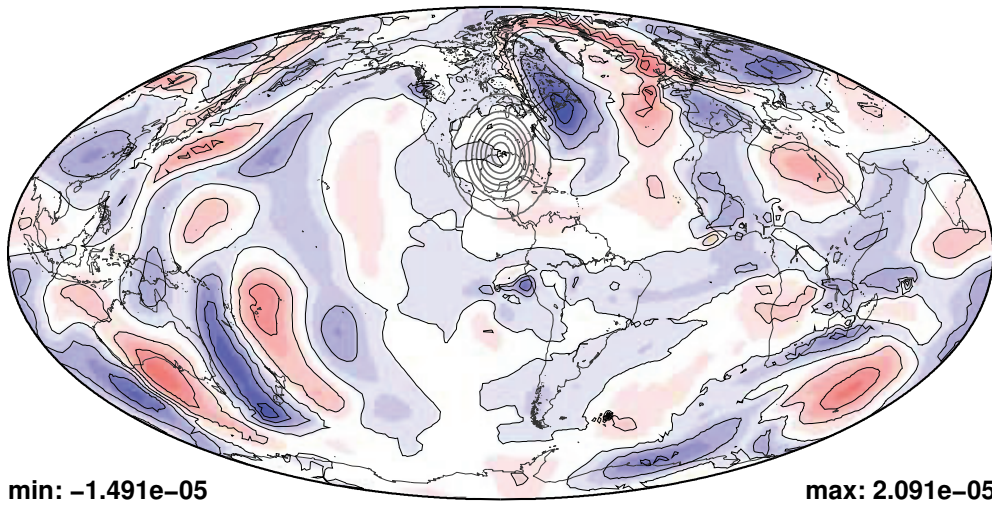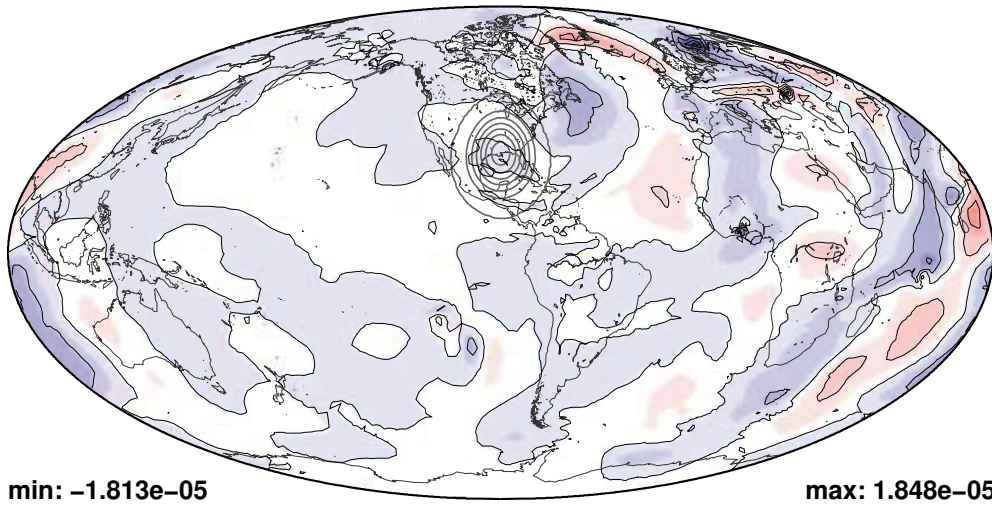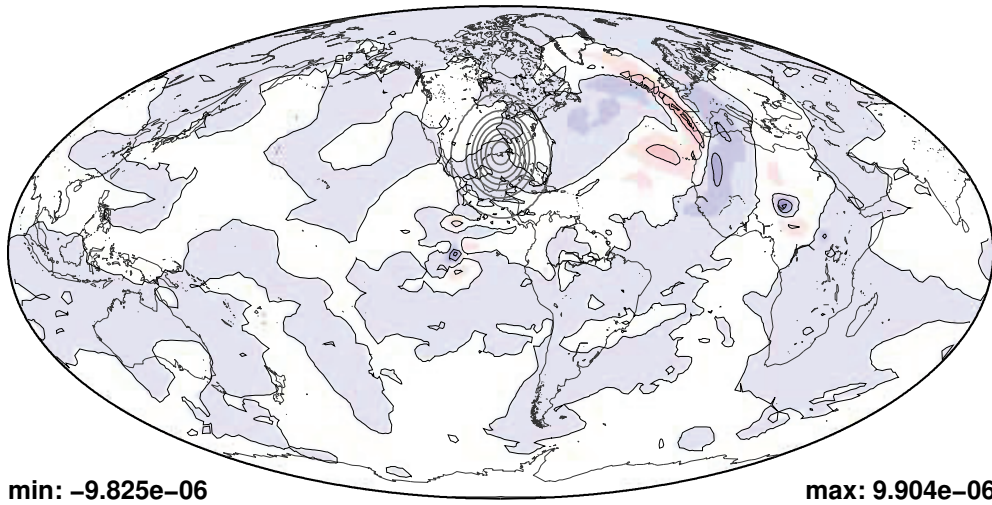
Figure 5.48: Experiment 1: difference of vorticity after 5, 10 and 15 days

min: –315.502   **max: 211.232**

min: –395.245   **max: 517.698**

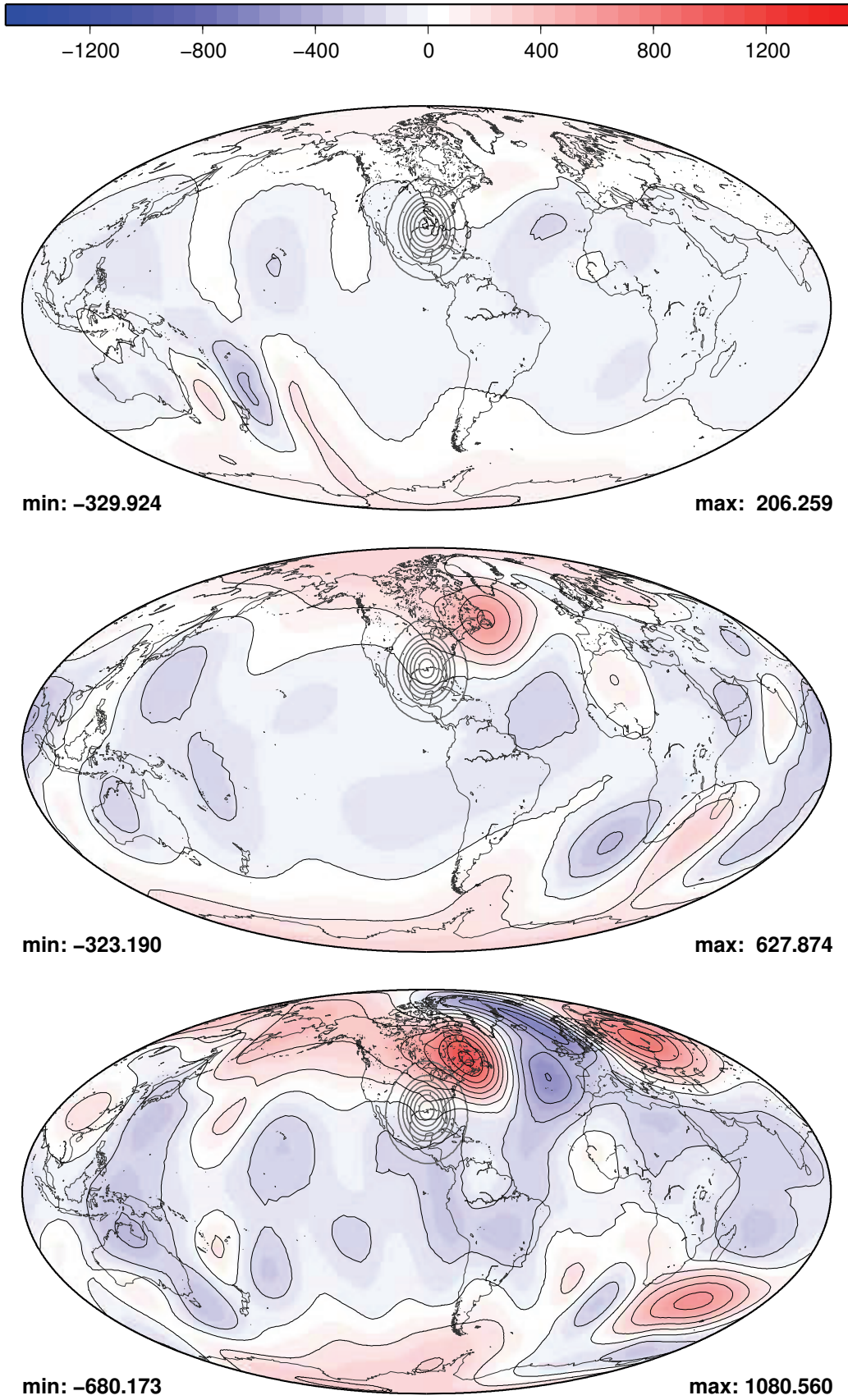**min: –745.305**   **max: 1064.310**
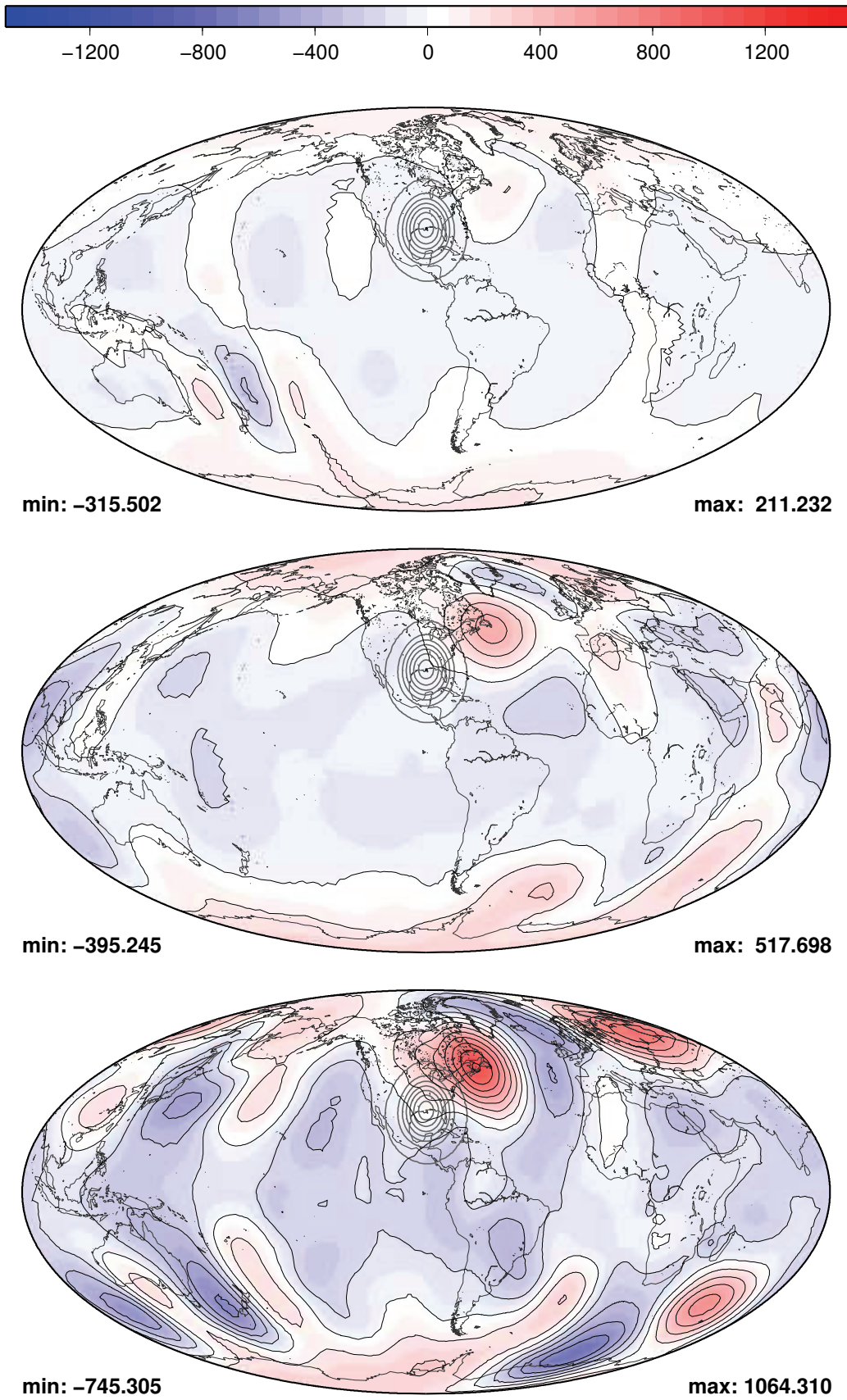
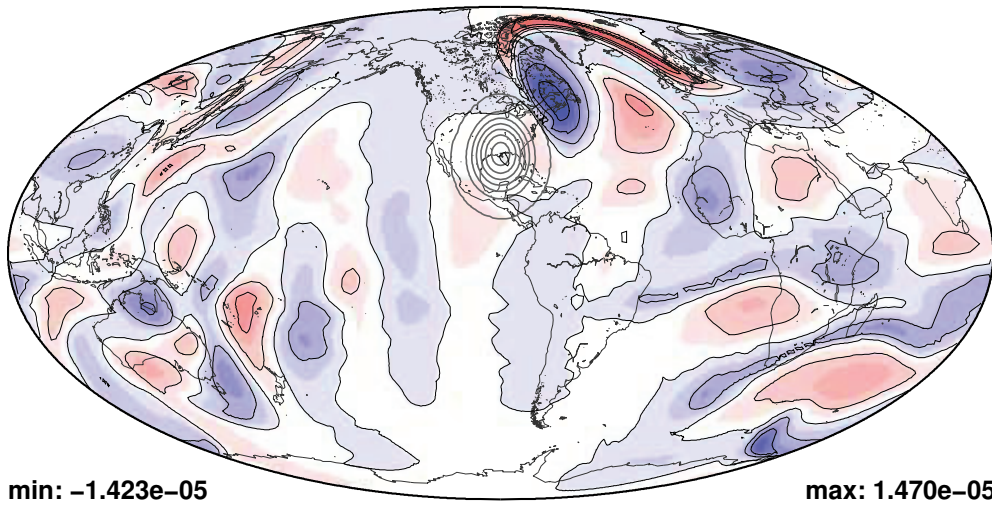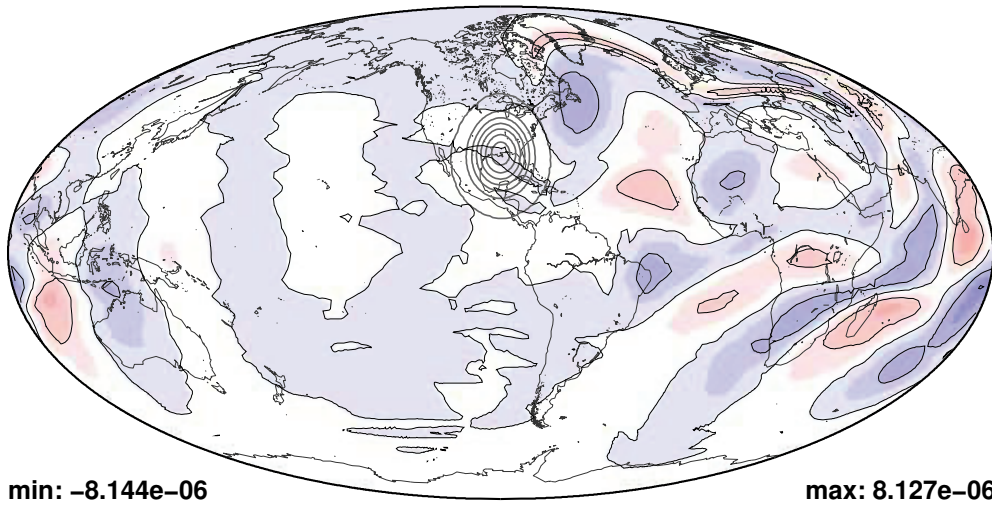Figure 5.49: Experiment 2: difference of geopotential after 5, 10 and 15 days
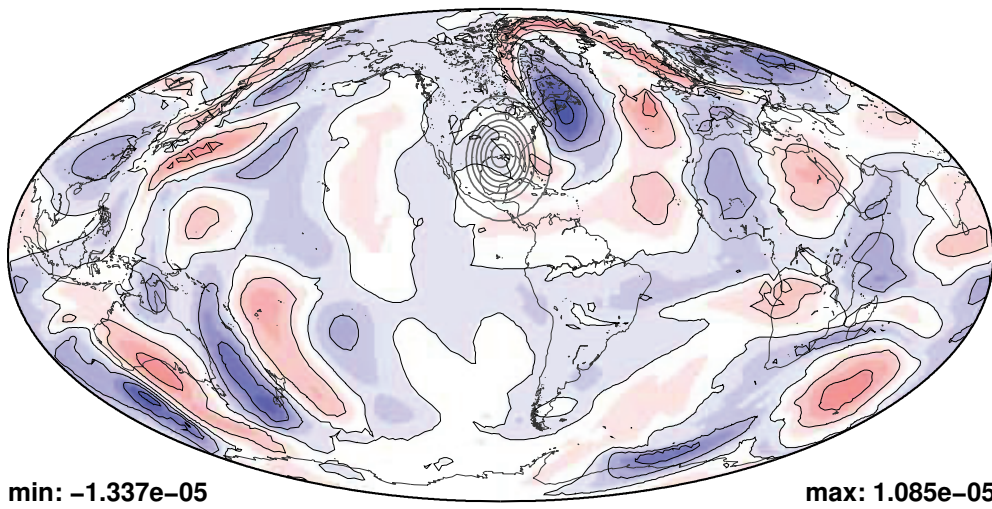
Figure 5.50: Experiment 2: difference of vorticity after 5, 10 and 15 days

min: −343.604   max: 194.333

min: −381.763   max: 520.135

min: −779.507   max: 903.745

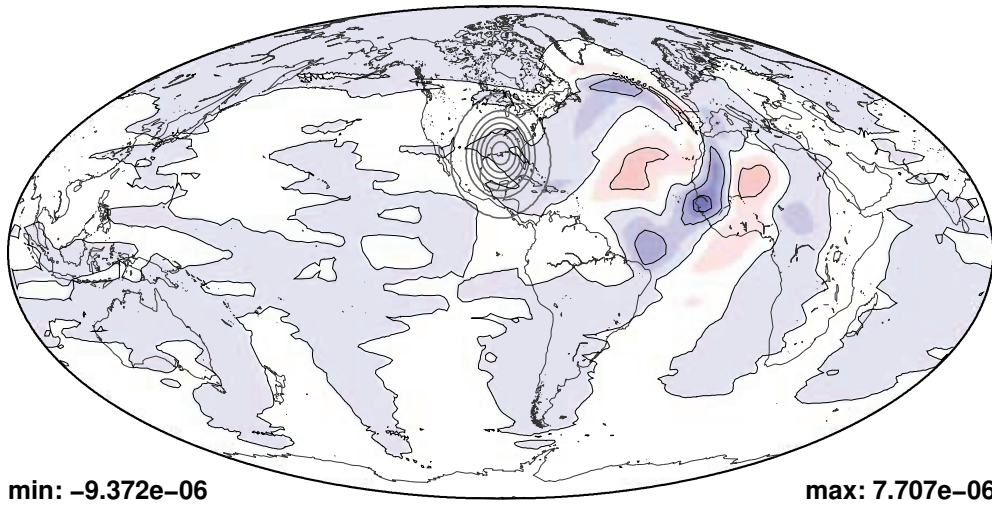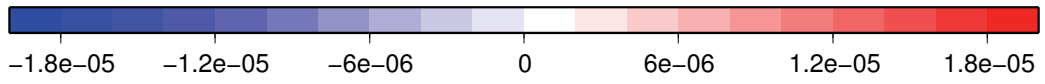Figure 5.51: Experiment 3: difference of geopotential after 5, 10 and 15 days

min: −7.655e−06   **max: 1.070e−05**

min: −1.446e−05   **max: 1.349e−05**

min: −1.900e−05   **max: 1.342e−05**

Figure 5.52: Experiment 3: difference of vorticity after 5, 10 and 15 days

min: −360.524   **max: 202.670**

min: −380.128   **max: 669.236**

min: −858.858   **max: 922.645**
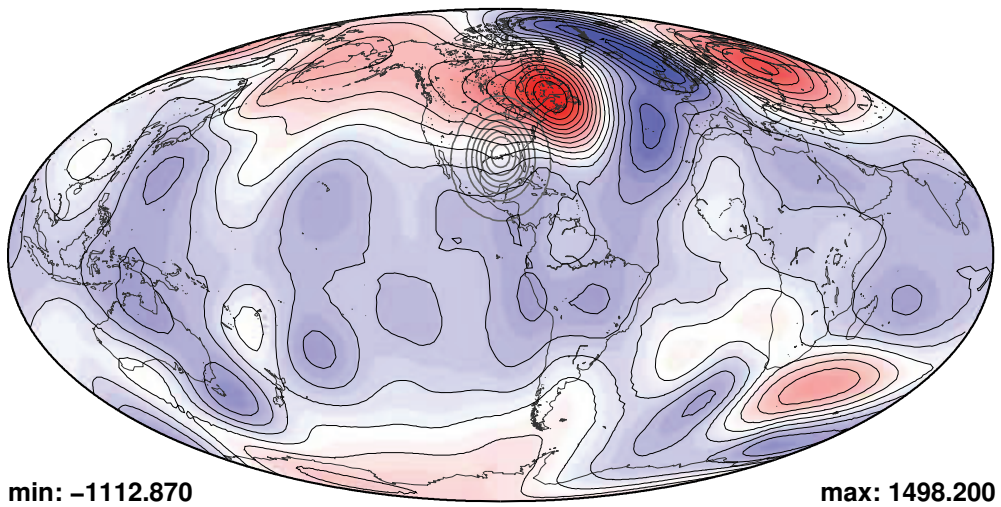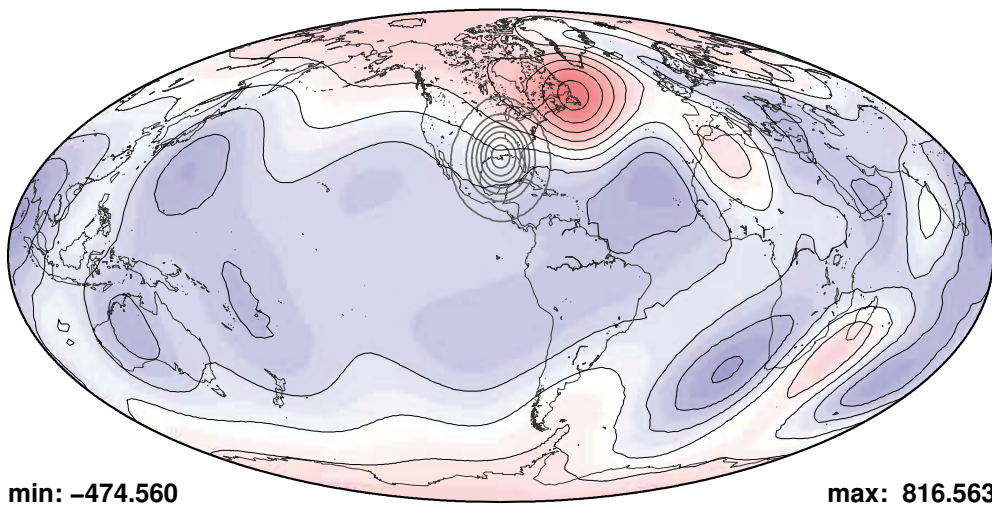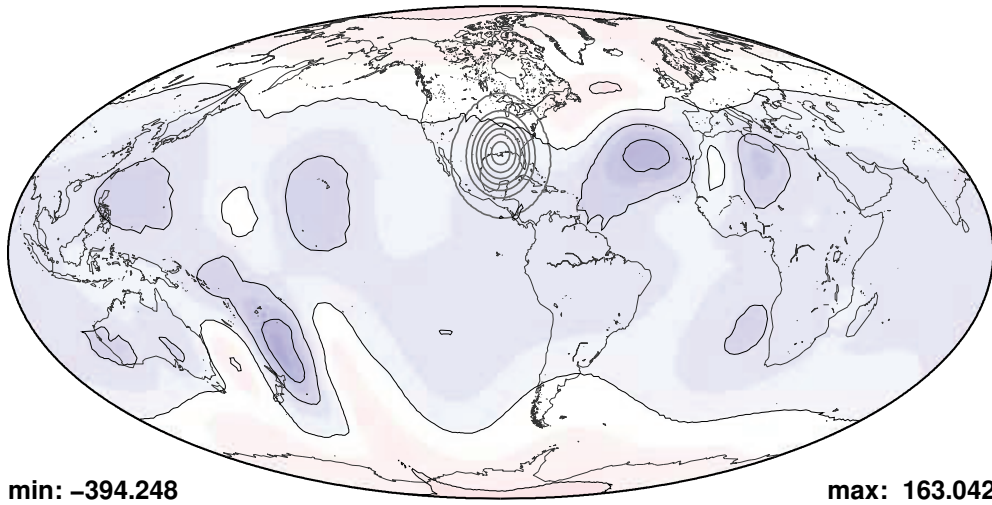
Figure 5.53: Experiment 4: difference of geopotential after 5, 10 and 15 days

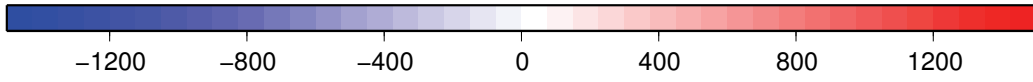Figure 5.54: Experiment 4: difference of vorticity after 5, 10 and 15 days

min: –329.924   max: 206.259

min: –323.190   max: 627.874

min: –680.173   max: 1080.560

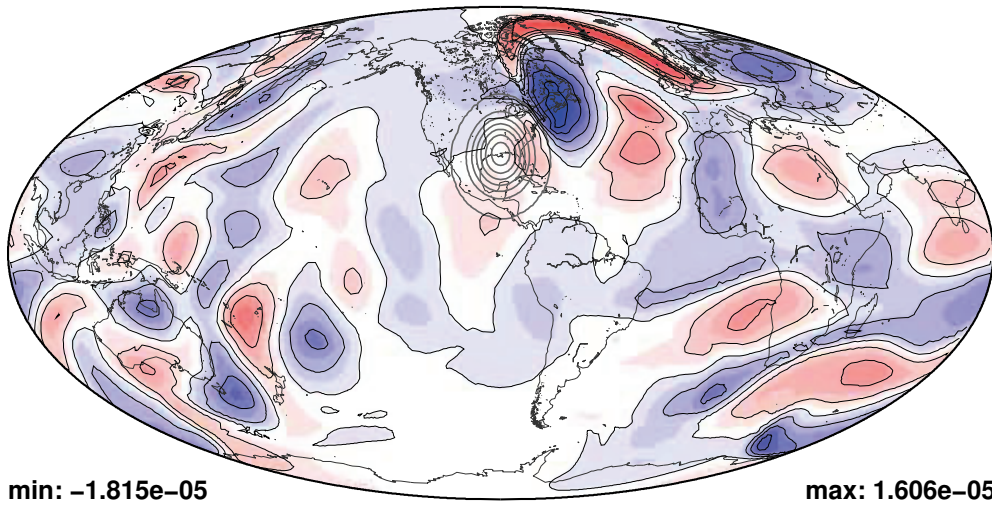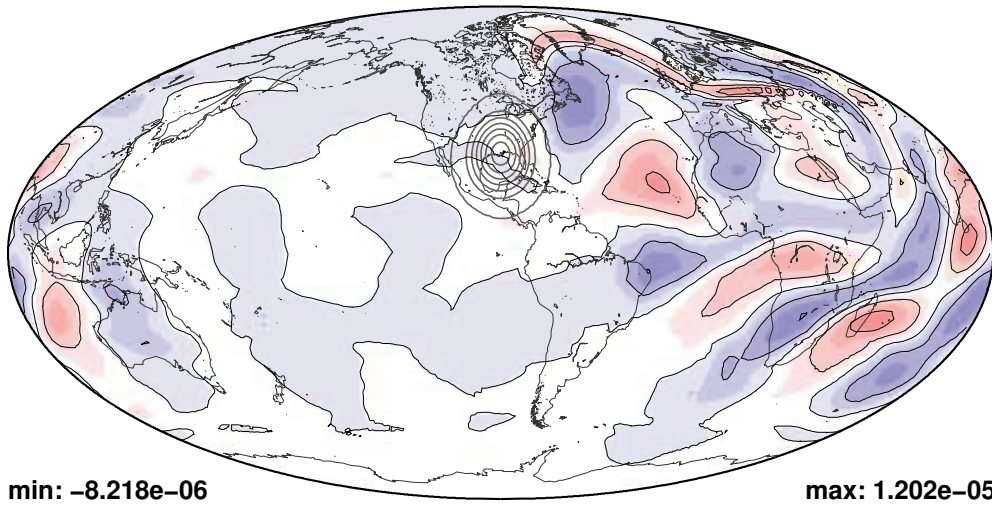Figure 5.55: Experiment 5: difference of geopotential after 5, 10 and 15 days

Figure 5.56: Experiment 5: difference of vorticity after 5, 10 and 15 days

min: −394.248   **max: 163.042**

min: −474.560   **max: 816.563**

min: −1112.870   **max: 1498.200**

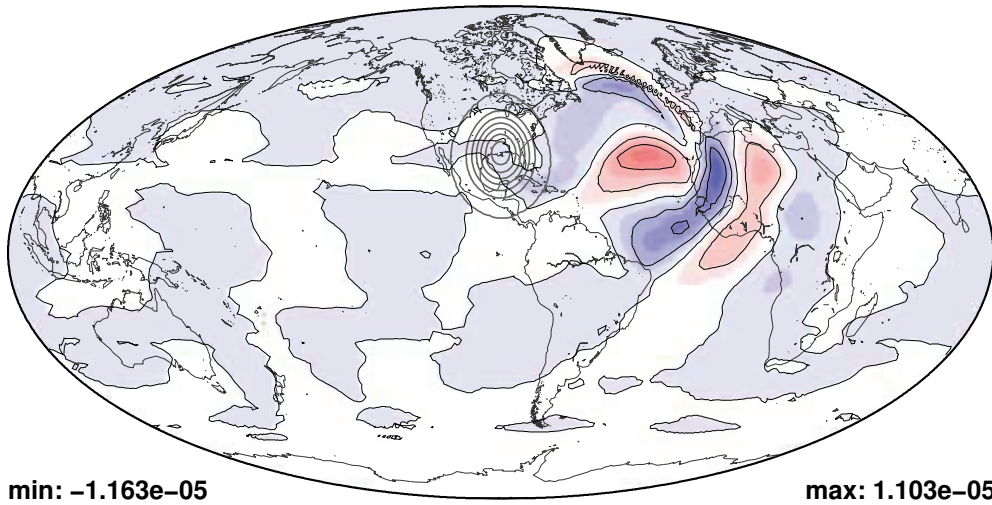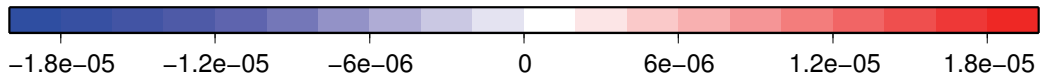Figure 5.57: Experiment 6: difference of geopotential after 5, 10 and 15 days

Figure 5.58: Experiment 6: difference of vorticity after 5, 10 and 15 days

min: –321.423   **max: 217.308**

min: –322.943   **max: 638.534**

min: –609.527   **max: 1297.870**
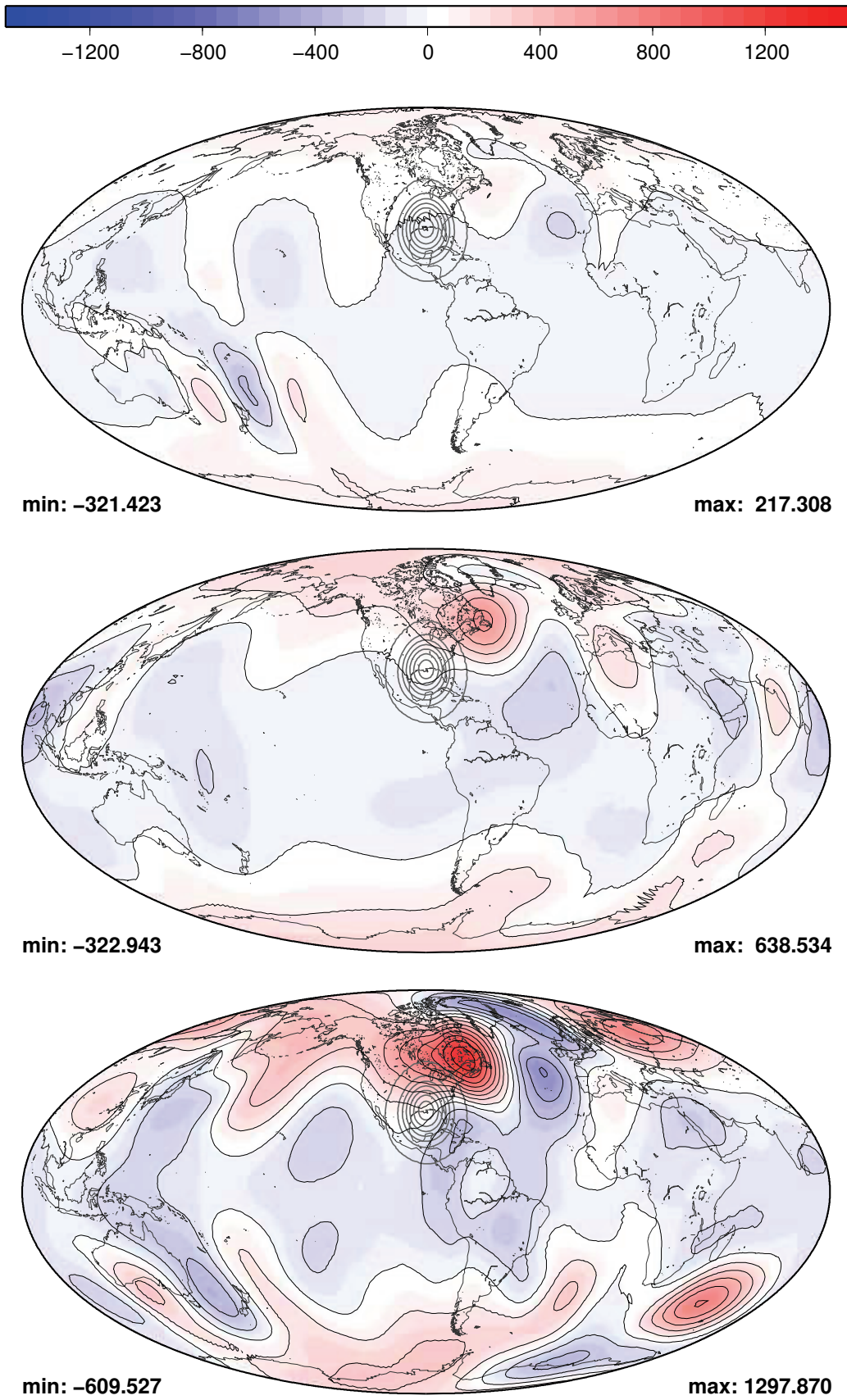
Figure 5.59: Experiment 9_9: difference of geopotential after 5, 10 and 15 days

min: –6.677e–06   max: 8.488e–06

min: –6.610e–06   max: 1.221e–05

min: –1.582e–05   max: 1.510e–05
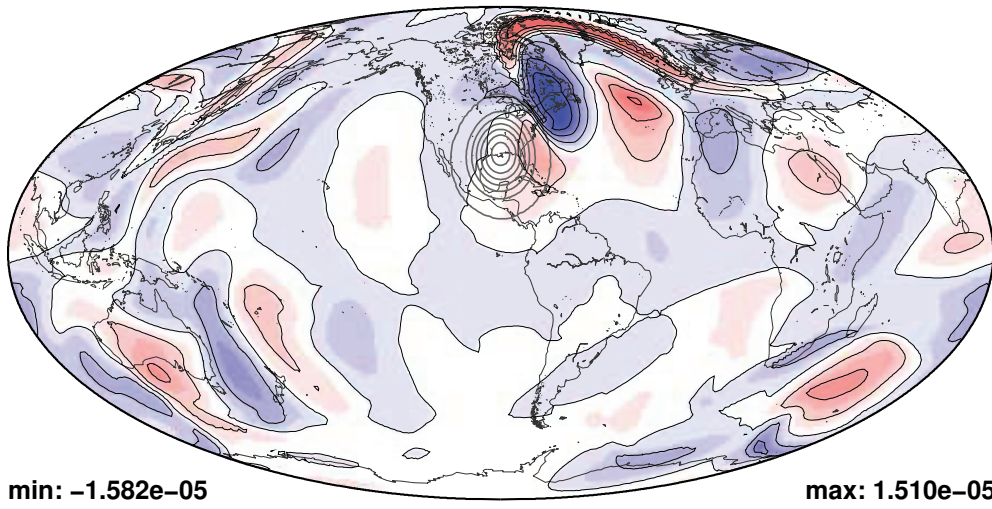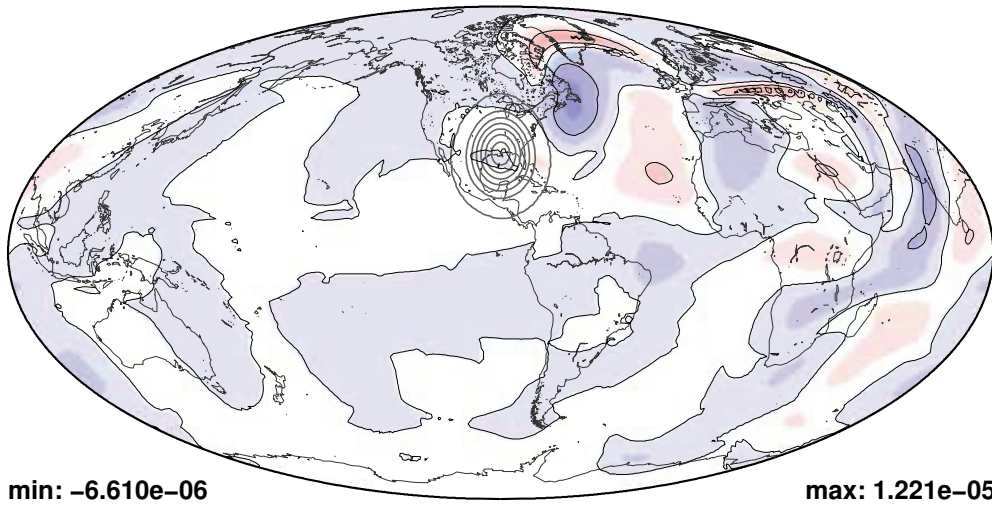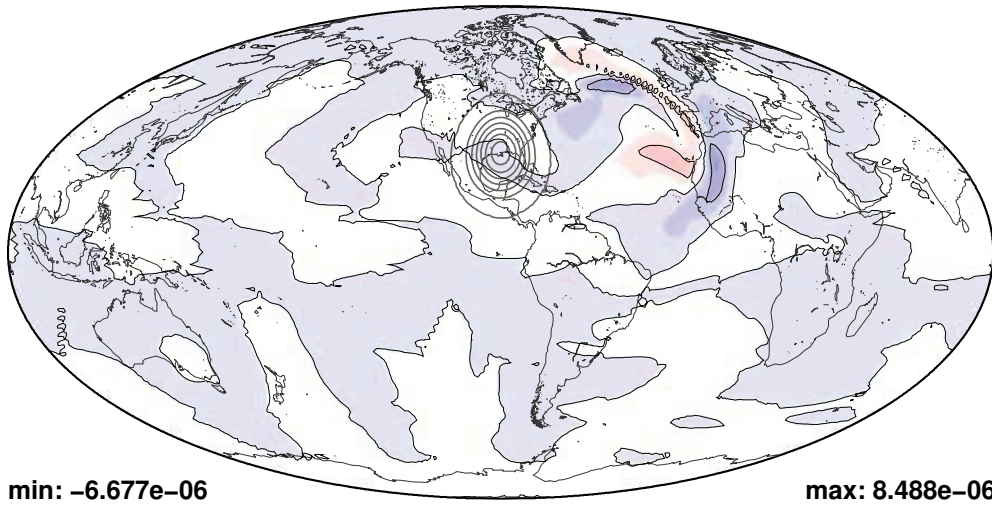
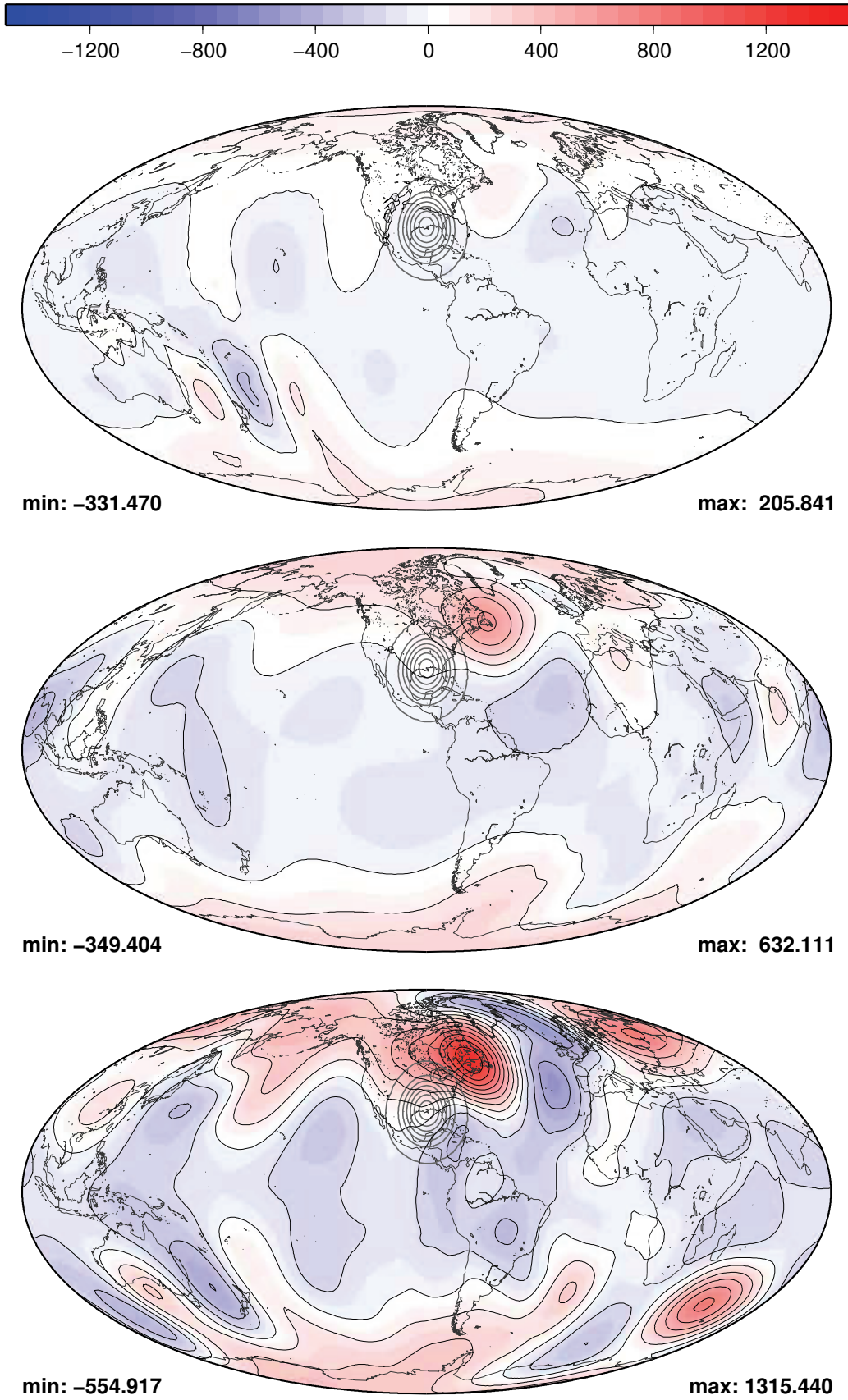Figure 5.60: Experiment 9_9: difference of vorticity after 5, 10 and 15 days

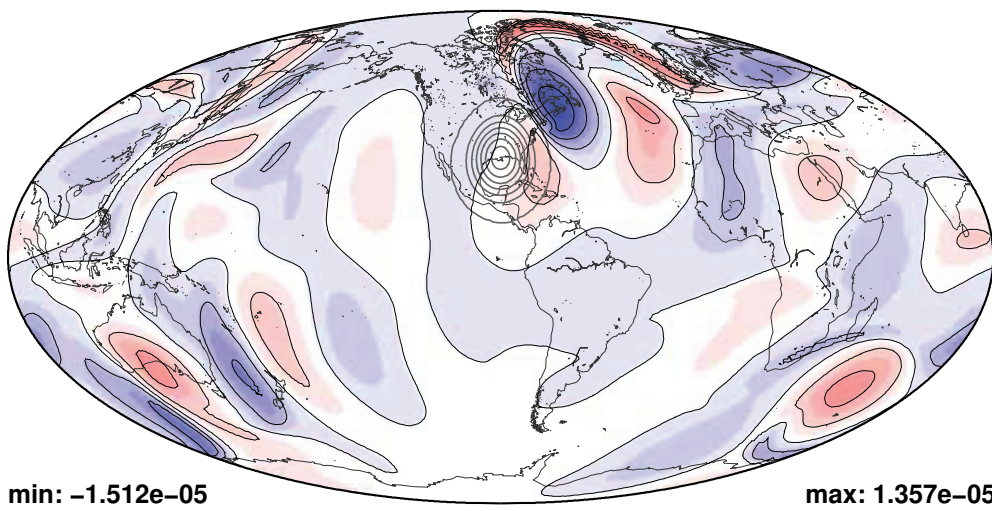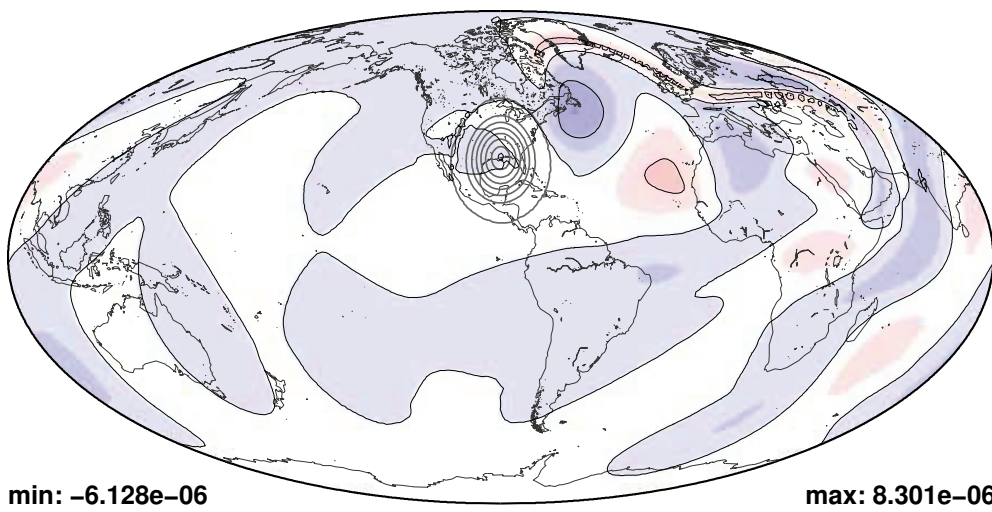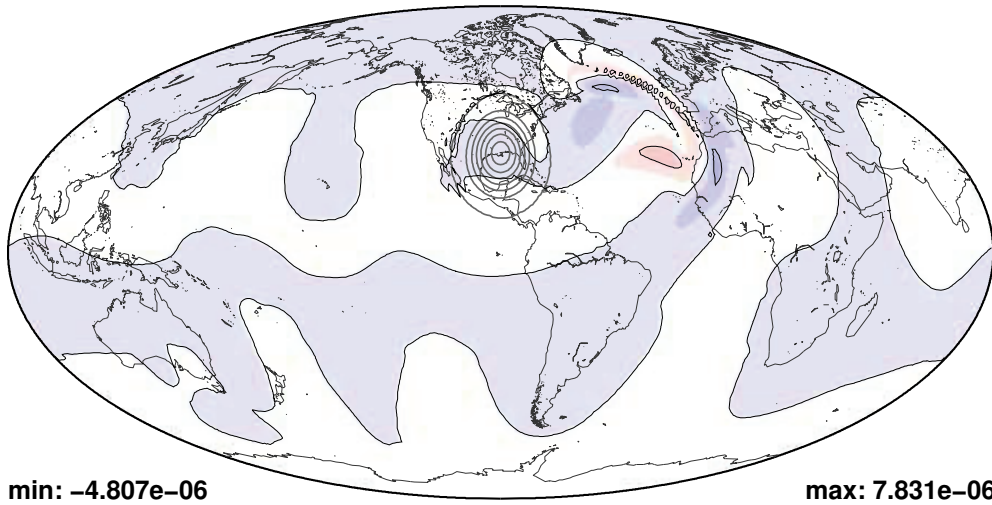Figure 5.61: **FEM*m*E**: difference of geopotential after 5, 10 and 15 days

Figure 5.62: **FEM***m***E**: difference of vorticity after 5, 10 and 15 days

experiments themselves as in this area the highest differences occur.

In the discussion we concentrate on the situation after 15 days because there the biggest differences can be observed. From the figures after day 5 and 10 one can learn that the differences develop over the time and intensify over the last 5 days.

In the geopotential fields the differences in the tropics are small in comparison to those of the high latitudes and the reference model has higher values than **PLASMA-FEM*m*E**. In the northern hemisphere one can detect a wave number 3 structure. Very strong north east of the mountain getting less intense eastwards. In the southern hemisphere a wave number 4 around the south pole is visible. The highest amplitude can be found west and east of South Africa, with higher values of the reference model in the Atlantic Ocean and lower in the Indian Ocean. An exception from that patterns are the two experiments with the static grids, 5 and 6. There the differences west of the mountain are much weaker for both, the northern and southern hemisphere. But the phase shift of the Rossby waves are the strongest observed. All the other experiments evolve very similar. Only the amplitudes of the differences to the reference model make them distinguishable. They maximum difference vary between 900m and 1300m, the minimum between 550m and 860m. Remarkable in experiment 5 is the red eye south east of Africa. It has a slightly different shape than in the other simulations. Again it should be emphasised, that the geographical description does not imply that the model uses the topography of the "real" earth for the experiments. But on the globe this description make specifications of local features much easier.

Eye-catching in the vorticity plots are on one side the Rossby wave features north east of the mountain with a pronounced tail of positive deviation form the spectral model north the wave. On the other side there are high amplitudes at the antipode of the mountain. The reason is presumably a phase shift between the vorticity patterns there, too. In experiment 5 and 6 this pattern are more dispersive than in the others. In experiment 4 one can detect a small disturbance with a high amplitude close to the Falklands. That is responsible for the highest extrema of all simulations. Only in experiment 3 big differences north west of the mountain can be detected. The development of the extremal values in the vorticity is not so uniform as for the geopotential. A steady growth of those values can be observed. But with the vorticity in some of the experiments the extremal after 5 days are bigger than after 10, like in experiment 1 and 5. Or they stay on the same level until day 10 and intensify afterwards, like in experiment 5 and 6.

In total all the experiments can handle this test case and the results show good agreement among each other. One cannot decide which of the results is best, as there is no "true" solution. But all simulations are stable and those with dynamic grid adaption catches well the flow structures.

5.4.6   Summary of test case 5 results

The 6 main points of the test case 5 experiments are:

1. Dynamic mesh generation with average criterion is superior to maximum criterion.

2. **FEM*m*E** conserves mass and nearly relative vorticity.

3. Reasonable development of Rossby wave in all experiments.

4. Phase shift of Rossby wave evolution in comparison to spectral reference model.

5. Dynamic adaptive grid generation catches flow features.

6. Noticeable loss of mass and energy after day 8 in the experiments with dynamic grid adaptation.

In subsection 5.4.3 the question was posed, if dynamic grid adaptation pays off? For test case 5 with the current dynamical core this answered must be answered with no as there are more disadvantages than advantages. Though the grid adapts to the flow features well, there is no clear improvement of the results in comparison to the other experiments. On the contrary there are two big disadvantages. First, dynamic mesh adaptation is numerically expensive and second, especially in this case, the noticeable loss of mass and energy after day 8 is a clear indication, that the current dynamical core cannot keep important properties of the flow regime. As this loss is not observed in the same extent in the experiments with static grid, besides experiment 6, there is the suspicion that the adaption criterion itself must be improved. Power et al. (2006) have used an adjoint model to estimate the errors of an adaptive ocean model. This concept could be applied to SWMs.
Moreover Lagrange-Galerkin schemes in general do not conserve any quantity. Hence, at least improvement of the mass conservation, e.g. as proposed by Behrens and Mentrup (2005), should be investigated.

5.5 Test case: Unsteady solid body rotation

This test case was proposed by Matthias Läuter (2004). It describes an unsteady solid body rotation (USBR) that is forced by orography. The orography is somewhat artificial, but the setup is an analytical solution to the spherical SWE, the only one so far with an unsteady solution. Thus, this test case is very attractive for adaptive techniques, as one can test the adaption process due to its unsteadiness and can control the error at the same time.
The initial velocities are chosen in that way, that the initial situation is repeated every day. Unfortunately the numerical properties of this test case are such that small inaccuracies can easily turn to an unstable situation. Hence, this is also a challenge to run this test case stable for a longer period.

5.5.1 Test case USBR on the globe

The key features of this test case are the angle α, the vector $\vec{c}$, the matrix $\mathbf{M}$ and the functional $\vec{\varphi}_t$:

$$\vec{c}(\alpha) = (-\sin\alpha, 0, \cos\alpha)^T \tag{5.52}$$

$$\mathbf{M}(t) = \begin{pmatrix} \cos(\Omega t) & \sin(\Omega t) & 0 \\ -\sin(\Omega t) & \cos(\Omega t) & 0 \\ 0 & 0 & 1 \end{pmatrix} \tag{5.53}$$

$$\vec{\varphi}_t(\vec{c}) = \mathbf{M}(t) \cdot \vec{c}(\alpha) \tag{5.54}$$

The flow crosses the equator with the angle α. For the simulations presented here it is set to $\alpha = \dfrac{\pi}{4}$. The angular velocity Ω is slightly modified for the purpose of better comparison of the results after each day. If the initial situation should be repeated after exactly one day, as postulated by Läuter, then

$$\Omega = \frac{2\pi}{86400s} \approx 7.2722 \cdot 10^{-5} \text{ s}^{-1}. \tag{5.55}$$

Usually instead of a full day, one sideric day is chosen, that lasts only 86146 s. But then, the initial situation would not occur again after one day, but after one sideric day. That would be unfavourably as one like to take time steps as fractions of one hour and that is no
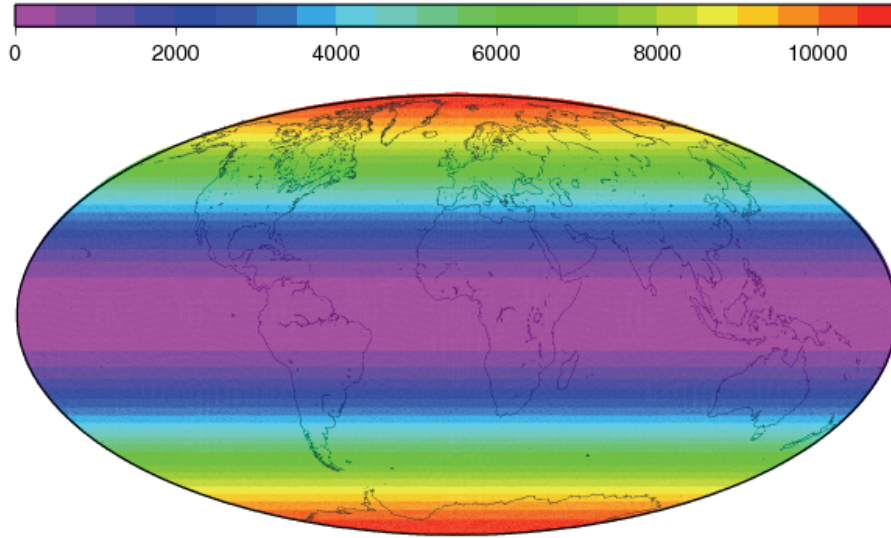
Figure 5.63: Test case USBR: orography normalised by g

fraction of one sideric day.

The orography ϕ_{Ho} is set to

$$\phi_{Ho}(\vec{x}) = \frac{(\vec{\Omega} \cdot \vec{x})^2}{2}. \tag{5.56}$$

Figure 5.63 displays the field. There is no orography at the equator and it is rising to both poles, where the maximum is reached.
With the orography ϕ_{Ho} and the functional $\vec{\varphi}_t$ the geopotential is determined by

$$\phi(\vec{x},t) = \breve{\phi} + \phi_{Ho}(\vec{x}) - \frac{1}{2}(U_o\,\vec{\varphi}_t(\vec{c}) \cdot \vec{e}_r + \vec{\Omega} \cdot \vec{x})^2 + c_o \tag{5.57}$$

$$\breve{\phi} = d_o - c_o$$

$$c_o = \frac{1}{2}\,(\Omega\,r_e)^2 + c_1$$

$$c_1 = 13,383 \text{ m}^2\text{ s}^{-2}$$

$$d_o = 133,681 \text{ m}^2\text{ s}^{-2}$$

$$U_o = \frac{2\,\pi r_e}{12\,\text{d}} \approx 38.58 \text{ m s}^{-1}.$$

The constant c_o and c_1 are set in that way, that the initial disturbance $\widehat{\phi}(\vec{x},0)$ always has a positive value. In that case the Helmholtz solver converges faster and improves the results. Figure 5.64 shows the initial situation of the geopotential.
U_o is set as in test case 2 and it specifies together with the functional $\vec{\varphi}_t$ the velocity

$$\vec{v}(\vec{x},t) = U_o\,\vec{\varphi}_t(\vec{c}) \times \vec{e}_r. \tag{5.58}$$

The relative vorticity can then be calculated as

$$\psi(\vec{x},t) = \frac{2\,U_o}{r_e^2}\Big[z \cos\alpha - x \cos\Omega t \sin\alpha + y \sin\Omega t \sin\alpha\Big] \tag{5.59}$$

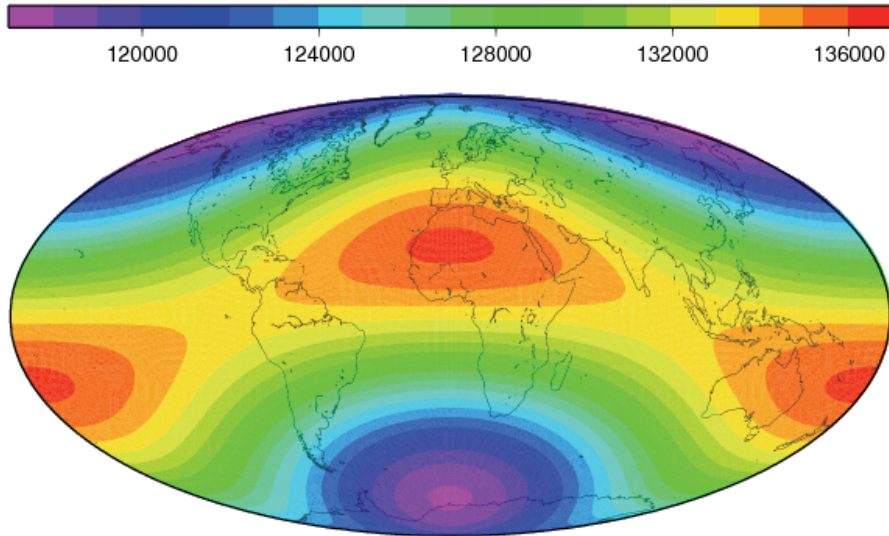Figure 5.65 gives the initial situation of vorticity and velocity.

Figure 5.64: Test case USBR: initial geopotential

5.5.2 Test case USBR on the unit sphere

A dimensionless version on the unit sphere using the characteristic values defined in equations (2.12) to (2.16) is obtained in the following way.

The vector $\vec{c}$ is free of any dimension. The matrix $\mathbf{M}$ changes to

$$\mathbf{M}(\tilde{t}) = \begin{pmatrix} \cos(\mu\tilde{t}) & \sin(\mu\tilde{t}) & 0 \\ -\sin(\mu\tilde{t}) & \cos(\mu\tilde{t}) & 0 \\ 0 & 0 & 1 \end{pmatrix} \tag{5.60}$$

and hence the functional $\vec{\varphi}$ to

$$\vec{\varphi}_{\tilde{t}}(\vec{c}) = \mathbf{M}(\tilde{t}) \cdot \vec{c}(\alpha). \tag{5.61}$$

The dimensionless position vector $\widetilde{\vec{x}}$ is on the unit sphere just $\vec{e}_r = (\tilde{x}, \tilde{y}, \tilde{z})^T$.
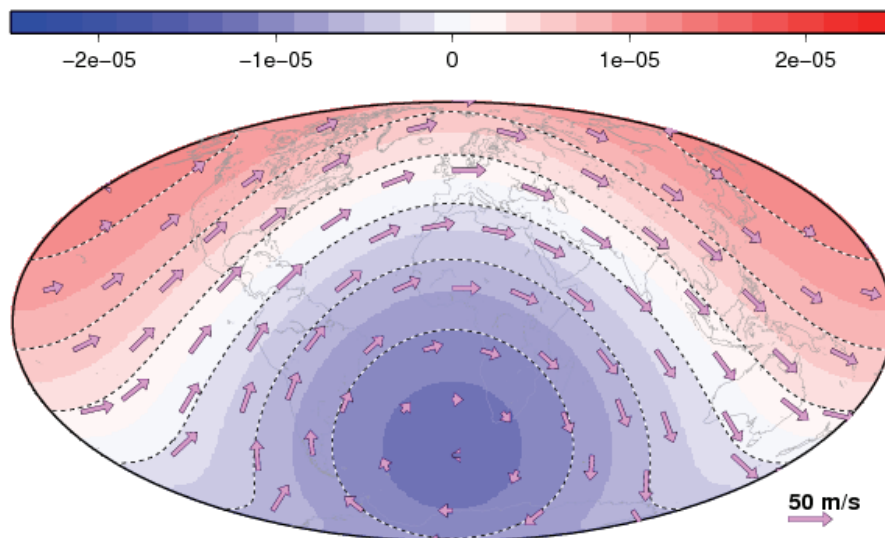

Figure 5.65: Test case USBR: initial vorticity and velocity

The velocity is normalised by U to

$$\widetilde{U}_o = U^{-1} \cdot U_o \tag{5.62}$$

$$\widetilde{v}(\vec{e}_r, \tilde{t}) = \widetilde{U}_o \, \vec{\varphi}_{\tilde{t}}(\vec{c}) \times \vec{e}_r \tag{5.63}$$

The relative vorticity becomes

$$F\widetilde{\psi}(\vec{e}_r, \tilde{t}) = \frac{2\,U\widetilde{U}_o}{L}\Big[\tilde{z}\cos\alpha \,-\, \tilde{x}\cos\mu\tilde{t}\sin\alpha \,+\, \tilde{y}\sin\mu\tilde{t}\sin\alpha\Big] \tag{5.64}$$

with

$$U = LF\mu^{-}1$$

results in

$$\widetilde{\psi}(\vec{e}_r, \tilde{t}) = \frac{2\,\widetilde{U}_o}{\mu}\Big[\tilde{z}\cos\alpha \,-\, \tilde{x}\cos\mu\tilde{t}\sin\alpha \,+\, \tilde{y}\sin\mu\tilde{t}\sin\alpha\Big]. \tag{5.65}$$

The orography ϕ_{Ho} changes to

$$G\,\widetilde{\phi}_{Ho}(\vec{e}_r) = \frac{(F\widetilde{\vec{\Omega}} \cdot L\vec{e}_r)^2}{2} \tag{5.66}$$

with

$$\widetilde{\vec{\Omega}} \cdot \vec{e}_r = \begin{pmatrix} 0 \\ 0 \\ 1 \end{pmatrix} \cdot \begin{pmatrix} \tilde{x} \\ \tilde{y} \\ \tilde{z} \end{pmatrix} \,=\, \tilde{z}$$

and

$$G = (\nu\,\mu^{-1}L\,F)^2$$

finally to

$$\widetilde{\phi}_{Ho}(\vec{e}_r) = \frac{\mu^2}{2\,\nu^2}\,\tilde{z}^2. \tag{5.67}$$

Using the above described relations the geopotential (5.57) transforms to

$$G\,\widetilde{\phi}(\vec{e}_r, t) = G\,\overline{\phi} \,+\, G\,\widetilde{\phi}_{Ho}(\vec{e}_r) \,-\, \frac{1}{2}(U\widetilde{U}_o\,\vec{\varphi}_{\tilde{t}}(\vec{c}) \cdot \vec{e}_r \,+\, FL\tilde{z})^2 + c_o \tag{5.68}$$

$$\widetilde{\phi}(\vec{e}_r, t) = \overline{\phi} \,+\, \widetilde{\phi}_{Ho}(\vec{e}_r) \,-\, \frac{1}{2\,\nu^2}(\widetilde{U}_o\,\vec{\varphi}_{\tilde{t}}(\vec{c}) \cdot \vec{e}_r \,+\, \mu\tilde{z})^2 + \widetilde{c}_o \tag{5.69}$$

with

$$\overline{\phi} = G^{-1}(d_0 - c_o)$$

$$\widetilde{c}_o = G^{-1}\,c_o$$

5.5.3   Experimental settings and results

As already mentioned this test case easily tends to evolve instabilities. Due to this fact a reduced time step is used. In this test case the time step is set to $\Delta t = 300s$ for the non adapting setups. In all experiments with grid adaptation instabilities occurs within the first days. For the analysis of this problem the time step is further reduced to $\Delta t = 90s$.

Non adaptive setups

Three experiments with non adaptive setups are performed, **FEMmE** on level 4 and **PLASMA-FEMmE** on level 9 and 10 (**PF9** and **PF10**). All experiments are stable for at least 15 days. The Figures 5.66 and 5.67 show the development of the solid body rotation for the first day every 8 hours with **PF10**.
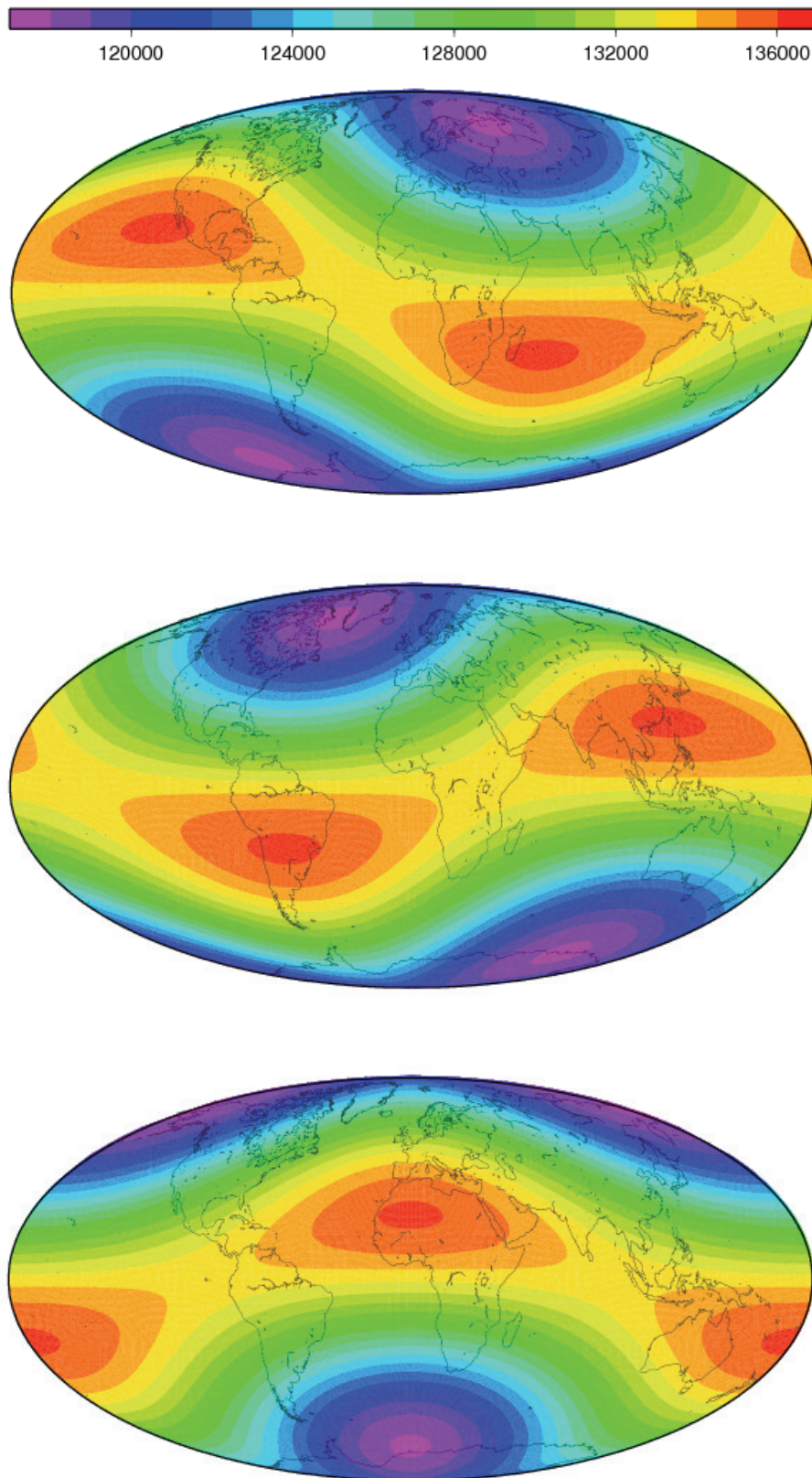
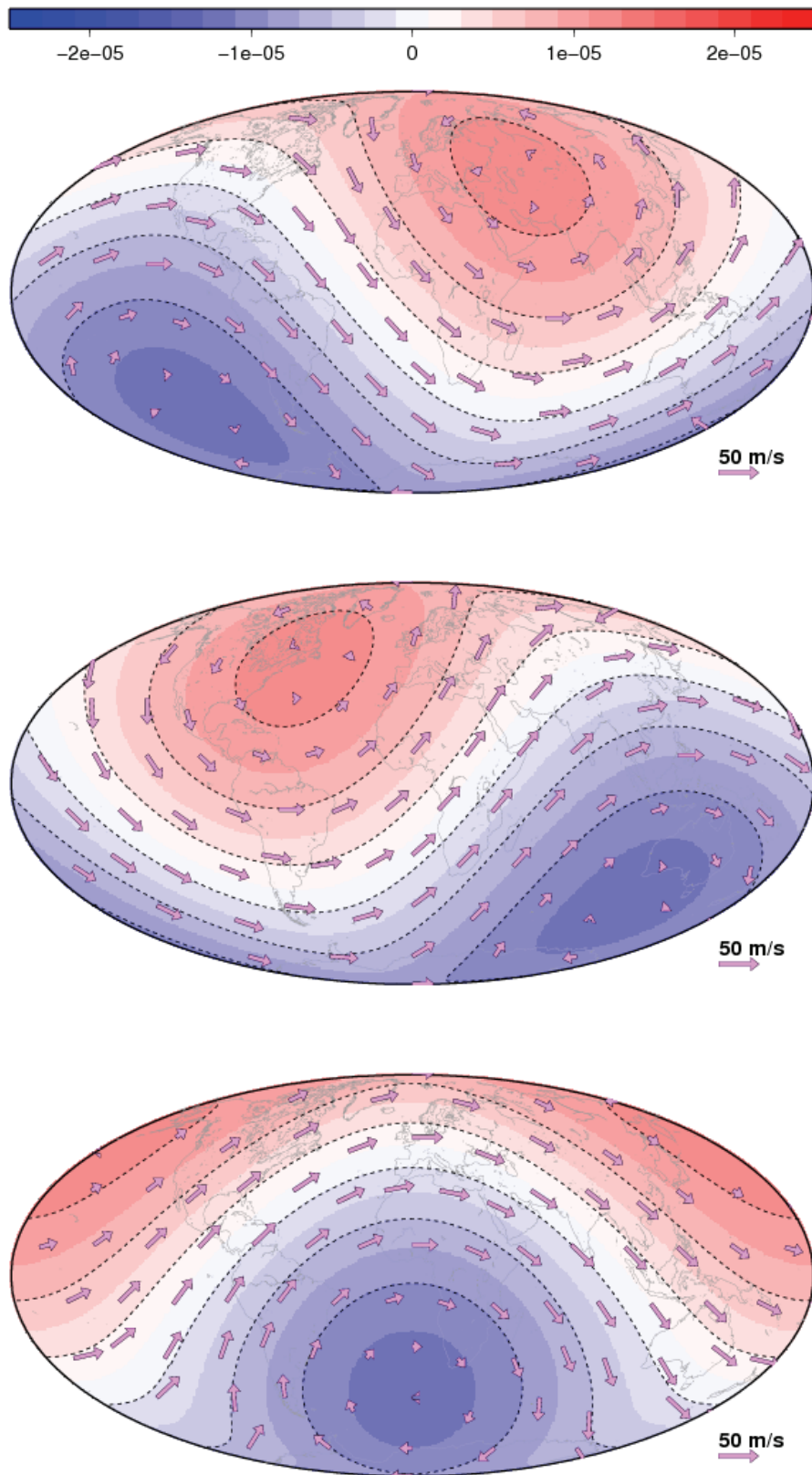Figure 5.66: Test case USBR: development of geopotential after 8h, 16h and 24h

Figure 5.67: Test case USBR: development of vorticity and velocity after 8h, 16h and 24h

On the next pages the conservation properties and errors of geopotential and vorticity for the first 5 days are given.

Eye-catching are the result of **PF10** experiment. In many of the figures they are indistinguishable from the results of **FEM*m*E**. Only for both vorticities, the potential enstrophy and both l_∞ errors they can be easily distinguished. In all the other figures both time series are very close to each other. This leads to the conclusion that one needs twice as much grid points of the *amatos* grids to reach the same resolution, same conservation properties and same errors as in the regular refined grids of **FEM*m*E**. The operator tests in section 5.3.3 give a similar picture. So this result holds not only for the operators, but also for a time dependent SW system.

Comparing the conservation properties the results for **FEM*m*E** and **PLASMA-FEM*m*E** are similar to those of the previous test cases. The time series of the vorticities show conservation for both, as the deviation form zero are small. No trend can be observed. **FEM*m*E** fluctuates less than both **PLASMA-FEM*m*E** time series.

The ratio of first moments show mass conservation for **FEM*m*E** and **PF10**. **PF9** gains mass of about 0.5‰ and 0.4‰ in the second moments. In that respect the two other experiments lose a bit more than 0.1‰. But as in test case 5 the second moments are no conservation property for this test case. Remarkable in these time series are the wavy progression with a period of a half day.

None of the experiments conserves neither total energy nor potential enstrophy. **PF9** gains 0.5‰ of total energy, where as the other two lose 0.3‰. All experiments lose potential enstrophy, between 1.2‰ and 2.2‰ until day 5.

The normalised errors of the geopotential are between 1‰ and 2‰ in the first 5 days. In respect of the l_1 and l_2 error **PF9** gives slightly better results than the other two experiments, where as comparing the maximum error the situation is vice versa. All time series rise linearly in a wavy pattern with a period around one third of a day.

The normalised errors of vorticity are 1 to 2 orders of magnitude bigger than those of the geopotential. Here **PF9** always has a bigger error than **FEM*m*E** and **PF10**. In the case of the l_1 and l_2 error these errors arise by a factor of 2 during the first half day for **PF9**. In the next 9 hours these errors are nearly halved in the **FEM*m*E** and **PF10** experiment. For experiment **PF9** they proceed to grow but with a notedly smaller amount. After that these time series for all three experiments rise with the same slope. The periodic behaviour of that rise is one day for the latter experiments and has a higher frequency for **PF9** besides the first two days of the l_1 error. The l_∞ error gives a different picture. After the rise in the first half day the errors seems to stay at that level; around 3% for **FEM*m*E** and **PF10**, between 10 and 20% for the other experiment.

On the pages 96 to 99 errors of the geopotential of each experiment after one, three and five days are presented. As the error is increasing with time for each point of time another scale is chosen.

All errors show a dipole structure on the northern and southern hemisphere around each pole. The error pattern after each day stay at the same position, but the absolute values are increasing. The extreme values of the error pattern are connected to the extreme values of the geopotential field itself. Along the zero meridian the errors are shifted northwards from the centre of the extrema, along the date line southwards.

In respect to the geopotential the error patterns of **PF10** and **FEM*m*E** look very similar. There are small differences in the absolute values of the extremes and the location of the contour lines. But altogether one can conclude that both experiments give the same results, not only in the global integrals but also in the individual flow patterns.
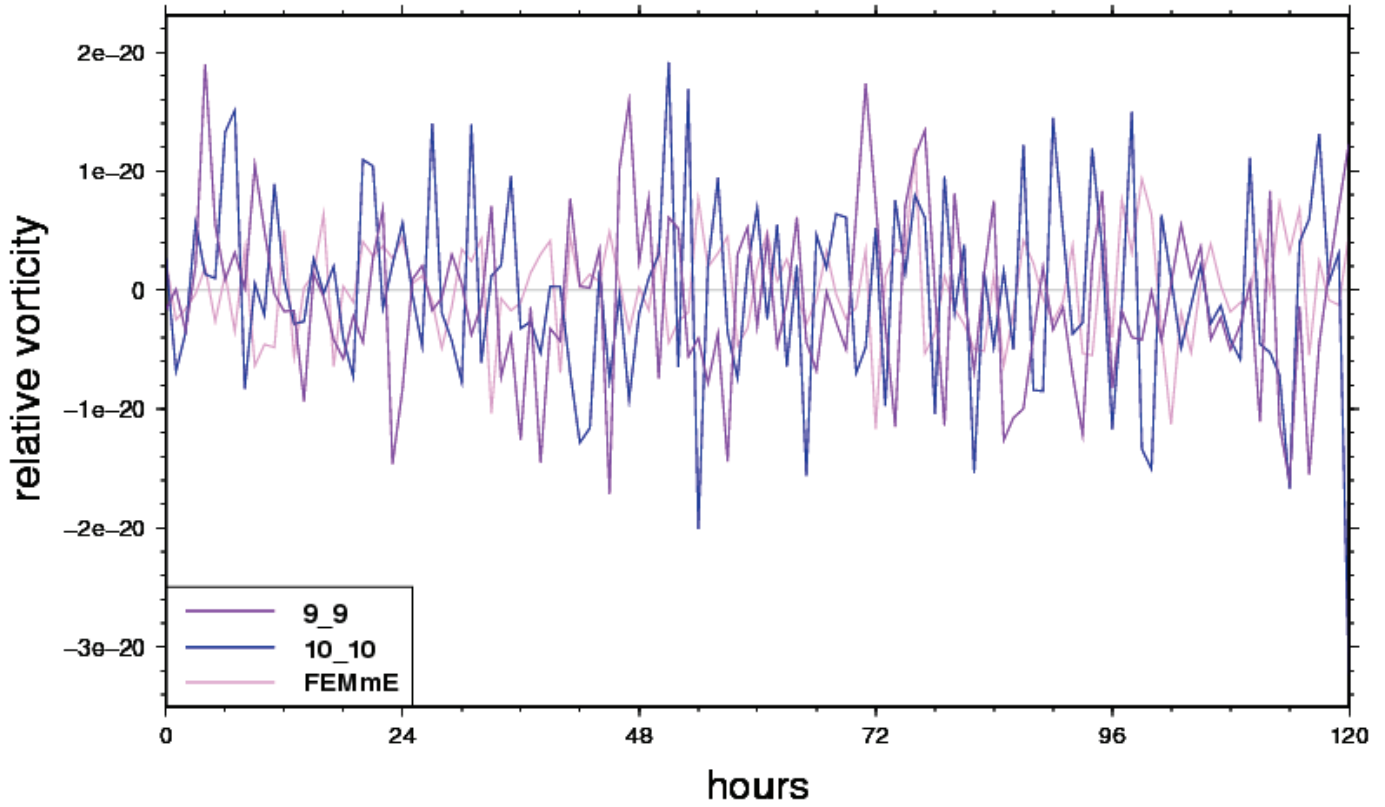
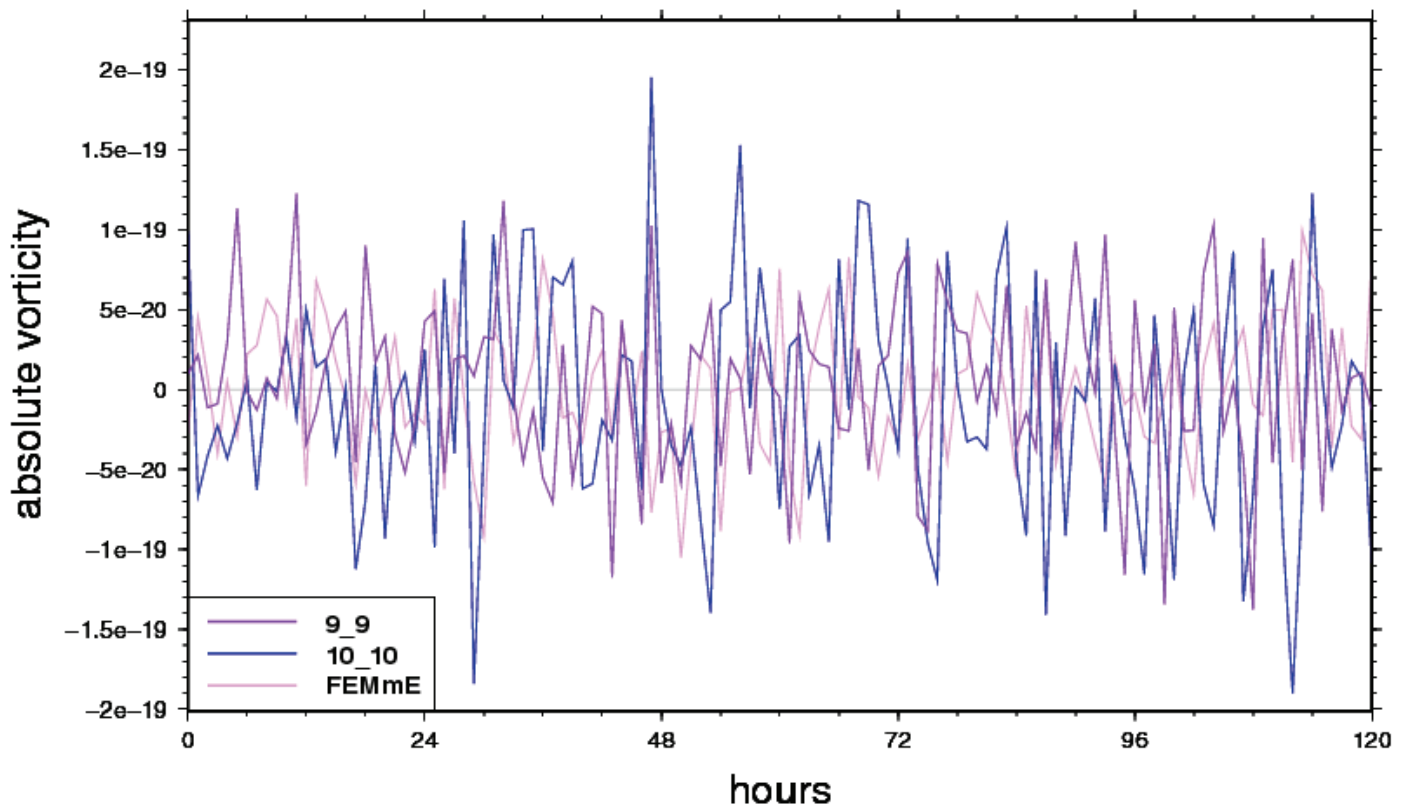Figure 5.68: Test case USBR: relative vorticity

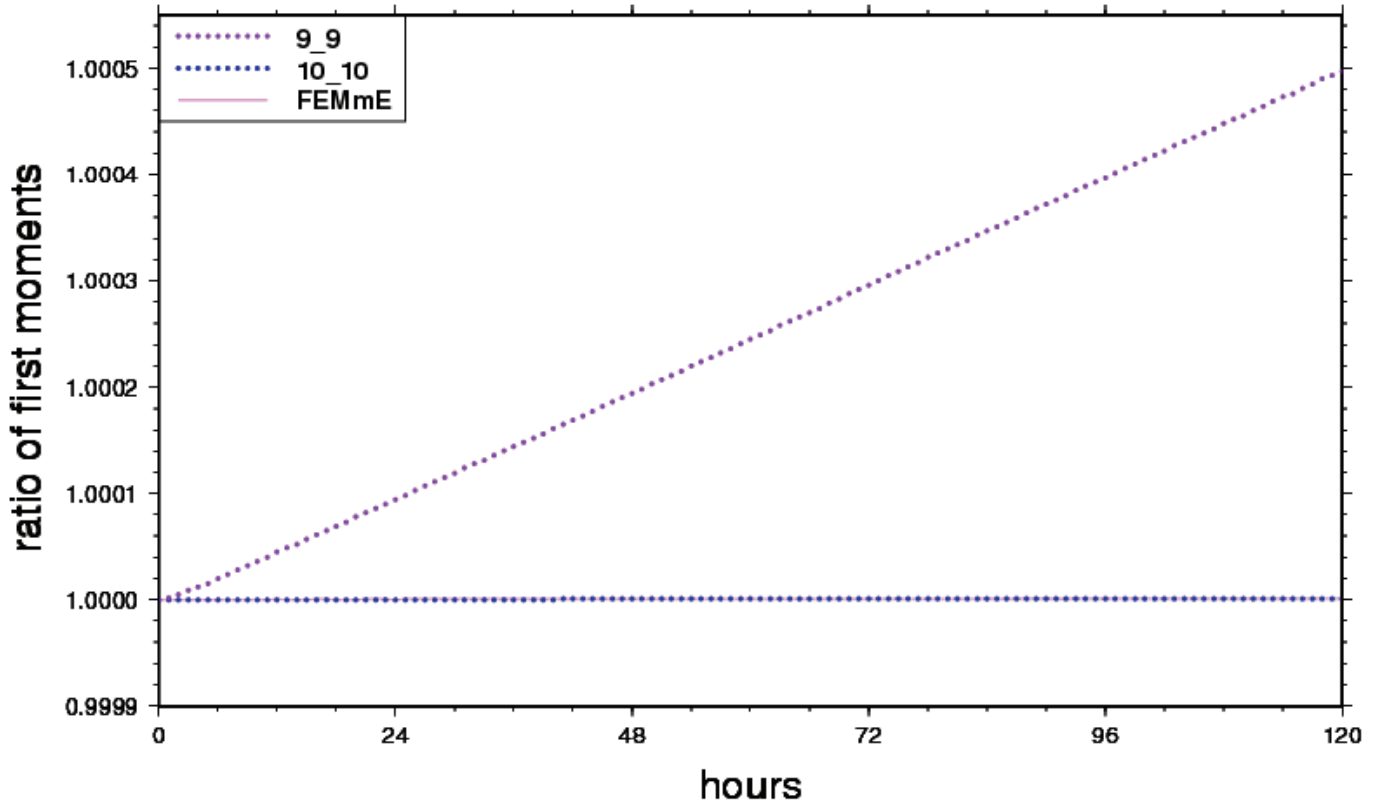Figure 5.69: Test case USBR: absolute vorticity

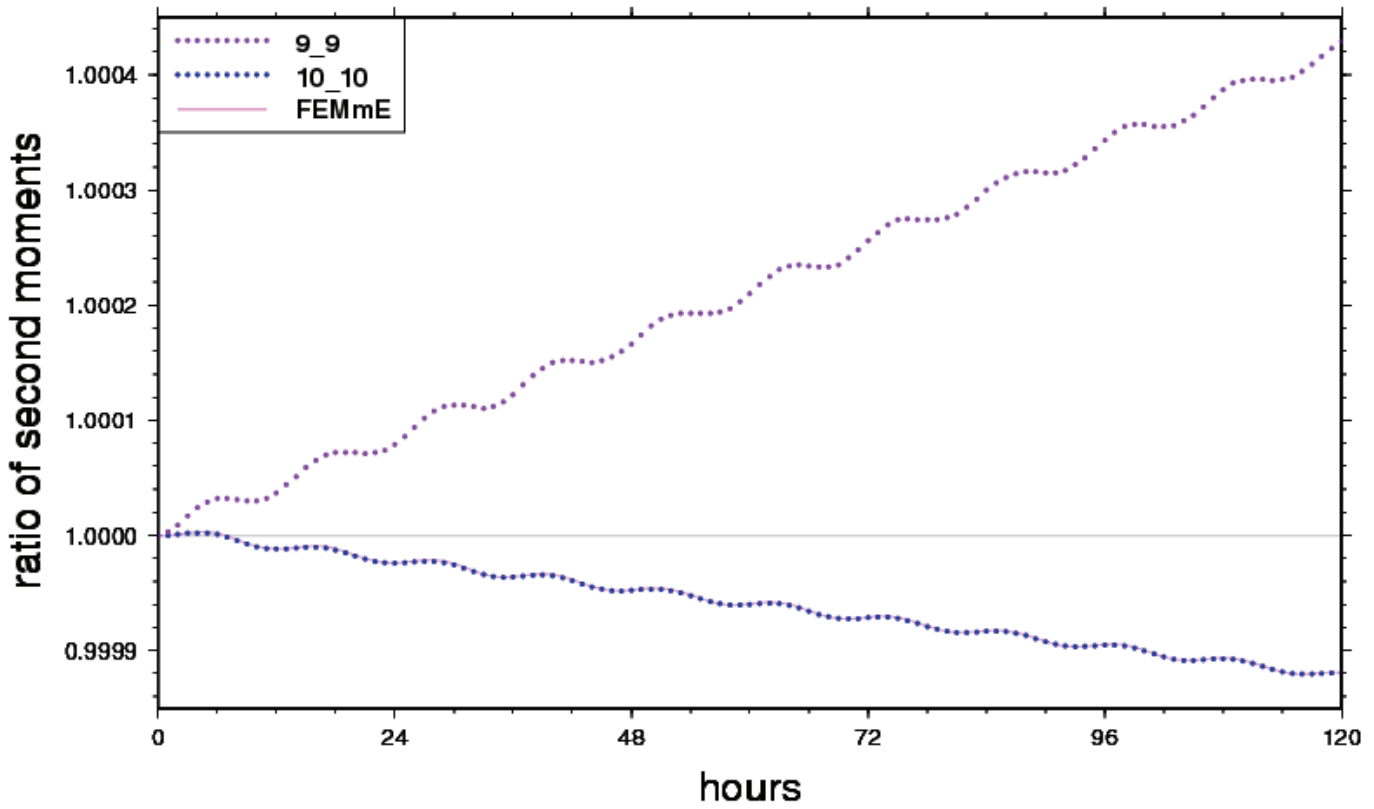Figure 5.70: Test case USBR: ratio of first moments

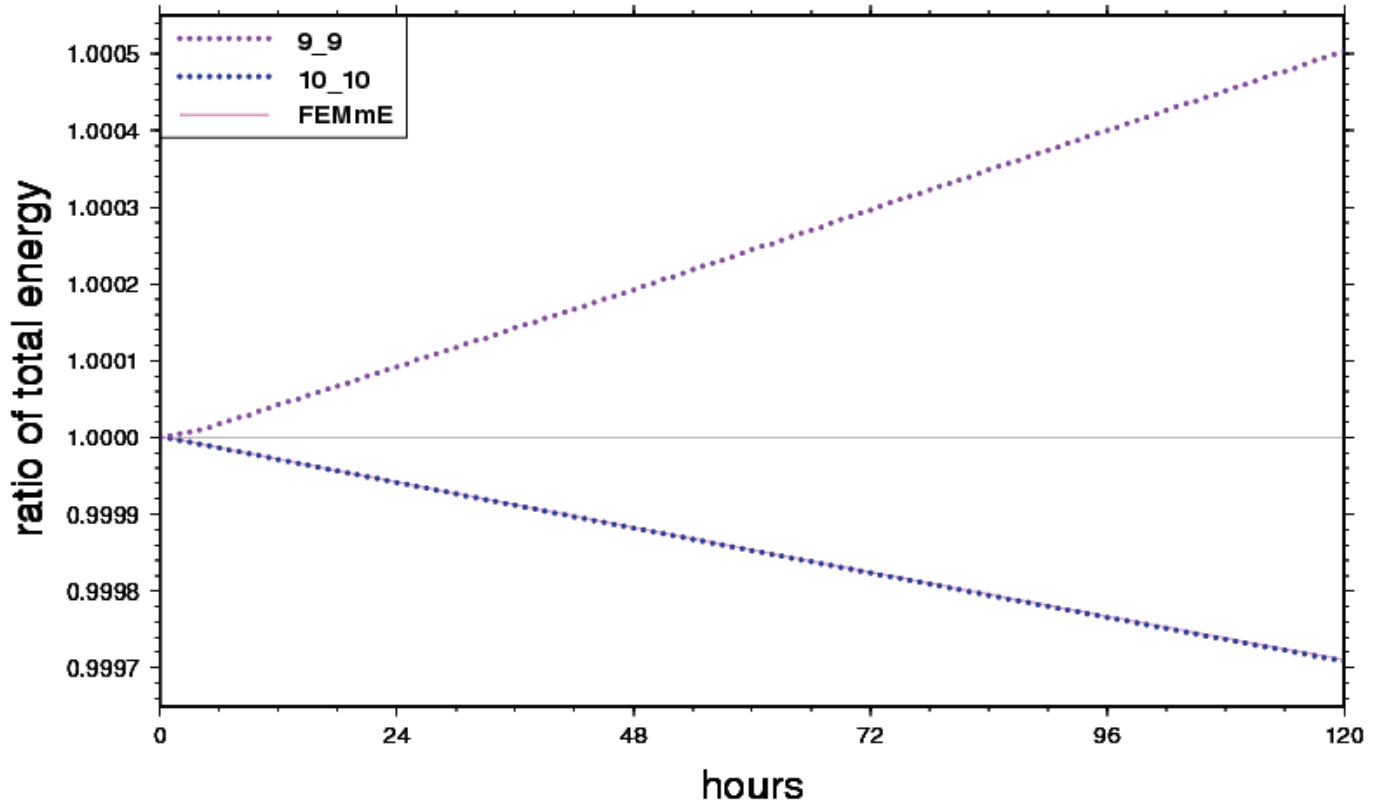Figure 5.71: Test case USBR: ratio of second moments

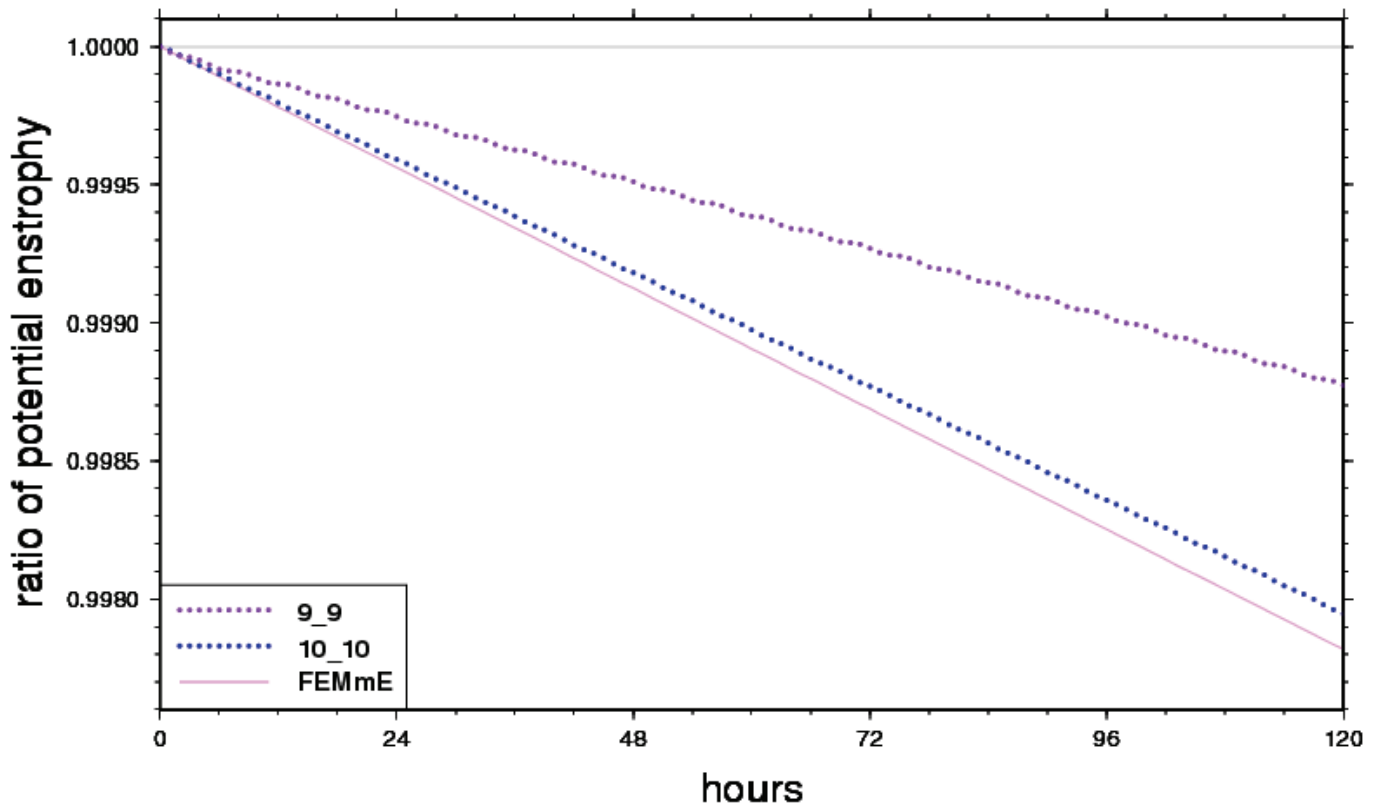Figure 5.72: Test case USBR: ratio of total energy

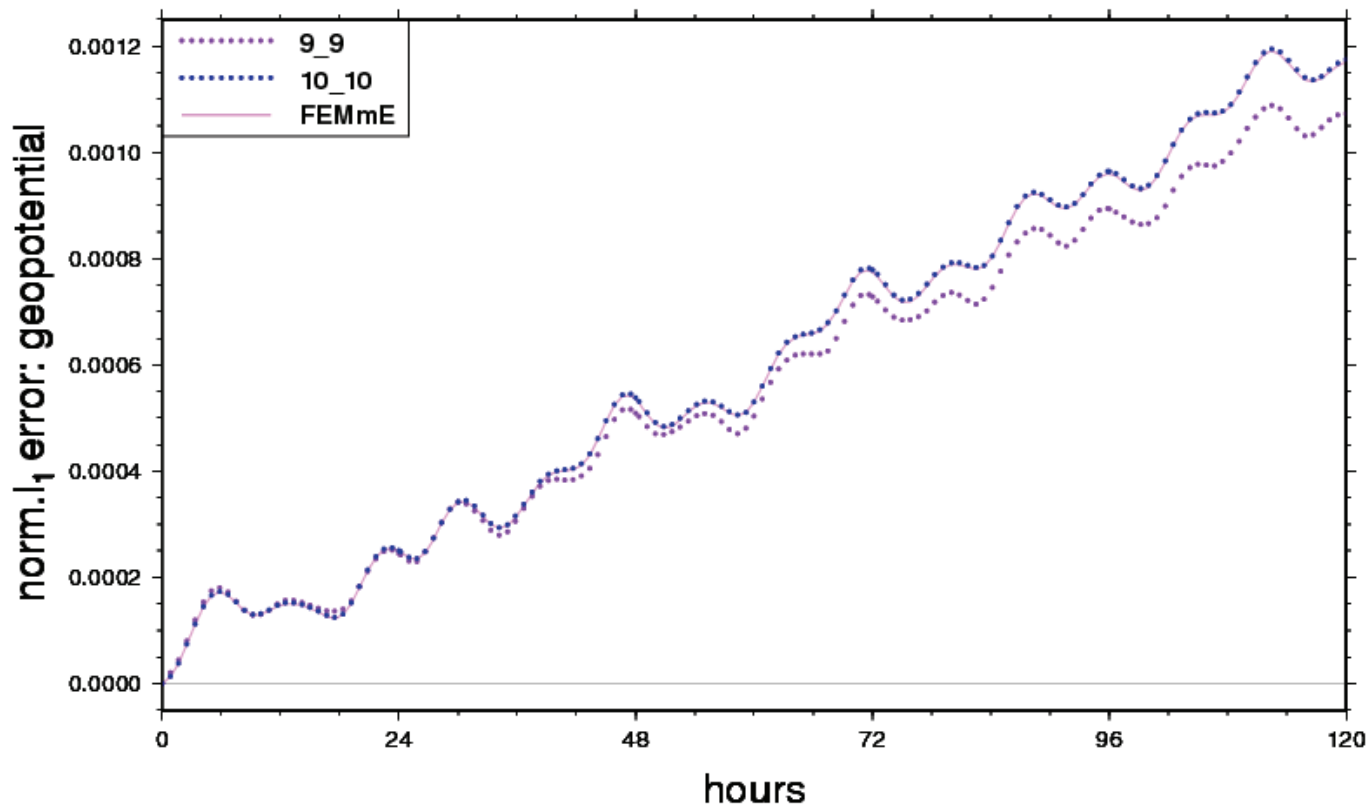

Figure 5.73: Test case USBR: ratio of potential enstrophy

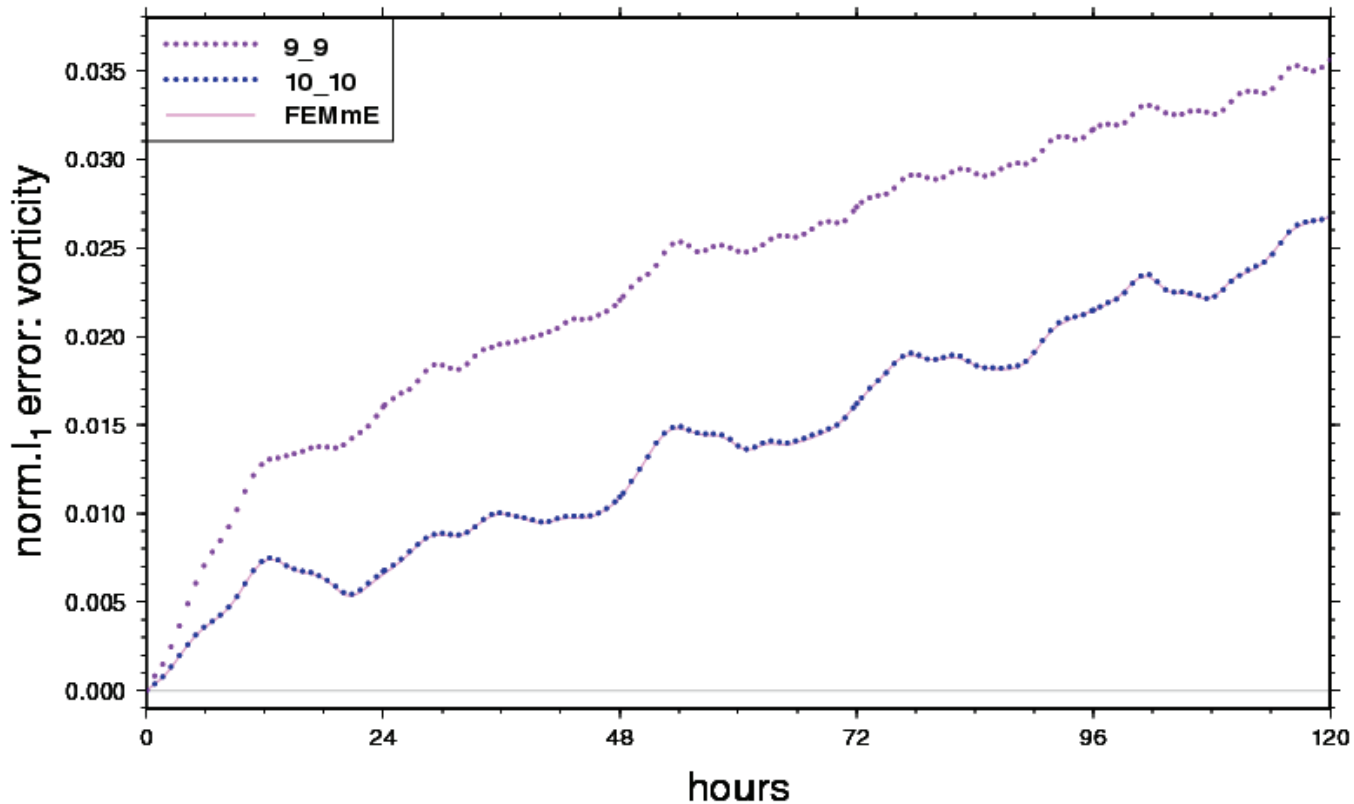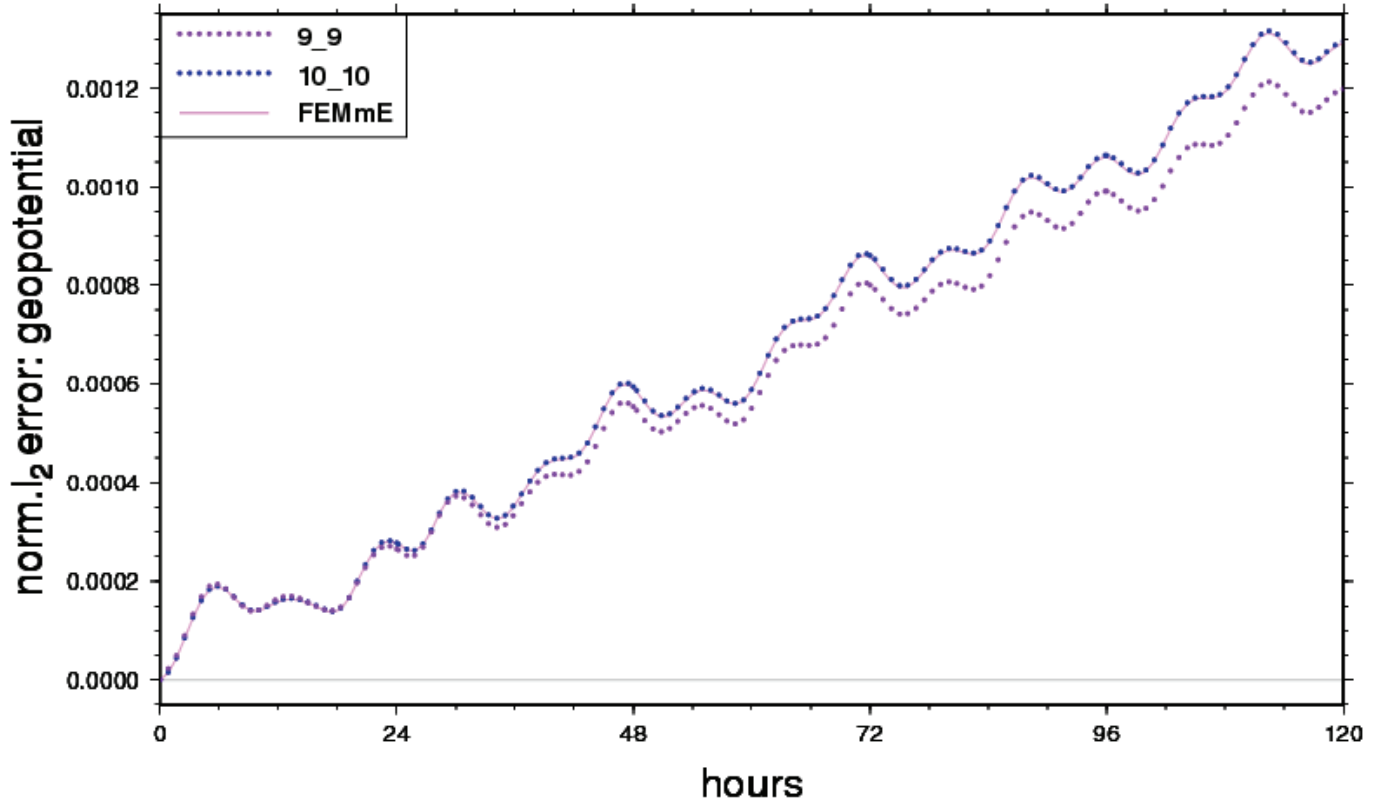Figure 5.74: Test case USBR: normalised l_1 error of geopotential
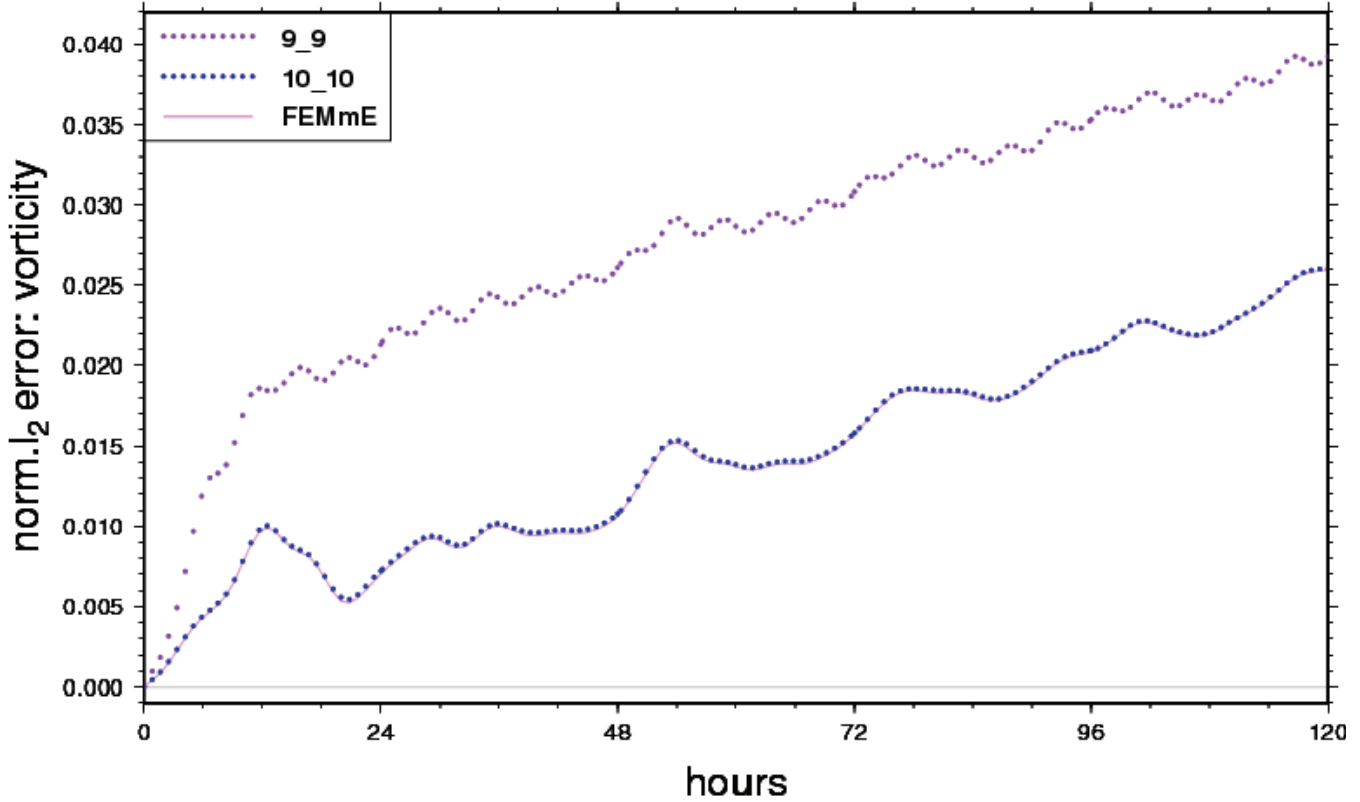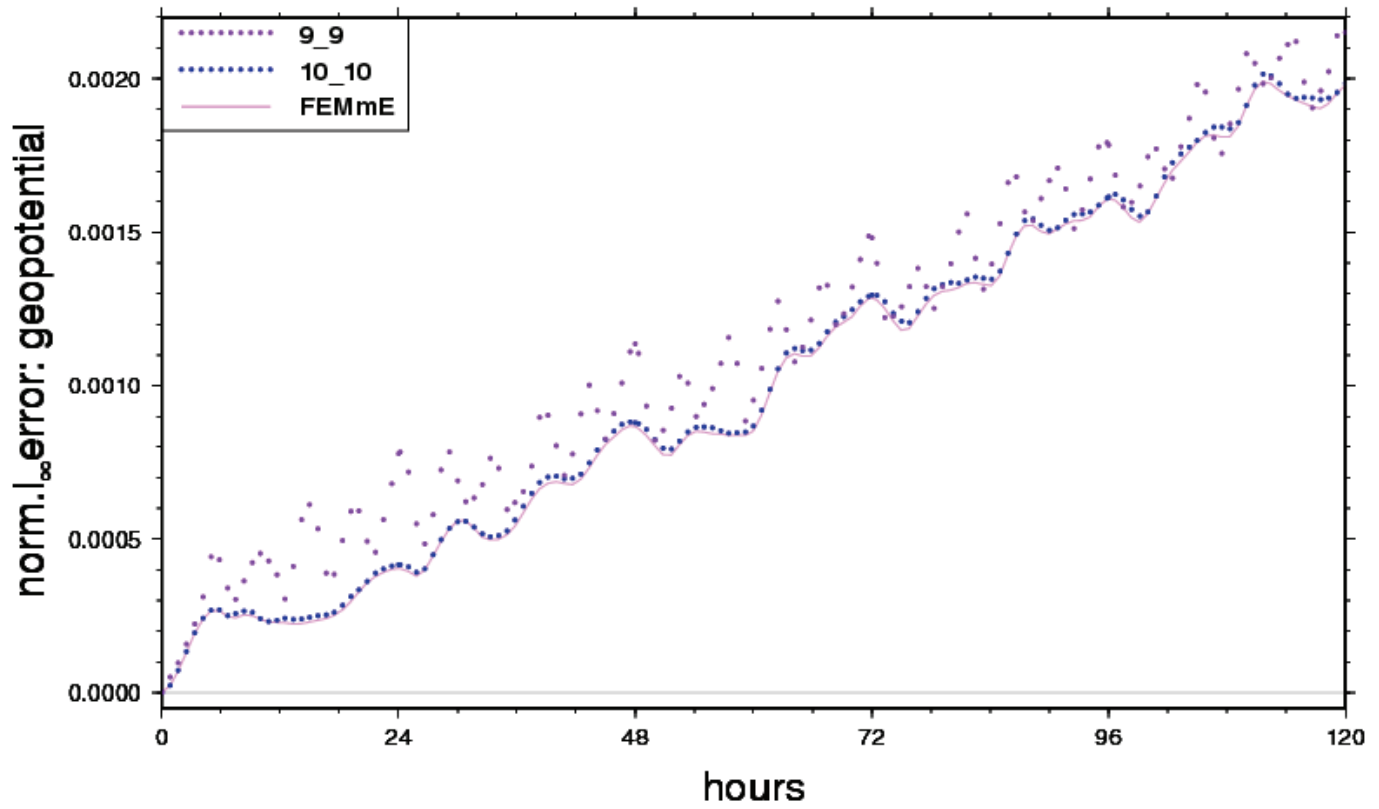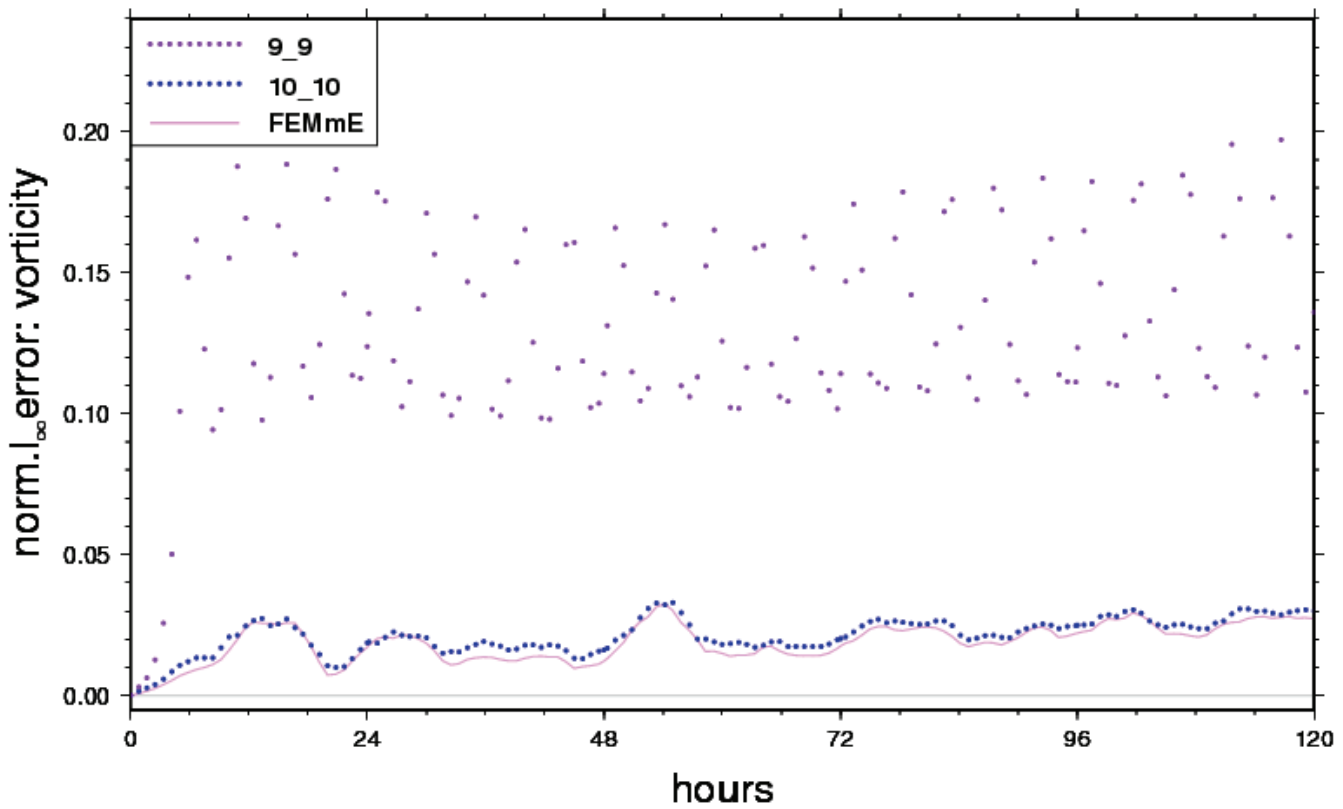

Figure 5.75: Test case USBR: normalised l_1 error of vorticity

Figure 5.76: Test case USBR: normalised l_2 error of geopotential

Figure 5.77: Test case USBR: normalised l_2 error of vorticity

Figure 5.78: Test case USBR: normalised l_∞ error of geopotential

Figure 5.79: Test case USBR: normalised l_∞ error of vorticity

min: −41.758   max: 94.059

min: −46.441   max: 50.350

min: −45.782   max: 48.864

Figure 5.80: Test case USBR: error of geopotential after day 1: **PF9**, **PF10**, **FEM**m**E**

Figure 5.81: Test case USBR: error of geopotential after day 3: **PF9**, **PF10**, **FEM***m***E**
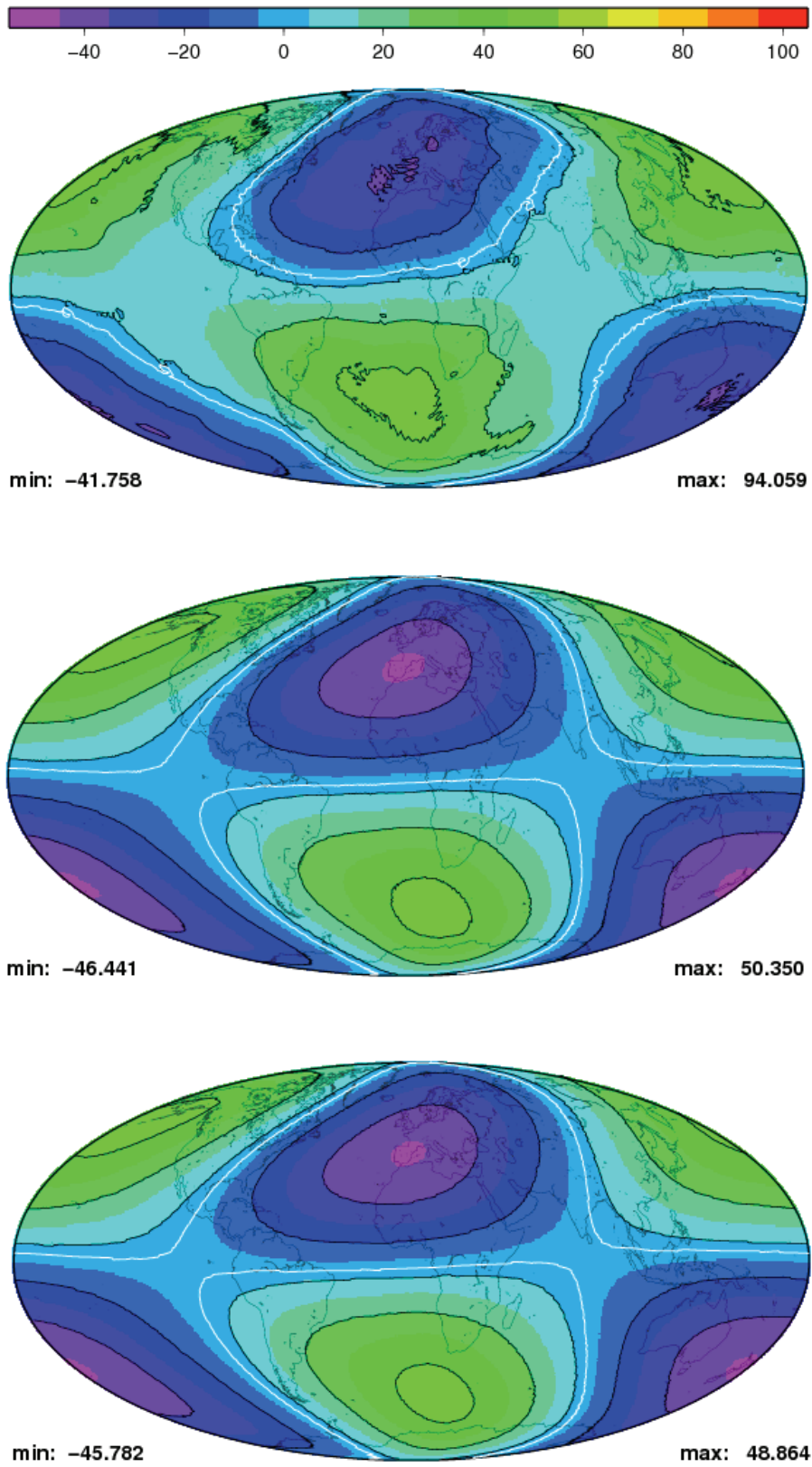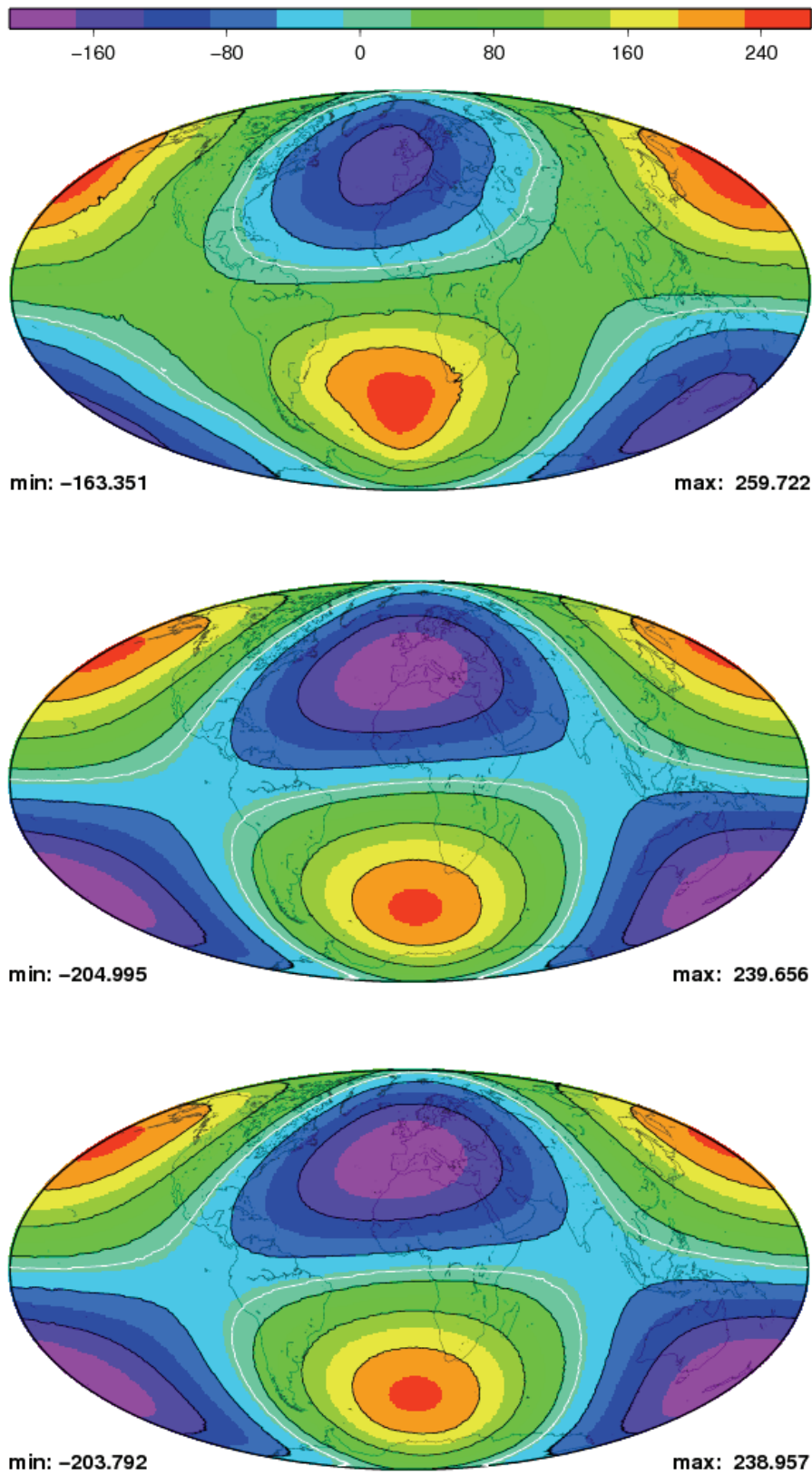
Figure 5.82: Test case USBR: error of geopotential after day 5: **PF9**, **PF10**, **FEM***m***E**
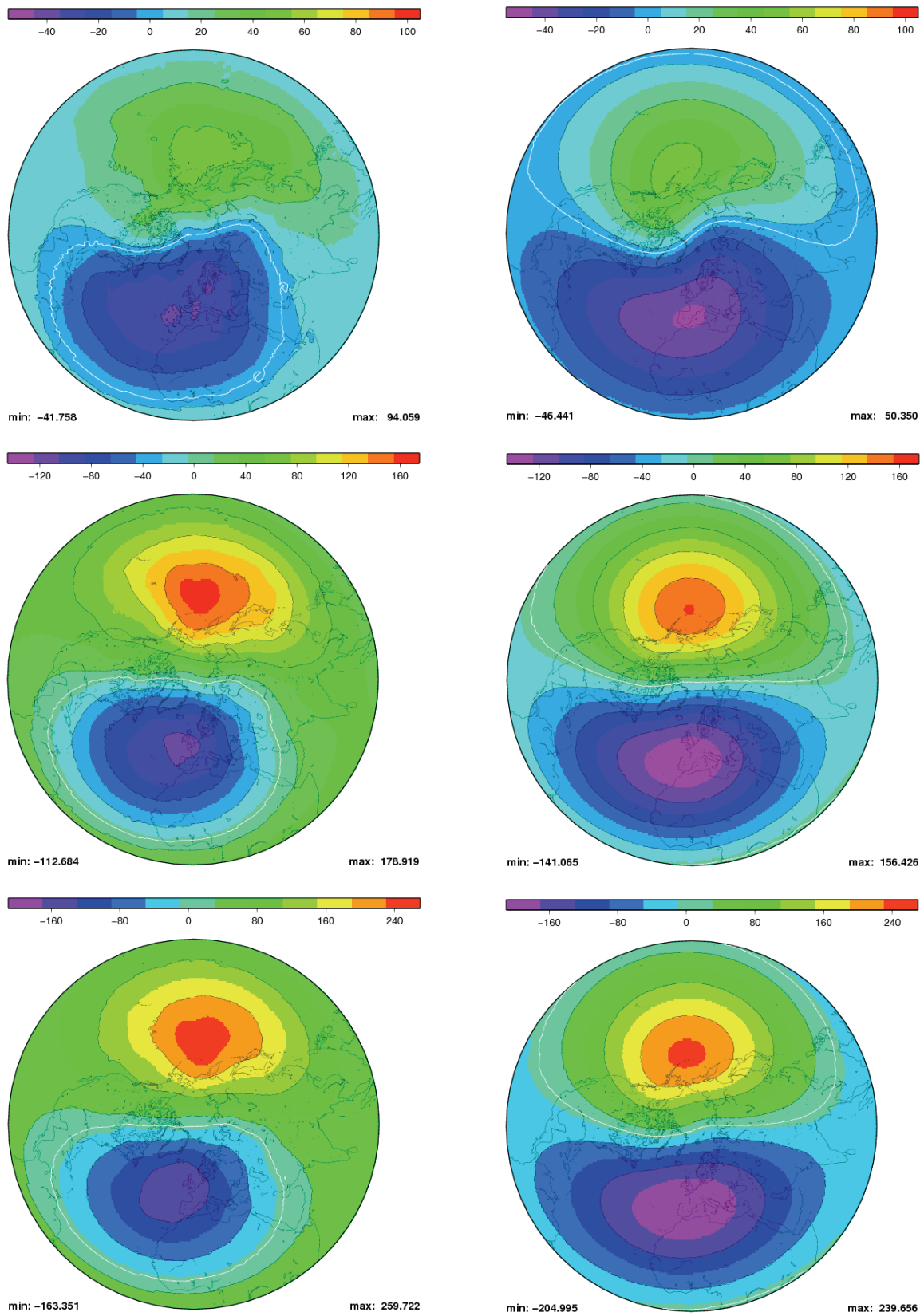
Figure 5.83: Test case USBR: **PF9** and **PF10** error of geopotential after day 1, 3 and 5 North polar stereographic projection

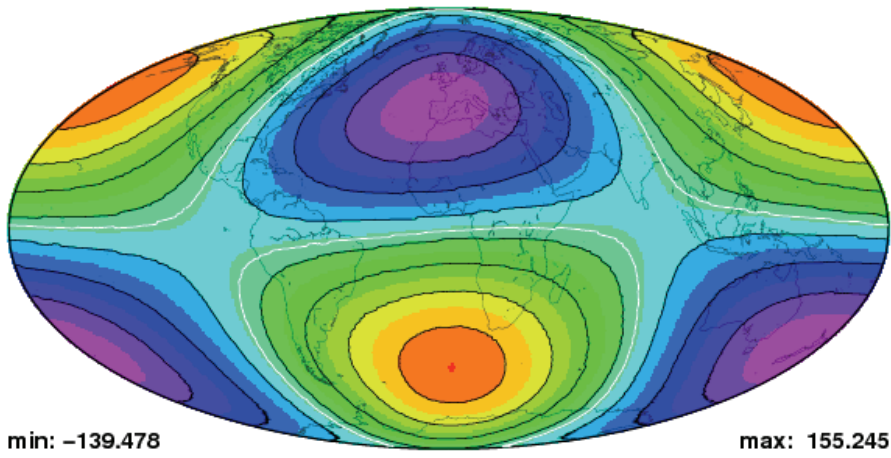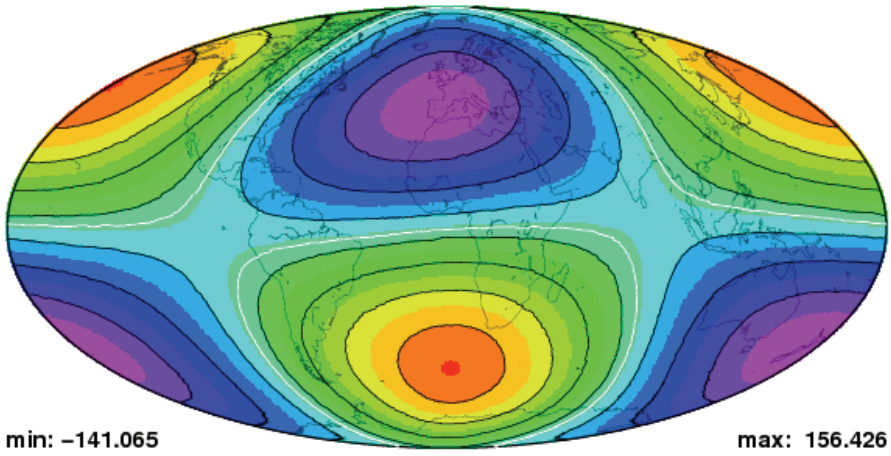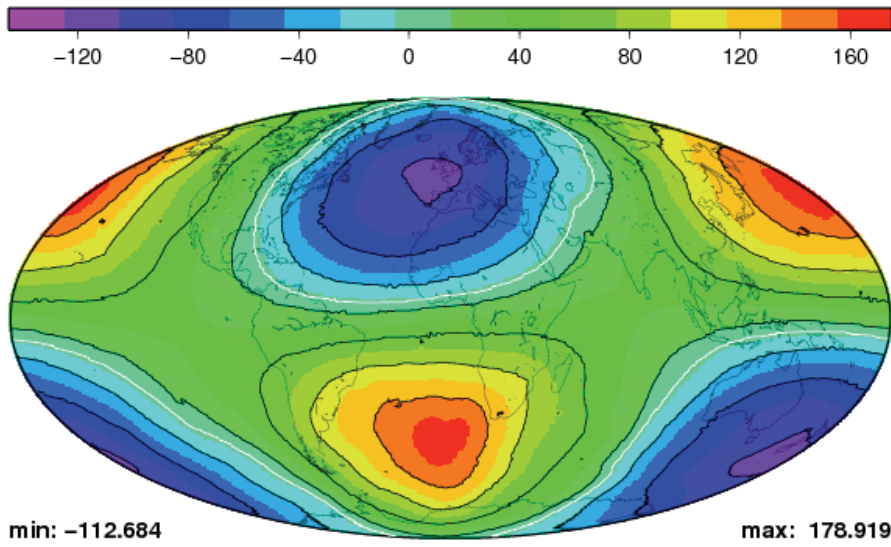Figure 5.84: Test case USBR: error of vorticity after day 1: **PF9**, **PF10**, **FEM***m***E**

Figure 5.85: Test case USBR: error of vorticity after day 3: **PF9, PF10, FEMmE**

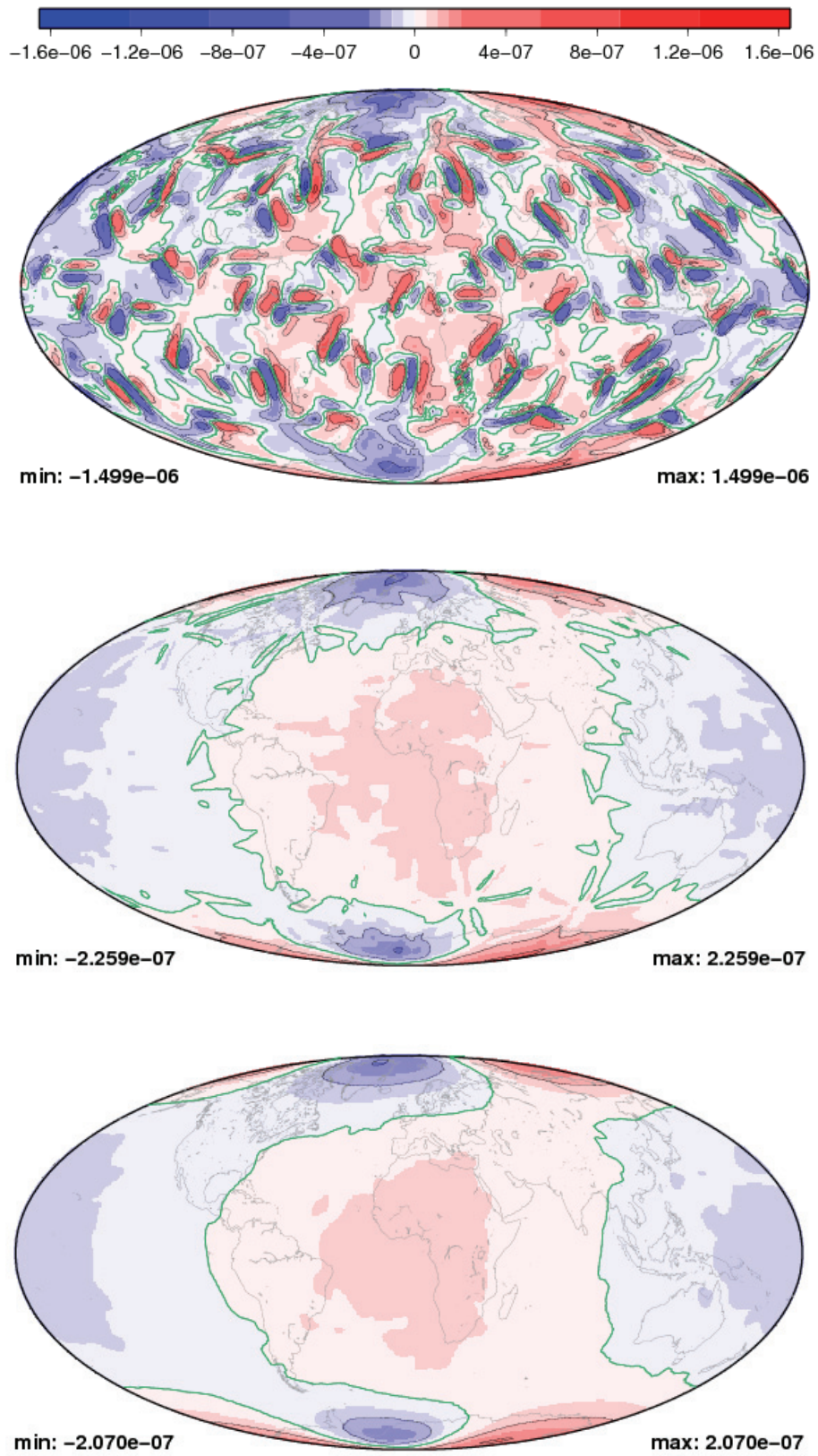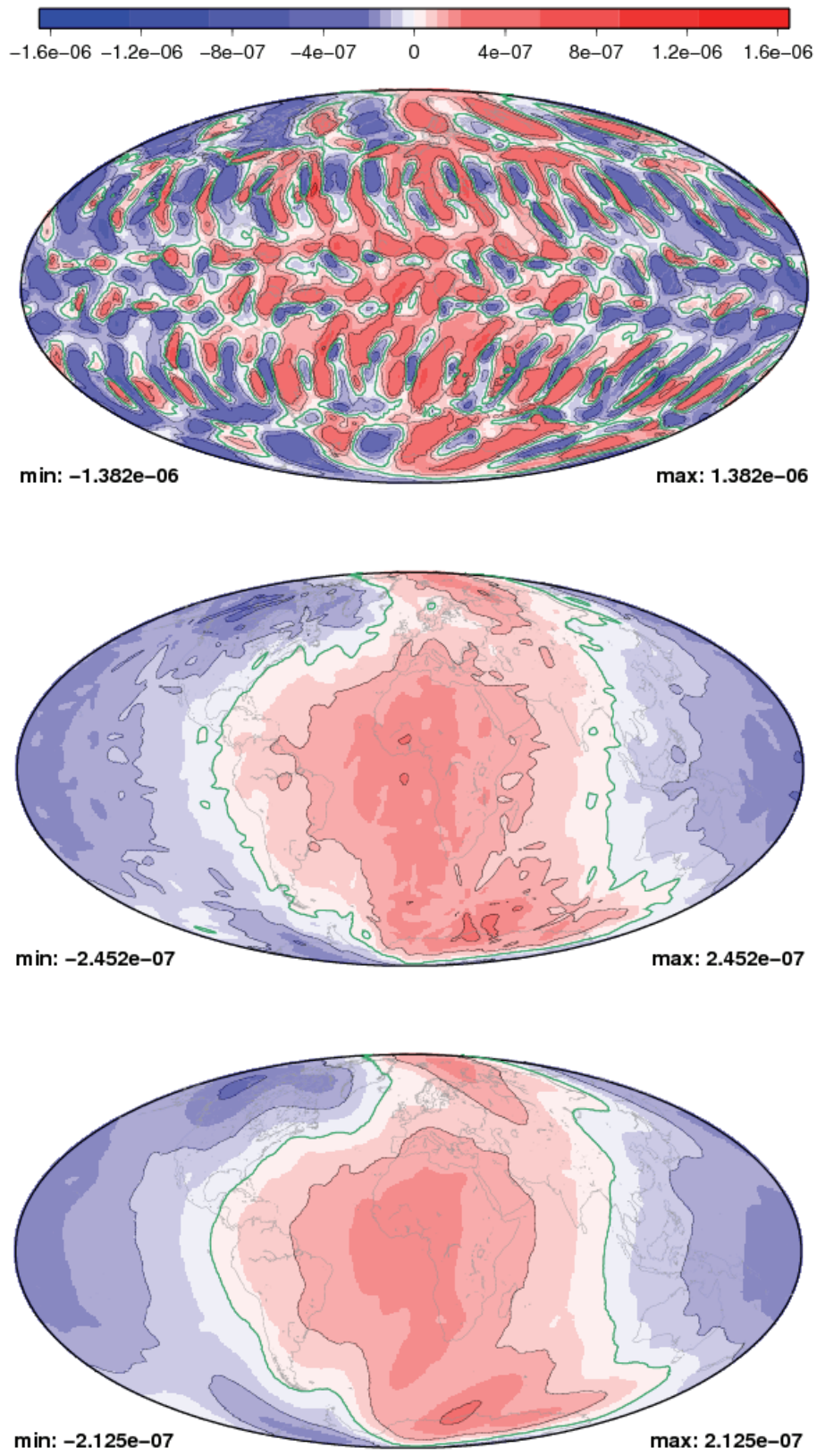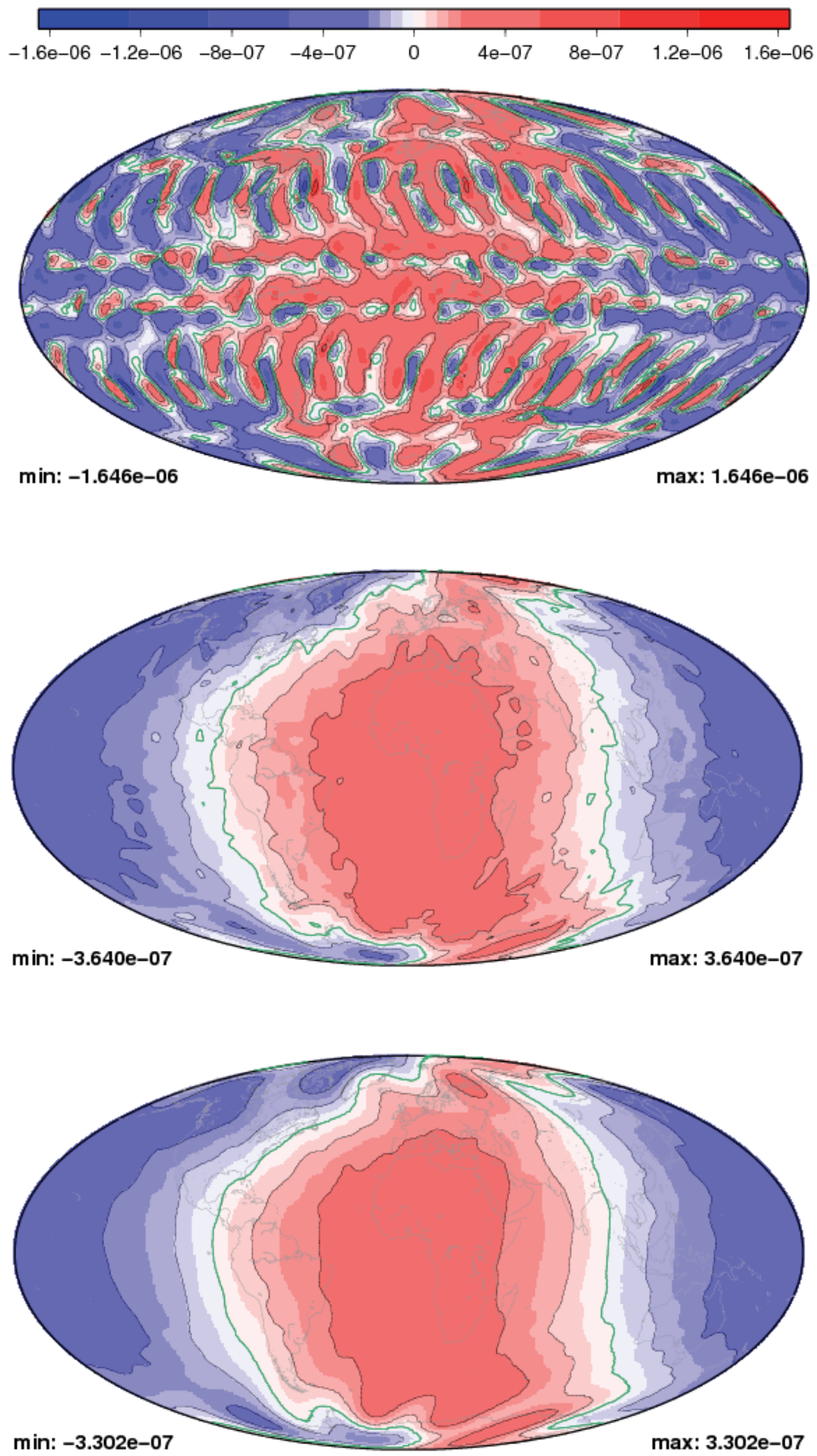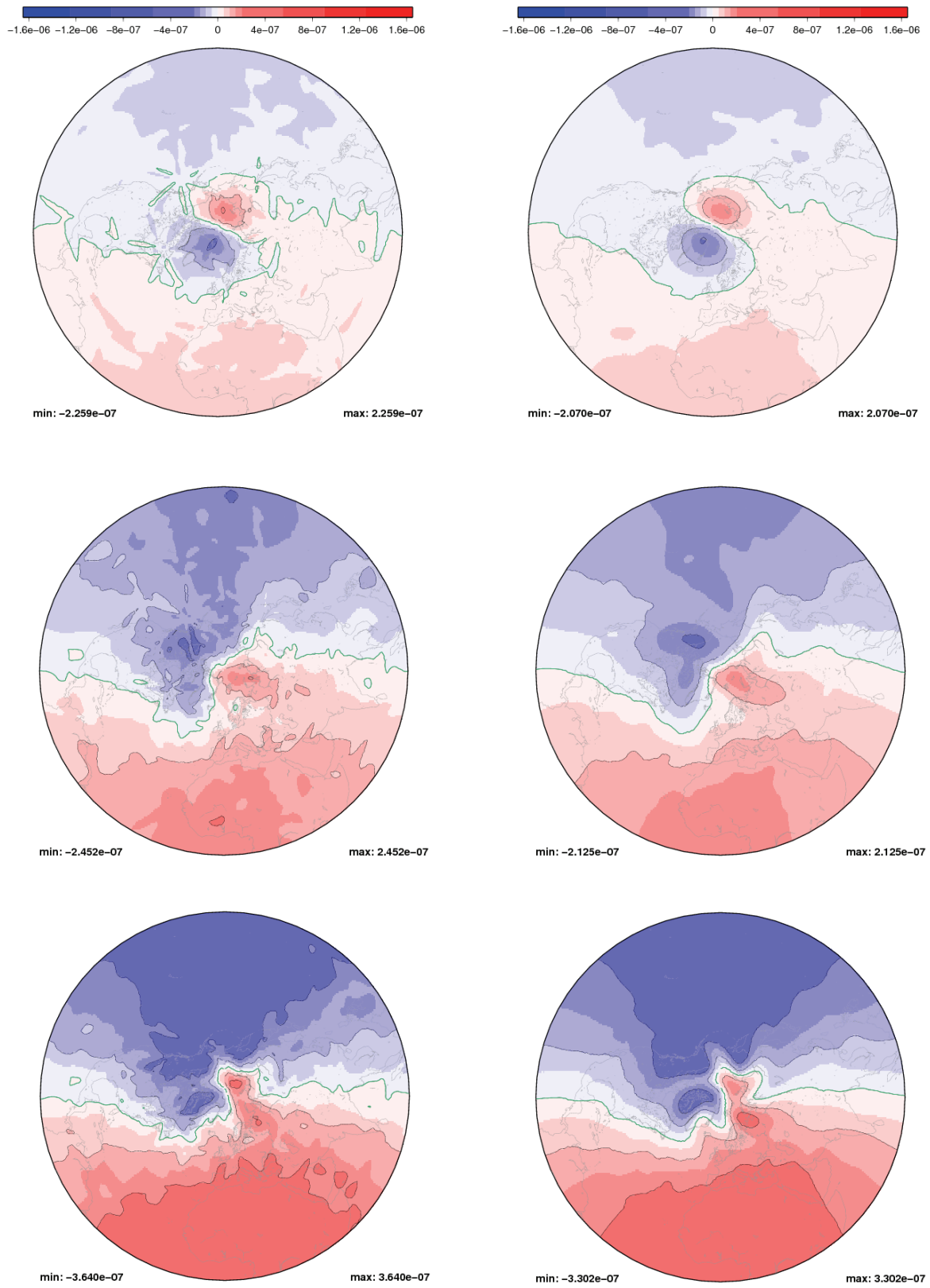Figure 5.86: Test case USBR: error of vorticity after day 5: **PF9**, **PF10**, **FEM**m**E**

Figure 5.87: Test case USBR: **PF10** and **FEM**m**E** error of vorticity after day 1, 3 and 5 North polar stereographic projection

The error patten of **PF9** are noisier, in particular visible after the first day. The location of the most positive and negative difference to the reference is the same as in the other two experiments. But the maximum difference is higher and the minimum difference smaller. So, the grid used in **PF9** introduces additional features and seems to be less suitable for this test case.

The stereographic plots of the northern hemisphere for **PF9** and **PF10** on page 99 are illustrating the above mentioned points.

This figure is followed by error plots of the vorticity on the next four pages. All plots use the same scale. As the error of **PF9** is by a factor of nearly five bigger the linear scale is modified in the vicinity of zero. Here the resolution is seven times higher than elsewhere to show detailed error structures for the **PF10** and **FEM***m***E** experiments.

Eye-catching are not only the higher errors of **PF9**, but also the different structure. One can classify these noisy patterns in three different regions. A polar one with wave number 5 structure. In the mid and low latitudes wave number 20 is visible. This region is interrupted by three bands where the errors are smaller or have the opposite sign.

In the other two experiments two zones can be distinguished. One located around the zero meridian where the vorticity of the model runs are higher than the reference and the region around the date line where the situation is vice versa. In contrast to the geopotential errors here both experiments can be well distinguished. On page 103 with the stereographic plots of the northern hemisphere they can be compared best. The error pattern are similar but those of **FEM***m***E** are smoother. This is another hint that for the numerical schemes used here the grid of **FEM***m***E** has better properties than the ones provided by *amatos*.

Adaptive setups

In all experiments using adaptive setups of **PLASMA-FEM***m***E** instabilities have arisen within the first 12 hours. In this paragraph an analysis of the problem is given.

Acting as a prototype following setup is chosen. The coarsest grid belongs to level 8, the finest to level 12. The minimum number of grid points is 15,000. Time step is set to $\Delta t = 90s$ and as refinement criterion the average criterion with the thresholds $\theta_{crs} = 0.6$ for coarsening and $\theta_{ref} = 1.6$ for refinement are taken. The watermark is set to $w = 0.3$ and the diminishing factor to $d = 0.9$.

Figure 5.88 gives an overview about the situation after 3 hours of simulation (120 time steps). At the top the adaptive grid is displayed, in the middle the error of geopotential and at the bottom the error of vorticity. The scale for the grid is adapted to this experiment and used in the following. The scale of the vorticity is that of the previous experiments. After 3 hours the instabilities are evolving. The maximum vorticity error is already one order of magnitude bigger and the maximum geopotential error twice as big than the biggest error observed within 5 days for the non adaptive experiments.

On can pick out two areas. One in the Atlantic close to Africa and one in the middle of the Pacific. The following discussion concentrates on the one in the Atlantic that is indicated by the black box in the vorticity plot. The left column of the next figure gives the details. In this region there are two instabilities evolving. The grid has already adapted to the left one. One hour or 40 time steps later the right column highlights the situation. Both errors have increased by one order of magnitude and the instability patterns start to propagate into the vicinity. The grid has adapted five times and has catched the two features. It refines there and coarsens elsewhere. Within the next two days the simulation stays stable, but the solid body rotation is destroyed and the grid adapts more and more often the more complex the flow develops.

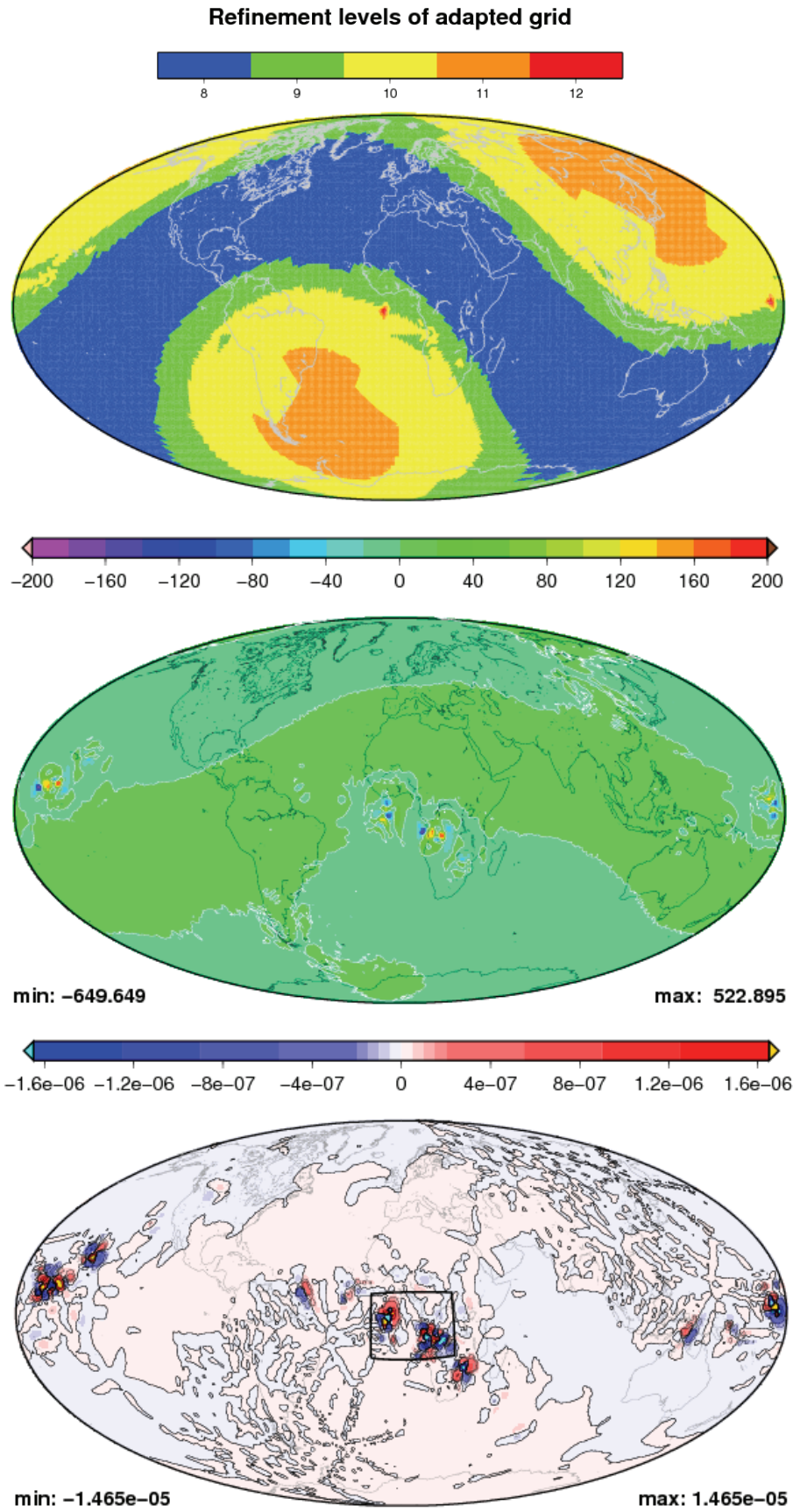Figure 5.88:   Test case USBR: snapshot of adaptive setup after 120 time steps
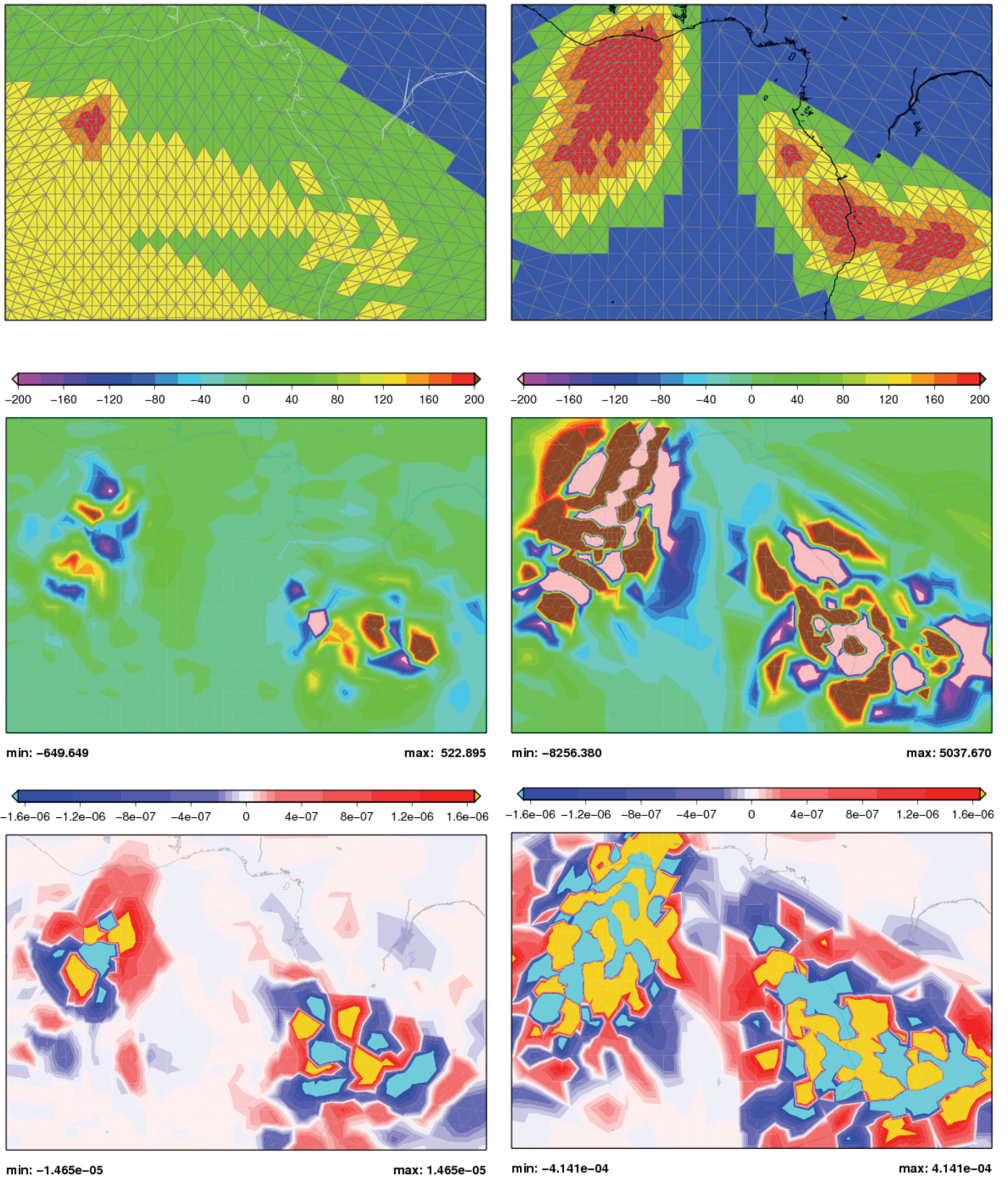Grid, error of geopotential and error of vorticity

Figure 5.89: Test case USBR: details of adaptive setup after 120 and 160 time steps
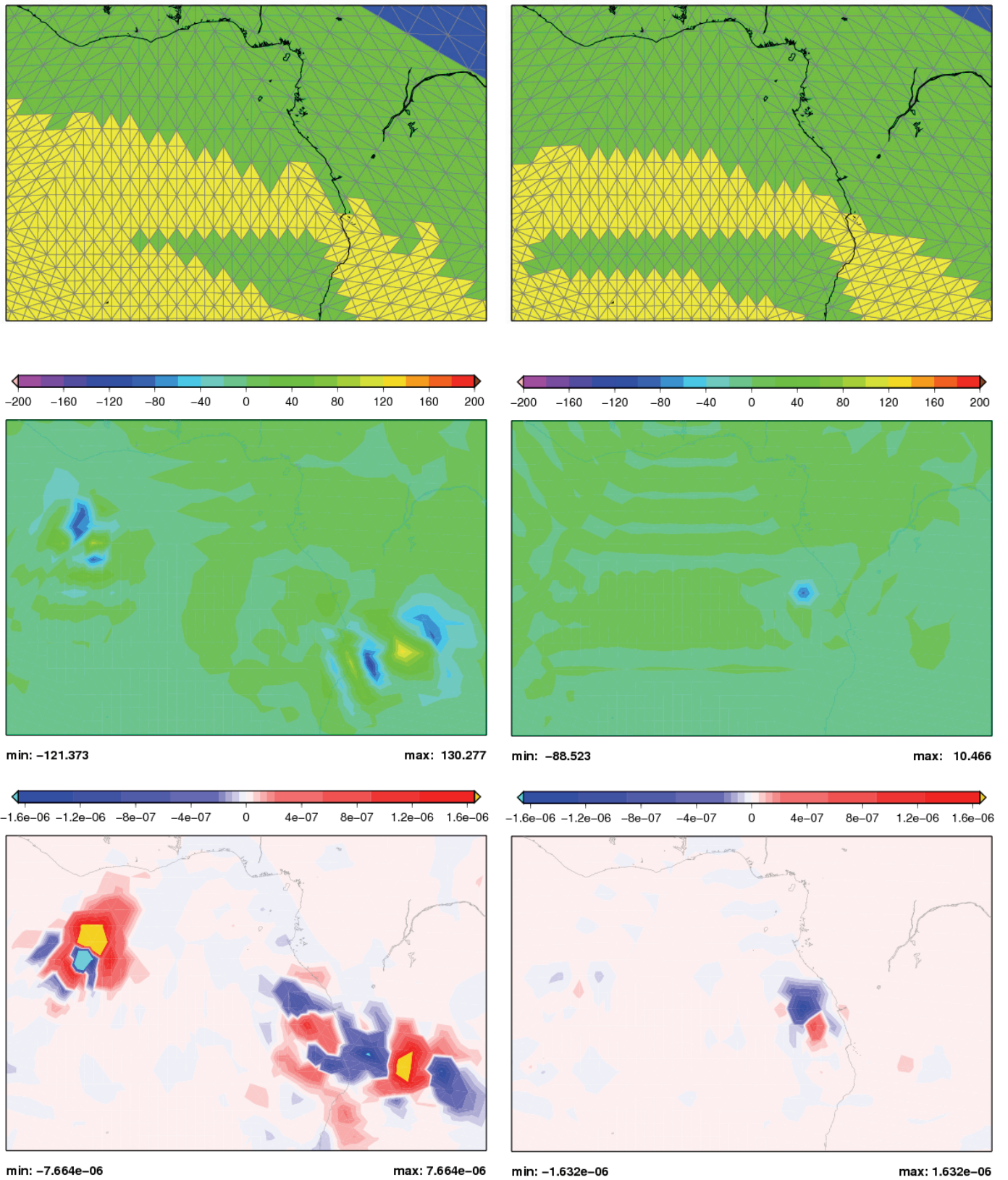Grid, error of geopotential and error of vorticity

Figure 5.90: Test case USBR: details of adaptive setup after 80 and 40 time steps Grid, error of geopotential and error of vorticity

Remains the question where, when and why do these instabilities arise in the adaptive setup?

The left and right column of Figure 5.90 shows the situation one hour earlier each. The adaption cycle has started 3 times in each hour. After 40 time steps first evidence of the problem is already visible. At least in the vorticity error in the region of the instabilities larger errors are detected.

Figures 5.91 and 5.92 on the next two pages shows the situation after 36, 33, 30 and 28 time steps. In between no grid adaptation takes place, so all figures show the same grid. That is the one of the top right panel in Figure 5.90. On top of each column the error of geopotential is presented using a four times finer scale than before. In the middle the velocity error is given. The colour scale corresponds to the length of the error arrows, the green arrows give the amount and direction of the error. Displayed are all arrows with an length bigger than $0.01\ ms^{-1}$. In all other grid points the error is smaller. The bottom figures are the vorticity error likewise with a finer scale. The minimum and maximum number beneath each plot give the maximum and minimum error of that quantity on the whole sphere at that point of time for comparison.

From Figure 5.92 one learns that the instability first is detectable in the vorticity error. No indication of it in the geopotential error, at least the errors in the areas in mind are not remarkable high. So it can be concluded that there might be a problem with calculation the velocities. But at time step 28 there are other points with a larger velocity error in the neighbourhood and the crucial point in the vorticity field is not exceptional in regard of the velocity error. It should be emphasised particularly that the velocity errors observed are very small. The absolute velocity in that area is around $25\ ms^{-1}$ that is 2500 times bigger than the threshold for an error arrow.

Following the above considerations the questions when and where this instabilities starts has been answered. But it is still unclear why. The vorticity is not a prognostic quantity of the used SW system. So there is no reason why a disturbance of the vorticity should lead to the instabilities.

Remains a close inspection of the grid. The two grid points with the highest vorticity error after 36 time steps can be singled out. Both are at the interface between level 8 and 9 and both have an asymmetrical neighbourhood. The northern point has 5 neighbours, one belong to level 9, two to level 8 and the other two are on the interface. The southern point has 8 neighbours. Five of them belong to level 9, one to level 8 and again two at the interface. It can be expected that *amatos* creates more points with that kind of neighbourship. If that is a problem one should expect that in other test cases similar instabilities arise, if they are only grid dependent. So far with **PLASMA-FEMmE** none has been observed. On the other side in all adaptive experiments with this test case instabilities are observed. Thus the author concludes that the adaptive setup in this test case fails due to the complex interaction of the grid, the adaption process, the flow pattern and the way the numerical calculations are done.

5.5.4   Summary of test case USBR results

The main points of the test case USBR experiments are:

1. Non adaptive mesh generation can handle this test case.

2. Twice as much grid points are needed with **PLASMA-FEMmE** to reach same accuracy as **FEMmE**.
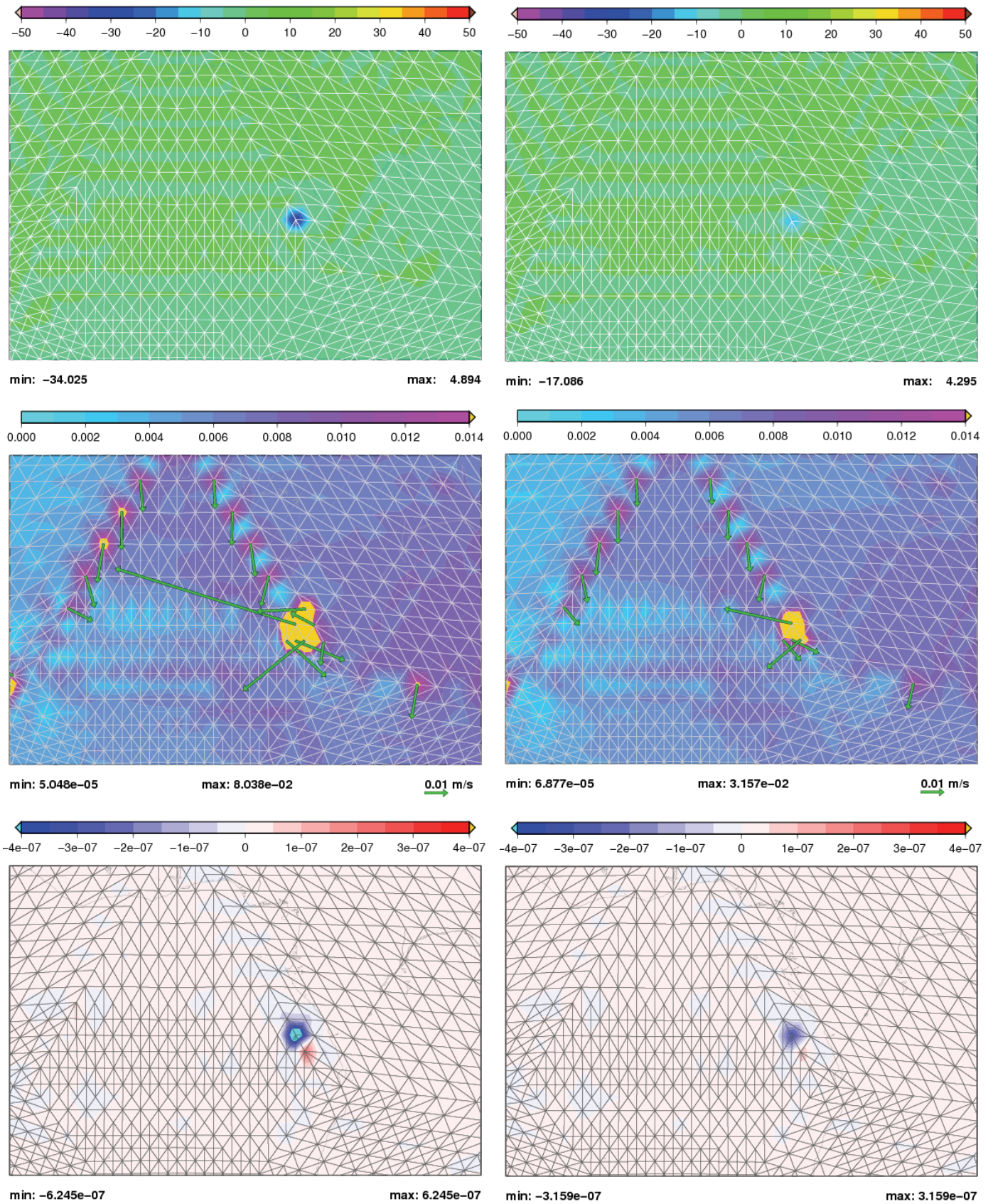
Figure 5.91: Test case USBR: details of adaptive setup after 36 and 33 time steps
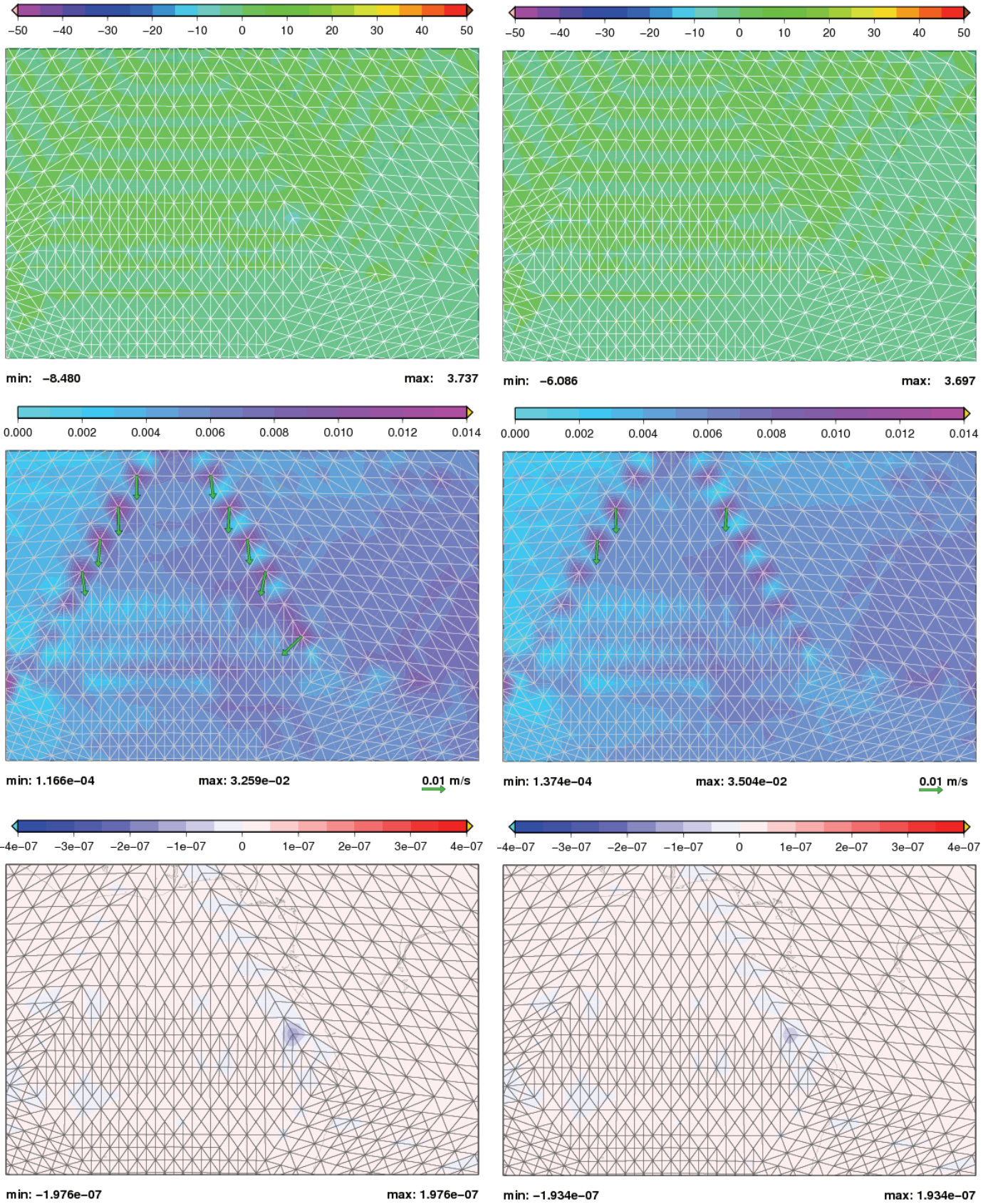Error of geopotential, velocity and vorticity

Figure 5.92: Test case USBR: details of adaptive setup after 30 and 28 time steps
Error of geopotential, velocity and vorticity

3. Conservation properties and error evolution are as expected and similar to test case 5 results.

4. Instabilities arise in the experiments with dynamic grid adaptation. One single cause cannot be identified. Interaction of *amatos*, design of test case and numerics are candidates for further inspection.

Especially the last point is a disappointing result as this test case is the only one with a non stationary analytic solution. Thus it allows to compare the numerical error dependent on the grid properties. Here it must be concluded that this comparison cannot be performed.

5.6 Conclusions and outlook

Besides the last one many promising results have been obtained with **PLASMA-FEM*m*E** that show the potential of this approach. With *amatos* the grid can easily adapt to the interesting features of the flows. The vorticity is a substantial part of the adaption process and therefore should play a major role in the indicator function. Another positive result is that no numerical reflections at the interfaces between the different grid levels are observed. Unfortunately in the last test case there is evidence for releasing instabilities at the grid interfaces. Nevertheless with **PLASMA-FEM*m*E** a tool for further investigations in the field of adaptive grids in atmospheric modelling is available that is capable of generating reasonable results.

The different orders of the normalised errors of geopotential and vorticity together with behaviour of the dynamic grid adaption in the time series of the relative vorticity are good reasons not to use the vorticity as a prognostic variable in the SWM as it is done for example in **PLASMA-P** (Läuter 2004). Though the relative vorticity is a conservative quantity in the SWE, the numerical difficulties advise to use the advective form of the SWE with geopotential and velocity as prognostic variables. On the other side on can take advantage of the higher sensitivity of the vorticity and use it for diagnosis of the flow and in the grid adaption process.

In comparison with **FEM*m*E** the loss of the conservation property of mass with most of the grids provided by *amatos* is a drawback. Here further research in direction of conservative schemes as proposed by Behrens and Mentrup (2005) should improve the results. The outcome of test case 2 makes clear that a minimum number of grid points must be used to obtain reasonable results. This number should be more than 15,000. Dynamic grid adaptation can reduce the numerical errors without increasing the number of grid points and hence the numerical effort. Experiment 2 and 4 of test case 2 give an impressing example of that. On the other side, the results of test case 5 show that dynamic grid adaptation in more realistic flow regimes increases the CPU time by a factor up to 4 without improving the results. Indeed, it should be noted that the used code is an academic one that was not developed under code optimisation aspects. Improvements in this direction will lead to faster results. Another option for reducing the CPU time is running the grid adaption not each time step but only after a limited number of time steps with an unchanged grid. Further investigations in this direction have to be done before making statements of the impact of this procedure on the numerical results. But nevertheless as shown static grid adaption really improves the results without increasing the numerical effort.

The instability problem of the last test case is a weak spot. In-depth examinations are necessary to understand the complex interaction between all involved processes. As no such thing has been observed in the other test cases a better understanding might solve this problem.

Also crucial is the grid adaption criterion. Though the important role of the vorticity has been shown the results of test case 5 reveals that there are additional physical features involved that also should be taken into account. An adjoint model as e.g. proposed by Power et al. (2006) for oceanic currents is a possible choice. Though such a model will enhance the numerical costs further the advantage would be that all physical processes that govern the flow can be taken into account at the same time.

So there are many options for future research. They should help to understand the mechanisms that are responsible for the instabilities, the loss of the conservation properties and the growth of the errors. Consequently this will lead to better grids and better numerical properties of the SWM.

> A work as this is never finished, one must simply declare it finished
> when one has within limits of time and circumstances, done what is possible.

> So eine Arbeit wird eigentlich nie fertig, man muss sie für fertig erklären,
> wenn man nach Zeit und Umständen das Mögliche getan hat.

Johann Wolfgang von Goethe, Italienische Reise, 16. März 1787

Appendix A

Derivation of spherical SWE

This derivation is taken from Heinze and Hense (2002). A concept to obtain the SWE (equations (2.3) and (2.4)) from the principles of conservation of mass and momentum is presented. The first is described by the continuity equation (A.1), the latter by the equation of motion (A.2).

$$\frac{d\rho}{dt} = -\rho \, \nabla \cdot \vec{v} \tag{A.1}$$

$$\frac{d\vec{v}}{dt} = -\frac{1}{\rho} \nabla p \, - \, 2 \, \vec{\Omega} \times \vec{v} \, - \, \vec{g} \tag{A.2}$$

where ρ is density, p is pressure, $\vec{\Omega}$ is the angular velocity of the earth's rotation and $\vec{g}$ is gravity with $g = |\vec{g}|$. Let r be the radial direction, r_b and r_t bottom and top of a layer that can vary in space and time, and r_0 any constant reference height (e.g. sea level height). The geopotential ϕ and orography ϕ_H are then defined by

$$\phi = g(r_t - r_0) \quad \text{and} \quad \phi_H = g(r_b - r_0). \tag{A.3}$$

Assuming incompressibility, $\rho = const$ in the fluid layer, equation (A.1) is reduced to

$$\nabla \cdot \vec{v} = 0. \tag{A.4}$$

Introducing a integrated radial velocity v_r^* and using the tangential component of velocity as well as the tangential operators as defined in chapter 2

$$v_r^* \, (r^*) = \int\limits_{r_0}^{r^*} \left(\nabla \cdot \vec{v} - \nabla_S \cdot \vec{v}_S \right) dr \tag{A.5}$$

and assuming $\nabla_S \cdot \vec{v}_S$ to be constant in radial direction, one gets

$$v_r^* \, (r_t) - v_r^* \, (r_b) = \int\limits_{r_b}^{r_t} \left(\nabla \cdot \vec{v} - \nabla_S \cdot \vec{v}_S \right) dr =$$

$$\int\limits_{r_b}^{r_t} \underbrace{\nabla \cdot \vec{v}}_{0} \, dr - \nabla_S \cdot \vec{v}_S \int\limits_{r_b}^{r_t} 1 \, dr = -\left(\nabla_S \cdot \vec{v}_S \right) \cdot \left(r_t - r_b \right). \tag{A.6}$$

If the layer consists of any material the velocities at the top and the bottom are given by

$$v_r^*(r_b) = \frac{dr_b}{dt} \quad \text{and} \quad v_r^*(r_t) = \frac{dr_t}{dt}. \tag{A.7}$$

Combining the equations (A.3), (A.6) and (A.7) one gets

$$\frac{d(\phi - \phi_H)}{dt} = -(\phi - \phi_H)\nabla_S \cdot \vec{v}_S. \tag{A.8}$$

In the same way as $\vec{v}$ in equation (2.2) $\vec{\Omega}$ can be split in a radial part, indicated by r, and a part tangential to the sphere, indicated by S. Applying this procedure to the Coriolis part $(\vec{\Omega} \times \vec{v})$ of equation (A.2) we receive

$$(\vec{\Omega} \times \vec{v})_r = \vec{\Omega}_S \times \vec{v}_S \tag{A.9}$$

$$(\vec{\Omega} \times \vec{v})_S = \frac{1}{2}f(\vec{e}_r \times \vec{v}_S) + v_r(\vec{\Omega}_S \times \vec{e}_r) \tag{A.10}$$

with $v_r = \vec{e}_r \cdot \vec{v}$. Next, equation (A.2) is multiplied with $\vec{e}_r$ and a scale analysis is performed:

$$\underbrace{\frac{dv_r}{dt}}_{I} = -\underbrace{\frac{1}{\rho}(\nabla p \cdot \vec{e}_r)}_{II} - \underbrace{2(\vec{\Omega}_S \times \vec{v}_S) \cdot \vec{e}_r}_{III} - \underbrace{g}_{IV}. \tag{A.11}$$

I and III are much smaller than the other terms in the considered flow regime. Omitting them we get the hydrostatic approximation

$$\frac{1}{\rho}\nabla p \cdot \vec{e}_r = \frac{1}{\rho}\frac{\partial p}{\partial r} = -g. \tag{A.12}$$

Assuming the pressure vanishes at the top of the system, we integrate equation (A.12) from any arbitrary height r_1 to the top:

$$\frac{1}{\rho}\int_{r_1}^{r_t}\frac{\partial p}{\partial r}dr = -\int_{r_1}^{r_t}g\,dr \tag{A.13}$$

$$\frac{1}{\rho}\left[\underbrace{p(r_t)}_{0} - p(r_1)\right] = -g(r_t - r_0 + r_0 - r_1) \tag{A.14}$$

$$\frac{1}{\rho}p(r_1) = \phi + g(r_0 - r_1). \tag{A.15}$$

Let $\vec{x}$ be a point on the sphere and r_0 and r_1 the corresponding heights to that point with proportion factors $k_0, k_1 \in \mathbb{R}$. Then

$$r_1 = k_1 r_0, \quad r_0 = k_0|\vec{x}| \quad \text{and} \tag{A.16}$$

$$\nabla_S(r_0 - r_1) = k_0(1 - k_1)\nabla_S|\vec{x}| = \vec{0}, \tag{A.17}$$

because $\nabla_S|\vec{x}| = \vec{0}$ for any point $\vec{x} \in S$. Hence independently from any height r_1

$$\frac{1}{\rho}\nabla_S p = \nabla_S \phi. \tag{A.18}$$

Thus the tangential component of equation (A.2) is

$$\frac{d\vec{v}_S}{dt} = -\nabla_S \phi - f(\vec{e}_r \times \vec{v}_S) - 2v_r(\vec{\Omega}_S \times \vec{e}_r). \tag{A.19}$$

Defining the kinetic energy K by

$$K = \frac{1}{2}\,\vec{v}\cdot\vec{v} = \frac{1}{2}\,\vec{v}_S\cdot\vec{v}_S \;+\; \frac{1}{2}\,v_r^2 \tag{A.20}$$

the substantial derivative of K is

$$\frac{dK}{dt} = \underbrace{\vec{v}\cdot\frac{d\vec{v}}{dt}}_{I} = \underbrace{\vec{v}_S\cdot\frac{d\vec{v}_S}{dt}}_{II} + \underbrace{v_r\cdot\frac{dv_r}{dt}}_{III}\,. \tag{A.21}$$

Utilising that the rate of change of the radial velocity, $\frac{dv_r}{dt}$, is negligible in the hydrostatic approximation, part III vanishes. Multiplying equation (A.2) with $\vec{v}$ [part I] it is realised that there is no contribution of the Coriolis part to $\frac{dK}{dt}$ as $\vec{v}\cdot(\vec{\Omega}\times\vec{v}) = 0$. But multiplying equation (A.19) with $\vec{v}_S$ [part II] there is a contribution by the last term of equation (A.19). In consequence of the hydrostatic approximation this part must also be neglected.
Finally we get the SWE on the sphere

$$\frac{d(\phi - \phi_H)}{dt} = -\,(\phi - \phi_H)\,\nabla_S\cdot\vec{v}_S \tag{A.22}$$

$$\frac{d\vec{v}_S}{dt} = -\nabla_S\,\phi - f(\vec{e}_r\times\vec{v}_S). \tag{A.23}$$

Inserting the splitting of the geopotential (2.1), equations (2.3) and (2.4) are obtained.

References

Arakawa, A. and V. R. Lamb (1981). A potential enstrophy and energy conserving scheme for the shallow water equations. Monthly Weather Review 109, 18–36.

Bader, M., S. Schraufstetter, C. A. Vigh, and J. Behrens (2008). Memory efficient adaptive mesh generation and implementation of multigrid algorithms using Sierpinski curves. International Journal of Computational Science and Engineering. *In print*.

Bänsch, E. (1991a). An adaptive finite-element strategy for the three-dimensional time-dependent Navier-Stokes equations. Journal of Computational and Applied Mathematics 8(1), 3–28.

Bänsch, E. (1991b). Local mesh refinement in 2 and 3 dimensions. Impact of Computing in Science and Engineering 3(3), 181–191.

Barros, S. R. M., D. Dent, L. Isaksen, and F. G. Wollenweber (1995). The IFS model: A parallel production weather code. Parallel Computing 21(10), 1621–1638.

Baumgardner, J. R. (1995). A semi-implicit semi-Lagrange method for the shallow water equations on a triangular mesh. Talk given on October, 17 at GMD-SCAI, St.Augustin, Germany.

Behrens, J. (1998). Atmospheric and ocean modelling with an adaptive finite element solver for the shallow-water equations. Applied Numerical Mathematics 26(1-2), 217–226.

Behrens, J. (2003). amatos - Adaptive mesh generator for atmosphere and ocean simulation. API Documentation Version 2.0.0, Technische Universität München, Munich, Germany. 35 pp. Online available at `http://www.amatos.info`.

Behrens, J. (2004). Adaptive mesh generator for atmosphere and ocean simulation - amatos. Technical Report TUM-M0409, Technische Universität München, Munich, Germany. 18 pp.

Behrens, J. (2005). Multilevel optimization by space-filling curves in adaptive atmospheric modeling. In F. Hülsemann, M. Kowarschik, and U. Rüde (Eds.), Frontiers in Simulation - 18th Symposium on Simulation Techniques, pp. 186–196. Erlangen, Germany: SCS Publishing House.

Behrens, J. and L. Mentrup (2005). A conservative scheme for 2d and 3d adaptive semi-lagrangian advection. In Z.-C. Shi, Z. Shen, T. Tang, and D. Yu (Eds.), Contemporary Mathematics, Volume 383, pp. 219–234. Providence, Rhode Island, USA: American Mathematical Society.

Behrens, J., N. Rakowsky, W. Hiller, D. Handorf, M. Läuter, J. Päpke, and K. Dethloff (2005). amatos: Parallel adaptive mesh generator for atmospheric and ocean simulations. Ocean Modelling 10(1-2), 171–183.

Blikberg, R. and T. Sørevik (2003). Computing the shallow water equations on a sphere by finite volume methods. In R. Blikberg (Ed.), Nested parallelism in OpenMP with applications to adaptive mesh refinement, Phd thesis, Part D, pp. 1–31. University of Bergen, Norway: Parallab/Department of Informatics.

Bonaventura, L. (2004). The ICON project: Development of a unified model using triangular geodesic grid. In Proceedings of the ECMWF annual seminar on development in numerical methods for atmosphere and ocean modeling, Shinfield Park, Reading, UK, pp. 75–86. ECMWF.

Bonaventura, L., L. Kornblueh, Th. Heinze, and P. Rípodas (2005). A semi-implicit method conserving mass and potential vorticity for the shallow water equations on the sphere. International Journal of Numerical Methods in Fluids 47, 863–869.

Braess, D. (2001). Finite elements (2nd ed.). Cambridge, UK: Cambridge University Press. 352 pp.

Cassirer, K., R. Hess, C. Jablonowski, and W. Joppich (1996). The shallow water test cases for a global model with documentation of the results. Arbeitspapiere der GMD 999, GMD-SCAI, Schloss Birlinghoven, St. Augustin, Germany. 75 pp.

Deuflhard, P. and A. Hohmann (2003). Numerical analysis in modern scientific computing, An introduction (2nd ed.). New York, USA: Springer. 337 pp.

Dziuk, G. (1988). Finite elements for the Beltrami-operator on arbitrary surfaces. In S. Hildebrandt and R. Leis (Eds.), Partial differential equations and calculus of variations, Volume 1357 of Lecture Notes in Mathematics, pp. 142–155. Berlin, Germany: Springer.

Giraldo, F. X. (2000). Lagrange-Galerkin methods on spherical geodesic grids: The shallow water equations. Journal of Computational Physics 160(1), 336–368.

Hack, J. J. and R. Jakob (1992). Description of a global shallow water model based on the spectral transform method. NCAR Technical Note NCAR/TN-343+STR, National Center for Atmospheric Research, Boulder, Colorado, USA. 39 pp.

Hackbusch, W. (1986). Theorie und Numerik elliptischer Differentialgleichungen, 1. Aufl. Stuttgart, Germany: Teubner. 276 pp.

Heikes, R. and D. A. Randall (1995). Numerical integration of the shallow-water equations on a twisted icosahedral grid. Part II: A detailed description of the grid and an analysis of numerical accuracy. Monthly Weather Review 123, 1881–1887.

Heinze, Th. (1998). Ein numerisches Verfahren zur Lösung der Flachwassergleichung auf einer rotierenden Kugel mittels der Lagrange-Galerkin-Methode. Diploma thesis, Institut für Angewandte Mathematik, Rheinische Friedrich-Wilhelms-Universität, Bonn, Germany. 113 pp. Online available at `http://wwwissrech.iam.uni-bonn.de/lehre/diplom/diplom_heinze.ps.gz`.

Heinze, Th. and A. Hense (2002). The shallow water equations on the sphere and their Lagrange-Galerkin solution. Meteorology and Atmospheric Physics 81(1-2), 129–137.

Houghton, J., Y. Ding, D. Griggs, M. Noguer, P. van der Linden, X. Dai, K. Maskell, and C. Johnson (Eds.) (2001). Climate change. The scientific basis. Contributions of working group I to the third assesment report of the Intergovernmental Panel on Climate Change. Cambridge, UK: Cambridge University Press. 882 pp.

Jablonowski, C., M. Herzog, J. E. Penner, R. C. Oehmke, Q. F. Stout, B. van Leer, and K. G. Powell (2006). Block-structured adaptive grids on the sphere: advection experiments. Monthly Weather Review 134, 3691–3713.

Lanser, D., J. G. Blom, and J. G. Verwer (2001). Time integration of the shallow water equations in spherical geometry. Journal of Computational Physics 171, 373–393.

Läuter, M. (2004). Großräumige Zirkulationsstrukturen in einem nichtlinearen adaptiven Atmosphärenmodell. Ph. D. thesis, Stiftung Alfred-Wegener-Institut für Polar- und Meeresforschung, Potsdam, Germany. 135 pp.

Leveque, R. J., J. O. Langseth, M. J. Berger, and S. Mitran (2000). CLAWPACK 4.0, a software package for conservation laws and hyperbolic systems. Technical report, University of Washington, Washington, USA. Online available at http://www.amath.washington.edu/~claw.

Majewski, D., D. Liermann, P. Prohl, B. Ritter, M. Buchhold, T. Hanisch, G. Paul, W. Wergen, and J. Baumgardner (2002). The operational global icosahedral-hexagonal gridpoint model GME: description and high resolution tests. Monthly Weather Review 130, 319–338.

Oehmke, R. (2003). High performance dynamic array structures. Ph. D. thesis, University of Michigan, Department of Electrical Engineering and Computer Science, Ann Arbor, Michigan, USA.

Oehmke, R. and Q. F. Stout (2001). Parallel adaptive blocks on a sphere. In Proceedings of the 11th SIAM Conference on Parallel Processing for Scientific Computing. SIAM, USA. Online available at http://www.eecs.umich.edu/~qstout/pap/SIAMPP01.ps, 9 pp.

Pesch, L. (2002). A finite-volume discretization of the shallow-water equations in spherical geometry. Diploma thesis, Meteorologisches Institut, Rheinische Friedrich-Wilhelms-Universität, Bonn, Germany. 92 pp.

Pichler, H. (1997). Dynamik der Atmosphäre (3. aktualisierte Aufl.). Heidelberg, Germany: Spektrum Akademischer Verlag. 572 pp.

Power, J. P., M. D. Piggot, F. Fang, G. J. Gorman, C. C. Pain, D. P. Marshall, A. J. H. Goddard, and I. M. Navon (2006). Adjoint goal-based error norms for adaptive mesh ocean modelling. Ocean Modelling 15, 3–38.

Ringler, T. D. and D. A. Randall (2002). A potential enstrophy and energy conserving numerical scheme for solution of the shallow-water equations a geodesic grid. Monthly Weather Review 130, 1397–1410.

Rípodas, P., L. Bonaventura, and L. Kornblueh (2005). New reference solutions for the Williamson et al. (1992) shallow water test cases. Online available at http://icon.enes.org.

Rivara, M. C. (1984). Mesh refinement processes based on the generalized bisection of simplices. SIAM Journal of Numerical Analysis 21, 604–613.

Schwarz, H. R. and N. Klöckler (2004). Numerische Mathematik, 5. überarb. Aufl. Stuttgart, Germany: Teubner. 573 pp.

Staniforth, A. and J. Côté (1991). Semi-Lagrangian integration schemes for atmospheric models - A review. Monthly Weather Review 119, 2206–2223.

Stuhne, G. R. and W. R. Peltier (1999). New icosahedral grid-point discretizations of the shallow water equations on the sphere. Journal of Computational Physics 148(1), 23–58.

Temperton, C. and A. Staniforth (1987). An efficient two-time-level semi-Lagrangian semi-implicit integration scheme. Quarterly Journal of the Royal Meteorological Society 113, 1025–1039.

Thuburn, J. (1997). A PV-based shallow-water model on a hexagonal-icosahedral grid. Monthly Weather Review 125, 2328–2347.

Thuburn, J. (2008). Some conservation issues for the dynamical cores of NWP and climate models. Journal of Computational Physics 227(7), 3715–3730.

Tomita, H., M. Tsugawa, M.Satoh, and K.Goto (2001). Shallow water model on a modified icosahedral grid by using spring dynamics. Journal of Computational Physics 174(2), 579–613.

Williamson, D. L., J. B. Drake, J. J. Hack, R. Jakob, and R. N. Swarztrauber (1992). A standard test set for numerical approximations to the shallow water equations in spherical geometry. Journal of Computational Physics 102(1), 211–224.

Dank